A Novel Control Technique for Active Shunt Power Filters for Aircraft Applications

Elisabetta Lavopa, M.Eng

Submitted to the University of Nottingham for the degree of Doctor of Philosophy, June 2011.

Abstract

The More Electric Aircraft is a technological trend in modern aerospace industry to increasingly use electrical power on board the aircraft in place of mechanical, hydraulic and pneumatic power to drive aircraft subsystems. This brings major changes to the aircraft electrical system, increasing the complexity of the network topology together with stability and power quality issues. Shunt active power filters are a viable solution for power quality enhancement, in order to comply with the standard recommendations. The aircraft electrical system is characterized by variable supply frequency in the range 360-900Hz, hence the harmonic components occur at high and variable frequencies, compared to the terrestrial 50/60Hz systems. In this kind of system, fast and accurate algorithms for the detection of the reference signal for the active filter control and robust high-bandwidth control techniques are needed, in order for the active filter to perform the harmonic elimination successfully.

In this thesis, two novel algorithms are proposed. The first algorithm is a frequency and harmonic detection technique, particularly suitable for tracking the variable supply frequency and the harmonic components of voltages and currents in the aircraft electrical system. Complete identification of the reference signal for the active filter control is possible when applying this technique. The second algorithm is a control technique based on the use of multiple rotating reference frames. Only the measurement of the voltage at the Point of Common Coupling and the active filter output current are needed, hence no current sensors are required on the distorting loads. Both the techniques have been validated by means of simulation and experimental analysis. The results show that the proposed methods are effective for a successful harmonic compensation by means of active shunt filters, in the More Electric Aircraft environment.

Contents

List of Figures

List of Tables

Chapter 1

Introduction

The latest research about civil aircraft systems has moved towards the increasing use of electric power in place of other conventional sources like mechanical, hydraulic, pneumatic power. This technological trend is known as the More Electric Aircraft.

Recent advances in the areas of power electronics, electric devices, control electronics, and microprocessors have allowed fast improvements in the performance of aircraft electrical systems. The use of more electric power brings significant advantages for the operation of the whole system. These advantages are listed here.

Advantages of the increasing use of electric power in the aircraft system:

- optimization of the performance

- optimization of the life cycle cost

- reduction of weight and size of the equipment

- increased reliability

Important changes are brought to the aircraft electrical system due to the increasing use of electric power on board. These changes are listed below.

Consequences of the increasing use of electric power on the aircraft electrical system:

- **more** electrical loads

- **more** complex topology of the electrical network

- **more** generation demand

- **more** power electronic equipment

- **more** stability issues

- **more** power quality issues

These aspects have to be taken into account when designing the devices in the system. It is crucial to guarantee that not only the device itself functions properly according to the specifications, but also that the interaction with the whole system respects the required conditions. In a system like the aircraft power network, the amount of generated power cannot be considered as infinite compared to the demanded power. Furthermore, maximum reliability is required from all the subsystems, hence multiple levels of redundancy and high fault tolerance level characterize the devices. Strict limitations are imposed on the stability and the power quality of the aircraft power system, in order to guarantee its optimal performance. Particularly, limitations on the voltage and current harmonics injected by the distorting loads are strictly recommended by aircraft regulations. In order to respect these conditions, the power electronic devices used on board have to be designed in order to inject the minimum amount of harmonics and the harmonics which exceed the maximum allowed level have to be eliminated or compensated.

Shunt active power filters provide an effective solution for the harmonic elimination and the improvement of the power quality in this kind of system. The shunt active filter works as a controlled current source which injects into the grid an amount of harmonic current equal to the one drawn by the distorting loads. A closed-loop control system is implemented so that the active filter injects a current which follows the reference signal, corresponding to the harmonic content of the load.

The main challenge encountered when designing an active filter for an aircraft power system is related to the supply fundamental frequency, which is chosen to be variable in the range 360-900Hz (frequency-wild power system). Due to such values of fundamental frequency, the harmonic components occur at high frequencies, compared to the terrestrial 50/60Hz electric grid. The two main issues which have to be addressed when designing the control for an active filter are: the generation of the reference signal and the reference signal tracking. These two issues are related to the two main objectives of the work presented in this thesis. Both objectives have been analysed and a solution to both challenges has been investigated and validated through simulation and experimental work.

In order to generate the reference signal for the active filter, an accurate estimation algorithm is required. The high frequency harmonic content of the current drawn by the distorting load has to be detected in real-time and fed into the control system. This work proposes a real-time detection algorithm based on the Discrete Fourier Transform (DFT), which can estimate the fundamental frequency and phase and the amplitudes and phases of the harmonics. This technique is suitable for the aircraft frequency-wild system.

In order to track the reference, a robust and accurate control method has to be applied. This work proposes a control technique based on the detection of the voltage at the Point of Common Coupling (PCC) between the power supply, the active filter and the distorting loads. Multiple rotating reference frames are implemented in order to develop as many control loops as the harmonics to be compensated. The harmonic content of the current drawn by the distorting loads is estimated on the basis of the measurement and analysis of the PCC voltage, hence no current sensors on the load are needed. In this way, the active filter can work as a plug-and-play system that can eliminate the harmonics at the point of the network where it is installed.

The main goals of this work, and the proposed solutions to achieve them are summarized in table 1.1.

	Goal	Proposed solution
1	Generating the reference	Real-time DFT-based detection algorithm
2	Tracking the reference	Control technique based on the PCC voltage detection

Table 1.1: Main objectives of the thesis

1.1 Structure of the thesis

The thesis is structured in the following way.

In Chapter 2 the concept of the More Electric Aircraft is presented. The chapter describes how the challenges posed by the More Electric Aircraft are related to the work proposed in this project and how the proposed solutions can improve the operating conditions of the aircraft power network.

Chapter 3 presents a novel technique for frequency and harmonic estimation based on the Discrete Fourier Transform (DFT). This technique allows the estimation of fundamental frequency, fundamental phase angle and harmonic amplitudes and phases of a time-varying distorted signal in real time. The results obtained from the simulation and experimental validation are presented and discussed.

The DFT-based detection technique is compared with a standard Phase-Locked Loop in Chapter 4. Simulation and experimental validation show the differences between the performances of the two algorithms. The results are presented and discussed in this chapter.

Chapter 5 presents a multiple reference frames control technique based on the measurement of the voltage at the PCC. This technique allows the harmonic compensation to be performed without using any sensor on the distorting load, but only on the PCC and on the active filter itself. The multiple reference frame implementation is discussed, along with the decoupling technique between the different frames. A description of the control structure and the design of the controllers is given.

The results obtained from the simulation and experimental validation of the voltage detection control technique proposed in Chapter 5 are given in Chapter 6 and Chapter 7 respectively. From the comparison between Chapter 6 and Chapter 7 a good accordance between the simulation and experimental results can be seen.

In Chapter 8, conclusions are drawn from the work presented and the goals achieved. Also, areas of further research are highlighted.

Chapter 2

The More Electric Aircraft

2.1 Introduction

This chapter describes the concept of the More Electric Aircraft, its characteristics and advantages with respect to the conventional aircraft system. The consequences of the choice of the new technology on the aircraft electric system are listed. The chapter finally describes how the challenges posed by the More Electric Aircraft are related to the work proposed in this project and how the proposed solutions can improve the operating conditions of the aircraft power network, particularly with regard to the power quality and harmonic cancellation by means of power active shunt filters.

2.2 The More Electric Aircraft concept

The More Electric Aircraft follows the technological trend in modern aircraft to increasingly use electrical power on board of the aircraft in place of mechanical, hydraulic and pneumatic power to drive aircraft subsystems [1] [2] [3]. Recent advances in the areas of power electronics, electric devices, control electronics, and microprocessors have allowed a fast improvement in the performance of aircraft

7

electrical systems.

The increased use of electrical power presents significant advantages such as optimization of the performance and the life cycle cost of the aircraft, reduction of the fuel consumption, and reduction of the weight and size of the system equipment as well as the potential for improved condition monitoring and maintenance cycles. However the More Electric Aircraft brings major changes in the aircraft electrical power system, such as an increase of electrical loads and power electronic equipment, a more complex topology for the electrical network, significantly higher levels of electrical distribution which in turn result in greater power quality and stability problems [4].

The schemes in figures 2.1 and 2.2 show the distribution of the power sources in the conventional aircraft and the More Electric Aircraft respectively [5]. In the first scheme it can be seen that the conventional aircraft subsystems operate by means of different kinds of power sources. The second scheme shows that the electrical power generated on board of a More Electric Aircraft is much higher than in the conventional aircraft and most of the subsystems are electrically operated. The electrical power on board of a More Electric Aircraft is about 1MW magnitude [5].

The subsystems conventionally supplied by electrical power are: energy storage system, engine starting system, ignition system, de-icing system, landing gear control, anti-skid control system, passenger cabin services, avionics, lighting systems. In the More Electric Aircraft, the electrically powered subsystems are: flight control systems, electric anti-icing, environmental systems, electric-actuated brakes, utility actuators, fuel pumping. In the conventional aircraft the distribution network is a point-to-point topology in which all the electrical wirings are distributed from the main bus to the different loads through relays and switches. This kind of distribution network leads to expensive and heavy wiring circuits, and it is not suitable for a system where bigger electrical power is involved. In the More Electric Aircraft, different kinds of loads are used which require different levels of voltage, therefore the future aircraft electrical systems will employ multi-voltage level hybrid DC and AC systems. As a result, different kinds of power electronic converters such as AC/DC rectifiers, DC/AC inverters and DC/DC choppers are

Figure 2.1: Power sources distribution on the conventional aircraft
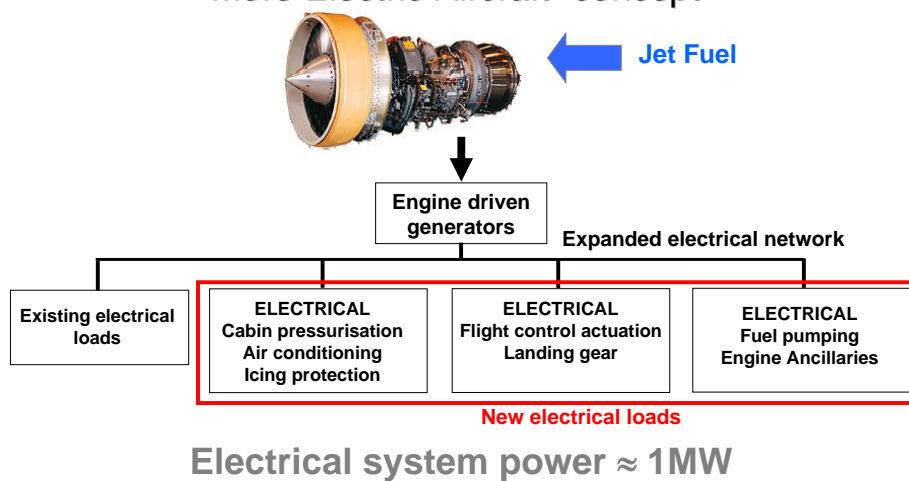
Figure 2.2: Power sources distribution on the More Electric Aircraft

required [6].

The typical aircraft electrical system of the past was the twin 28 VDC system. It was commonly used on twin-engined aircraft, where each engine powered a 28 VDC generator. Due to the increase in the power requirements, the electrical generation on board of the aircraft changed into the 115 VAC system. The AC distribution in the aircraft power network can be at constant frequency, equal to 400Hz, or at variable frequency, from 360Hz to 900Hz. In the first case, the frequency-wild power from the AC generator is converted to 400Hz constant frequency 115VAC power by means of a solid-state Variable-Speed/Constant-Frequency (VSCF) converter [7] [8]. In the second case, the power is distributed at variable frequency and converted locally for the loads which need constant frequency supply, by means of power electronics converters [9] [10].

In the latest research concerning the More Electric Aircraft, great attention is being paid on the ever increasing levels of power requirements, due to the replacement of many non-electrical loads with electrical ones. In order to meet the high power requirements, a distribution system characterized by a voltage level equal to 230 VAC, with frequency variable between 360Hz and 900Hz, and 540 VDC is considered the most viable solution. Figure 2.3 shows the general scheme of one half of an aircraft power network (assuming a symmetrical system). In the scheme the main parts of the network are the two electrical generators connected to the engine, the AC and DC buses, the loads connected to them, the electronic power converters and the active filters installed for harmonic compensation.

Generally the aircraft power system is symmetrical, with two generators G1 and G2 and two Auxiliary Power Units APU1 and APU2 connected to each engine. The loads can be classified as essential and non-essential. Each generation channel supplies a set of non-essential loads, while the essential loads are supplied by both generators in parallel. The electrical power is distributed at different levels of voltage: 230 VAC, 115 VAC, 540 VDC, 28 VAC.
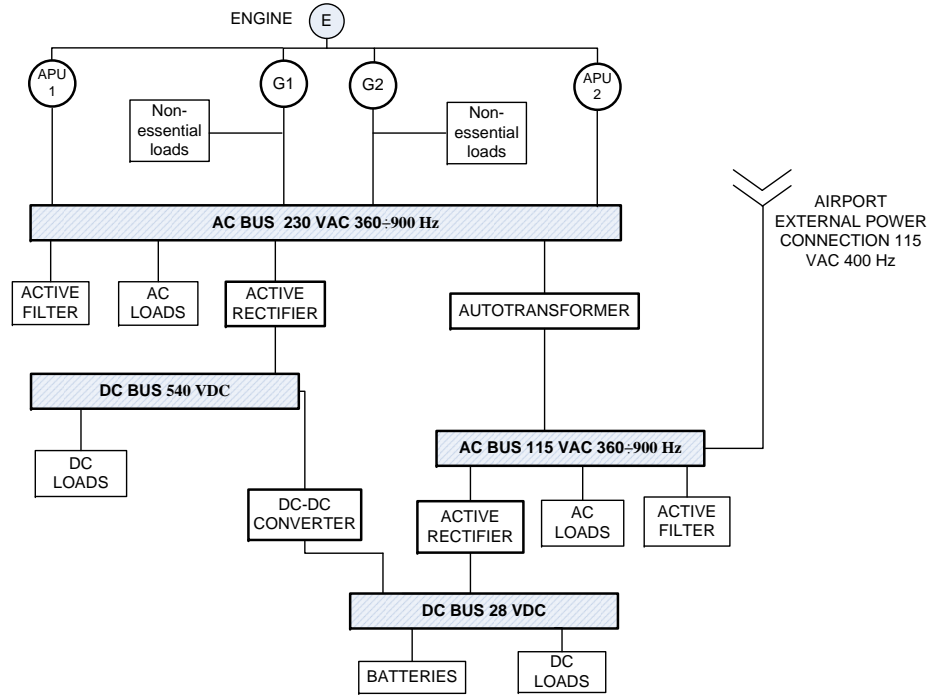
Figure 2.3: Scheme of an aircraft power network (half)

2.3 Power quality in the aircraft power system

Due to the presence of a large number of power electronic devices on board of the More Electric Aircraft, it is important to address the power quality issue in order to guarantee a correct and efficient operation of the electrical system and its stability.

Recently revised airborne electrical system environmental standards such as DO-160D [11] and ISO-1540 [12] introduced stringent limits on the harmonic level of the currents which the user equipment can draw from the supply. The aircraft power system represents a weak network where the amount of generated power is limited and matters like size and weight of the equipment and the wiring have a crucial importance. High-current harmonics can cause severe voltage distortion, unbalance in the aircraft electric power system and can lead to interference with the aircraft communication system as well as sensitive control and navigation equipment. Power electronic converters should be designed in such a way as to

reduce the harmonic distortion or filtering solutions can be implemented in order
to compensate for the harmonics generated by the distorting loads.

In an aircraft power system, designing a converter that can meet the power quality
requirements is challenging because of the high fundamental frequency (400Hz at
constant frequency or 360-900Hz at variable frequency). Achieving low input
current distortion and unity power factor at such high frequencies requires much
wider control bandwidth compared to what is necessary for terrestrial 50/60Hz
systems.

Several studies have been carried out on the operation and control of the power
electronic converters on board of the aircraft, and different solutions have been
investigated in order to limit the voltage and current harmonic distortion. In
[13] the authors investigate the power quality problems related to the dynamic
interaction between AC/DC converters with active power factor correction (PFC)
and the power supply. A solution for the elimination of the undesirable interactions
by means of proper damping of the PFC converter input filter is proposed and
validated. In [14] the design of a zero-voltage-switching active-clamped isolated
low-harmonic SEPIC rectifier is presented, for aircraft applications. The design
is carried out in order to meet the power quality requirements and harmonic
distortion limits recommended by the regulations.

In order to compensate for the harmonics injected by the distorting loads in the
system, it is not only necessary to utilize converters with a suitable topology and
design which meet the power quality standards, but it is also important to imple-
ment filtering. Traditionally, several topologies of passive filters have been utilized
for the elimination of the harmonics. The most popular configuration is the L-C
tuned filter which works like a low-impedance path for the harmonic component to
be eliminated. However, passive filters present several drawbacks, such as ageing
and tuning problems, series and parallel resonances, bulk passive components and
low flexibility in the compensation characteristics. These drawbacks represent a
strong limitation in the choice of passive filters in a system like the aircraft elec-
tric network, because of the weight and size of the components, and the variable
supply frequency.

Active power filters represent a feasible solution to the problems caused by the non-linear loads. The active filters can compensate for the harmonics, correct the power factor and work as a reactive power compensator, thus providing enhancement of the power quality in the system. In [15] the performance of an aircraft power system is investigated and harmonic compensation by means of a shunt active power filter is analysed. In [16] an active power filter is designed for harmonic compensation, power factor correction and minimization of the load unbalance, for an aircraft power system with Variable-Speed Constant-Frequency (VSCF) generating system.

The main challenge related to the implementation of harmonic compensation by means of an active filter in a system like the aircraft power network is, as mentioned above, the fundamental frequency, which varies in a range of high values, compared to the conventional 50/60Hz of terrestrial systems. In order for the control of the active filter to work properly, it is necessary to perform an accurate calculation of the reference and to implement a control technique with high bandwidth or generally able to track high frequency harmonics.

With regard to the calculation of the reference for the active filter control, in this project a novel frequency and harmonic detection technique is proposed. It is suitable for the accurate calculation of the reference in a system where the supply frequency is variable and ranges between high values.

With regard to the active filter control, this project proposes a novel control technique based on the decoupling between different rotating reference frames and the detection of the harmonic content on the basis of the voltage at the Point of Common Coupling (PCC). This technique is suitable for a system like the aircraft power network. The current harmonics injected by a group of non-linear loads can be detected by measuring the harmonic content of the voltage at the point where the active filter is connected. In this way there is no need to employ current transducers on each of the distorting loads, and the same active filter can be utilized as a plug-and-play device that compensates the harmonic distortion in different points of the distribution bus. The active filter can be connected in order to provide harmonic compensation locally for a specific distorting load or for a

big group of loads (for an adequate power level). These characteristics represent a big advantage in a system where the size and the weight of the equipment have a crucial importance.

In the future development of More Electric Aircraft power systems, a coordinated control of several active filters through the use of a communication network would bring advantages like better control of the power quality in any point of the network, control of local energy storage to assist with fault clearance and supply distribution.

2.4 Summary

In this chapter the concept of the More Electric Aircraft has been presented and explained. The use of electrical power in place of other conventional sources of power to run the aircraft subsystems presents several advantages in terms of efficiency, maintenance, cost, size and weight, but it introduces major changes in the aircraft power system. The consequence of this is a more complex electric network, with increased power quality and stability problems. An effective solution for power quality improvement in this kind of system is the power active shunt filter. For the work presented in this thesis a novel solution for the calculation of the reference for the active filter control and a novel control technique are proposed. The proposed techniques are suitable for applications in the More Electric Aircraft power system.

Chapter 3

Real-time Frequency and Harmonic Estimation Technique

3.1   Introduction

This chapter presents a novel technique for frequency and harmonic estimation based on the Discrete Fourier Transform (DFT). This technique allows the estimation of fundamental frequency, fundamental phase angle and harmonic amplitudes and phases of a time-varying distorted signal in real time. The technique has been validated both through simulation analysis and experimental tests. Section 3.2 presents the state of the art of the most common harmonic detection techniques. Sections 3.3 and 3.4 describe the frequency detection algorithm, by explaining its mathematical foundations, and present the simulation results. In sections 3.5 and 3.6 the technique for the estimation of harmonic amplitudes and phases and the simulation results are presented. Sections 3.7 and 3.8 present the results obtained by means of the experimental validation. In section 3.9 some considerations about the transient analysis of the harmonic estimation are discussed.

3.2 Overview of frequency and harmonic estimation techniques

A fast and exact estimation of fundamental line frequency, phase and harmonic content of the current drawn by a non-linear load is required in order to calculate an accurate reference signal for the active filter control algorithm, to achieve precise harmonic compensation. Several algorithms for frequency estimation and harmonic analysis have been proposed in the literature. Some of the most important and commonly used methods are listed here and described.

One of the first methods used for harmonic and frequency detection is the Recursive Discrete Fourier Transform (RDFT) [17–21]. This method utilizes a state variable representation of the time-discrete signal and a recursive deadbeat observer. Such a technique was developed in order to overcome problems of real time computational complexity related to DFT calculations.

A widely used method for frequency estimation is the least squares error technique [22–25], where the aim is to minimize the square error between the measured signal and the modelled signal. The performance of the algorithm is affected by the width of the observation window, the choice of the sampling frequency, the choice of the reference time, and the Taylor Series truncation.

Another broadly used technique is the Kalman Filter [26–31], a recursive stochastic technique that gives an optimal estimation of state variables of a given dynamic system from noisy measurements. At every iteration step a prediction of the state is calculated on the basis of the state at the previous step and the measurement and the prediction is corrected in order to minimize the error. The main drawback of Kalman filter-based algorithms is represented by the choice of the initial covariance matrices of the model and measurement errors.

The Phase Locked Loop (PLL) is also widely used for frequency and phase detection [32–37]. Its basic configuration consists of a feedback loop which includes a phase detector, a low-pass filter and a voltage controlled oscillator. The PLL provides fast and robust frequency estimation, even for distorted and unbalanced

conditions; however in some cases its performance can be affected by a wrong choice of the centre frequency, undesired oscillations due to harmonics and sub-harmonics, transient errors due to a narrow bandwidth chosen to achieve a good noise rejection. The PLL technique will be described in more detail in this chapter. Furthermore a comparison with the technique proposed in this work will be presented in Chapter 4.

Other categories of techniques for frequency and harmonic detection are: genetic algorithms, wavelet transform, PQ theory, neural networks [38–43].

In this project an algorithm based on the Discrete Fourier Transform is proposed for frequency and harmonic detection. It gives real-time estimation of fundamental frequency, fundamental amplitude, fundamental phase, and harmonic amplitudes and phases, for a noisy distorted signal with time-varying amplitude and frequency. The frequency and phase estimation provided by this method is characterized by high accuracy and low sensitivity to harmonic distortion and noise. It shows good tracking performance for signals with variable frequency. Also, the harmonic amplitudes and phases are identified with high accuracy. The characteristic parameters of the algorithm can be easily set. Furthermore, for a given set of parameters, the estimation can be performed for a broad range of frequencies and amplitudes of the signal, without the need to re-tune the initial settings.

A description of this estimation technique is given in the next section.

3.3   Frequency estimation technique

The technique here proposed to detect the fundamental frequency is based on the principle that, in the FFT spectrum of a signal, the fundamental component has the highest amplitude. When the exact value of fundamental frequency is unknown it can be detected, within the limits of the frequency resolution, by finding the highest component in the voltage (or current) spectrum and calculating its corresponding frequency. In the hypothesis that an initial estimate of frequency is known, the spectrum of the signal can be scanned in a narrow range of frequency

around the first estimate, in order to find the highest spectral component within the leakage sideband. This process can be iterated by means of a closed-loop control system. The leakage is due to the time domain truncation occurring when windowing the signal for spectral analysis. For this kind of frequency analysis and for its application it is preferable that the spread of the spectral lines is in a short interval of frequency (*short-range leakage*), because if the spread is long (*long-range leakage*) harmonic interference can occur so that larger errors result, as will be explained further on in this chapter. To avoid long-range leakage, suitable windows must be applied to the signal. Among different types of window, a normalized Hamming window has been chosen. It was observed that the performance obtained using this window was particularly good in terms of short-range leakage characteristics, compared to other types of window.

In the hypothesis that a rough idea of the value of frequency is known, which is often the case in an electrical power system, an initial value f_1 is chosen for the estimate. Given the initial estimate f_1, it is possible to obtain an estimate Δf of the difference between f_1 and the actual value of the fundamental frequency. The estimated Δf depends on the amplitudes of three spectral components [44]: the one at f_1 and the two adjacent ones at $f_1 \pm df$, where df is the spectral resolution chosen to represent the signal in the frequency domain. Δf is calculated according to (3.1):

$$\Delta f = \frac{1.5 \cdot df \cdot am_1 \cdot (am_{11} - am_{12})}{(am_1 + am_{11}) \cdot (am_1 + am_{12})} \tag{3.1}$$

where am_1 is the amplitude of the spectral line at frequency f_1, am_{11} and am_{12} are the amplitudes of the right and the left components at $f_1 + df$ and $f_1 - df$ respectively. The mathematical demonstration of (3.1) is presented in Appendix A of [45].

The three amplitudes can be calculated by means of a procedure based on the Discrete Fourier Transform, as follows. The voltage or current in a sinusoidal single-phase circuit can be represented by a rotating vector, as well as a complex quantity with real and imaginary parts which vary sinusoidally in the time domain. It is possible to express this complex quantity with the following exponential

function:

$$Ae^{j\varphi} = A cos(\varphi) + jA sin(\varphi) \tag{3.2}$$

where

$$\varphi = \int_0^t \omega(t)dt \tag{3.3}$$

A is the amplitude and ω is the angular frequency. The real and imaginary parts are the projections on a pair of cartesian axes of a vector rotating with speed $\omega(t)$. In a three-phase system the voltage (or current) is represented by a rotating vector, and this vector can be expressed as the sum of a positive, a negative and a zero sequence component. The three voltages v_a, v_b, v_c are commonly expressed using a reference frame $\alpha\beta0$ defined as follows:

$$\begin{cases} \overline{v_{\alpha\beta}} = v_\alpha(t) + jv_\beta(t) = \frac{2}{3}\left[v_a(t) + v_b(t)e^{j\frac{2}{3}\pi} + v_c(t)e^{j\frac{4}{3}\pi}\right] \\ v_0(t) = \frac{1}{3}\left[v_a(t) + v_b(t) + v_c(t)\right] \end{cases} \tag{3.4}$$

where $v_a(t)$, $v_b(t)$, $v_c(t)$ are the phase voltages expressed in the time domain. It is possible to prove that if the three voltages v_a, v_b, v_c form a positive sequence of voltages, $\overline{v_{\alpha\beta}}$ is a vector rotating at speed $+\omega$, whereas if it forms a negative sequence of voltages, it is represented by a vector rotating at $-\omega$ (where the positive sense is anti-clockwise by convention). A distorted three-phase voltage (or current) can then be represented as the sum of as many rotating vectors as the harmonics it is composed of, rotating at speed $\pm m\omega$ (+ for positive sequence harmonics and - for negative ones), where m is the harmonic order. This concept is mathematically expressed by the Discrete Fourier Transform:

$$\overline{X_{\alpha\beta}}(k) = \sum_{n=0}^{N-1} \overline{x_{\alpha\beta}}(n)e^{-j2\pi kn/N} \qquad k = 0, 1, ..., N-1 \tag{3.5}$$

Where $\overline{X_{\alpha\beta}}(k)$ is the frequency domain signal, expressed in the discrete frequency

variable k , N is the number of samples of the signal, $\overline{x_{\alpha\beta}}(n)$ is the time domain signal, expressed in the discrete time variable n. The complex exponential functions in the Discrete Fourier Transform are *harmonically related*, because their frequencies are multiples of the fundamental frequency. In order to extract the mth harmonic component from the signal, this needs to be represented in a new reference frame rotating at the same speed as the rotating vector corresponding with that harmonic, which means at speed $\pm m\omega$. In this new reference frame, the vector corresponding to the mth harmonic is the only component appearing as a DC quantity and for this reason the only one having non-zero mean value over a time interval equal to a multiple of the fundamental period. This concept will be explained in better detail in section 5.2. The transformation from the stationary reference frame to the rotating one can be carried out by multiplying the entire signal by another complex exponential function with amplitude equal to 1 and frequency equal to $\pm m\omega$.

In the proposed algorithm the input signal, which can represent either a three-phase voltage or a three-phase current, is transformed from the *abc* system of coordinates into the $\alpha\beta0$ reference frame and then expressed by means of its $\alpha\beta$ components (where α and β components are respectively the real and imaginary part of $\overline{v_{\alpha\beta}}$). The signal is then transformed into three different reference frames rotating respectively at ω_1 , $\omega_1 + d\omega$, $\omega_1 - d\omega$, by multiplying it by the complex quantities $e^{-j\omega_1 t}$, $e^{-j(\omega_1+d\omega)t}$, $e^{-j(\omega_1-d\omega)t}$. This procedure allows the three spectral lines at the three frequencies ω_1 , $\omega_1 + d\omega$, $\omega_1 - d\omega$ to be extracted, which, in the frequency spectrum, corresponds to the extraction of the spectral line corresponding to the frequency f_1 and the two lines next to it. These signals are windowed by means of a Hamming window and their mean values are calculated. These mean values yield the amplitudes and phases of the signal components at frequencies f_1, $f_1 + df$ and $f_1 - df$, and the three amplitudes can be used to calculate the frequency correction factor Δf as in (3.1). The value Δf is then minimized using a closed loop system and a Proportional Integral controller, in order to estimate the value of the fundamental frequency. The estimated frequency is then multiplied by 2π and integrated to obtain the estimated phase of the fundamental signal and this is used to calculate the three amplitudes am_1, am_{11} and am_{12} using the DFT algorithm.

Figure 3.1 shows an example of the calculation of Δf. The initial estimate of frequency f_1 is 400Hz but the actual frequency of the analyzed signal is 460Hz. The spectral resolution chosen for the analysis is 200Hz. Δf is calculated using equation (3.1) on the basis of the amplitudes am_1, am_{11} and am_{12}, and it is equal to +60Hz, hence, added to f_1, it gives 460Hz as the estimate of the actual frequency. The way equation (3.1) works can be also explained in a more intuitive way. As the three spectral lines at f_1 and $f_1 \pm df$ belong to the leakage of the fundamental, if the fundamental component is on the right hand side of f_1, am_{11} will be bigger than am_{12} so the algorithm will search for the spectral line with the highest amplitude in the portion of the spectrum on the right hand side of f_1.
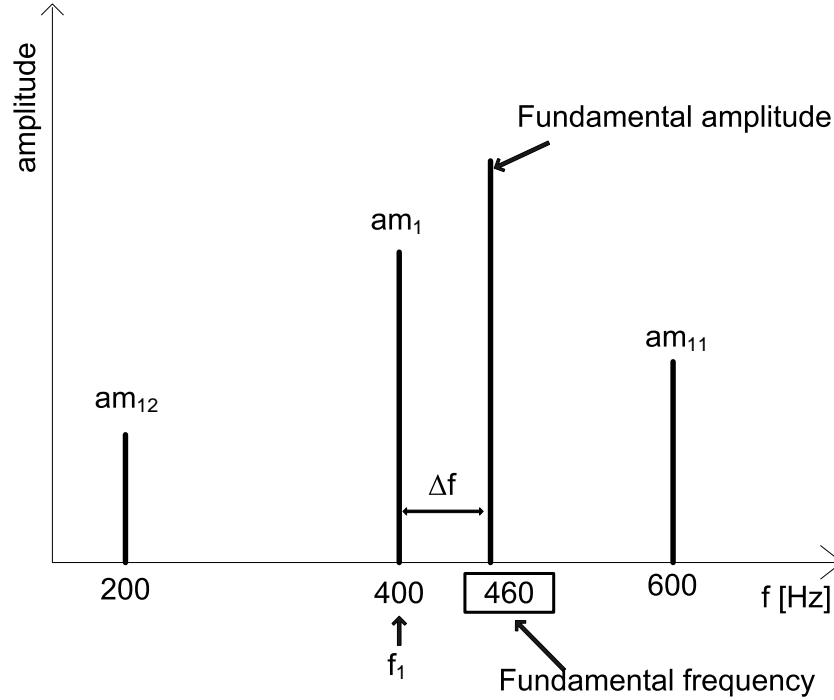
Figure 3.1: Example of Δf calculation when the actual value of frequency is 460Hz and the initial estimate is 400Hz

Figure 3.2 presents the scheme of the proposed DFT algorithm. The blocks named "DFT" contain the calculation of the spectral components at the frequencies f_1 and $f_1 \pm df$. Figure 3.3 shows in better detail the block that calculates am_1. The blocks that calculate am_{11} and am_{12} are similar to the one in the figure. The proposed technique can be implemented in real time and applied to a vector that contains the last n samples of the signal [46]. The n points buffer is updated

at every step with a First In First Out logic. The $\alpha\beta$ vector representing the input signal is multiplied by the complex quantity $e^{-j\theta_1}$ in order to transform it into the reference frame rotating at ω_1. The signal is also multiplied by the Hamming window (also in the form of a n point buffer which is fixed). The mean value of the vector obtained from the multiplication is calculated, by summing all its components and dividing the sum by its length. A scaling factor equal to 1.8519 is also applied in the mean value calculation, in order to compensate for the multiplication by 0.54 introduced by the Hamming window. The mathematical expression of the Hamming window is shown in (3.6).

$$w(i) = 0.54 - 0.46cos\left(\frac{2\pi i}{n}\right) \tag{3.6}$$

Where i is an integer number with values $0 \leq i \leq n$.

The mean value calculation yields an average vector, whose amplitude and phase are the amplitude am_1 and the phase variation $\Delta\vartheta_1$ which, summed with the phase ϑ_1, gives the fundamental phase φ_1.
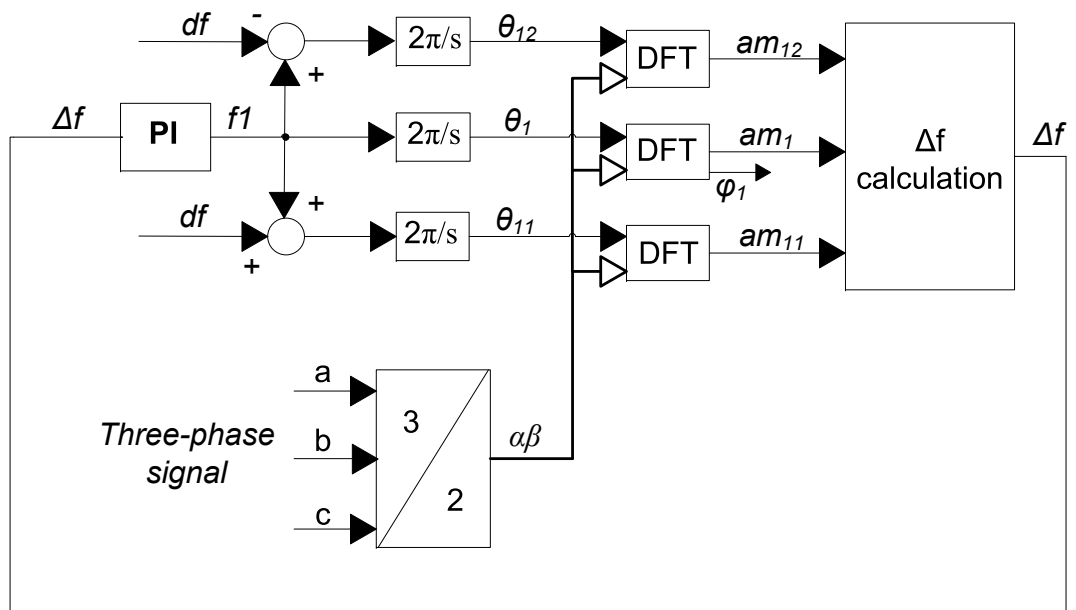
Figure 3.2: Scheme of the DFT algorithm
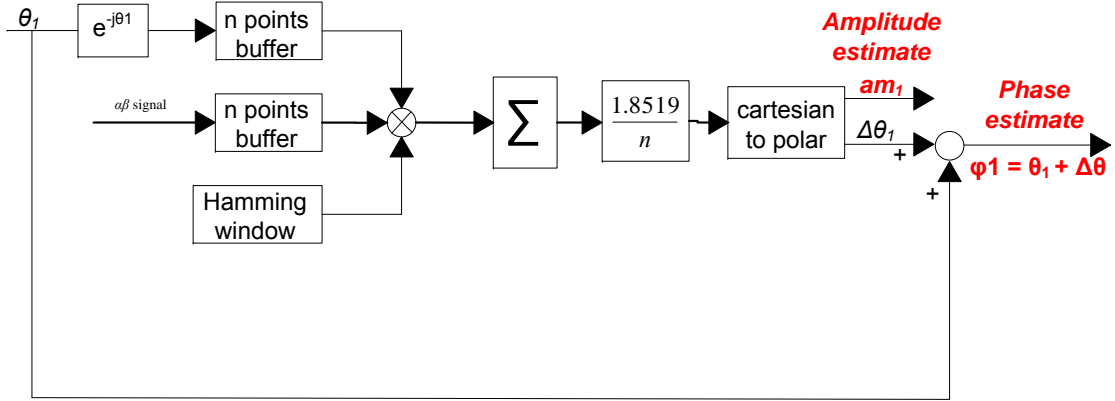
Figure 3.3: DFT block diagram for the calculation of the amplitude am_1 and the phase φ_1

3.3.1 Choice of algorithm parameters

In order to perform in real time all the calculations described above, a limited portion of the input signal is analyzed, which means a limited observation window is used to observe and process the signal. A fixed length buffer is used to store the analyzed portion of the signal and at every sampling step the buffer is updated with a new acquired sample, discarding the oldest one (First In First Out logic). This buffer of samples is weighted by means of a normalized Hamming window of the same length and the mean value of the weighed portion of the signal is calculated. The observation window T_{obs} (which should be an integer multiple of the fundamental period) and the spectral resolution df are related by the following relation:

$$df = \frac{1}{T_{obs}} = \frac{1}{nT_s} = \frac{f_s}{n} \tag{3.7}$$

where n is the number of samples contained in one observation window and f_s is the sampling frequency, which is chosen taking into account the computational capability of the microprocessor used for the digital implementation. The choice of T_{obs} and df is a crucial point in the algorithm design. A large observation window - high T_{obs} - makes the spectral resolution smaller, thus improving the

resolution of the spectrum. However it increases the computational effort as a higher number of samples of the signal are required in order to perform all the calculations in one step. Hence, in this case, the technique is less able to track high speed transients of frequency. A narrow observation window decreases the computational time but on the other hand it worsens the spectral resolution: in this case harmonic interference can occur, as the two spectral lines next to the one in f_1 might correspond with some harmonic components, resulting in an error in the frequency estimation. Therefore, in order to choose an appropriate set of parameters for the algorithm, a compromise should be found, between a high value of T_{obs}, corresponding with a small value of df (high spectral accuracy) and a small value of T_{obs} (low spectral accuracy).

3.3.2 Analysis of a sinusoidal signal

If the signal contains a single sinusoidal component and the observation window is not an integer multiple of the fundamental period, the amplitudes of the spectral components obtained by means of the DFT are independent of the portion of signal being analyzed. They only depend on the length of the observation window (the number of samples).

For example, assuming that a 400 Hz three phase sinusoidal signal having amplitude equal to 1 is analysed using an 8 point buffer sampled at 8 kHz, the frequency resolution of the DFT is 1000 Hz (according to (3.7)). If the initial estimate of frequency is 400 Hz, it is possible to calculate the DFT amplitudes at -600 Hz, 400 Hz and 1400 Hz, which are equal to $am_{12} = 0.4627$, $am_1 = 0.9333$ and $am_{11} = 0.4627$ respectively. If the signal amplitude was not 1 the DFT results would be multiplied by the actual signal amplitude. The value obtained from (3.1) is not affected by the signal amplitude and would be equal to 0 in the proposed example. Since the portion of the signal being analysed is smaller than a period of the signal itself, there is an error in the calculated signal amplitude as well as a strong leakage effect. Equation (3.1) provides a correct calculation of the signal frequency after several iterations, as the frequency error is minimized by a PI controller so Δf converges to zero at the steady-state, regardless of the initial

estimate f_1. Similarly any single sinusoidal signal would produce constant am coefficients, independent of the portion of the signal being analysed. For example, the calculation of the DFT amplitudes at the same frequency as the previous case, with an 800 Hz signal would give $am_{12} = 0.0846$, $am_1 = 0.5988$ and $am_{11} = 0.9082$ resulting in $f = 379$ Hz, close to the correct value of 400 Hz.

3.3.3 Analysis of a distorted signal

When the signal contains several sinusoidal components, the DFT values are the sum of the DFT of each sinusoid due to the linearity property of DFT. Since the DFT values are complex, the amplitude of the sum of the DFT values is not the sum of the amplitudes. Moreover the DFT amplitudes become functions of the portion of the signal being analysed. Since it is difficult to give a mathematical representation of the DFT amplitudes when the signal is distorted, they have been calculated by analysing all the possible portions of the signal supposing that the signal is composed of a fundamental component at 400 Hz and a single harmonic. The calculation has been repeated considering different harmonics having attenuations, with respect to the fundamental component, in the range [-20 dB -60 dB]. The DFT amplitudes and the Δf values have been calculated using buffers of 8 points and 20 points. The latter value corresponds to one complete period of the 400 Hz signal, given the sampling frequency of 8 kHz. This also implies that the DFT frequency resolution equals 400 Hz and the spectral component amplitudes will be calculated at 0 Hz, 400 Hz and 800 Hz. The mean values of Δf together with their standard deviations are given in tables 3.1 and 3.2.

The influence of the harmonics rapidly decreases with their amplitude. This is shown by the fact that Δf is closer to zero when the harmonic amplitude decreases, zero is the value that would be obtained if the 400Hz signal was sinusoidal, with an initial estimate equal to 400Hz. Increasing the size of the buffer clearly makes the method less sensitive to the signal harmonic content as shown by a comparison of tables 3.1 and 3.2. The buffer size affects the sensitivity of the technique to the harmonics also because of the possible harmonic interference occurring between the leakage of the fundamental and the leakage of the harmonics at frequencies $f_1 \pm df$.

Attenuation of the harmonic with respect to the fundamental	Harmonic order							
	2nd harmonic		3rd harmonic		5th harmonic		7th harmonic	
	mean [Hz]	std [Hz]	mean [Hz]	std [Hz]	mean [Hz]	std [Hz]	mean [Hz]	std [Hz]
-20 dB	0.012	25.6	0.364	42	0.600	37	0.061	12.5
-40 dB	0.009	2.56	0.003	4.2	0.009	3.7	0.000	1.25
-60 dB	0.001	0.256	0.000	0.42	0.000	0.37	0.000	0.125

Table 3.1: Effect of the harmonics using an 8 points buffer

Attenuation of the harmonic with respect to the fundamental	Harmonic order							
	2nd harmonic		3rd harmonic		5th harmonic		7th harmonic	
	mean [Hz]	std [Hz]	mean [Hz]	std [Hz]	mean [Hz]	std [Hz]	mean [Hz]	std [Hz]
-20 dB	0.34	19.7	0.120	9.2	0.000	0.084	0.000	0.022
-40 dB	0.002	1.97	0.002	0.92	0.000	0.008	0.000	0.002
-60 dB	0.000	0.197	0.000	0.092	0.000	0.001	0.000	0.000

Table 3.2: Effect of the harmonics using a 20 points buffer

The chance of interference is higher when the frequency resolution is increased, which means a smaller buffer size is used. This is a rule of thumb that has to be carefully applied. For example, when 20 points are analyzed the frequency $f_1 + df$ is coincident with the second harmonic at 800 Hz and the estimation error heavily depends on the second harmonic amplitude. The buffer size choice should then consider that the frequencies $f_1 \pm df$ have to be far enough from any large harmonic components of the signal.

3.3.4   Algorithm tuning

Due to the presence of the harmonics, the calculated Δf value has an offset with respect to the actual frequency error and can oscillate. It was found that the standard deviation of the calculated Δf decreases with the same rate as the harmonic amplitude. The standard deviation of Δf limits the bandwidth reachable by the DFT algorithm. It is possible to filter out the Δf oscillations and obtain a flat frequency estimate by a proper selection of the PI gains, eventually reducing the DFT bandwidth. As a rule of thumb, when the standard deviation of Δf is below a few percent of the signal fundamental frequency it is possible to obtain a good dynamic performance. The tolerable value of the Δf offset depends on the required accuracy of the frequency estimation technique because the frequency estimate will have a bias equal to the average value of Δf. It is worth highlighting that the bias in the frequency estimate does not correspond to an error in the estimation of the phase of the signals. This will be demonstrated by the results shown in the next sections and means that the fundamental signal component can be accurately tracked even when there is an error in the frequency estimate. It can be concluded from the considerations above that an 8 points buffer is a good choice when the harmonic level is below -20 dB, otherwise a larger buffer has to be chosen or some signal pre-filtering is necessary. It is important to remark that, even if the computational burden is not a primary concern, an excessive buffer size would compromise the transient performance of the frequency estimation algorithm. When fast changes of the fundamental frequency are expected, the buffer size should be kept as small as possible in order to allow good frequency tracking

Fundamental frequency (initial estimate) [Hz]	400 Hz
Fundamental amplitude	40
Fundamental phase [deg]	0
5th harmonic amplitude	8
5th harmonic phase [deg]	50
7th harmonic amplitude	4
7th harmonic phase [deg]	70
11th harmonic amplitude	2.5
11th harmonic phase [deg]	110
13th harmonic amplitude	2
13th harmonic phase [deg]	130

Table 3.3: Input signal for fundamental frequency and phase estimation

also in transient conditions.

3.4 Frequency and phase estimation: simulation results

A simulation has been carried out in Matlab Simulink in order to test the proposed algorithm for fundamental frequency and phase estimation. The input signal has the characteristics listed in table 3.3. The harmonic distortion of this signal represents a critical condition for an aircraft power system, and it is related to the aircraft power quality recommendations [12].

The characteristic parameters of the algorithm have been chosen with the values reported in table 3.4.

Sampling frequency [Hz]	12 kHz
Observation interval T_{obs}	
Case (a)	T
Case (b)	$\frac{2}{3}T$
Case (c)	$\frac{1}{2}T$
Case (d)	$\frac{2}{5}T$
Buffer length n	
Case (a)	30
Case (b)	20
Case (c)	15
Case (d)	12
Frequency PI controller s domain	
Case (a)	$k_p = 0.4; \; k_i = 640$
Case (b)	$k_p = 0.4; \; k_i = 900$
Case (c)	$k_p = 0.4; \; k_i = 1200$
Case (d)	$k_p = 0.4; \; k_i = 1500$

Table 3.4: Frequency detection algorithm parameters

In case (a) the observation interval has been set to one fundamental period T. In case (b), (c) and (d) it has been set to different portions of the period. The PI controller gains were tuned in each case using a trial-and-error procedure, to obtain the fastest response possible.

Figure 3.4 shows the response of the frequency estimation to a step change of frequency from 400 Hz to 800 Hz, occurring at 0.1 s. All the cases from (a) to (d) are represented in the figure. The characteristics of the steady-state and dynamic response for the four cases are reported in table 3.5. The fastest response is observed for case (d) as the smaller the buffer the faster the response. Using one entire period of the fundamental for the signal analysis gives high accuracy at the steady-state because there is no truncation of the signal in the DFT analysis. However the dynamic response is slower because a longer time is required in order to fill and update the signal buffer and this time may last longer than the frequency transient that is to be tracked.
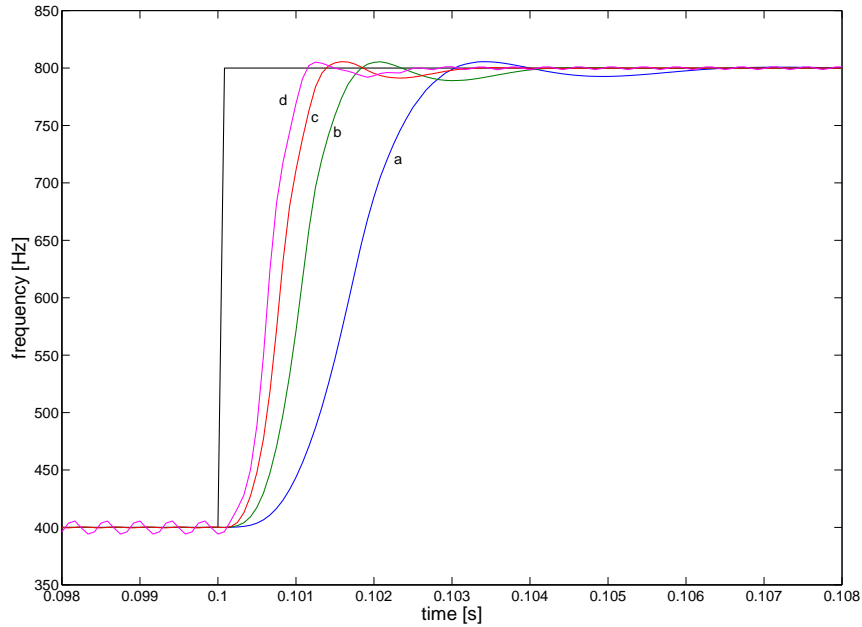
Figure 3.4: Response to a frequency step for different buffer sizes

Figures 3.5 to 3.8 show the response of the fundamental phase estimation to a step change of frequency from 400 Hz to 800 Hz, occurring at 0.1 s. All the cases from

	case (a)	case (b)	case (c)	case (c)
Maximum overshoot [%]	1.37	1.37	1.37	1.37
Delay time [s]	0.1017	0.1011	0.1008	0.1006
Rise time [s]	0.0015	0.0009	0.0007	0.0006
Settling time 5% [s]	0.1027	0.1016	0.1012	0.101
Peak time [s]	0.1034	0.1021	0.1016	0.1012
Steady-state oscillation max amplitude (% of the steady-state value)	0.00075	0.0063	0.0325	0.25
Steady-state error [Hz]	0	0	0	0.0078

Table 3.5: Transient and steady-state performance of the frequency step estimation

(a) to (d) are represented in the figures. In these figures, the phase estimate is compared with the fundamental phase of the input signal used in the simulation. It can be noticed that the smaller the buffer of samples the faster the response. This depends on the fact that, when processing the signal with a bigger buffer, the computational time increases and the estimation transient is longer. In the case (a) the phase estimate locks to the actual phase in 0.004 s, after the frequency step occurs. In the cases (b), (c) and (d) the phase estimate settles in 0.0025 s, 0.002 s and 0.0015 s respectively.
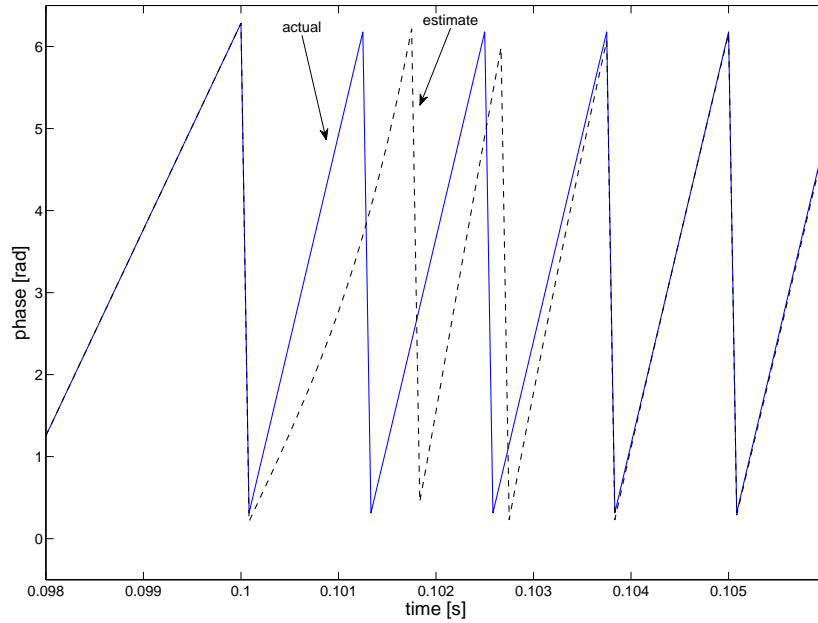
Figure 3.5: Response of the phase estimate to a frequency step. Case (a)
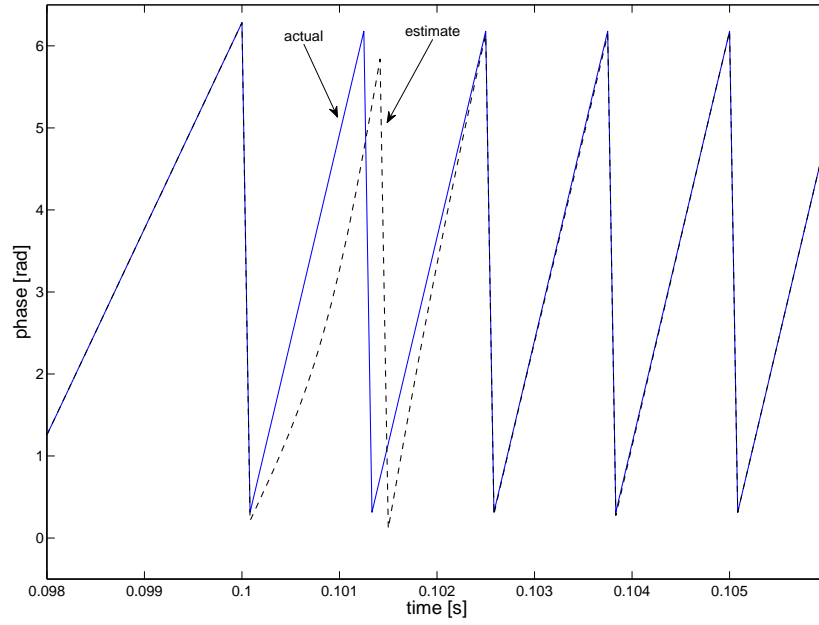
Figure 3.6: Response of the phase estimate to a frequency step. Case (b)
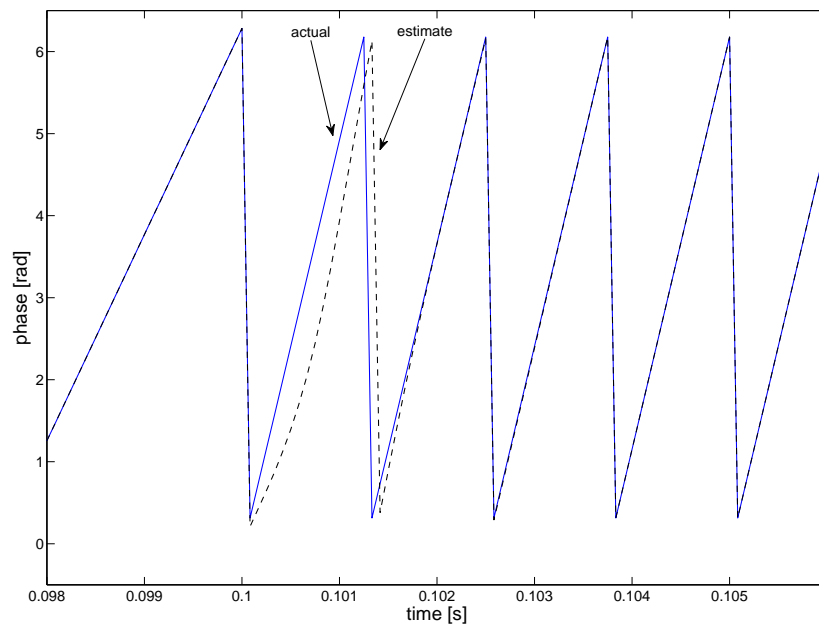
Figure 3.7: Response of the phase estimate to a frequency step. Case (c)
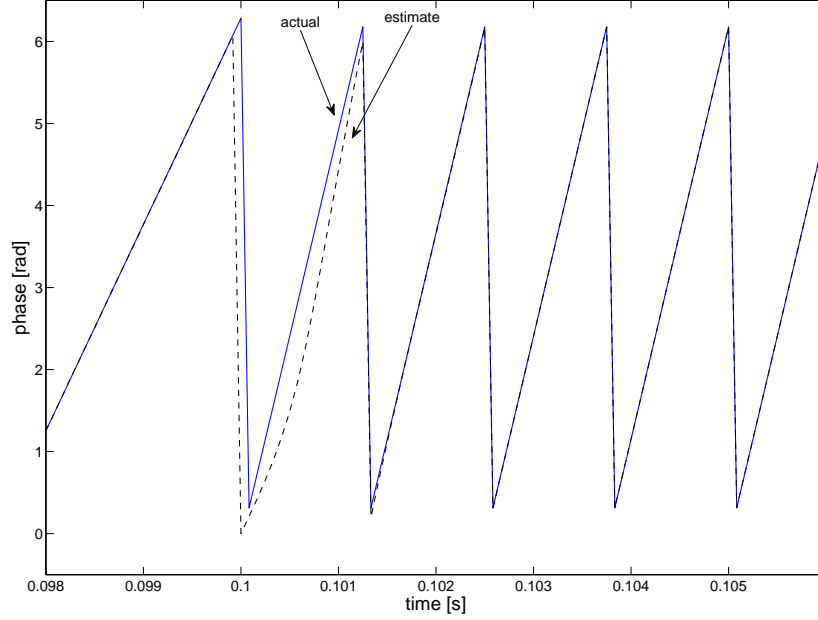
Figure 3.8: Response of the phase estimate to a frequency step. Case (d)

3.5 Harmonic estimation technique

In the previous sections, the DFT technique for the real-time estimation of the fundamental frequency and the fundamental phase has been described. The same technique can be also used for the estimation of the harmonic amplitudes and phases of a distorted signal. There are two ways in which the harmonic estimation algorithm can be implemented: in the first one, the DFT is applied to the whole distorted signal and the different harmonic components are extracted. In the second method, the fundamental component, estimated by means of the DFT technique described above, is subtracted from the signal. In this way only the distorted part of the signal is analysed using the same DFT technique, in order to extract the harmonics.

In order to estimate the mth harmonic component, the distorted signal (or the distorted signal minus the fundamental) is multiplied by the exponential function $e^{(-j)(\pm m)(\varphi_1)}$, where + is used for positive sequence harmonics and - for negative

sequence harmonics. The average value of the complex quantity obtained after the multiplication gives the information about the amplitude and phase of the harmonic.

The schemes representing the two methods are shown in figures 3.9 and 3.10. The harmonic estimation structure is similar to the one represented in figure 3.3 except no use of the Hamming window is made in this case.
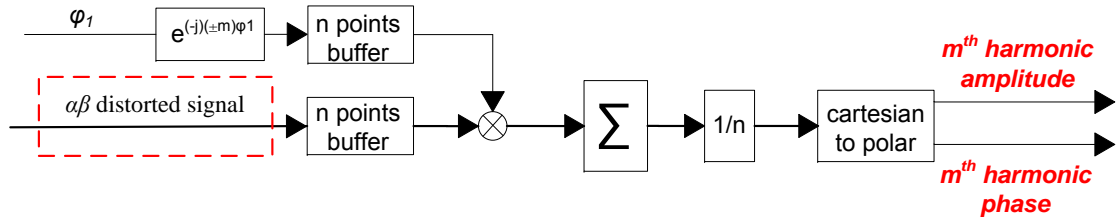
Figure 3.9: Scheme of the DFT algorithm for harmonic estimation. No subtraction of the fundamental
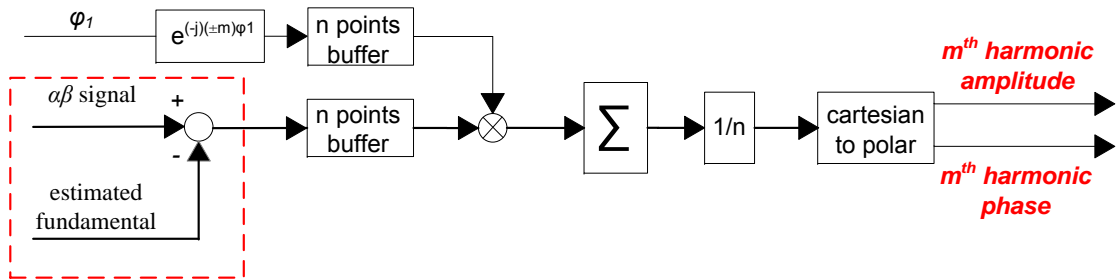
Figure 3.10: Scheme of the DFT algorithm for harmonic estimation. Subtraction of the fundamental

The choice of the buffer length is based on the same considerations made in the previous sections.

The two methods have been implemented in simulation, for an input signal with

the characteristics reported in table 3.3. It has been observed that the second
method, where the subtraction of the fundamental is applied, yields a more accu-
rate estimation of the harmonic components, compared to the first method. This
is shown in the results presented here.

Figures 3.11 to 3.18 show the comparison between the estimate of the harmonic
amplitudes and phases obtained using the two methods, for the 5th, 7th, 11th and
13th components. The amplitude estimates, presented in the upper half of each
figure, are shown in terms of percentage error, the phase estimates, in the lower
half of each figure, are shown in terms of absolute value of the error in degrees.
The comparison has been carried out implementing the algorithm in the condition
d of table 3.4, i.e. a 12 points buffer, which is the most critical condition.
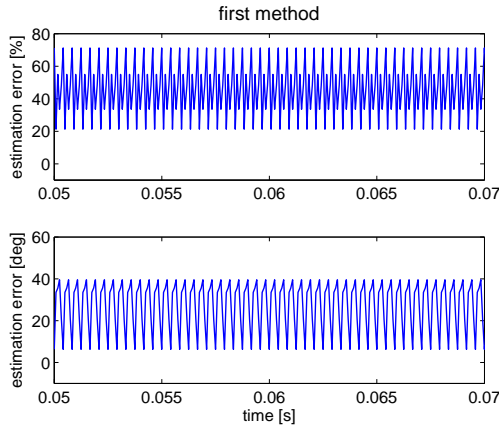
Figure 3.11: 5th harmonic
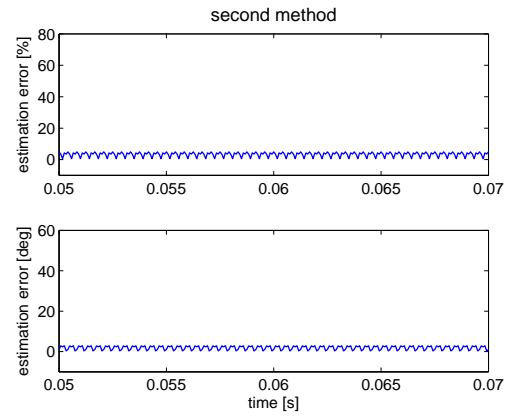
Figure 3.12: 5th harmonic
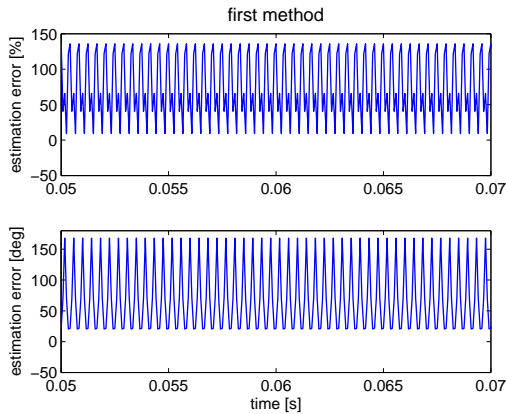
Figure 3.13: 7th harmonic
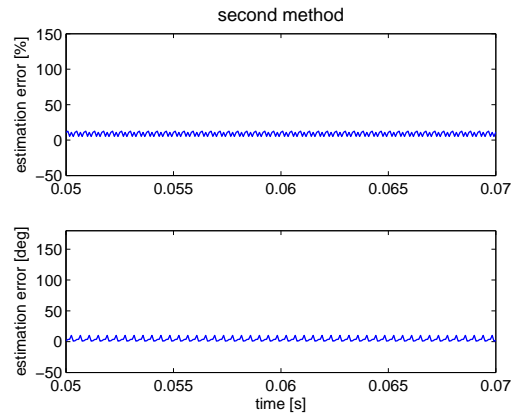
Figure 3.14: 7th harmonic

These figures show that the second method provides a more accurate estimate of
the harmonic amplitudes and phases. Hence the subtraction of the fundamental
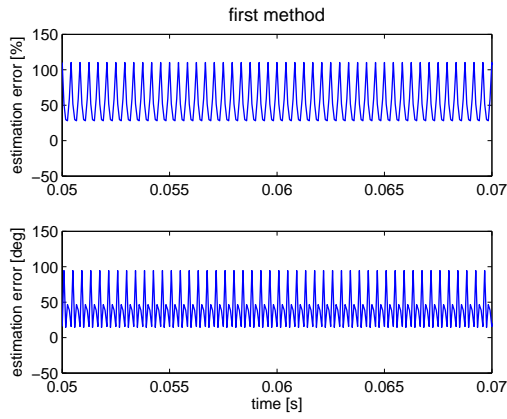
Figure 3.15: 11th harmonic estimate
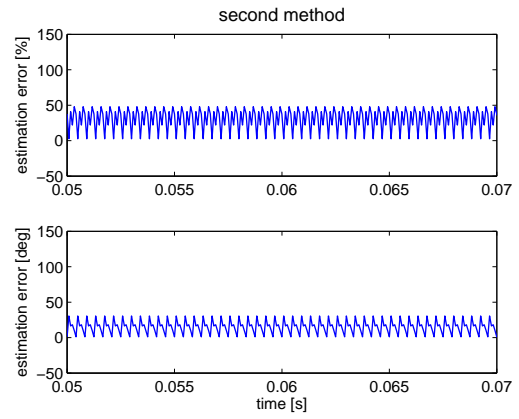
Figure 3.16: 11th harmonic estimate
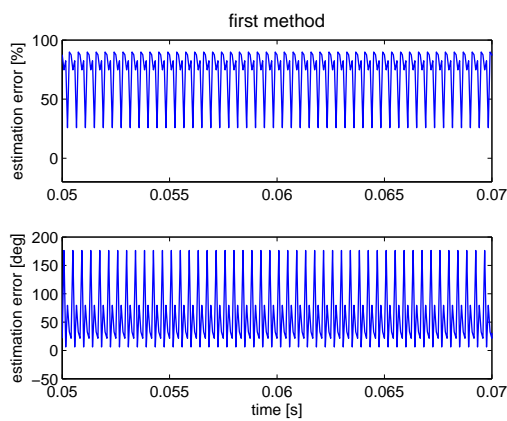
Figure 3.17: 13th harmonic
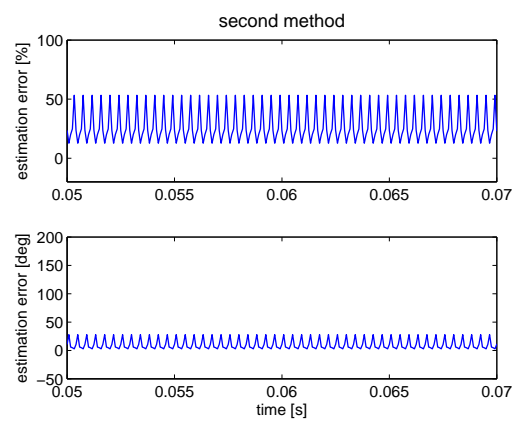
Figure 3.18: 13th harmonic

Sampling frequency [Hz]	12 kHz
Buffer length n	
Case (a)	30
Case (b)	20
Case (c)	15
Case (d)	12

Table 3.6: Harmonic detection algorithm parameters

component has been applied for the harmonic estimation, and a thorough presentation of the results obtained from the simulation validation of this technique is given in the next section.

3.6 Harmonic estimation : simulation results

A simulation has been carried out in Matlab Simulink in order to test the proposed algorithm for the estimation of the harmonic amplitudes and phases. The input signal has the characteristics listed in table 3.3. The simulation has been repeated in four different cases, depending on the length of the buffer chosen for the signal analysis. The parameters of the algorithm are listed in table 3.6.

Figures 3.19 to 3.22 show the estimate of the harmonic amplitudes in terms of estimation percentage error. Figures 3.23 to 3.26 show the estimate of the harmonic phases in terms of absolute value of the estimation error. The fundamental frequency varies as a step from 400 Hz to 800 Hz occurring at 0.1 s.

3.6.1 Relative phase of the harmonics with respect to the fundamental

In the previous sections the results for the estimation of the harmonic amplitudes and phases have been presented. In that case the fundamental phase is 0 degrees
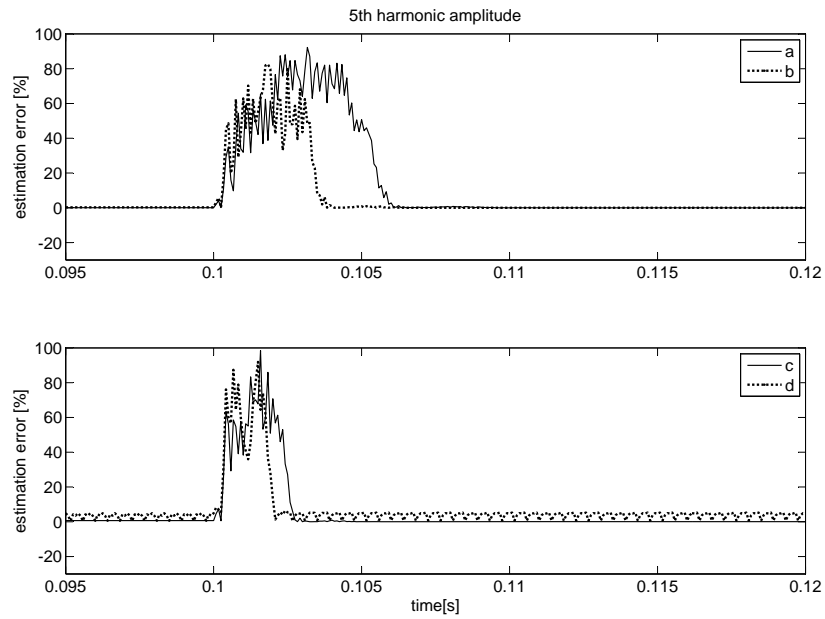
Figure 3.19: 5th harmonic amplitude estimate in the four cases
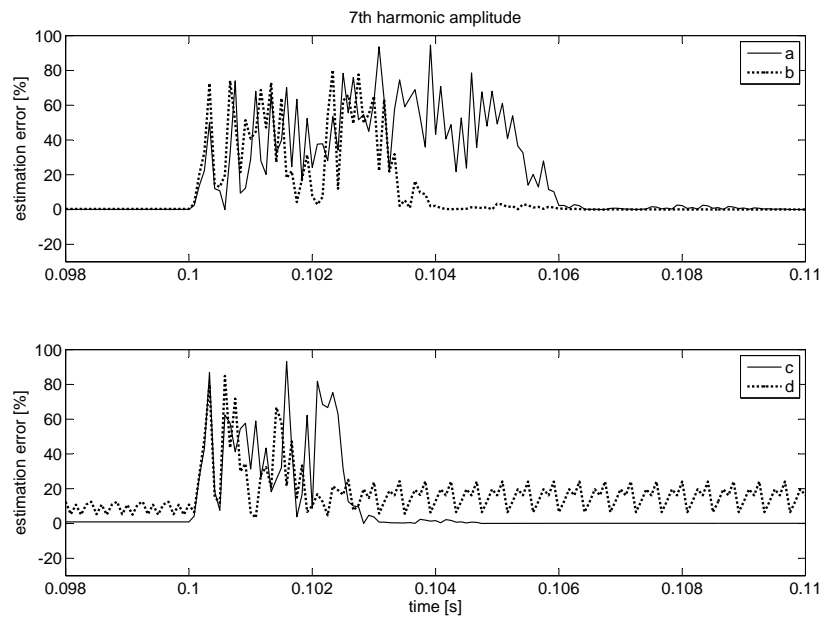
Figure 3.20: 7th harmonic amplitude estimate in the four cases
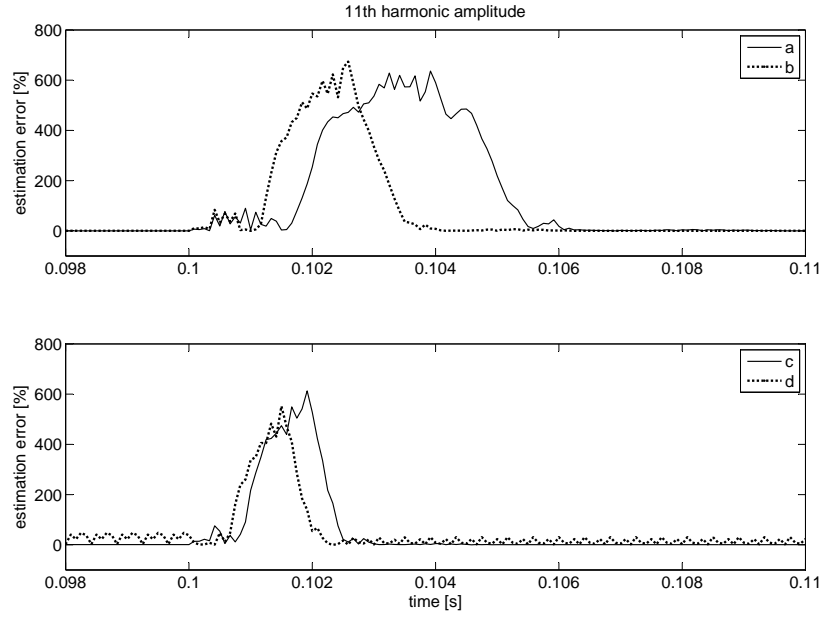
Figure 3.21: 11th harmonic amplitude estimate in the four cases
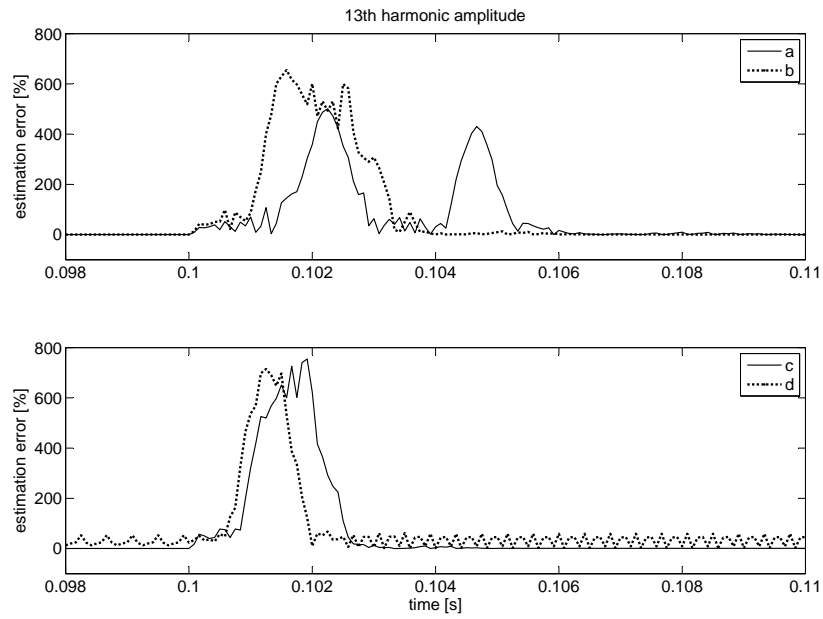
Figure 3.22: 13th harmonic amplitude estimate in the four cases
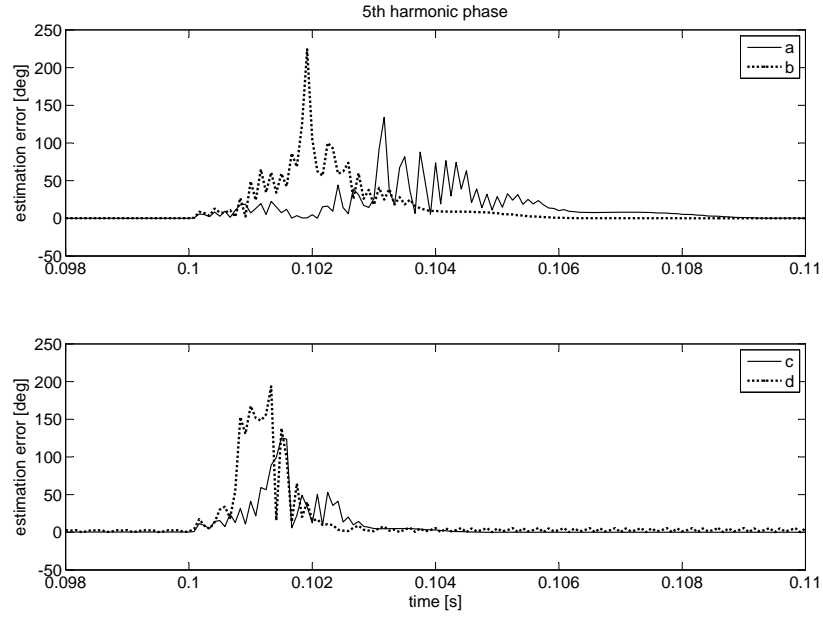
Figure 3.23: 5th harmonic phase estimate in the four cases
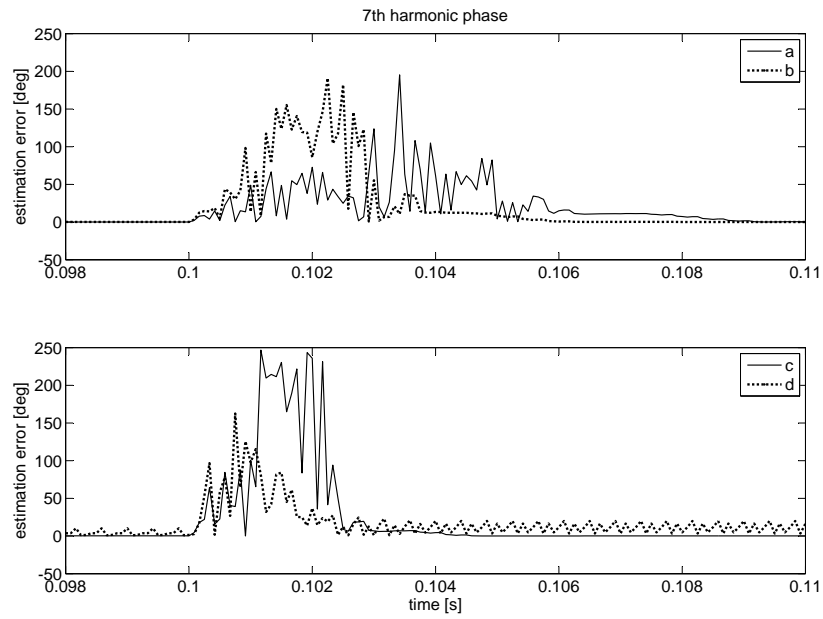
Figure 3.24: 7th harmonic phase estimate in the four cases
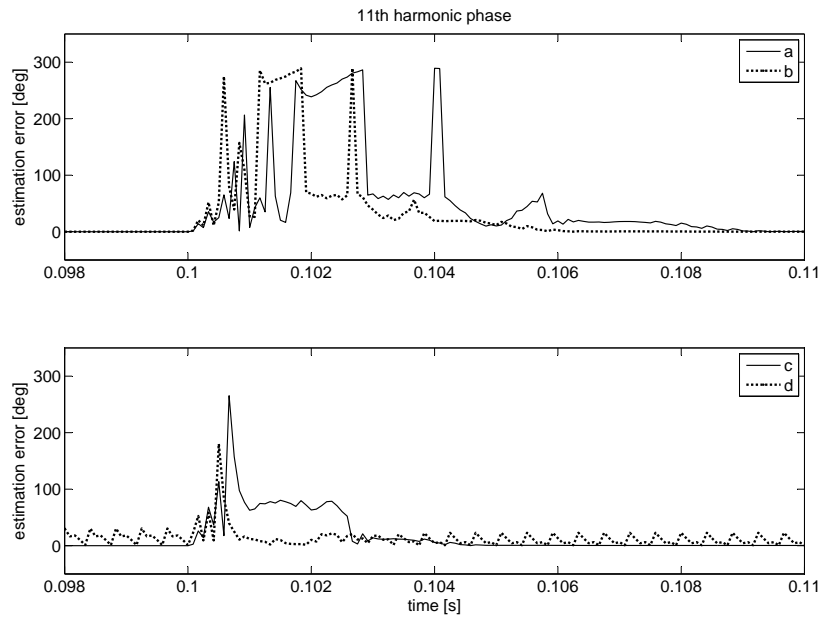
Figure 3.25: 11th harmonic phase estimate in the four cases
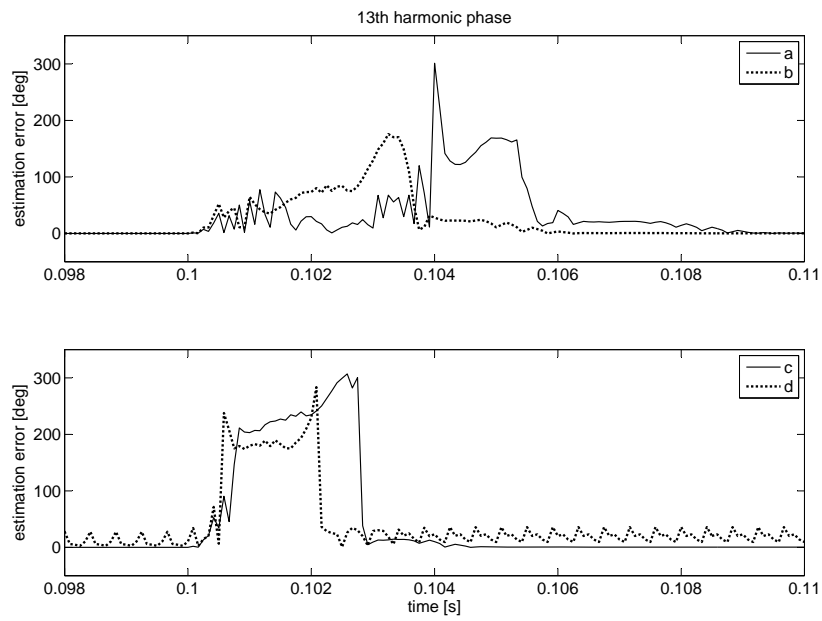
Figure 3.26: 13th harmonic phase estimate in the four cases

Fundamental frequency (initial estimate) [Hz]	400 Hz
Fundamental amplitude	40
Fundamental phase [deg]	15
5th harmonic amplitude	8
5th harmonic phase [deg]	50
7th harmonic amplitude	4
7th harmonic phase [deg]	70
11th harmonic amplitude	2.5
11th harmonic phase [deg]	110
13th harmonic amplitude	2
13th harmonic phase [deg]	130

Table 3.7: Input signal with fundamental initial phase different from zero

(table 3.3) and the harmonic phases have values different from zero. The proposed algorithm yields the expected values of phase as a result of the estimation, as can be seen in figures 3.23, 3.24, 3.25 and 3.26. The estimated values follow the ones listed in table 3.3. However, in general it is not possible to know the absolute initial phase of the fundamental, and the purpose of a phase estimation technique is to lock to its phase in a synchronous way. In the application for which this algorithm has been implemented, the signal to be identified is the voltage at the point of connection of an Active Shunt Power Filter with the power supply and one or more distorting loads. It is therefore important to lock to the phase of this voltage and fix its fundamental as a reference for the analysis of all the other variables that characterize the system. In this section, an input signal with fundamental initial phase different from zero is analysed. The results here presented will show how the estimation algorithm detects the relative phase of the harmonics with respect to the fundamental and how the absolute phase of the harmonics can be derived. Table 3.7 lists the characteristics of the input signal used for this case.

Considering that the fundamental initial phase in this case is 15 degrees, it is expected that the harmonic phases estimated by the algorithm are not the same as their absolute phases listed in the table. Figure 3.27 shows as an example the fundamental and the 5th harmonic component of a signal, in the $\alpha\beta$ plane. The amplitude and initial absolute phase of the fundamental are indicated as A_1 and θ_1 respectively. The amplitude and initial absolute phase of the 5th harmonic are indicated as A_5 and θ_5 respectively. If the two vectors were rotating at the same speed, the relative phase between the two of them would simply be the difference between the absolute phases θ_1 and θ_5. However the two vectors are not synchronous as the 5th harmonic rotates at 5 times the speed of the fundamental, so their relative position in the $\alpha\beta$ plane is defined by (3.8).

$$\theta_m(rel) = \pm \cdot [\theta_m(abs) - m \cdot \theta_1(abs)] \tag{3.8}$$

(3.8) takes into account the difference between the angular speed of the two vectors. $\theta_m(abs)$ and $\theta_m(rel)$ are respectively the absolute initial phase of the mth harmonic and its relative phase with respect to the fundamental. $\theta_1(abs)$ is the absolute initial phase of the fundamental. The + and - signs are used for positive and negative sequence harmonics respectively.

A simulation has been carried out in the conditions of case (a). The fundamental frequency varies as a step from 400 Hz to 800 Hz, occurring at 0.1 s. The fundamental initial phase is estimated as zero, regardless of its absolute value, because the algorithm locks to it, transforming all the variables into a reference frame synchronous with the fundamental. This is represented in figure 3.28. The fundamental phase becomes the zero reference for all the harmonics; the values of the estimated phase of the harmonics correspond with the values of the relative phases obtained by means of formula (3.8). In this case the absolute phases are the ones indicated in table 3.7. The relative phases, according to (3.8), are:

5th harmonic   25 degrees

7th harmonic   -35 degrees
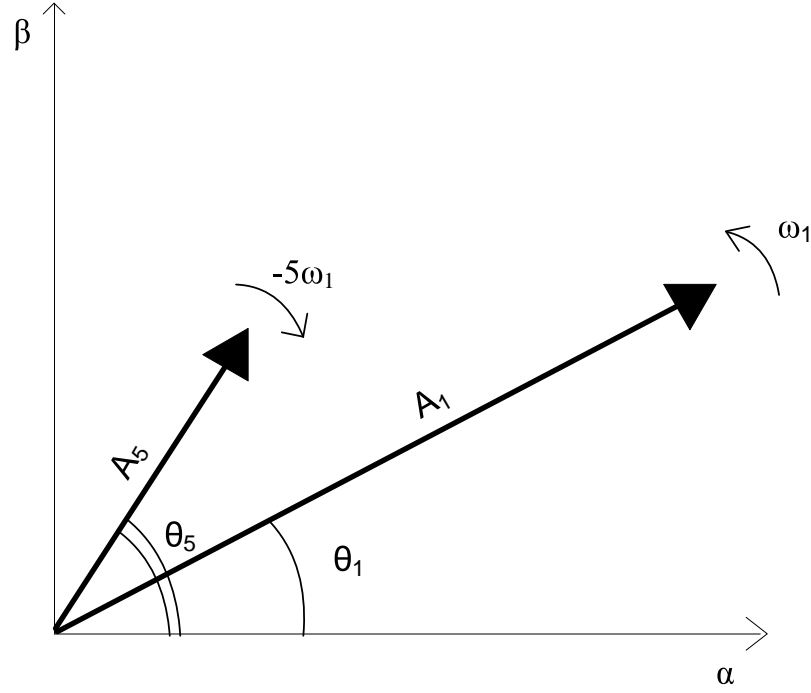
Figure 3.27: Fundamental and 5th harmonic on the $\alpha\beta$ plane

11th harmonic	55 degrees
13th harmonic	-65 degrees

Figures 3.29 to 3.32 show the result of the estimation of the initial phase of the harmonics. The absolute value of the estimation error is represented in these figures.

3.7 Frequency estimation: experimental results

An experimental validation has been carried out for the frequency and harmonic detection algorithm. The algorithm has been tested on a voltage signal generated by a programmable power supply, the Chroma 61705 [47]. The algorithm was implemented on the Texas Instruments TMS320C6713B 32 bit floating point Dig-
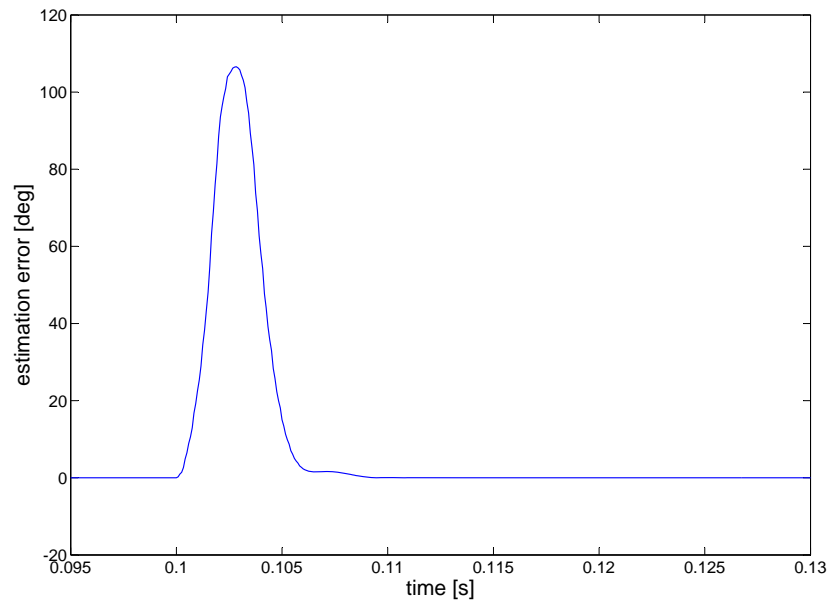
Figure 3.28: Estimate of the initial phase of the fundamental
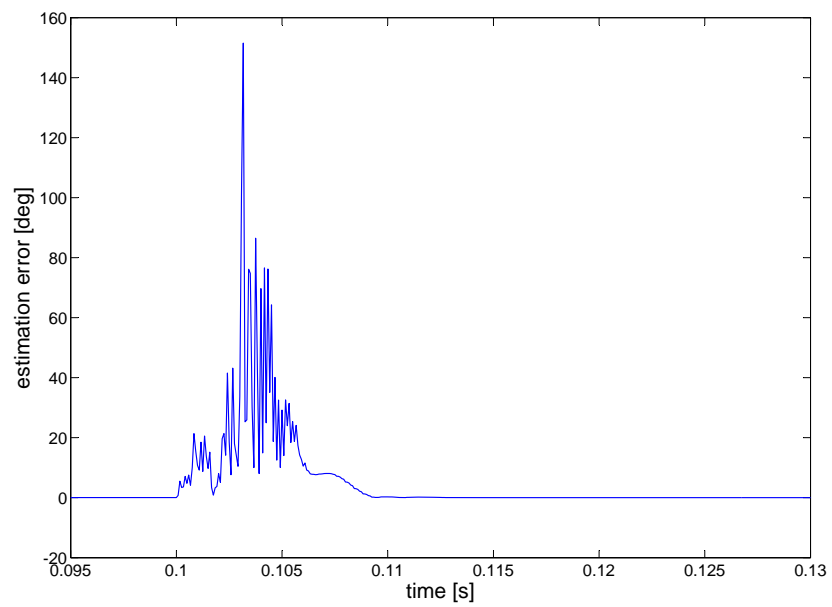
Figure 3.29: Estimate of the initial phase of the 5th harmonic
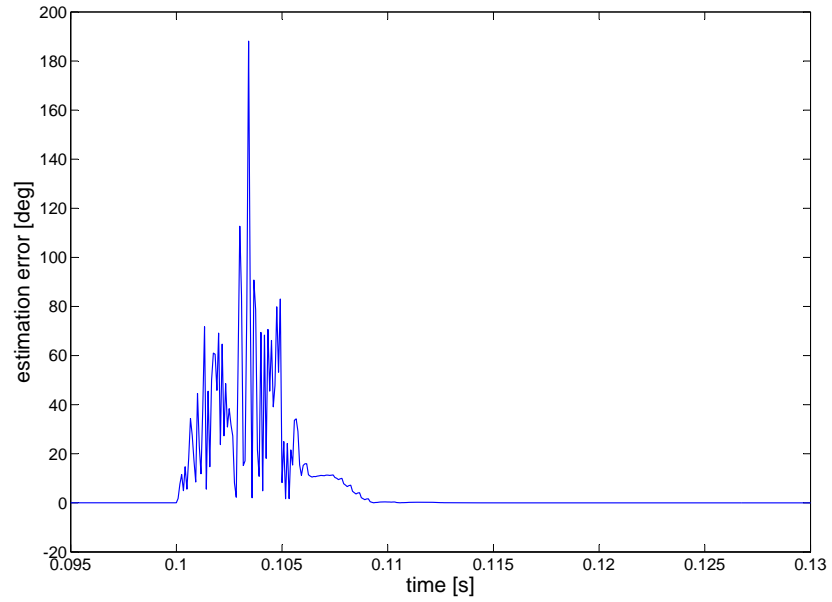
Figure 3.30: Estimate of the initial phase of the 7th harmonic
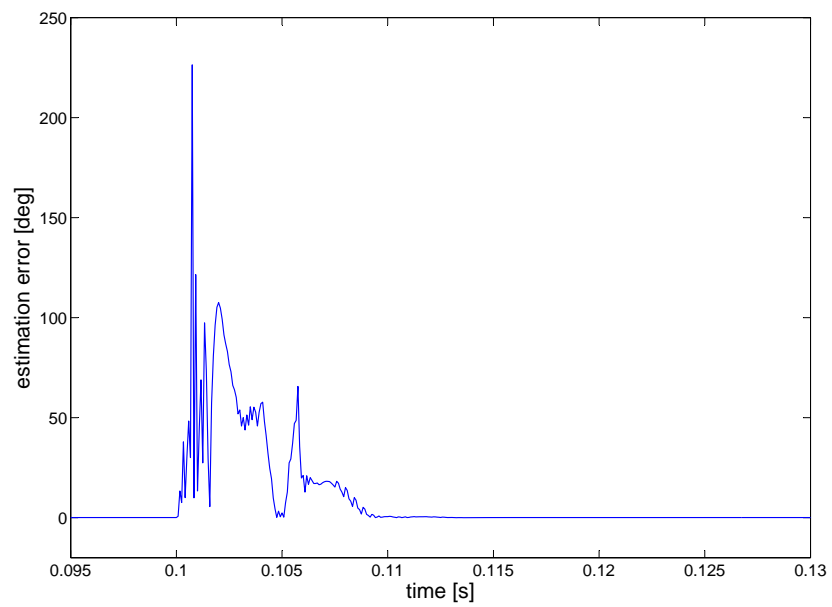
Figure 3.31: Estimate of the initial phase of the 11th harmonic
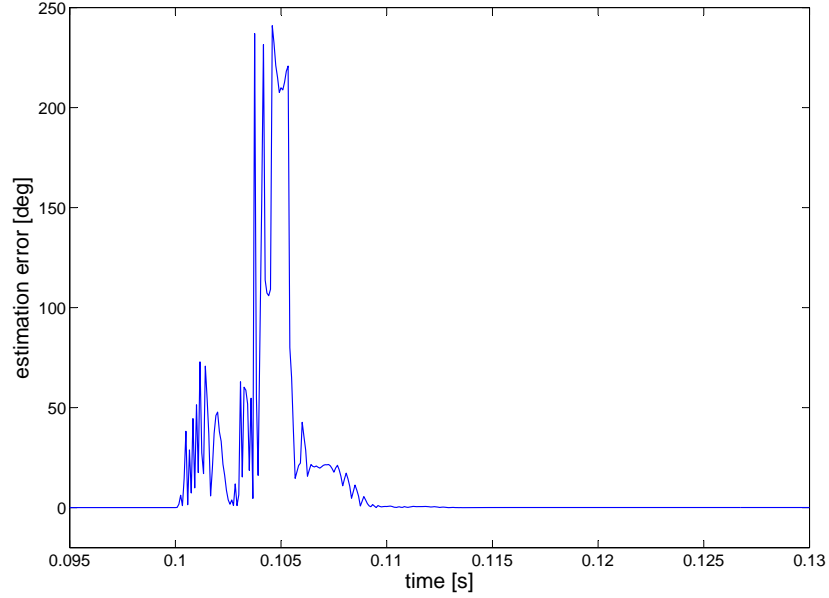
Figure 3.32: Estimate of the initial phase of the 13th harmonic

ital Signal Processor (DSP) [48]. The data acquisition was carried out by means of a Field Programmable Gate Array (FPGA) board, Actel ProAsic A500K050 Package PQ208 [49], with 12 bit Analog to Digital Converters LTC 1400 [50]. The voltage measurement was carried out by means of LEM LV 25-P voltage transducers [51].

In this section the experimental results for the frequency and fundamental phase estimation are shown. In the next section the experimental results for the harmonic estimation are reported.

The characteristics of the input signal voltage processed by the algorithm are listed in table 3.8. The voltage generated by the power supply is line-to-line voltage. The table lists the characteristics of the line-to-line voltage V_{ab} on the left hand side, and the characteristics of the phase-to-neutral voltage V_{an}. The latter is derived from the former by dividing the amplitude of each component by $\sqrt{3}$ and by adding ± 30 degrees to the phase of each component, depending whether the component is a negative or positive sequence. The table indicates the absolute

V_{ab}		V_{an}	
Fund. freq. [Hz]	400 Hz	Fund. freq. [Hz]	400 Hz
Fund. ampl. [V]	65.2	Fund. ampl. [V]	37.6432
Fund. phase [deg]	13.6	Fund. phase [deg]	-16.4; 0 (rel)
5th harm. amplitude [V]	10	5th harm. ampl. [V]	5.7735
5th harm. phase [deg]	-49.5	5th harm. phase [deg]	-19.5; -62.5 (rel)
7th harm. ampl. [V]	6.9	7th harm. ampl. [V]	3.9837
7th harm. phase [deg]	9	7th harm. phase [deg]	-21; -266.2 (rel)
11th harm. ampl. [V]	4.3	11th harm. ampl. [V]	2.4826
11th harm. phase [deg]	-36.7	11th harm. phase [deg]	-6.7; -173.7 (rel)
13th harm. ampl. [V]	2.6	13th harm. ampl. [V]	1.5011
13th harm. phase [deg]	10.5	13th harm. phase [deg]	-19.5; -166.3 (rel)

Table 3.8: Input signal for experimental validation

phase of each component and, for V_{an}, also the relative phase with respect to the fundamental, according to (3.8).

Figure 3.33 shows the input signal in the time domain. Figures 3.34 and 3.35 show the FFT spectrum of the signal.

The characteristic parameters of the algorithm have been chosen with the values reported in table 3.9. The sampling frequency chosen for the experimental implementation is 8 kHz, because of the computational limitations of the DSP. It should be noted that the 13th harmonic frequency occurs above the Nyquist frequency. The PI controller gains have been chosen by trial and error, in order to obtain the same dynamic response between each case in table 3.9 and its correspondent case in table 3.4.

Figure 3.36 shows the response of the frequency estimation to a step change of frequency from 400 Hz to 800 Hz. All the cases from (a) to (d) are represented in the figure. The characteristics of the steady-state and dynamic response in the four cases are reported in table 3.10. The slowest response is observed in case (a) as a buffer containing an entire period of the fundamental is analysed.
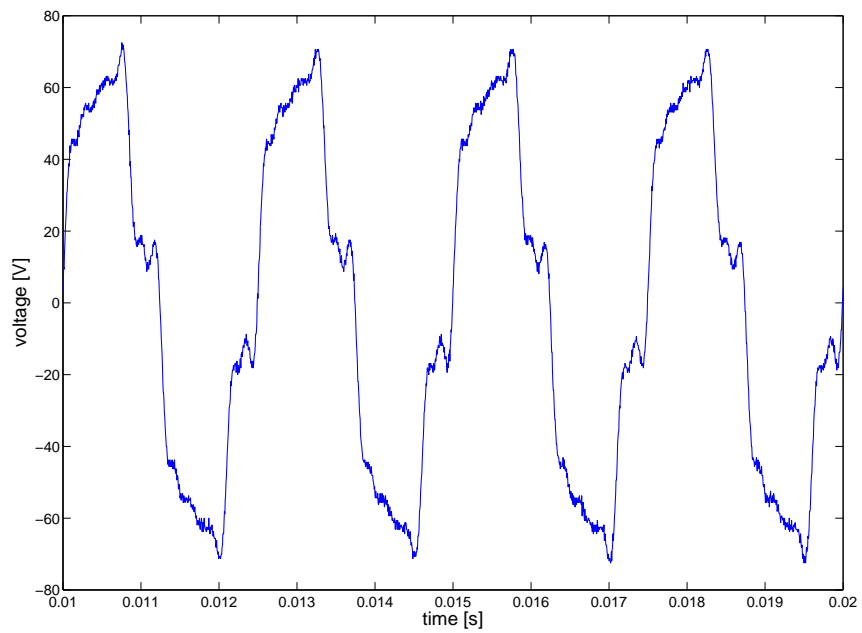
Figure 3.33: Input line-to-line voltage in the time domain
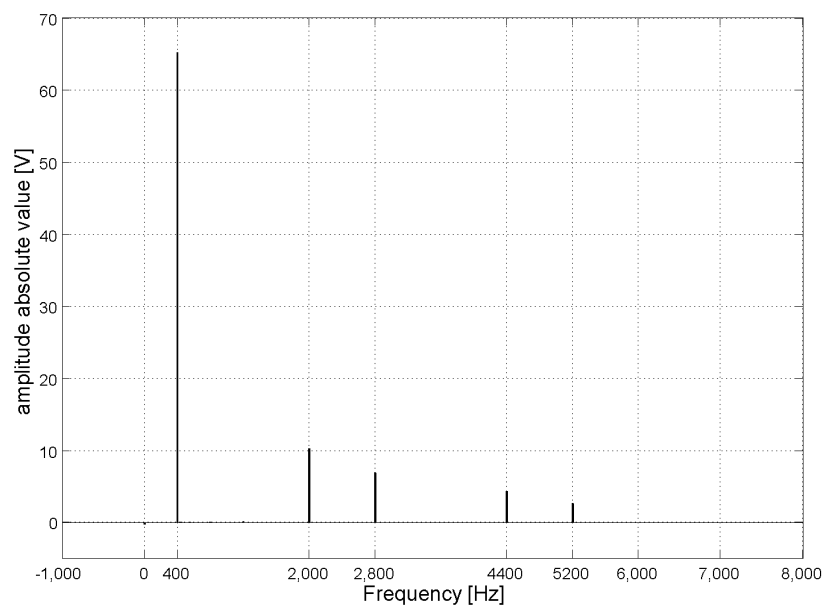
Figure 3.34: FFT spectrum of the amplitude of input line-to-line voltage
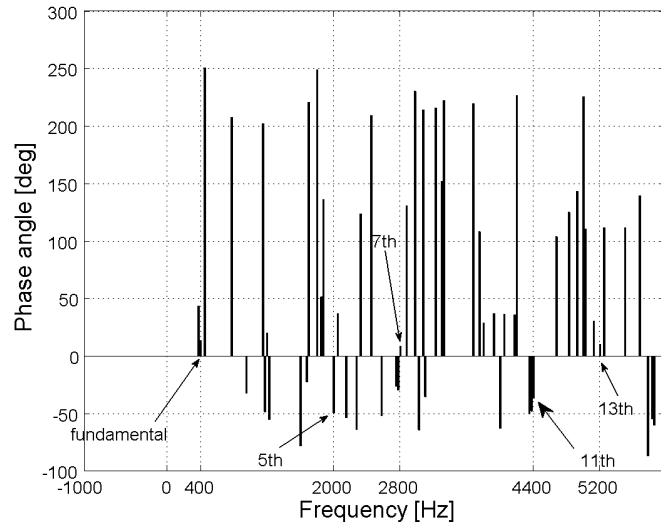
Figure 3.35: FFT spectrum of the phase of input line-to-line voltage
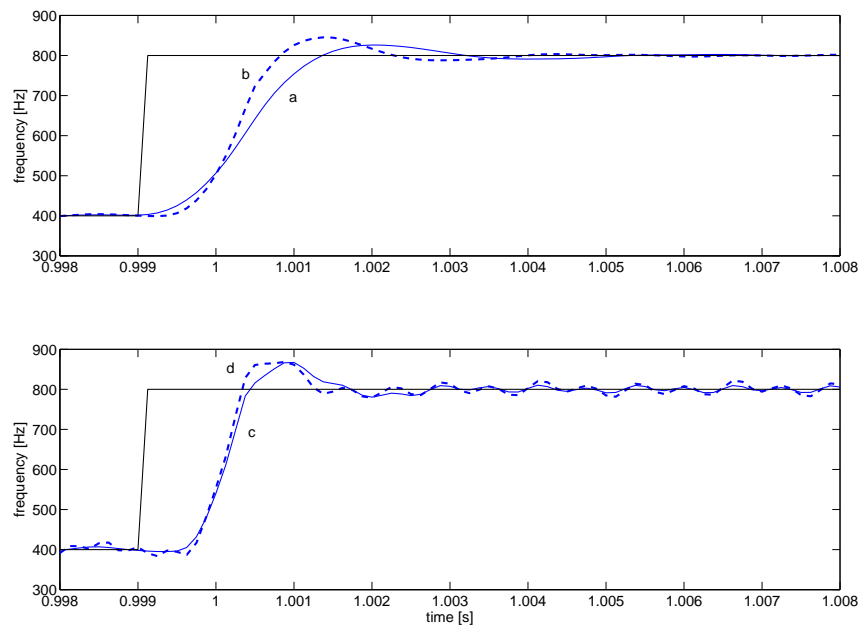
Figure 3.36: Experimental response to a frequency step for different buffer sizes

Sampling frequency [Hz]	8 kHz
Observation interval T_{obs}	
Case (a)	T
Case (b)	$\frac{3}{3}T$
Case (c)	$\frac{1}{2}T$
Case (d)	$\frac{2}{5}T$
Buffer length n	
Case (a)	20
Case (b)	15
Case (c)	10
Case (d)	8
Frequency PI controller s domain	
Case (a)	$k_p = 0.4;\ k_i = 640$
Case (b)	$k_p = 0.4;\ k_i = 820$
Case (c)	$k_p = 0.4;\ k_i = 1230$
Case (d)	$k_p = 0.4;\ k_i = 1550$

Table 3.9: Frequency detection algorithm parameters for the experimental implementation

	case (a)	case (b)	case (c)	case (c)
Maximum overshoot [%]	6.5	11.25	16.7	17.1
Delay time [s]	0.0004	0.0002	0.0001	0.0001
Rise time [s]	0.0014	0.0008	0.0005	0.0005
Settling time 5% [s]	0.0025	0.002	0.0014	0.0012
Peak time [s]	0.002	0.0014	0.001	0.0009
Steady-state oscillation max amplitude (% of the steady-state value)	0.25	0.5	2.5	5
Steady-state error [Hz]	0.0347	0.0308	0.0244	0.0095

Table 3.10: Transient and steady-state performance of the frequency step estimation

3.8 Harmonic estimation : experimental results

The harmonic estimation has been performed experimentally on the input signal described in the previous section. Figures 3.37 to 3.48 show the estimate of the amplitude and phase of each component, obtained by means of the experimental implementation of the algorithm at 8 kHz. The results are presented for each of the four cases in table 3.9. The amplitude estimates are reported in terms of percentage errors and the phase estimates are reported in terms of absolute value of the estimation error.

Only the 5th and 7th harmonic have been estimated as, with the fundamental at 400 Hz, the 11th and 13th harmonic occur at higher frequencies than the Nyquist frequency, which is equal to half the sampling frequency. In this particular example, the 11th and 13th harmonic occur at 4400 Hz and 5200 Hz respectively, which are bigger than 4000 Hz, the Nyquist frequency in this case. Section 3.6 presented the results obtained from the estimation of the 5th, 7th, 11th and 13th harmonics in simulation, with sampling frequency equal to 12 kHz and fundamental frequency varying as a step from 400 Hz to 800 Hz. When the fundamental frequency is 400 Hz, all the harmonics up to the 13th, which in that case occurs at 5200 Hz, are below the Nyquist frequency at 6000 Hz. According to Nyquist-Shannon Sampling Theorem [52], when the fundamental frequency is 800 Hz and the sampling frequency is 12 kHz, only the 5th and 7th can be estimated correctly. However, in simulation, it was possible to estimate also the 11th and 13th harmonic during the 800 Hz steady-state, because the signal in that case is not noisy and there are no other components which can interfere with the 11th and 13th harmonic in the frequency domain. 800 Hz is a particular case where all of the four harmonic components can be identified properly, even if the signal sampling does not respect the Shannon Theorem condition. This is shown in section 3.9.
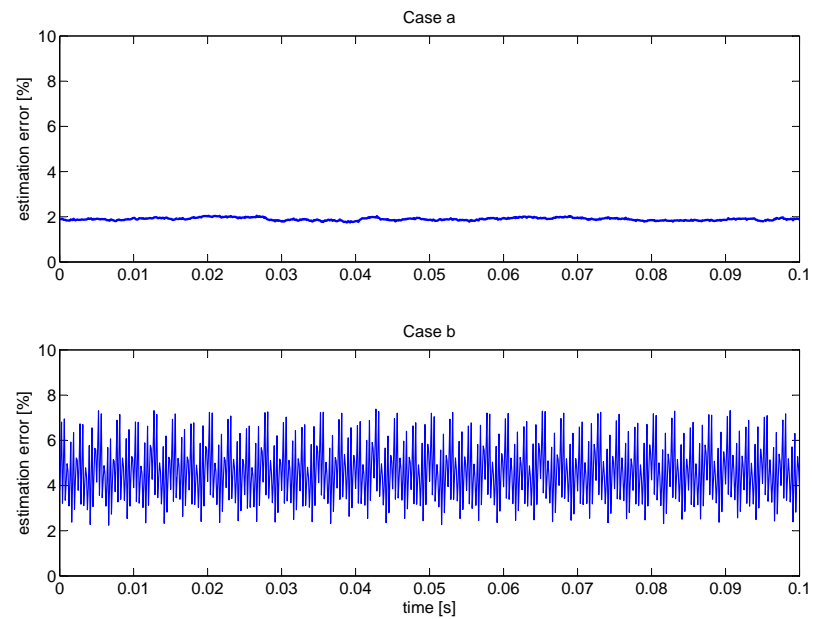
Figure 3.37: Fundamental amplitude estimated experimentally. Cases a and b
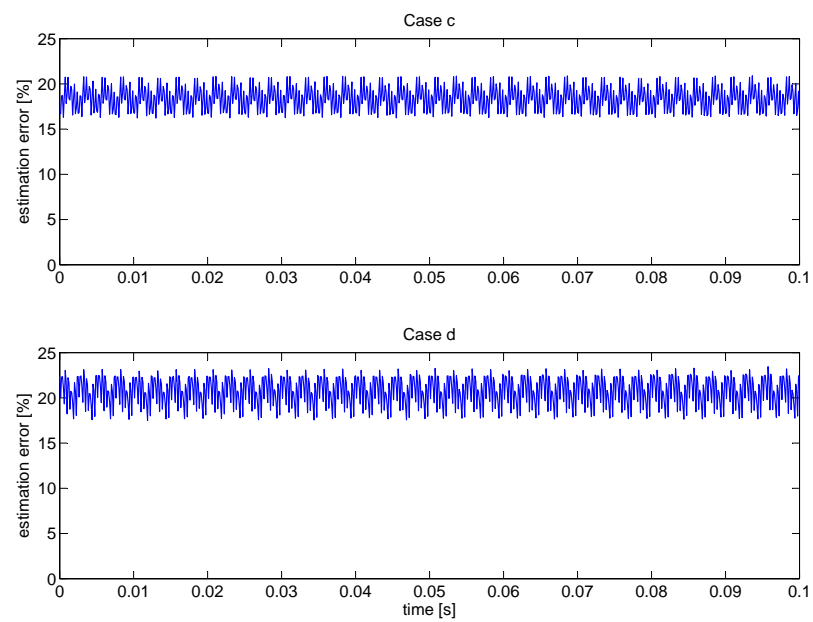
Figure 3.38: Fundamental amplitude estimated experimentally. Cases c and d
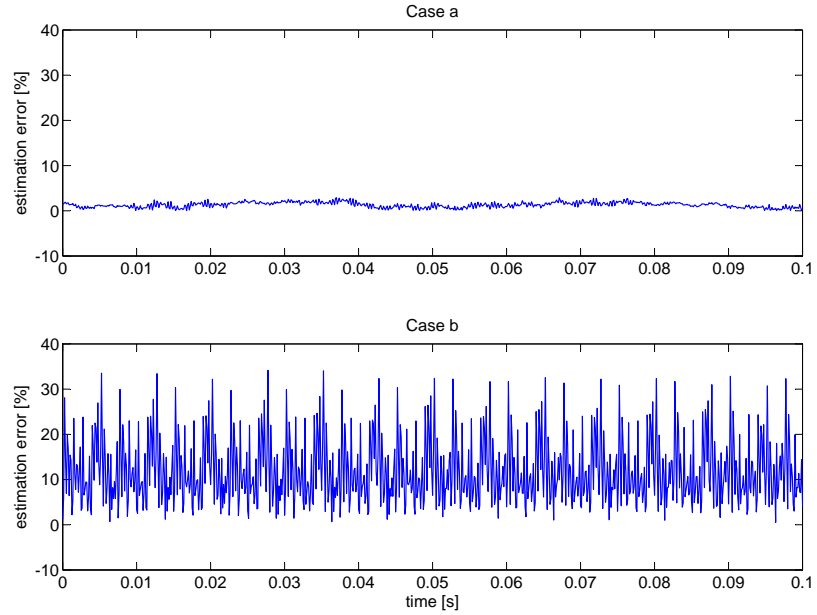
Figure 3.39: 5th harmonic amplitude estimated experimentally. Cases a and b
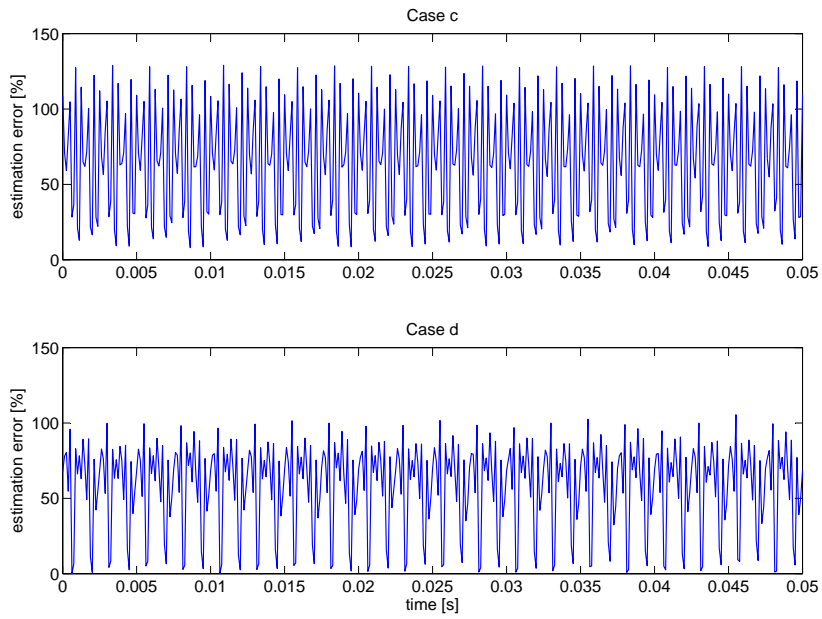
Figure 3.40: 5th harmonic amplitude estimated experimentally. Cases c and d
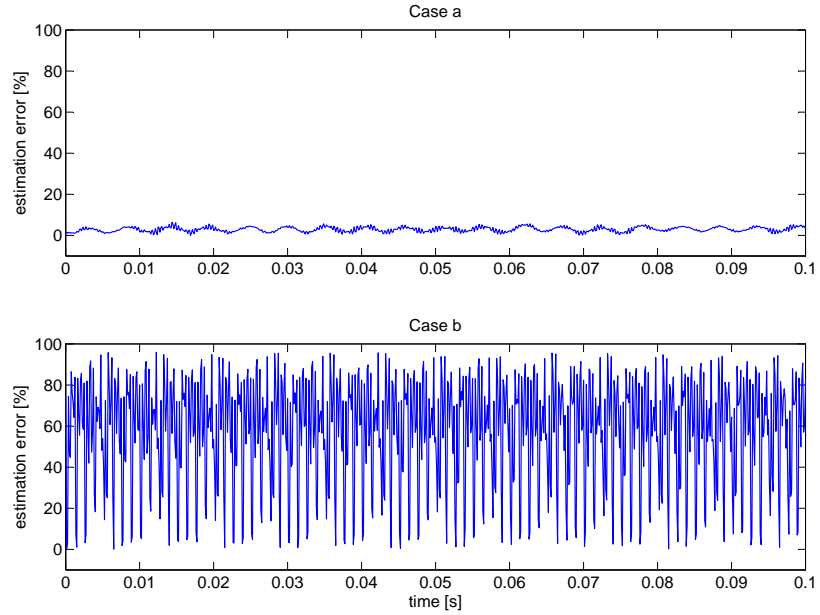
Figure 3.41: 7th harmonic amplitude estimated experimentally. Cases a and b
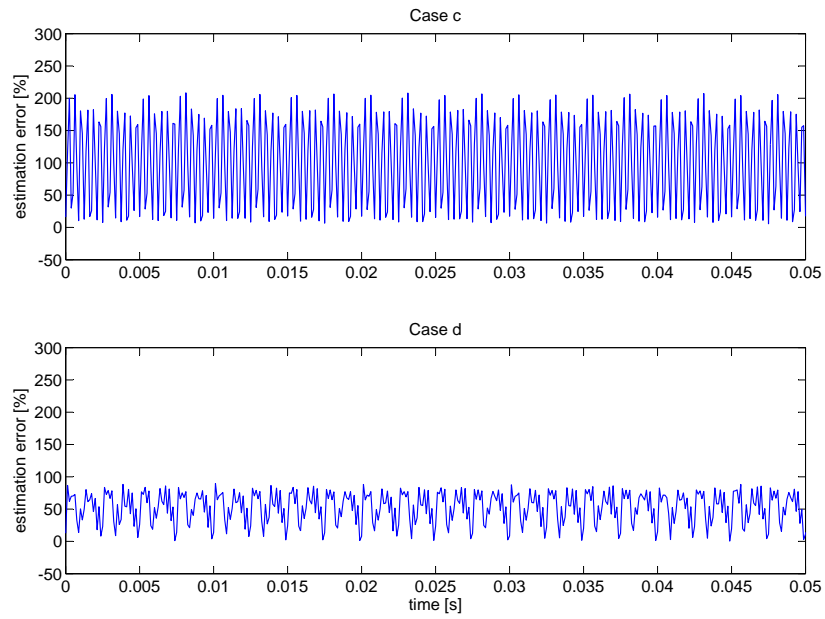
Figure 3.42: 7th harmonic amplitude estimated experimentally. Cases c and d
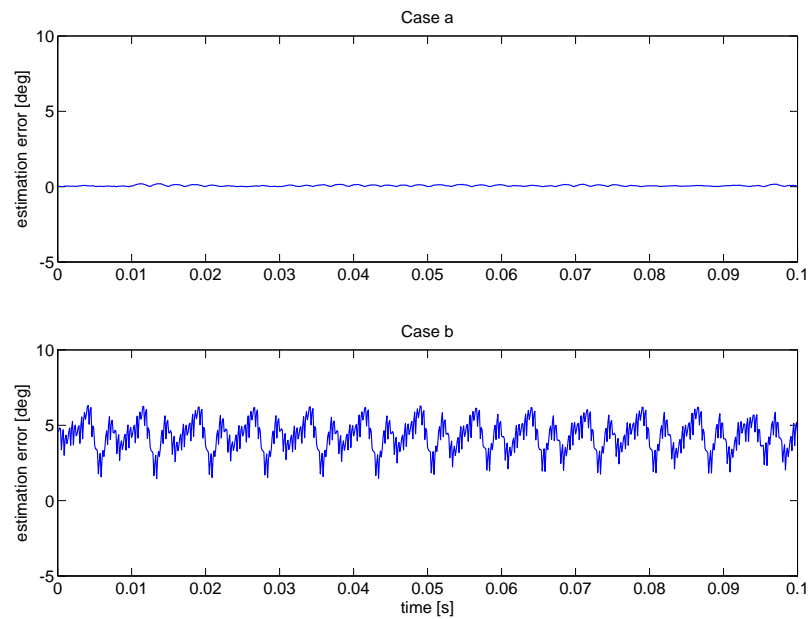
Figure 3.43: Fundamental phase estimated experimentally. Cases a and b
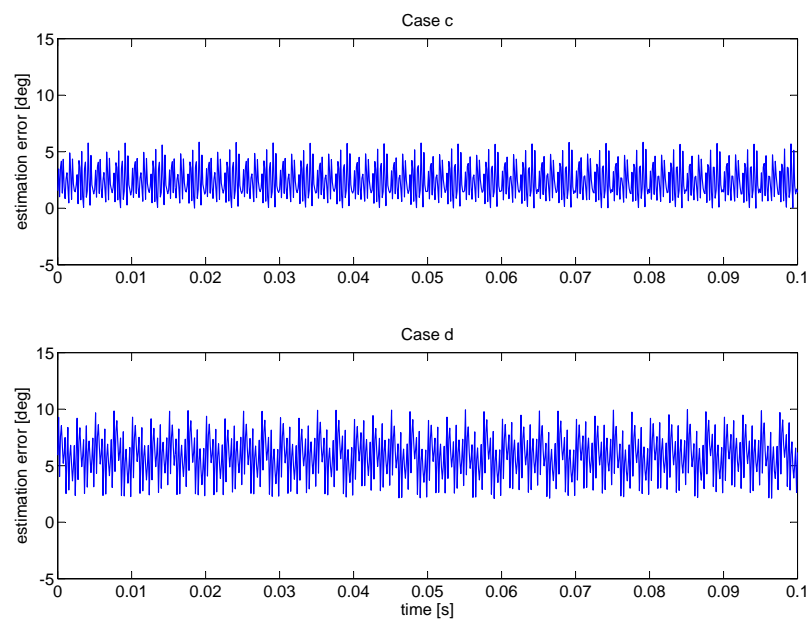
Figure 3.44: Fundamental phase estimated experimentally. Cases c and d
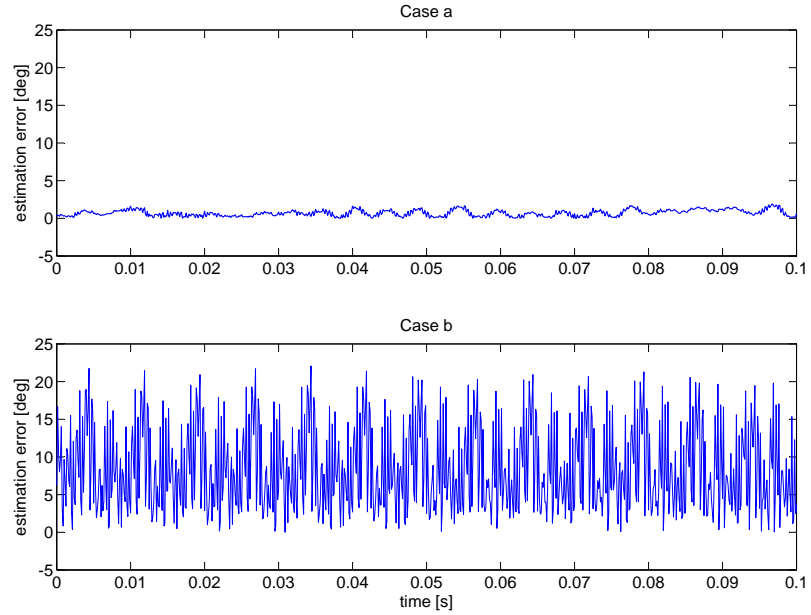
Figure 3.45: 5th harmonic phase estimated experimentally. Cases a and b
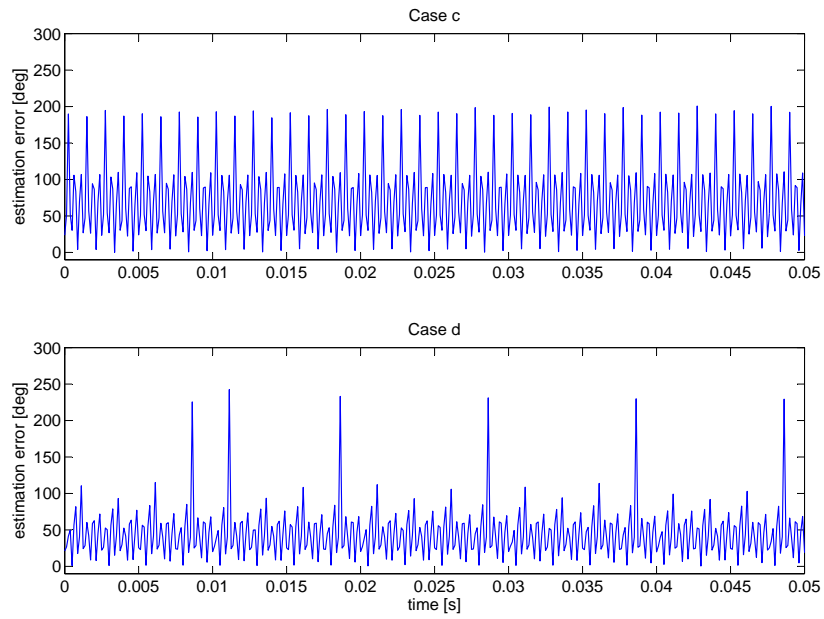
Figure 3.46: 5th harmonic phase estimated experimentally. Cases c and d
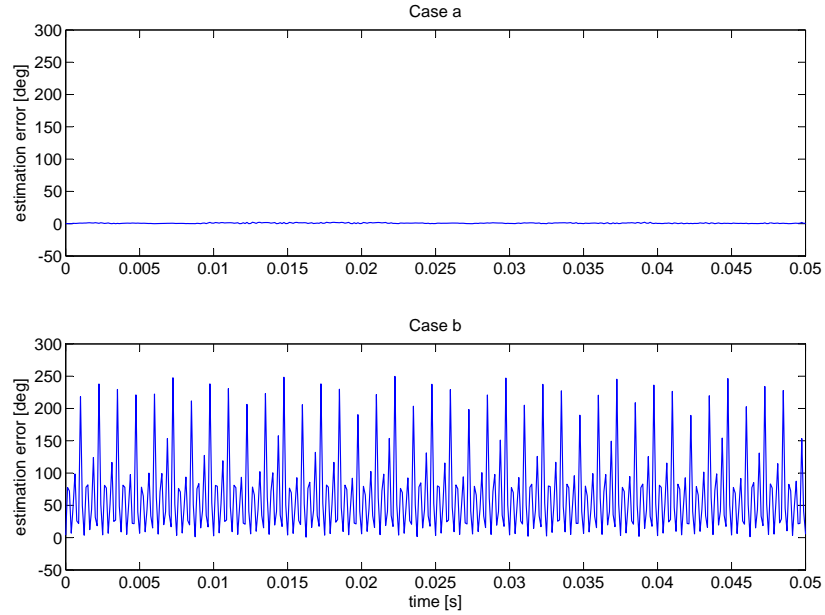
Figure 3.47: 7th harmonic phase estimated experimentally. Cases a and b
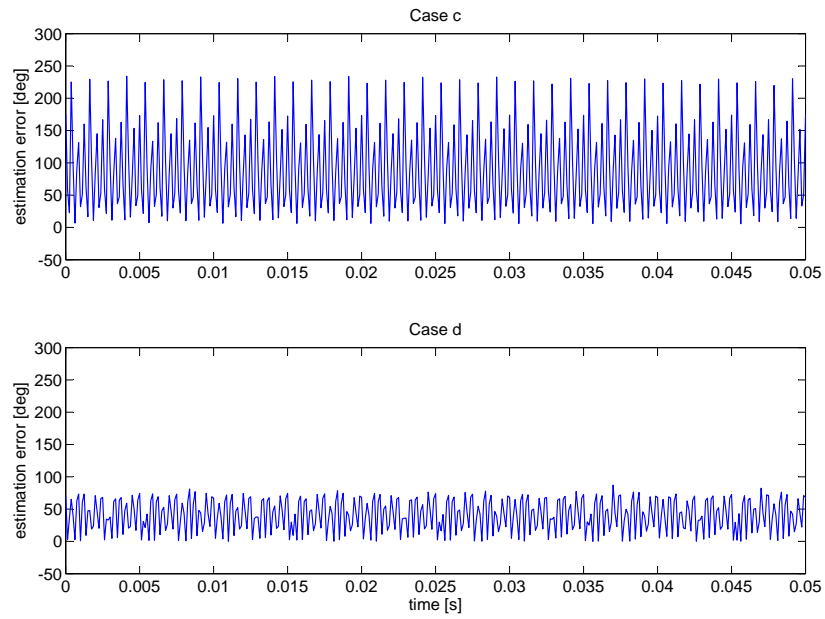
Figure 3.48: 7th harmonic phase estimated experimentally. Cases c and d

3.9 Harmonic estimation : transient analysis

According to the Nyquist-Shannon Sampling Theorem, a periodic signal with limited bandwidth is correctly sampled without loss of information if the sampling frequency is equal to or greater than twice the maximum frequency of the signal spectrum [52]. This condition must be observed for the proposed algorithm in order to provide an accurate estimate of the harmonics. Generally it is useful to use an anti-aliasing filter with cut-off frequency equal to the Nyquist frequency, i.e. half the sampling frequency. However, as it has been shown in the previous sections, in some cases it is still possible to estimate harmonic components above the Nyquist frequency, at the steady-state. This happens when the signal is not noisy and the harmonic components to be estimated are not affected by interference with other harmonics in the spectrum. Furthermore, in these cases, a correct steady-state estimate can be provided only at certain frequencies, as explained further on in this section.

An example of the loss of information that occurs when the Sampling Theorem is not applied properly is presented here. A distorted not noisy signal composed of a fundamental component plus 5th, 7th, 11th and 13th harmonics is considered. The sampling frequency is 12 kHz and the FFT analysis is performed using a 30 points observation window. The signal is represented as a complex quantity, in its $\alpha\beta$ components. With the sampling frequency equal to 12 kHz, the Nyquist frequency is 6000 Hz, so the signal can be analysed correctly if the maximum frequency of the spectrum, corresponding with the 13th harmonic, is below 6000 Hz. This happens if the fundamental frequency is smaller than 460 Hz. Figures 3.49 to 3.51 show the FFT spectrum of the signal in terms of power spectral density, for a signal with fundamental frequency equal to 400 Hz, 500 Hz and 700 Hz respectively.

Considering that only a signal with fundamental frequency not greater than 6000/13 = 461.5385 Hz can be estimated correctly in the above mentioned conditions, only in the case where the fundamental frequency is 400 Hz are all of the four harmonic components visible in the spectrum, as it can be seen in figure 3.49. The harmonic frequencies are 2000Hz, 2800Hz, 4400Hz and 5200Hz. Because of the symmetry properties of the FFT, the positive sequence harmonics, 7th and 13th, appear in
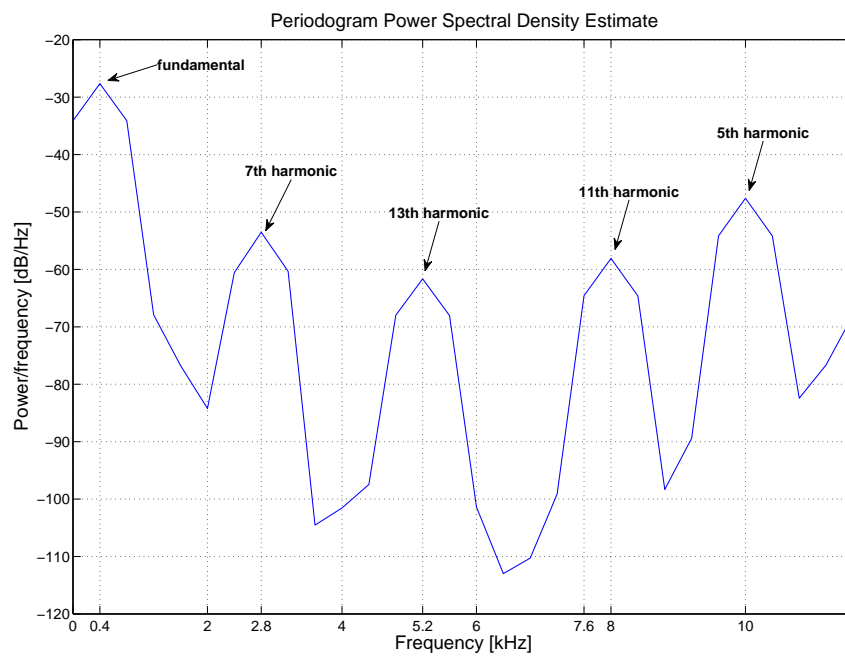
Figure 3.49: FFT spectrum with fundamental frequency 400 Hz
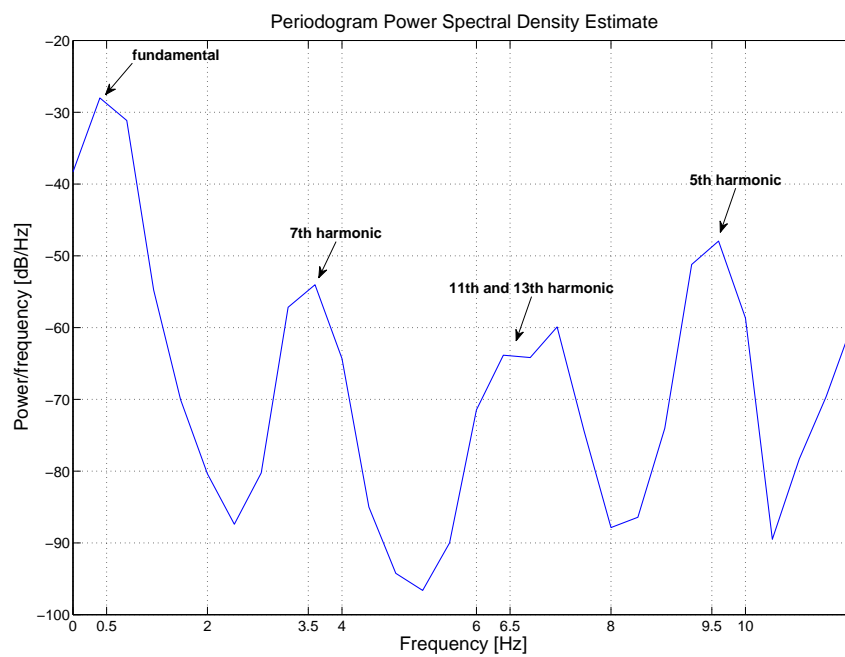
Figure 3.50: FFT spectrum with fundamental frequency 500 Hz
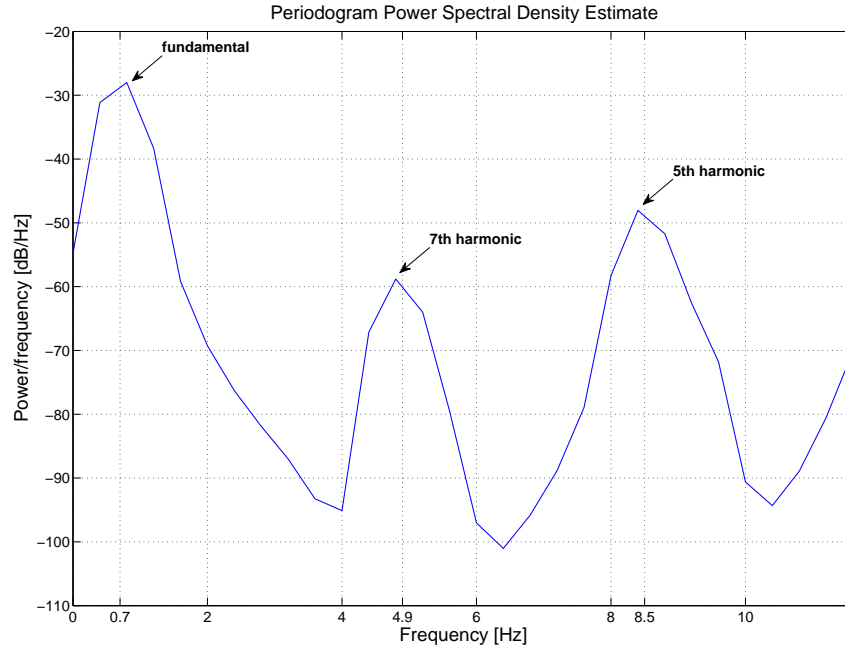
Figure 3.51: FFT spectrum with fundamental frequency 700 Hz

the left hand side of the spectrum, the negative sequence harmonics, 5th and 11th appear in the right hand side of the spectrum, at frequencies equal to 12000-2000 = 10000 Hz and 12000-4400 = 7600 Hz, as indicated in the figure.

For a signal with fundamental frequency equal to 500 Hz, not all of the four harmonic components are visible in the spectrum. The harmonic frequencies are 2500Hz, 3500Hz, 5500Hz and 6500Hz. The 7th and 13th harmonic appear at 3500 and 6500 Hz, the 5th and 11th harmonic appear at 12000-2500 = 9500 Hz and 12000-5500 = 6500 Hz. The 13th harmonic overlaps to the 11th harmonic in the spectrum so it is not identified properly.

For a signal with fundamental frequency equal to 700 Hz, the harmonic frequencies are 3500Hz, 4900Hz, 7700Hz and 9100Hz. As shown in the figure, the 11th and 13th harmonic are not identified in the spectrum.

Figure 3.52 shows the FFT spectrum in terms of power spectral density, for a signal with fundamental frequency equal to 800 Hz. 800 Hz is a particular case

where all of the four harmonic components are visible because of their position in the spectrum, although the Shannon Theorem condition is not respected.
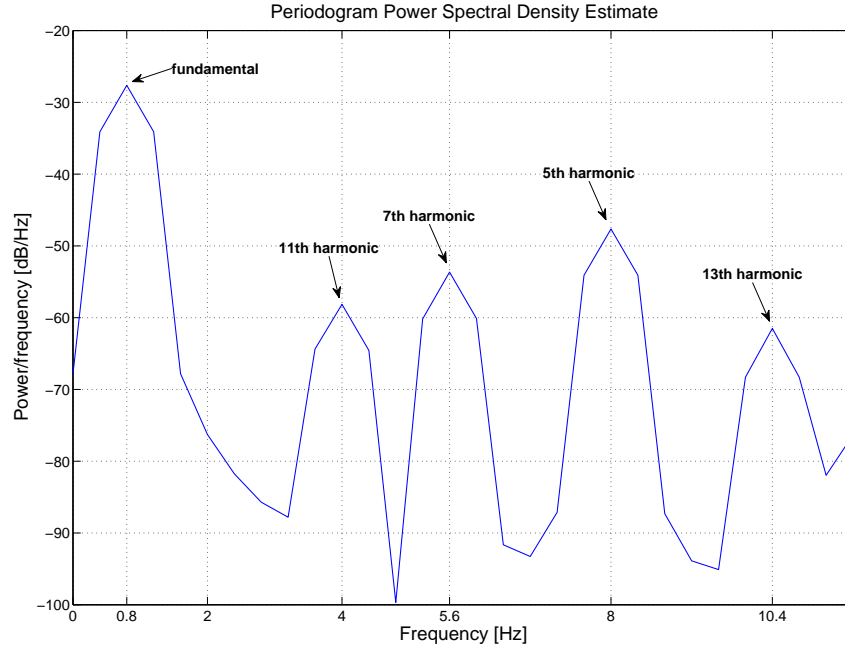
Figure 3.52: FFT spectrum with fundamental frequency 800 Hz

The performance of the proposed real-time DFT algorithm for harmonic estimation has been evaluated in simulation in order to show its behaviour in cases where the Shannon Theorem condition is valid and cases where it is not. Assuming that the sampling frequency is 12 kHz the maximum value of fundamental frequency such that the 5th, 7th, 11th and 13th harmonic can all be correctly estimated is 461.5385 Hz. Figures 3.53 to 3.59 show the estimates of the harmonic amplitudes and phases for a signal with harmonic distortion like in table 3.3, with fundamental frequency varying as a step from 200 Hz to 400 Hz, which are values below the maximum value for the validity of the Shannon Theorem condition. Figures 3.54 to 3.60 show the estimates of the harmonic amplitudes and phases for a signal with fundamental frequency varying as a step from 500 Hz to 700 Hz, which are values above the maximum value for the validity of the Shannon Theorem condition. For each of the two cases a buffer with size equal to one period of the fundamental at the minimum frequency in the step has been chosen. With the sampling frequency

equal to 12 kHz, for the 200-400 Hz step, the buffer size is 60 points; for the 500-700 Hz step it is equal to 24 points. From these figures it can be noticed that the steady-state accuracy of the estimate provided by the algorithm when the 200-400 Hz frequency step is applied is higher than in the case of a frequency step from 500 to 700 Hz. The transient response depends on the gains of the PI controller chosen for the frequency estimation, which in this case have not been tuned in order to yield a similar transient response for both cases, as the analysis in this section focuses only the steady-state performance of the harmonic estimation for different values of fundamental frequency.
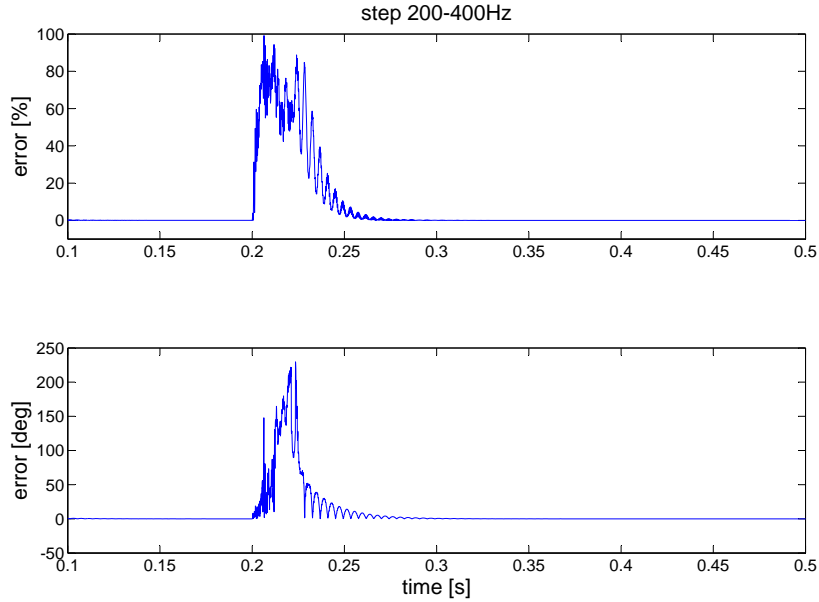
Figure 3.53: 5th harmonic

In order for the algorithm to be able to estimate all the harmonic components correctly, given a certain fundamental frequency, the sampling frequency should be increased. The limitation on the sampling frequency depends on the computational burden of the algorithm and the computational power of the digital processor. Given a sampling frequency of 8 kHz, the Nyquist frequency is 4 kHz, so the maximum fundamental frequency at which the algorithm is able to estimate all the harmonics up to the 13th is $4000/13 = 307.6923$ Hz.
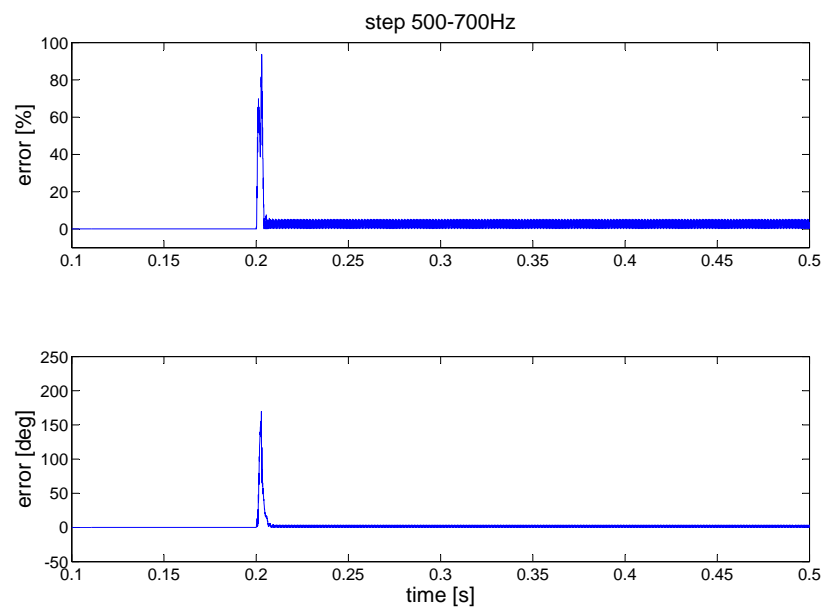
Figure 3.54: 5th harmonic
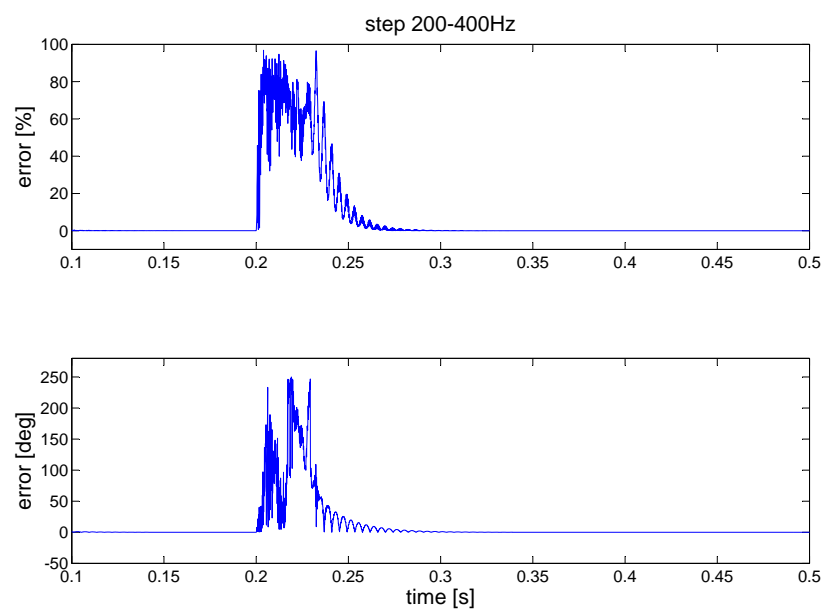
Figure 3.55: 7th harmonic
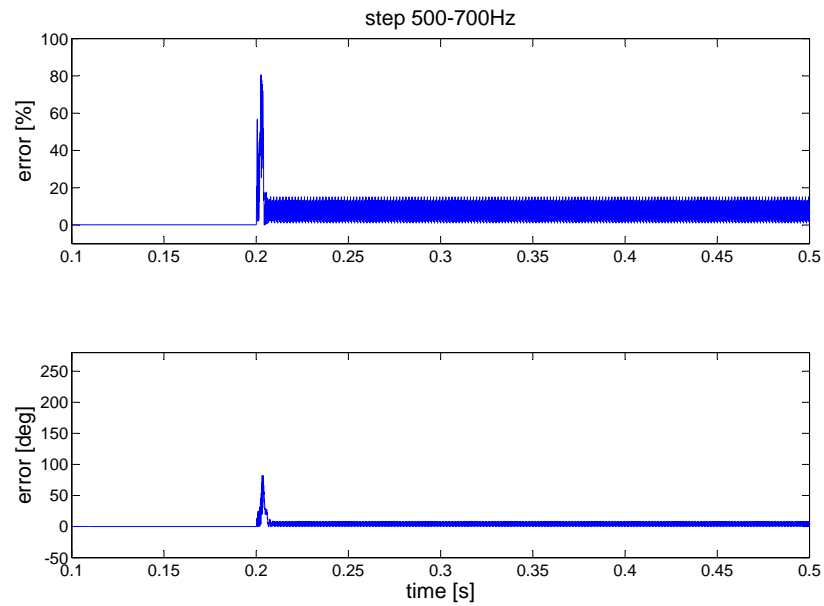
Figure 3.56: 7th harmonic
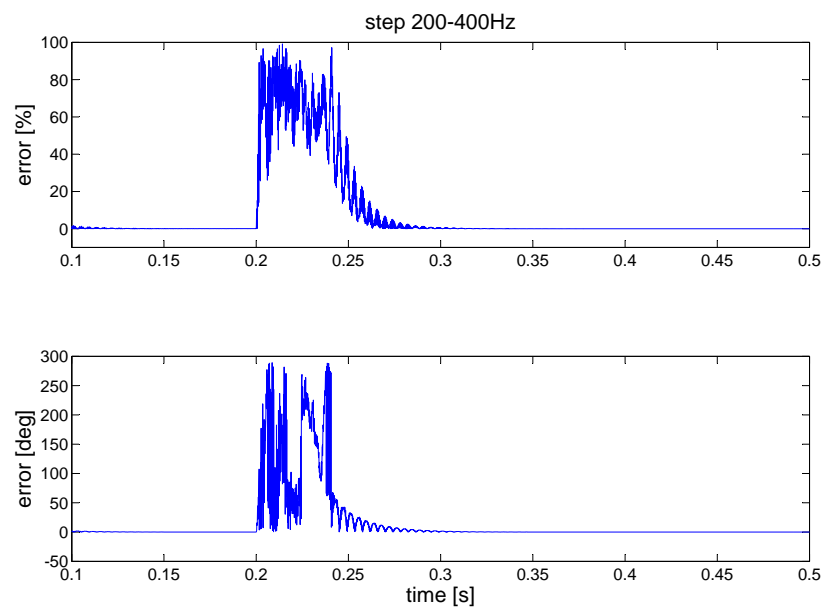
Figure 3.57: 11th harmonic
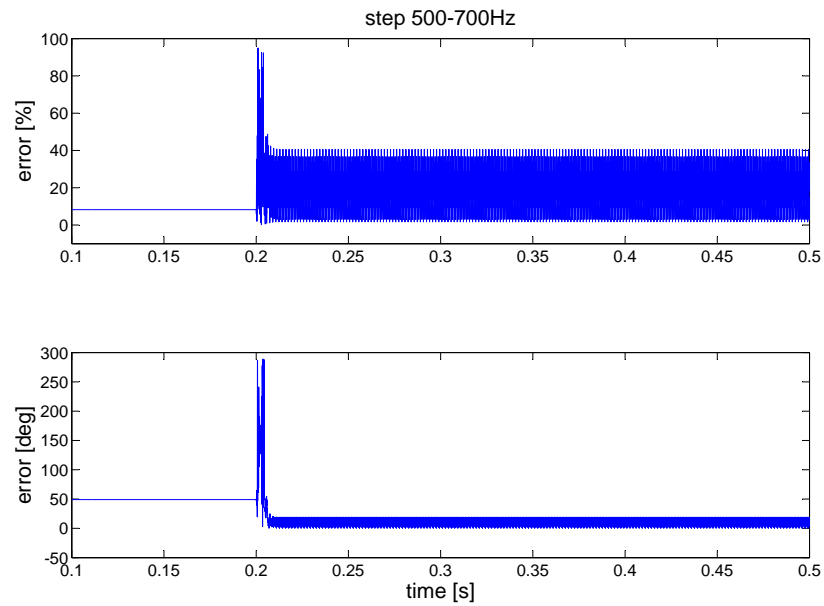
Figure 3.58: 11th harmonic
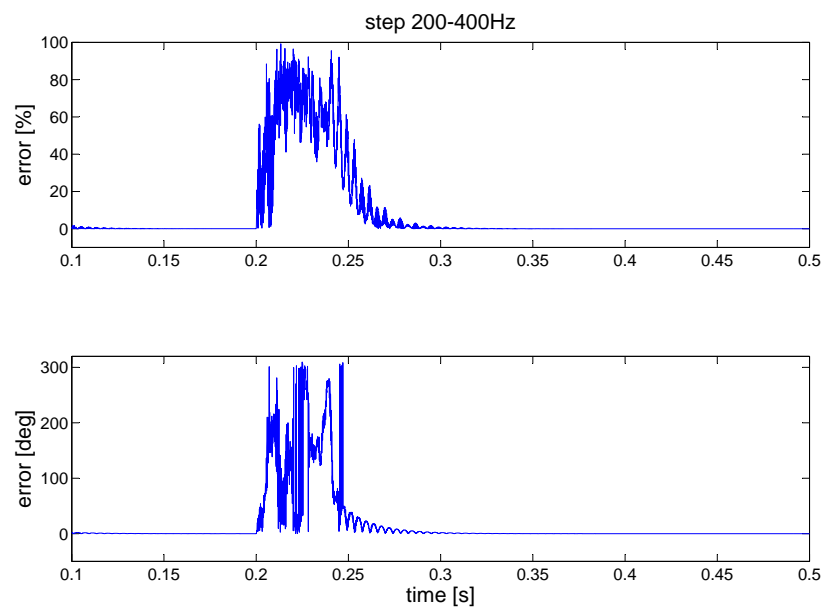
Figure 3.59: 13th harmonic
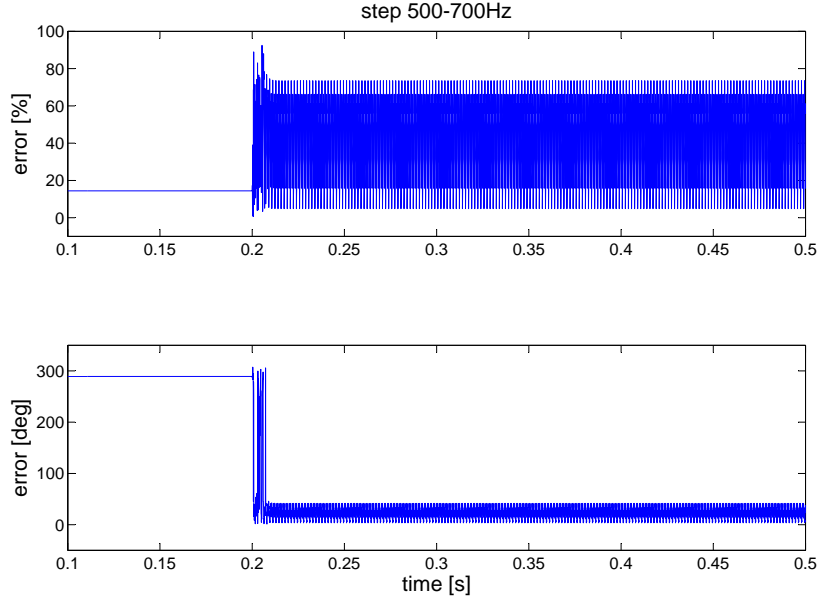
Figure 3.60: 13th harmonic

The harmonic estimation has been tested experimentally with input signals with fundamental frequency varying as a step with different values, to show the difference between the estimation performance in cases where the Shannon Theorem condition is valid and where it is not.

The first test has been carried out with a step of the fundamental frequency from 200 Hz to 400 Hz, which allows a correct estimation of the harmonics up to the 13th. The second test has been carried out with a step of the fundamental frequency from 500 Hz to 700 Hz. The distorted input signal is generated by means of the Chroma Programmable Power Supply, as described in section 3.7. The characteristics of the input signal are reported in table 3.8.

In the first case, step of frequency from 200 Hz to 400 Hz, the sampling frequency for the experimental implementation is 6 kHz and the buffer size is 30 points, which corresponds with one fundamental period at 200 Hz. In the second case, step of frequency from 500 Hz to 700 Hz, the sampling frequency is 8 kHz and the buffer size is 16 points, which corresponds with one fundamental period at 500

Hz.

Figures 3.61, 3.63, 3.65, 3.67 show the estimates of the harmonic amplitudes and phases for a signal with fundamental frequency varying as a step from 200 Hz to 400 Hz, which are values below the maximum value for the validity of the Shannon Theorem condition. Figures 3.62, 3.64, 3.66, 3.68 show the estimates of the harmonic amplitudes and phases for a signal with fundamental frequency varying as a step from 500 Hz to 700 Hz, which are values above the maximum value for the validity of the Shannon Theorem condition.
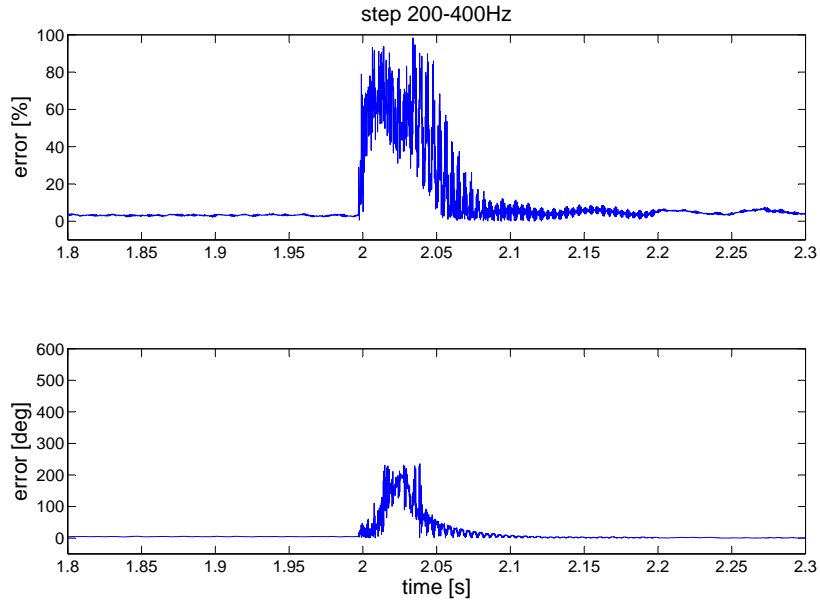
Figure 3.61: 5th harmonic

3.10 Summary

A real-time Discrete Fourier Transform for the estimation of the fundamental frequency and phase and harmonic amplitudes and phases of a distorted time-varying signal has been presented in this chapter. The mathematical characteristics of the algorithm and the method for tuning its parameters have been described. The
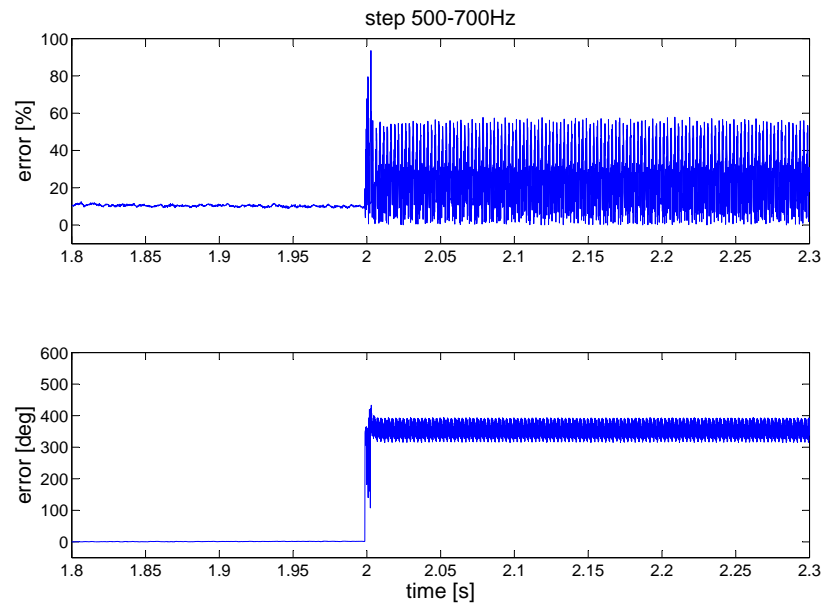
Figure 3.62: 5th harmonic
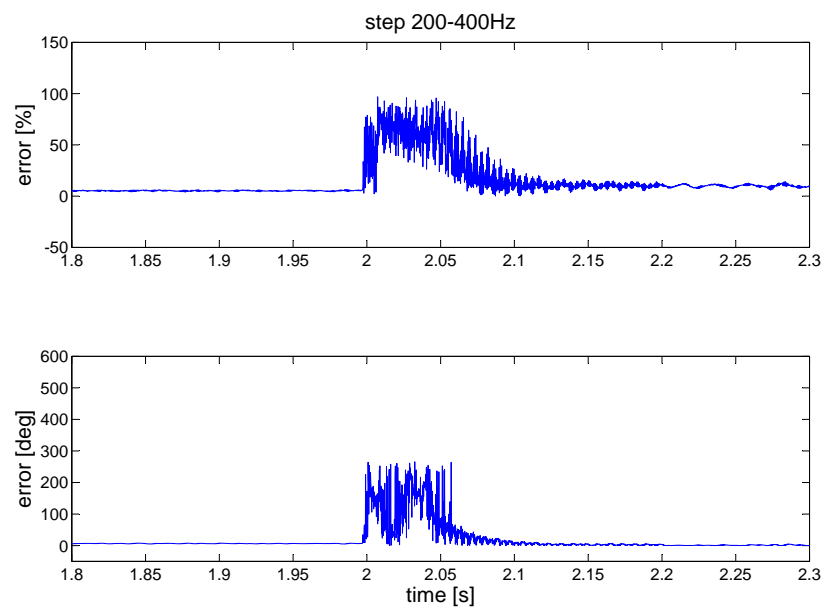
Figure 3.63: 7th harmonic
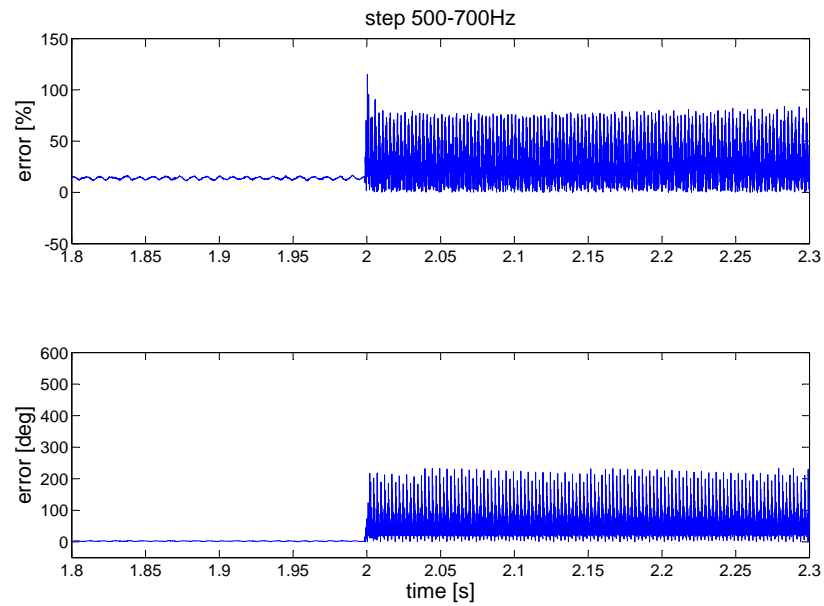
Figure 3.64: 7th harmonic
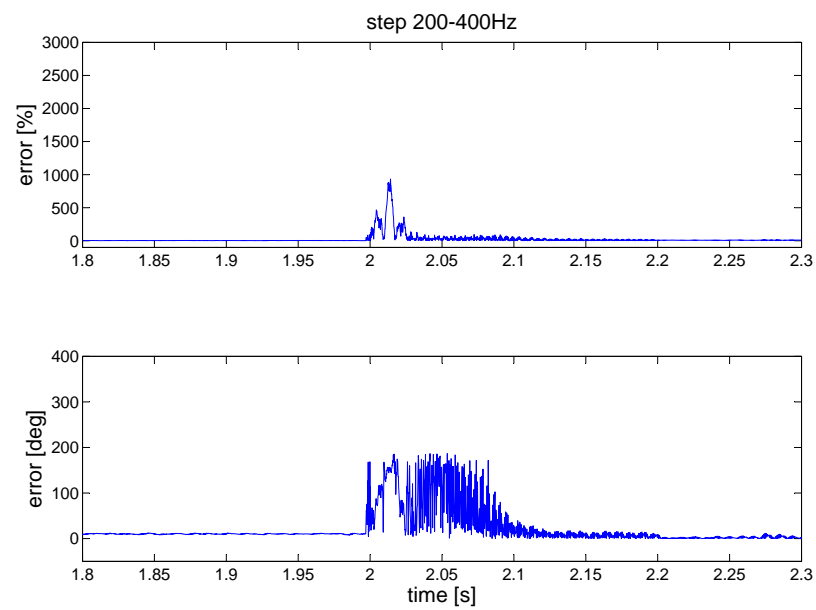
Figure 3.65: 11th harmonic
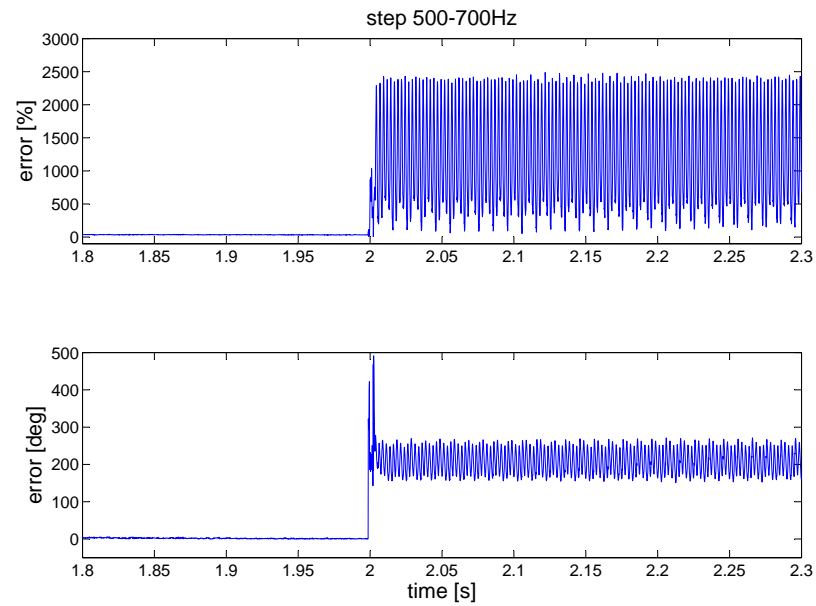
Figure 3.66: 11th harmonic
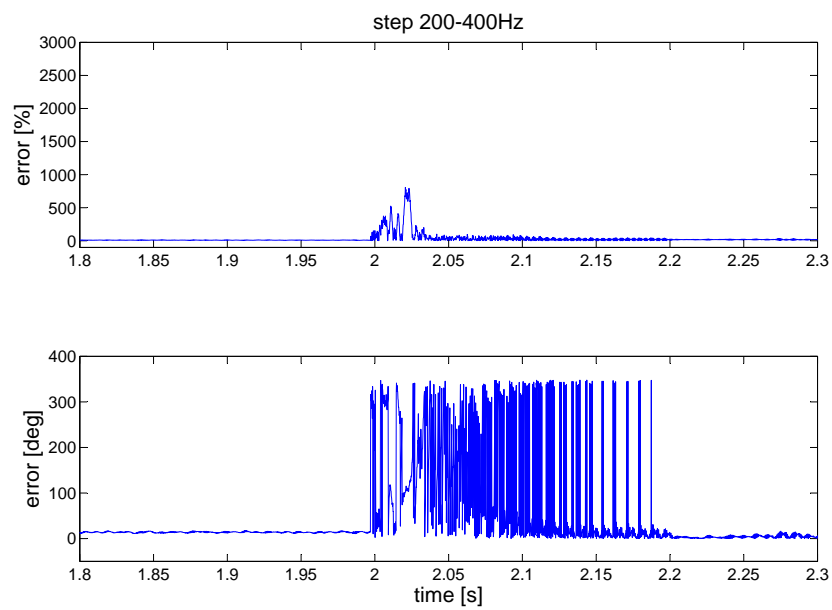
Figure 3.67: 13th harmonic
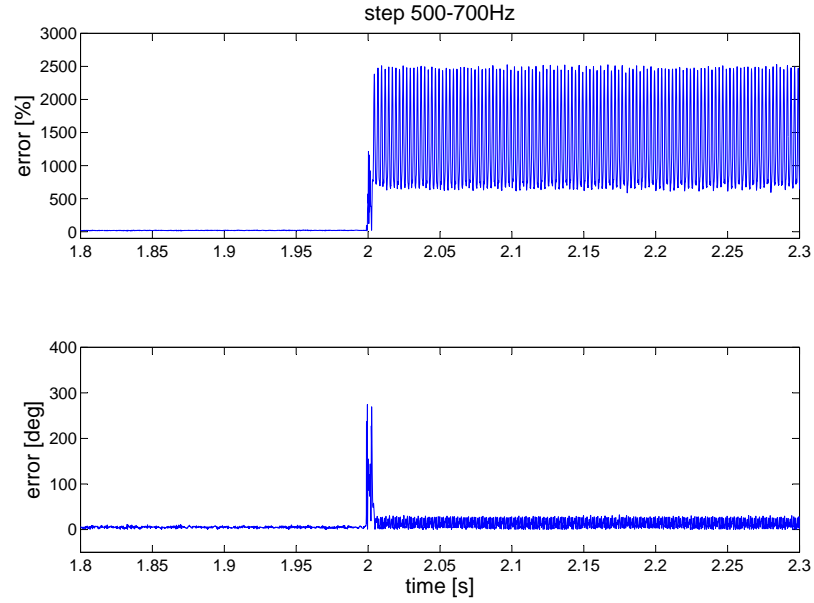
Figure 3.68: 13th harmonic

results obtained by means of simulation and experimental validation have been presented. A good accordance between the simulation and experimental results has been demonstrated. The results show that the proposed technique is able to perform a real-time Discrete Fourier Transform for the above mentioned type of signal. With a proper choice of the characteristic parameters, it can provide accurate estimation of a distorted time-varying signal, hence it is a viable solution for the detection of the reference signal for the control of an active shunt filter in the More Electric Aircraft environment.

Chapter 4

Comparison between the real-time DFT technique and the Phase Locked Loop

4.1 Introduction

This chapter presents a comparison between the real-time DFT technique for frequency and harmonic estimation, described in Chapter 3, and the Phase-Locked Loop (PLL). A comparison between the performance of a standard PLL and the proposed DFT has been made using computer simulations and it has been validated by means of experimental tests. The technique has been tested for frequency ranges typical for aircraft power systems, where the value of frequency changes between 360Hz and 900Hz. Section 4.2 describes the basic principles of the PLL and the way it works. Sections 4.3 and 4.4 present the simulation and experimental results respectively, for the comparison between the PLL and the proposed DFT technique. Comments about the advantages, disadvantages and performance of the two techniques are given in these two sections.

4.2 The Phase Locked Loop

A PLL is a device which causes one signal to track another one. It keeps an output signal synchronized with a reference input signal in frequency as well as in phase. The PLL can be considered as a servo system, which controls the phase of its output signal in such a way that the phase error between output phase and reference phase reduces to a minimum [53]. The functional block diagram of a PLL is shown in figure 4.1. It consists of a phase detector, a loop filter and a controlled oscillator.
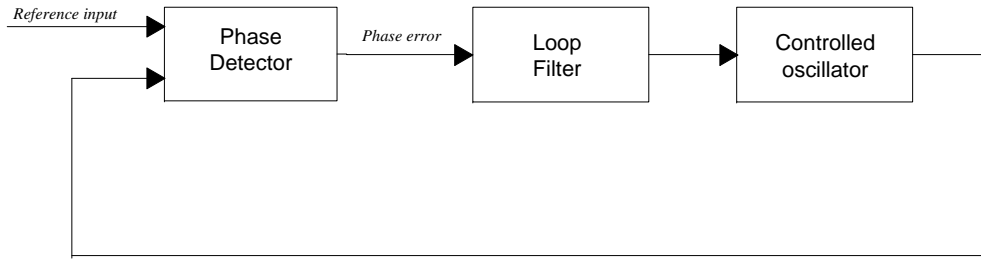
Figure 4.1: Block diagram representing the basic structure of the PLL

All types of PLL have the same basic structure and differ mainly because of the method of implementation of the phase detector. The most rudimentary type of phase detector is the zero-crossing detection. Product-type, or mixer, phase detectors are well-known and widely implemented and utilized [54, 55]. In three-phase systems the most common phase detector is the one based on the synchronous *dq* reference frame [54, 55]. The loop filter is a low-pass filter. It is used to suppress the noise and high-frequency signal components from the phase detector and provide a DC-controlled signal for the voltage-controlled oscillator. The voltage-controlled oscillators used in the PLL are similar to the ones used in other applications like modulation and automatic frequency control. The main requirements for the voltage-controlled oscillator are: phase stability, large frequency deviation, high modulation sensitivity, linearity of frequency versus voltage control and capability for accepting wide-band modulation [53].

The PLL analysed and implemented in this work has the structure shown in figure 4.2.
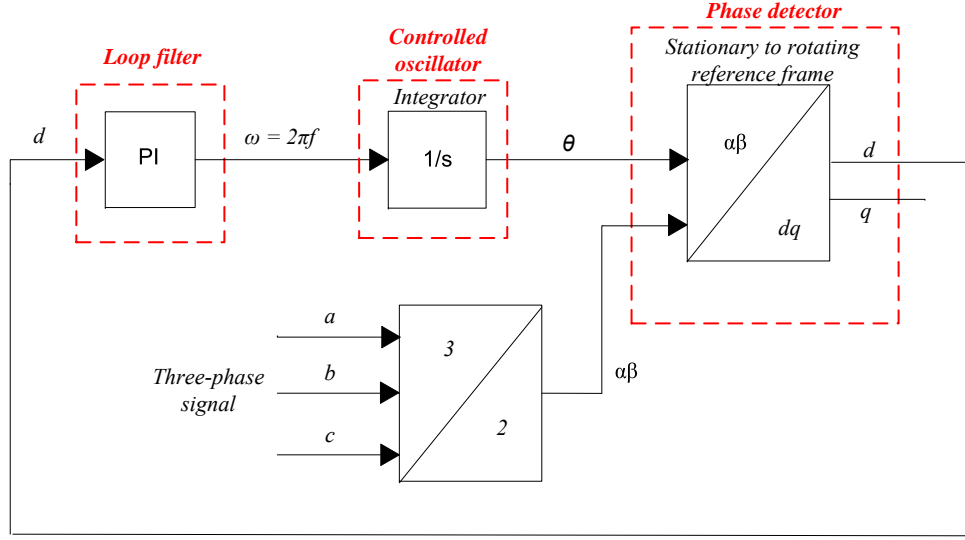
Figure 4.2: Block diagram of the implemented PLL

The phase detector is implemented with a synchronous dq rotating reference frame. The signal in its $\alpha\beta$ components is transformed into the dq components using the Park transformation as in (4.1).

$$\begin{cases} v_d(t) = v_\alpha(t)cos(\theta) + v_\beta(t)sin(\theta) \\ v_q(t) = -v_\alpha(t)sin(\theta) + v_\beta(t)cos(\theta) \end{cases} \tag{4.1}$$

where θ is the fundamental phase angle. The loop filter is represented as a Proportional Integral transfer function and the controlled oscillator is represented by an integrator. When the phase is locked, the dq signal $v_{dq} = v_d + jv_q$ is an imaginary number. The real component v_d is a function of the phase estimation error and it is used as an error signal minimized by the PI loop filter. The output of the PI loop filter is the estimated fundamental frequency ω that is integrated to give the phase θ. This angle is then used as a feedback in order to calculate the v_d and v_q components.

4.3 Comparison with the DFT algorithm: simulation results

The real-time DFT algorithm presented in Chapter 3 has been compared with the standard PLL described in the previous section, by means of a simulation validation, using the software Matlab Simulink.

4.3.1 Sinusoidal signal

For the first simulation validation the performance of the two algorithms has been compared when the input signal is a three-phase sinusoidal signal with its fundamental frequency changing as a step from 400 Hz to 800 Hz.

The two algorithms have been implemented in order to detect the fundamental frequency and the fundamental phase angle in two cases, corresponding to two different values of the signal amplitude.

In the first case the input signal rms value is 50V. The parameters of the two algorithms have been tuned in order to show similar performances in the frequency tracking, as it is shown in figure 4.3. The sampling frequency for both algorithms has been set to 8 kHz. The gains of the PLL loop filter have been selected according to the symmetrical optimum criterion [56], as explained below. For the DFT a buffer with size 20 has been chosen. The gains of the PI have been tuned by means of a trial and error procedure, in order to obtain a frequency response comparable to the one achieved with the PLL. Their proportional and integral values have been set to 0.4 and 640 respectively (s domain).

A brief description of the symmetrical optimum criterion utilized for the PLL loop filter design now follows. The representation (4.2) for the PLL loop filter transfer function is considered:

$$LF = K_{pll} \frac{1 + sT_{pll}}{sT_{pll}} \tag{4.2}$$

According to the method of symmetrical optimum [56], the loop filter gains K_{pll} and T_{pll} are selected such that the frequency response of the amplitude and phase of the open loop transfer function H_{ol} are symmetrical around the crossover frequency ω_c, which corresponds to the geometrical mean of the two corner frequencies of H_{ol}. Given a normalizing factor α, the parameters ω_c, K_{pll} and T_{pll} are related as shown in (4.3).

$$
\begin{aligned}
\omega_c &= \frac{1}{\alpha T_s} \\
T_{pll} &= \alpha^2 T_s \\
K_{pll} &= \left(\frac{1}{\alpha}\right)\left(\frac{1}{UT_s}\right)
\end{aligned}
\tag{4.3}
$$

where T_s is the sampling period and U is the amplitude of the input signal. It can be demonstrated that the normalizing factor α is related to the damping factor ξ by relation (4.4) [56].

$$\xi = \frac{\alpha - 1}{2} \tag{4.4}$$

Figure 4.4 compares the phase estimation errors obtained with the two techniques, for the sinusoidal signal with frequency step from 400 Hz to 800 Hz and rms equal to 50.

The input signal rms value has then been changed to 10 V, without re-tuning the parameters according to the new amplitude. Figure 4.5 shows the frequency estimate provided by the two algorithm in this case. It can be seen that the real-time DFT algorithm is not affected by the change of the signal amplitude, while the PLL performance is worse than in the previous case. In order for the PLL to yield a more accurate estimate of the frequency in this case, the PI loop filter gains should be re-tuned. On the other hand, the parameters of the DFT algorithm do not need to be tuned according to the change of the input signal amplitude.

Figure 4.3: Comparison of the frequency estimate for a sinusoidal signal. Step of frequency
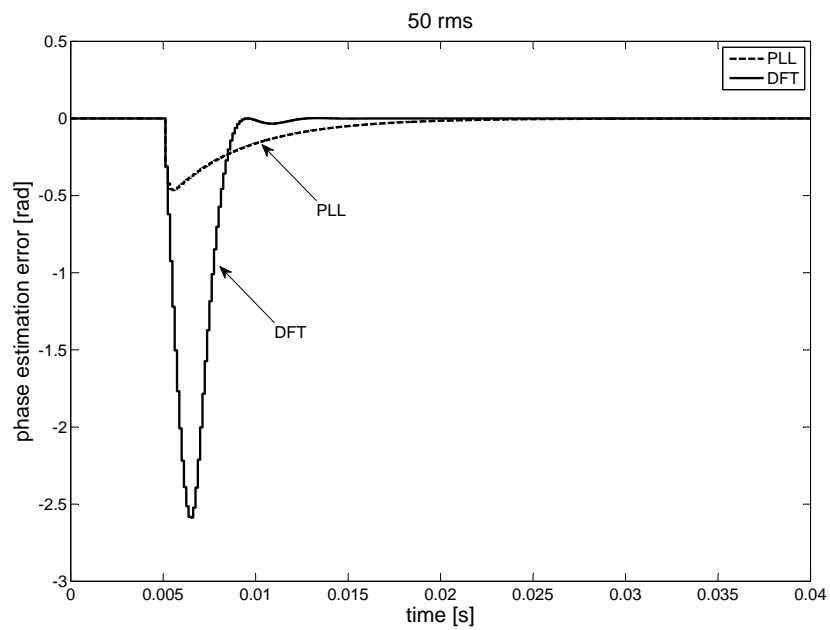
Figure 4.4: Comparison of the phase estimate for a sinusoidal signal

Figure 4.5: Comparison of the frequency estimate for a sinusoidal signal. Step of frequency

Figure 4.6 compares the phase estimation errors obtained with the two techniques, for the sinusoidal signal with frequency step from 400 Hz to 800 Hz and rms equal to 10.
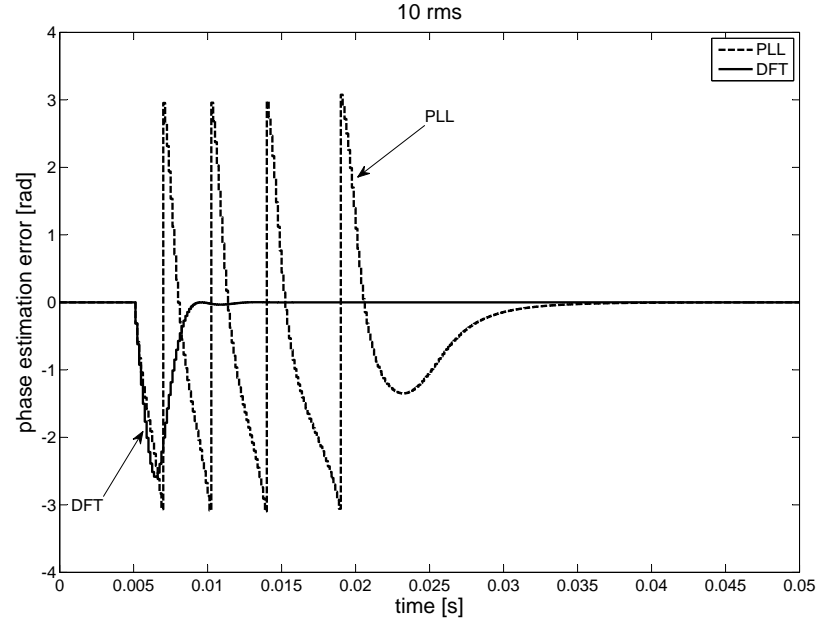
Figure 4.6: Comparison of the phase estimate for a sinusoidal signal

The characteristics of the frequency response in the two cases are reported in table 4.1.

4.3.2 Distorted signal

The second simulation validation has been carried out using a three-phase distorted noisy (noise with power spectral density equal to 10^{-7}) signal as input, with frequency variable as a ramp from 400 to 800 Hz, with slope 8000 Hz/s. The harmonic distortion is specified in table 4.2. Figure 4.7 shows the signal represented in the time domain.

Figure 4.8 shows the frequency estimate obtained with the two algorithms for a ramp of frequency, with the input signal described above. The PLL estimate has

	50 V		10 V	
	DFT	PLL	DFT	PLL
Maximum overshoot [%]	1.25	4.125	1.25	12.0825
Delay time [s]	0.0016	0.000125	0.0016	0.0038
Rise time [s]	0.0015	0.00025	0.0015	0.0171
Settling time 5% [s]	0.0026	0.000375	0.0026	0.0231
Peak time [s]	0.0034	0.000875	0.0034	0.0204
Steady-state oscillation max amplitude (% of the steady-state value)	0	0	0	0
Steady-state error [Hz]	0.0001	0.0665	0.0001	0.007

Table 4.1: Transient and steady-state performance of the frequency step estimation

5th harmonic amplitude [% of fundamental]	22
7th harmonic amplitude [% of fundamental]	10
11th harmonic amplitude [% of fundamental]	6.7
13th harmonic amplitude [% of fundamental]	5
17th harmonic amplitude [% of fundamental]	3
19th harmonic amplitude [% of fundamental]	2.2

Table 4.2: Input signal for fundamental frequency and phase estimation
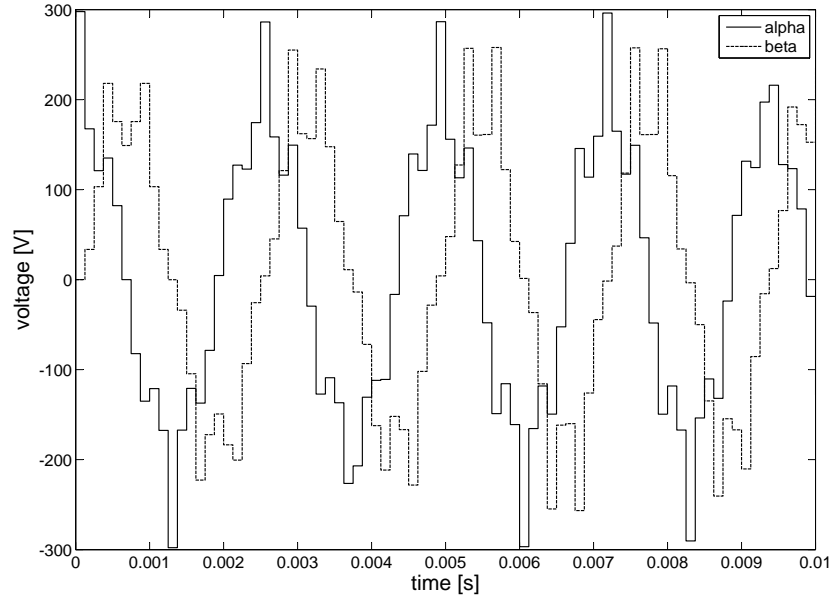
Figure 4.7: Distorted noisy signal for the simulation comparison

bigger oscillations compared to the DFT estimate, thus showing a bigger sensitivity to the harmonic distortion and the noise.

Figures 4.9 and 4.10 show the frequency estimation error and the phase estimation error respectively, for both algorithms. From these figures it can be seen that the DFT technique shows a reduced sensitivity to harmonics and noise. For both algorithms the phase estimation error is negligible at steady-state.

4.4 Comparison with the DFT algorithm: experimental results

The comparison between the proposed DFT technique and the PLL has been validated experimentally, using the same laboratory set-up described in section 3.7. In order to perform the tests, the input voltage signals have been generated by the Chroma programmable power supply, described in section 3.7.
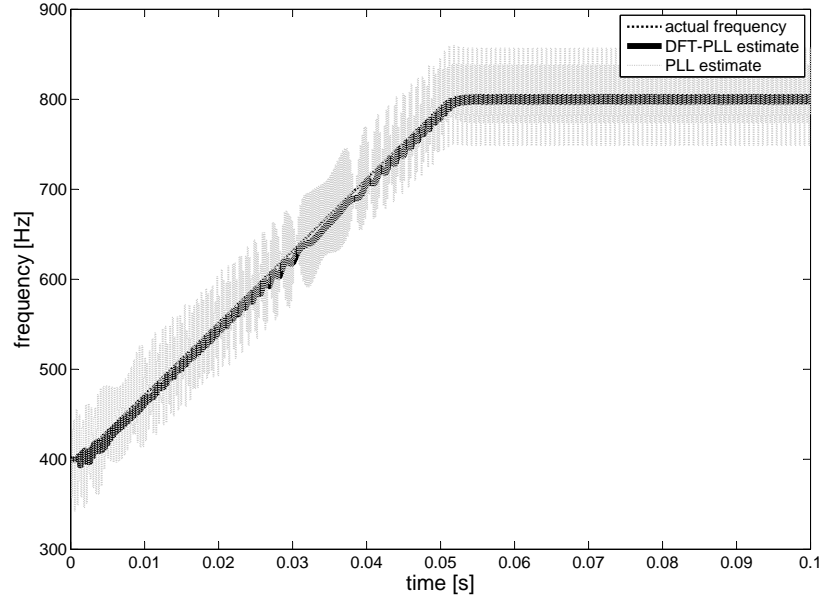
Figure 4.8: Comparison of the frequency estimate for a noisy and distorted signal. Ramp of frequency
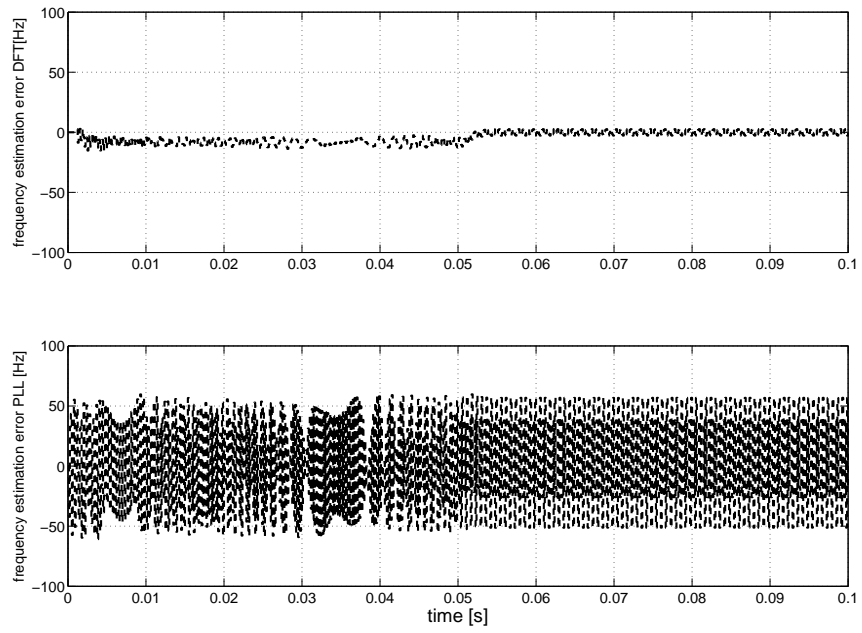
Figure 4.9: Frequency estimation error for both algorithms
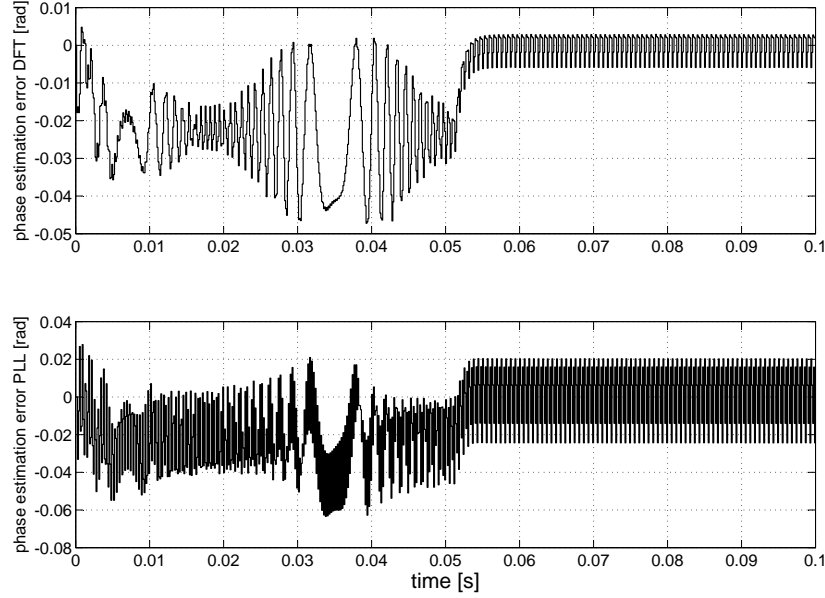
Figure 4.10: Phase estimation error for both algorithms

4.4.1   Sinusoidal signal

For the first test, a three-phase sinusoidal voltage has been generated. The fundamental frequency of the voltage changes as a step from 400 Hz to 800 Hz. The two algorithms have been implemented in order to detect the fundamental frequency and the fundamental phase angle in two cases, where the voltage amplitude is set to two different values.

In the first case the phase-to-neutral voltage is 50 V rms. The parameters of the two algorithms have been tuned in order to show similar performances in the frequency tracking, as it is shown in figure 4.11. It can be seen that, compared to figure 4.3, the frequency estimate provided by the PLL presents bigger oscillations in steady state. This is due to the noise in the experimental input voltage, which affects the PLL performance. In order for the PLL estimate to be less affected by the noise, the loop filter should be designed with a lower bandwidth, finding a compromise between the noise rejection and the speed of response at the tran-

sient. On the other hand, the DFT shows a good noise rejection, even though its parameters have not been changed with respect to the simulation case. The sampling frequency for both the algorithms has been set to 8 kHz. For the DFT a buffer with size 20 has been chosen and the proportional and integral gain of the PI controller for the frequency estimation have been set to 0.4 and 640 respectively (s domain). The gains of the PLL loop filter have been selected according to the symmetrical optimum criterion, in order to give the optimal step response for the above mentioned amplitude of the input signal.
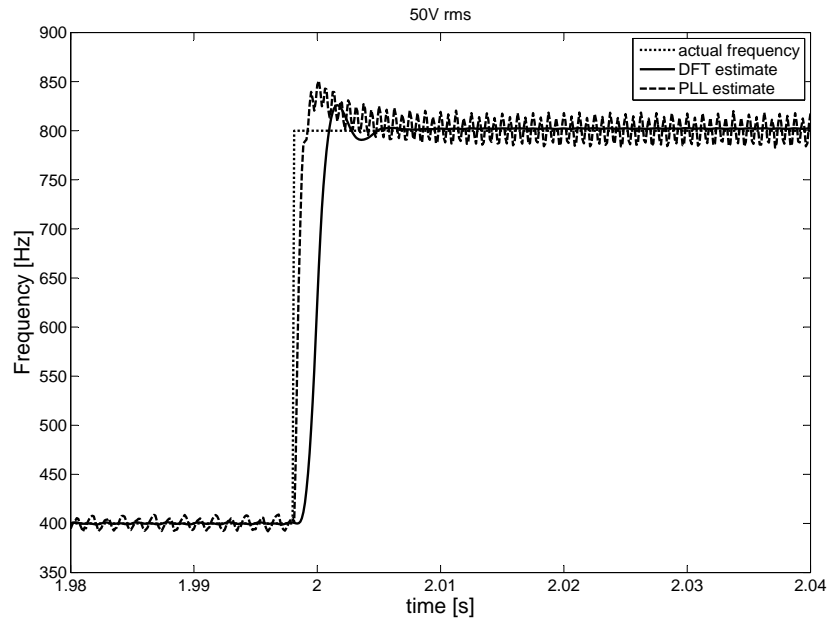
Figure 4.11: Comparison of the frequency estimate for a sinusoidal signal. Voltage rms 50V

Figure 4.12 compares the phase estimation errors obtained with the two techniques, for the 50V rms sinusoidal voltage with frequency step from 400 Hz to 800 Hz.

In the second case, the phase-to-neutral voltage rms value has been changed to 10 V, without tuning the parameters according to the new amplitude. Figure 4.13 shows the frequency estimate provided by the two algorithms in this case. It can be noticed that the real-time DFT algorithm is not affected by the change of the
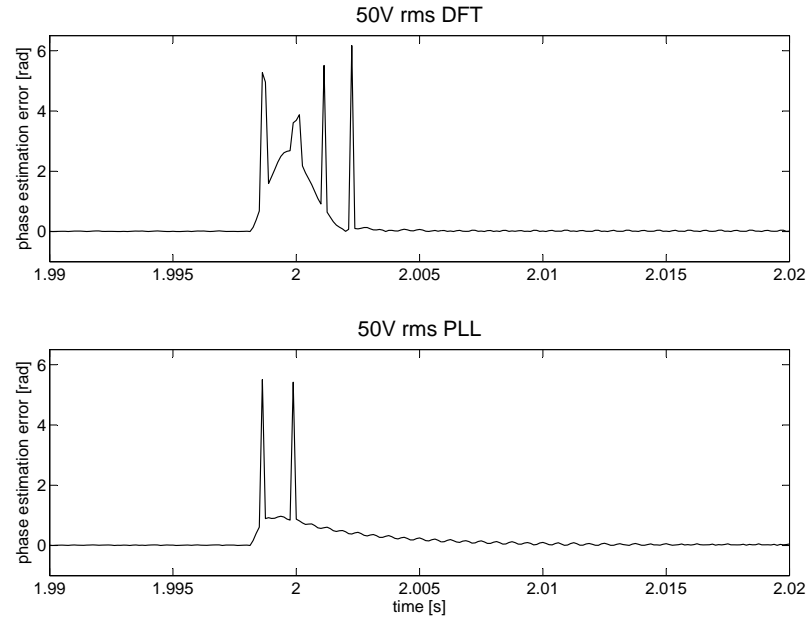
Figure 4.12: Comparison of the phase estimate for a sinusoidal signal

signal amplitude, while the PLL performance is worse than in the previous case. In order for the PLL to yield a more accurate estimate of the frequency in this case, the PI loop filter gains should be re-tuned. On the other hand, the parameters of the DFT algorithm do not need to be tuned according to the change of the input voltage amplitude.

Figure 4.14 compares the phase estimation errors obtained with the two techniques, for the 10V rms sinusoidal signal with frequency step from 400 Hz to 800 Hz.

The characteristics of the frequency response in the two cases are reported in table 4.3.

The computational time required from the two algorithms has been measured, for the digital implementation on the DSP processor. In order to perform all the calculation in one sampling step, the DFT requires 85 μs, the PLL requires 25 μs. The high computational time required from the DFT is due to the choice of
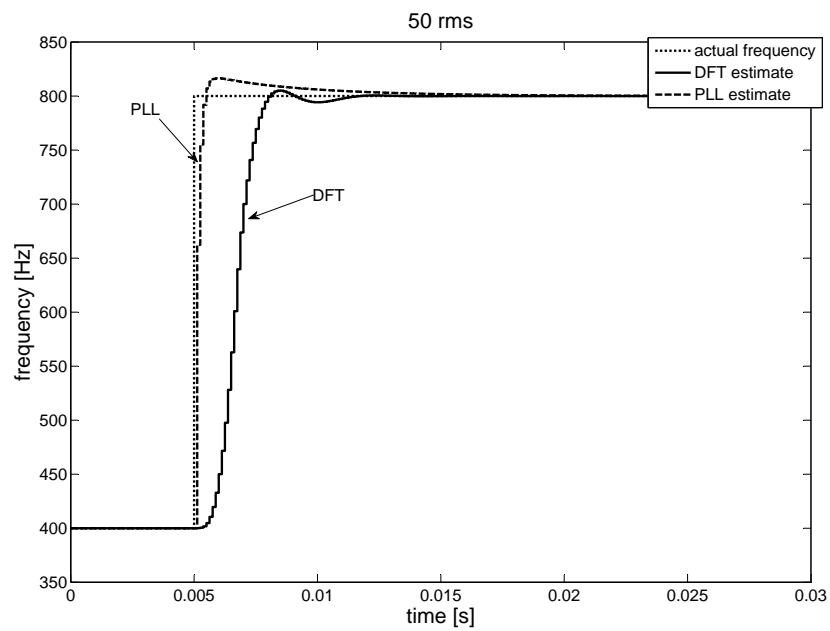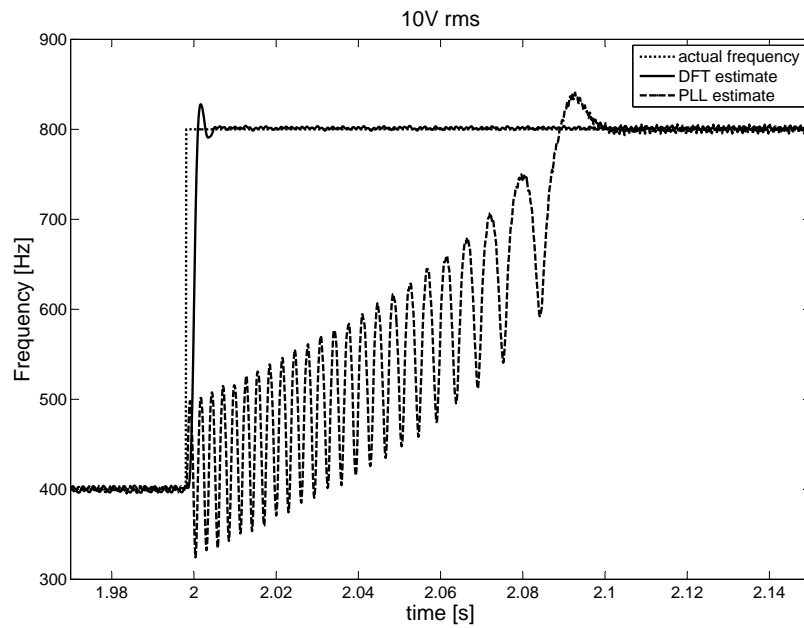
Figure 4.13: Comparison of the frequency estimate for a sinusoidal signal. Voltage amplitude 10V

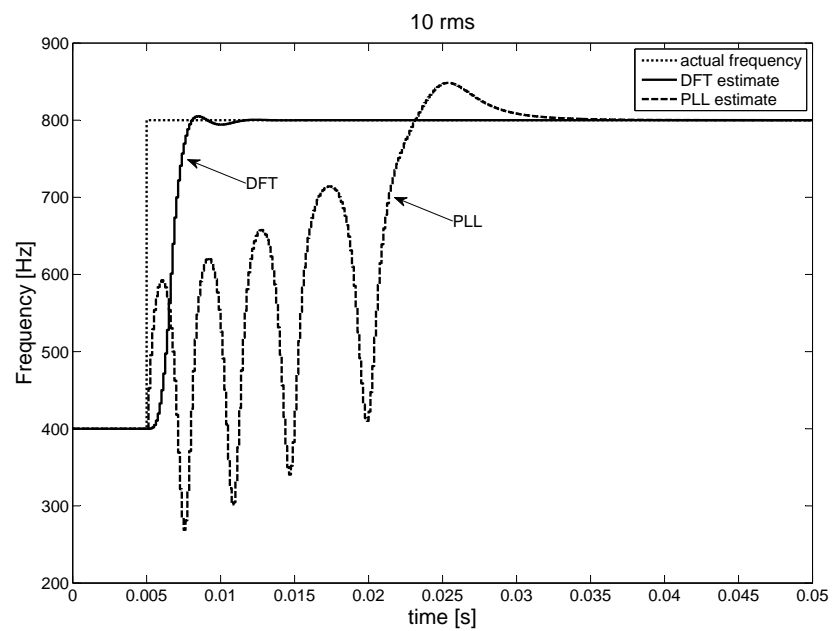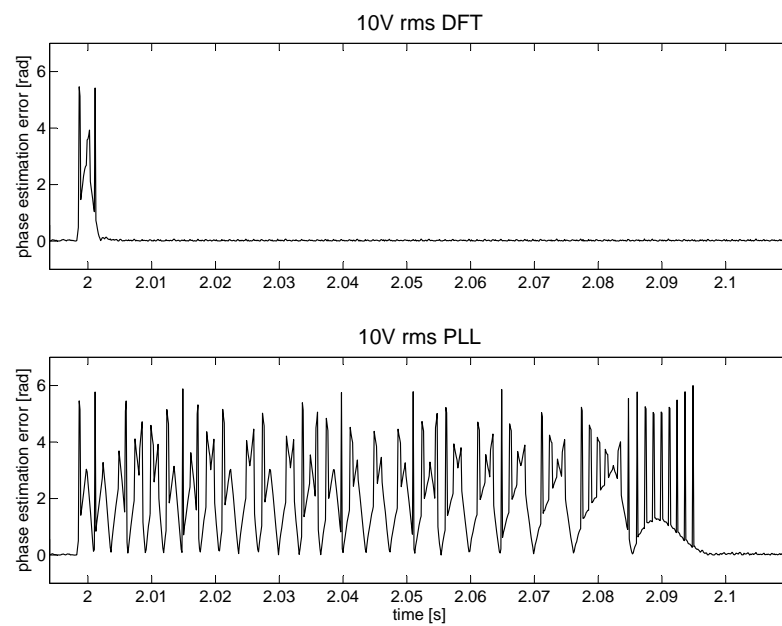Figure 4.14: Comparison of the phase estimate for a sinusoidal signal

	50 V		10 V	
	DFT	PLL	DFT	PLL
Maximum overshoot [%]	6.5	12.75	7	10
Delay time [s]	0.0019	0.0004	0.002	0.0464
Rise time [s]	0.0014	0.0006	0.0014	0.0889
Settling time 5% [s]	0.0041	0.0083	0.0042	0.0975
Peak time [s]	0.0036	0.0021	0.0036	0.0947
Steady-state oscillation max amplitude (% of the steady-state value)	0.15	5	0.625	1.175
Steady-state error [Hz]	0.0379	2.25	0.0361	1.4007

Table 4.3: Transient and steady-state performance of the frequency step estimation

the buffer size, which in this case is 20 points, equal to one entire period of the fundamental at 400 Hz (with 8 kHz sampling frequency). The buffer size could be set to a smaller value, like one quarter of the fundamental period, in that case the computational burden would significantly reduce.

4.4.2   Distorted signal

For the second test, a three-phase distorted voltage has been generated. The fundamental frequency of the voltage changes as a ramp from 400 Hz to 800 Hz, with slope 400 Hz/s. The phase-to-neutral voltage rms is equal to 50 V. The two algorithms have been implemented in order to detect the fundamental frequency and the fundamental phase angle of the input signal. The harmonic distortion of the voltage is specified in table 4.4. Figure 4.15 shows the voltage represented in the time domain.

Figure 4.16 shows the frequency estimate obtained with the two algorithms for the ramp of frequency, with the input signal described above. The PLL estimate has bigger oscillations compared to the DFT estimate, thus showing a bigger sensitivity to the harmonic distortion and the noise.

5th harmonic amplitude [% of fundamental]	15
7th harmonic amplitude [% of fundamental]	10
11th harmonic amplitude [% of fundamental]	6
13th harmonic amplitude [% of fundamental]	4

Table 4.4: Experimental voltage for fundamental frequency and phase estimation
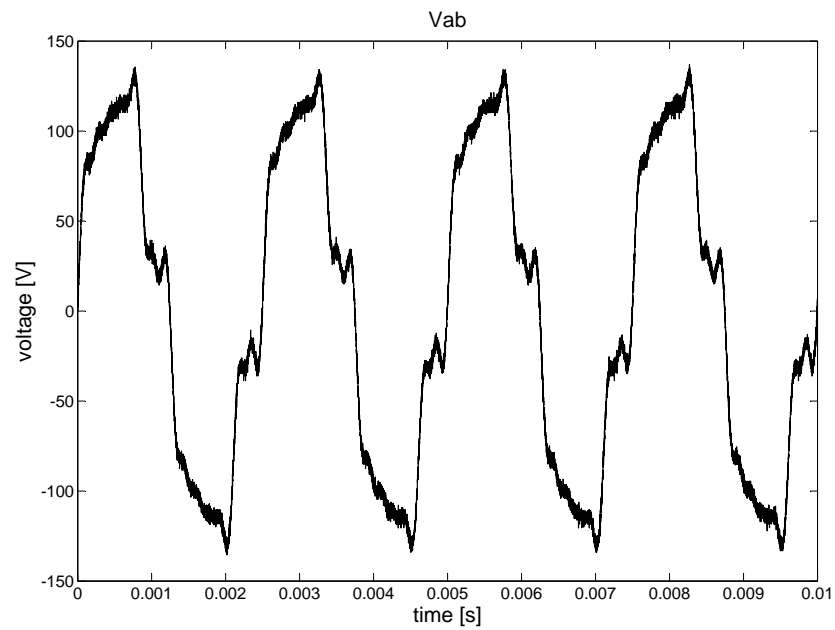
Figure 4.15: Distorted noisy voltage for the experimental comparison
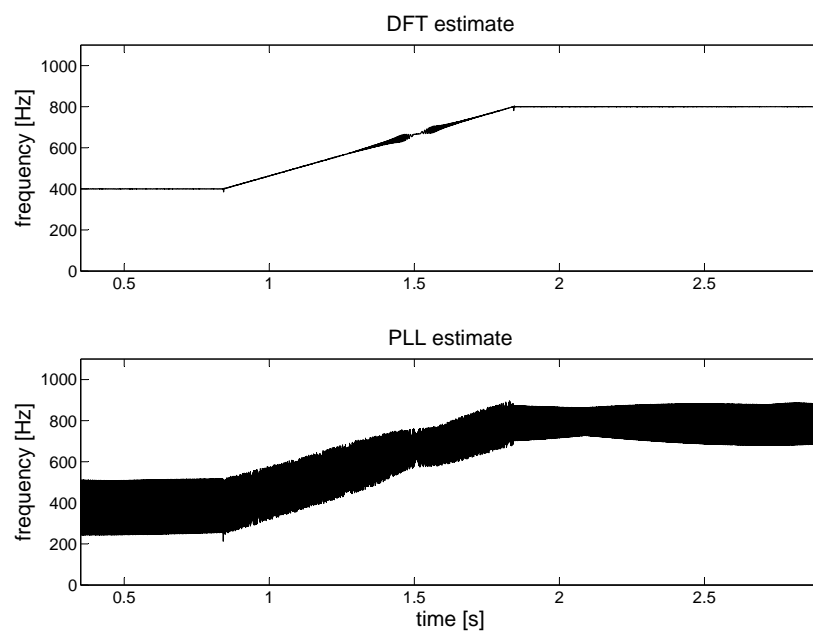
Figure 4.16: Comparison of the frequency estimate for a noisy and distorted voltage. Ramp of frequency

4.5 Summary

In this chapter a comparison between the real-time DFT algorithm presented in Chapter 3 and the Phase-Locked Loop has been presented. Simulation and experimental results show the difference between the performances of the two techniques, for the frequency estimation of sinusoidal or distorted signals with time-varying frequency, in the typical range of aircraft power systems. From the comparison it can be concluded that the DFT exhibits better dynamic performance and reduced sensitivity to harmonics, noise, and signal amplitude variations. In order to obtain a good performance from the PLL, it is necessary to tune the parameters, particularly the loop filter gains, depending on the characteristics of the signal which is to be identified. A compromise should be found between the desired speed of response and the steady-state accuracy. In terms of computational burden, the DFT implementation is characterized by higher execution time, on a digital processor board, compared to the PLL. However, the DFT implementation can be tuned and optimized in order to reduce the calculation time and still provide fast and accurate estimation of the frequency and the fundamental phase.

Chapter 5

Multiple Reference Frames Voltage Detection Control Technique

5.1   Introduction

This chapter presents a novel control technique for shunt active filters, based on the measurement of the voltage at the Point of Common Coupling (PCC). This technique allows the harmonic compensation to be performed without using any sensor on the distorting load, but only on the PCC and on the active filter itself, making it a plug-and-play sensorless system that can compensate for the harmonic distortion in any point of the network. The control technique is structured with multiple rotating reference frames, which are decoupled one from another. There is one control loop for the fundamental plus as many control loops as the harmonic components to be compensated. Section 5.2, Section 5.3 and Section 5.4 describe the decoupling technique, presenting the equations utilized and some examples. Section 5.6 describes the control technique, with the design criteria of the controllers and the dynamic characteristics of the control loops.

5.2   Decoupling the Rotating Reference Frames

In order to extract a harmonic component from the PCC voltage, it is represented in a *dq* reference frame rotating at the same speed as the angular frequency of the harmonic of interest by using the Park transformation. In the *dq* rotating frame the voltage appears as a DC component (the harmonic of interest) plus an AC component resulting from the sum of all the other harmonics, oscillating at frequencies equal to the relative angular speed between each of them and the angular speed of the rotating frame. In order to identify the harmonic and to reduce it to zero by means of an appropriately designed control, the DC component needs to be isolated from the others. A conventional way to do this is by using low-pass filters which cut off all the components leaving only the DC component, or band-pass filters which isolate the component of interest. Filters can heavily slow down the overall dynamics of the system and they introduce phase shifts that need to be taken into account in all the *dq* transformations. In the work presented here the use of low-pass or band-pass filters is totally avoided and the cancellation of each of the components observed on the *dq* rotating frame as oscillating quantities is achieved by adding to each of them an equal and opposite sinusoidal waveform. These sinusoidal waveforms are calculated on the basis of the characteristics of the voltage signal and from here on they will be named *decoupling terms*.

The calculation of the decoupling terms is performed on the basis of the relative angular speed with which a harmonic component (or the fundamental) is seen on a reference frame rotating at the frequency of another harmonic (or the fundamental). The relative angular speed can be calculated by means of (5.1).

$$\omega_{rel} = \omega_{abs} - \omega_{ref} \tag{5.1}$$

where ω_{ref} is the angular speed of the rotating reference frame, ω_{abs} is the absolute angular frequency of the component of interest, ω_{rel} is the relative angular frequency with which the component of interest is seen on the rotating reference frame. The angular frequencies are signed quantities, positive or negative depending on whether the harmonic component is a positive or negative sequence.

		Harmonic component				
		Fund.	5th	7th	11th	13th
	Fund.	DC	-6	+6	-12	+12
Frame	5th	+6	DC	+12	-6	+18
of	7th	-6	-12	DC	-18	+6
reference	11th	+12	+6	+18	DC	+24
	13th	-12	-18	-6	-24	DC

Table 5.1: Relative harmonic orders on the rotating frames of reference

According to the formula (5.1), on the reference frame rotating at the fundamental frequency, the 5th and 7th harmonic are seen as 6th harmonic. Table 5.1 shows for each harmonic component (including the fundamental) the harmonic order with which they are seen on all the other reference frames. The sign indicates the sense of rotation of the harmonic as seen when represented on the reference frame.

Figures 5.1 and 5.2 show an example of how the decoupling works. In Figure 5.1 a distorted signal composed of a fundamental component at 50Hz with amplitude 100 and a 5th harmonic with amplitude 20 is represented. The left hand column of the figure shows the *abc* component of the fundamental, of the 5th harmonic and the distorted signal respectively (looking from the top to the bottom), the right hand column shows the same components transformed into a *dq* frame rotating at 50Hz: the fundamental appears as a DC quantity in the new reference frame, the 5th harmonic appears as a 300Hz signal, i.e. like a 6th harmonic (according to the formula (5.1)), the distorted signal appears as an oscillating component at 300Hz with a DC offset equal to the amplitude of the fundamental.

Figure 5.2 shows how the *d* component of the distorted signal summed with the *d* axis decoupling term, which is equal and opposite to the oscillating component, gives as a result the DC quantity corresponding to the *d* component of the fundamental. Given a *dq* frame rotating at a certain harmonic frequency, the *d* and *q* components of the distorted signal have a DC offset corresponding to the *d* and *q* components of the harmonic synchronous with the rotating frame and an oscillating part corresponding to all the other harmonics as seen on that reference frame,
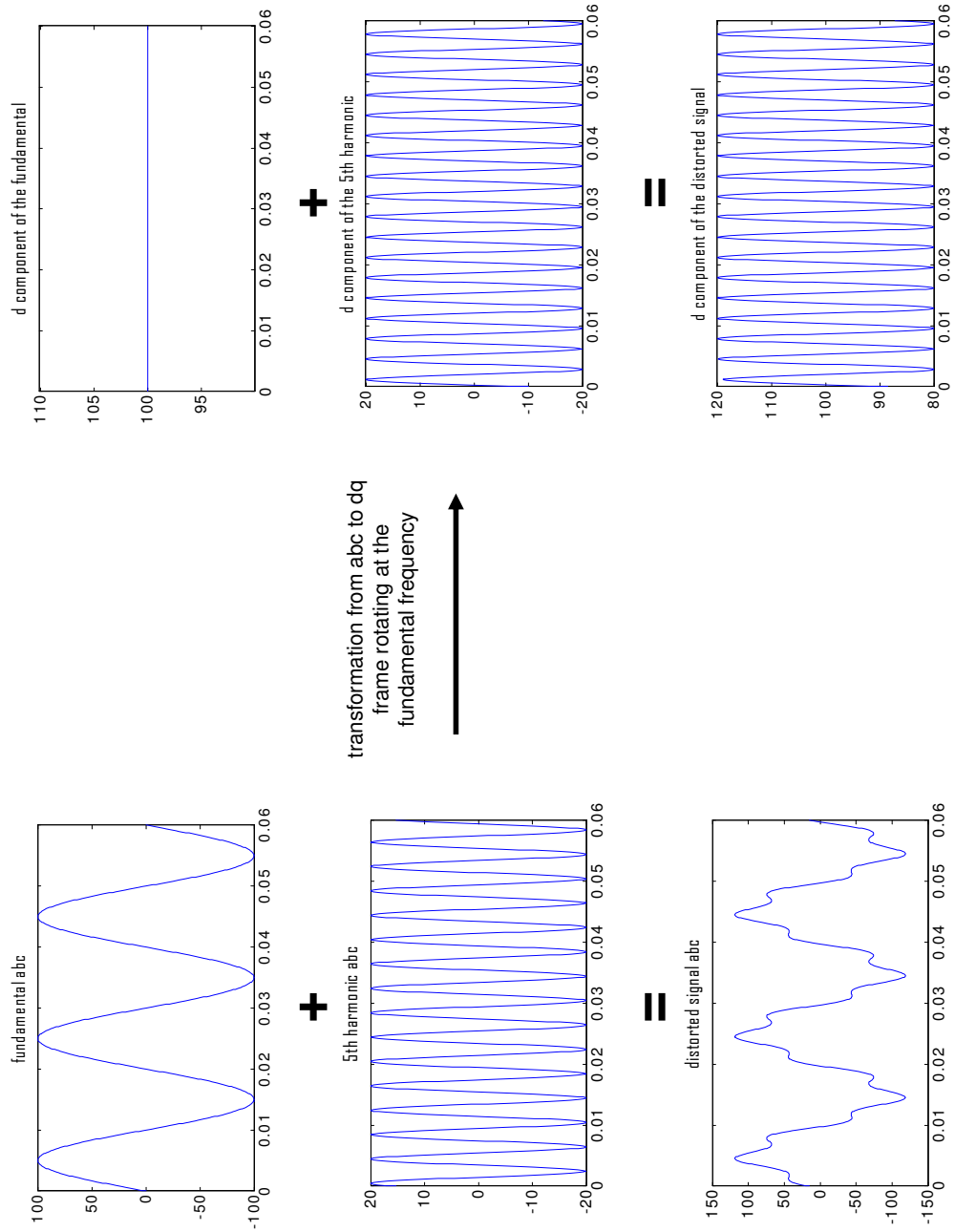
Figure 5.1: Distorted waveform on dq rotating frame without decoupling

hence the decoupling terms are calculated in order to be equal and opposite to each oscillating term so to cancel all the oscillations in the d and q components giving only the DC quantities corresponding to the harmonic of interest.
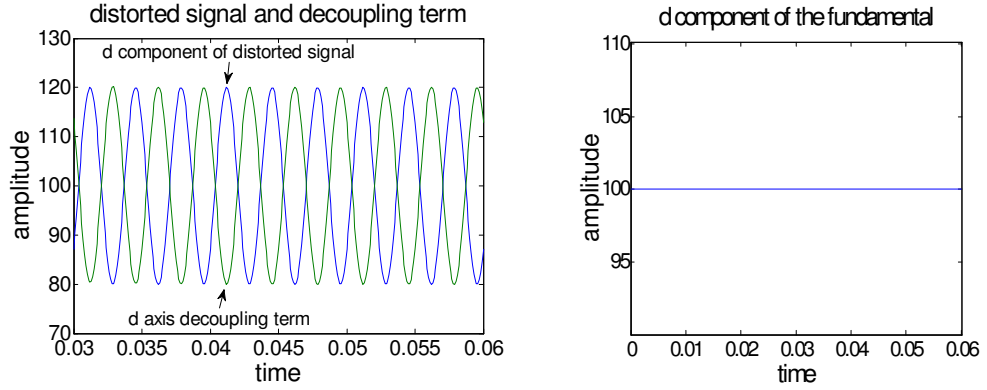
Figure 5.2: Distorted waveform on dq rotating frame with decoupling

5.3   Harmonic decoupling terms

For each rotating reference frame the d and q components of the distorted signal are summed with as many decoupling terms as the harmonics which the active filter is going to compensate. Given the rotating reference frame corresponding with the mth harmonic, the generic decoupling term corresponding with the nth harmonic is a sinusoidal waveform whose characteristics depend on the amplitude and phase of the harmonic and on the fundamental phase angle multiplied by a factor indicating what is the relative angular speed between the nth harmonic and the mth rotating reference frame.

All the decoupling terms are listed below, for the fundamental reference frame and the 5th, 7th, 11th and 13th harmonic. The symbols utilized in the formulas are:

A_h = amplitude of the hth harmonic component   for h = 1, 5, 7, 11, 13

Φ_h = phase of the hth harmonic component [rad]   for h = 1, 5, 7, 11, 13

ϑ_{fund} = fundamental phase angle $\qquad\qquad$ for $\vartheta_{fund} \in [0; 2\pi]$

The decoupling terms for each harmonic on the fundamental reference frame (represented with both their d and q components) are here listed. The decoupling terms for all the other reference frames are reported in Appendix B.

Reference frame rotating at the fundamental frequency

5th harmonic d component:

$$A_5 \cdot \sin\left(6\vartheta_{fund} + \Phi_5 - \frac{\pi}{2}\right) \qquad\qquad (5.2)$$

5th harmonic q component:

$$A_5 \cdot \sin\left(6\vartheta_{fund} + \Phi_5\right) \qquad\qquad (5.3)$$

7th harmonic d component:

$$A_7 \cdot \sin\left(6\vartheta_{fund} + \Phi_7 + \frac{\pi}{2}\right) \qquad\qquad (5.4)$$

7th harmonic q component:

$$A_7 \cdot \sin\left(6\vartheta_{fund} + \Phi_7\right) \qquad\qquad (5.5)$$

11th harmonic d component:

$$-A_{11} \cdot \sin\left(12\vartheta_{fund} + \Phi_{11} - \frac{\pi}{2}\right) \qquad (5.6)$$

11th harmonic q component:

$$-A_{11} \cdot \sin\left(12\vartheta_{fund} + \Phi_{11}\right) \qquad (5.7)$$

13th harmonic d component:

$$-A_{13} \cdot \sin\left(12\vartheta_{fund} + \Phi_{13} + \frac{\pi}{2}\right) \qquad (5.8)$$

13th harmonic q component:

$$-A_{13} \cdot \sin\left(12\vartheta_{fund} + \Phi_{13}\right) \qquad (5.9)$$

5.4 Examples of accurate and inaccurate decoupling

This section presents an example of how the decoupling is carried out properly when the decoupling terms are calculated correctly and an example that shows

the sensitivity of the decoupling accuracy against the accuracy in the calculation of the decoupling terms. In order for the decoupling to work properly the fundamental phase angle, as well as the amplitudes and phases of the harmonics, must be estimated with high accuracy, otherwise the sum between the d or q component of the signal on a certain reference frame and the decoupling terms will yield as a result a highly oscillating signal, instead of a DC signal. Ideally a correct decoupling gives as a result a perfectly DC signal, however in the real case, due to the inevitable errors in the estimation of the fundamental phase angle and the harmonic amplitudes and phases, the signal will contain a small oscillation. This oscillation is acceptable as long as it is significantly lower than the original oscillation due to the harmonics, as in this case the decoupling presents a significant advantage, especially in terms of control performance.

A simulation has been carried out using an input signal like the one represented in Figure 5.3, with the characteristics indicated in Table 5.2.
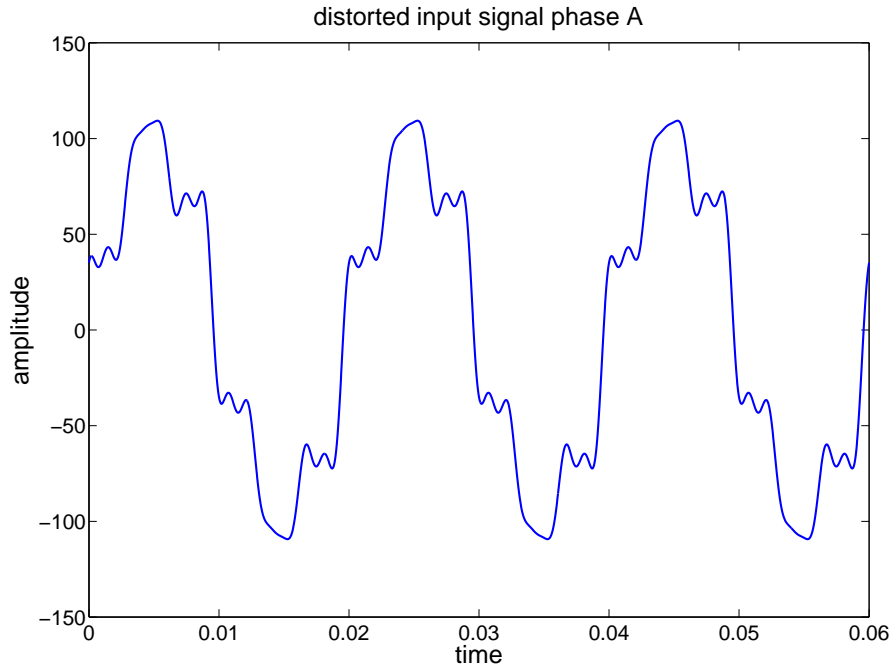
Figure 5.3: Distorted input signal

Figures 5.4 to 5.8 show the result of an ideal decoupling between all the rotating frames of reference, up to the 13th harmonic. It can be noticed that in this case

Fundamental frequency [Hz]	50 Hz
Fundamental amplitude	100
Fundamental phase [deg]	0
5th harmonic amplitude	20
5th harmonic phase [deg]	50
7th harmonic amplitude	10
7th harmonic phase [deg]	70
11th harmonic amplitude	7
11th harmonic phase [deg]	110
13th harmonic amplitude	5
13th harmonic phase [deg]	130

Table 5.2: Input signal for decoupling example

all the d and q components are pure DC quantities.
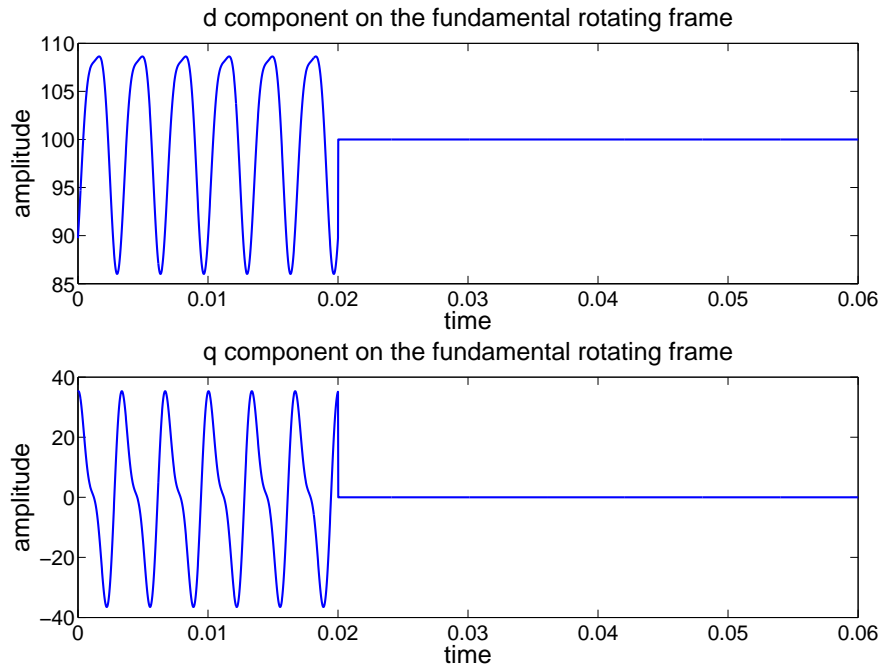
Figure 5.4: Fundamental d and q components

The reason why the dq components initially oscillate for a time interval equal to 0.02 s is that the identification of the fundamental and harmonic amplitudes and phases is carried out by means of the Discrete Fourier Transform, with a window of observation of the signal equal to one period of the fundamental, which at 50Hz corresponds to 0.02 s. The DFT algorithm takes a time equal to one observation window to start the identification. The case represented in these
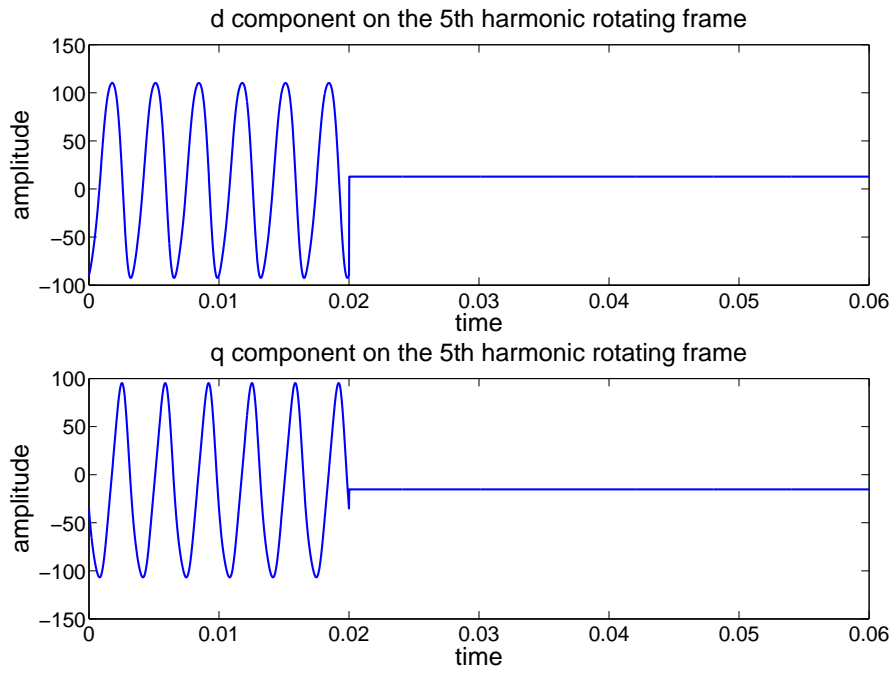
Figure 5.5: 5th harmonic d and q components
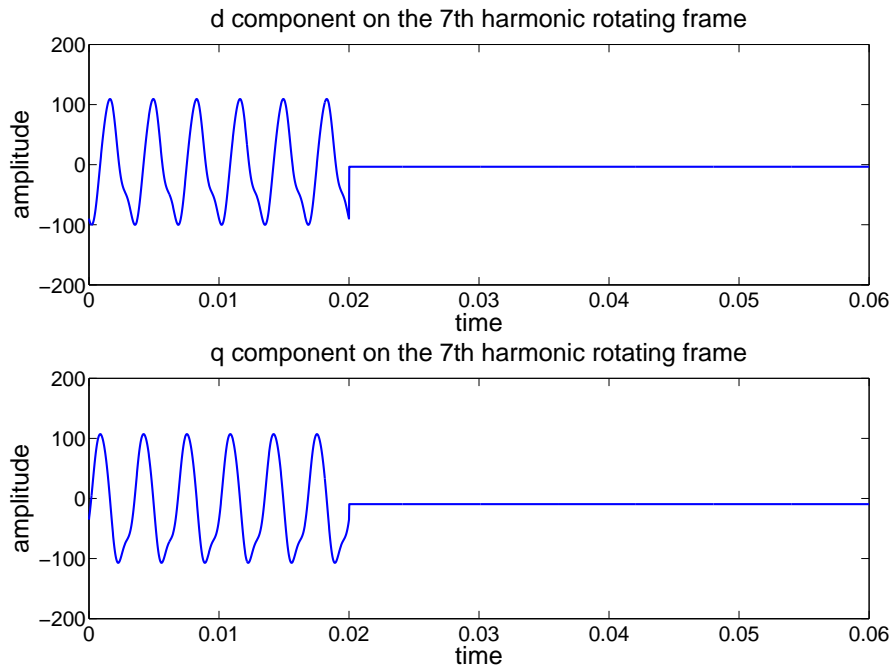
Figure 5.6: 7th harmonic d and q components
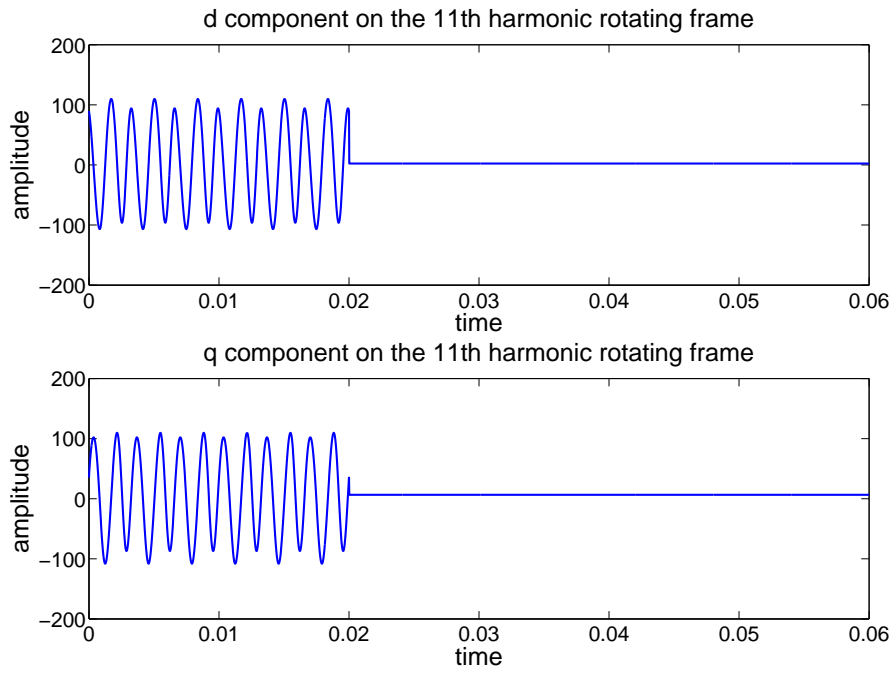
Figure 5.7: 11th harmonic d and q components
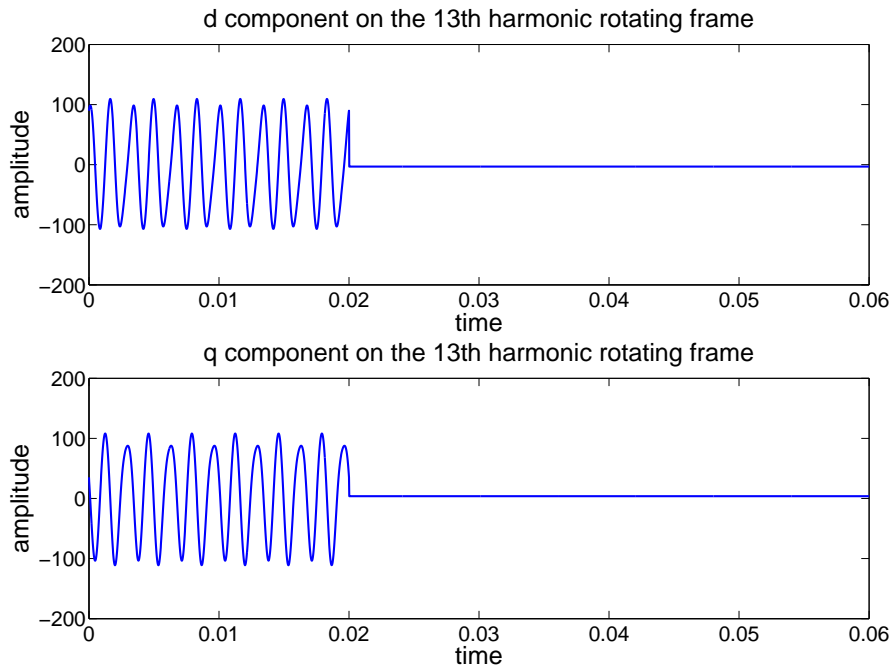
Figure 5.8: 13th harmonic d and q components

figures corresponds to an ideal decoupling, obtained in simulation by using an arbitrary input signal where all the harmonic components are known in amplitude and phase (see Table 5.2), the fundamental phase angle ϑ_{fund} utilized to calculate the decoupling terms is obtained from the *alpha* and *beta* components of the fundamental, as shown in the formula (5.10), where *alpha* and *beta* are obtained using the Clarke transformation.

$$\vartheta_{fund} = arctan(\frac{beta}{alpha}) \tag{5.10}$$

The possible causes of error when decoupling one reference frame from the others are: errors in the estimation of the fundamental phase angle, errors in the estimation of the amplitudes and phases of the fundamental and the harmonics. The estimation of the fundamental phase angle is a crucial point in the whole decoupling strategy performance: when the signal to be processed is distorted, it is not possible to obtain accurate results using conventional estimation methods for the phase, like the inverse tangent of the $alpha - beta$ components, or a conventional Phase Locked Loop, but more complex methods should be implemented, as explained in Chapter 3. The errors in the estimation of the harmonic amplitudes and phases are due to the inaccuracy of the harmonic detection method and they are ultimately related to the inaccuracy of the phase estimation. Here follows an example of how the inaccuracies in the fundamental phase angle and the harmonic detection can affect the decoupling. If the fundamental phase angle is calculated by means of the inverse tangent of the $alpha - beta$ components of the whole input signal, instead of its fundamental components, the resulting estimation error for the fundamental phase angle can be very high. Figure 5.9 shows the comparison between the angle obtained from the fundamental component and the one obtained using the whole distorted signal. Normally, in order to avoid such high inaccuracy in the phase estimation, better techniques are used, such as the Phase Locked Loop. Figure 5.10 shows the comparison between the angle obtained applying the PLL to the fundamental component and the one obtained applying the PLL to the whole distorted signal. In the examined case the signal is not noisy (see Figure 5.3) and although the distortion affects the accuracy of the PLL estimation the error is not very large. However this affects the accuracy of the

	amplitude		phase [deg]	
	actual value	estimated value	actual value	estimated value
fund	100	100	0	0
5th	20	20.56	50	36.7
7th	10	12.67	70	95.5
11th	7	7.7	110	110.6
13th	5	6	130	162.8

Table 5.3: Errors in harmonic detection due to inaccurate PLL estimation

harmonic estimation, as specified in Table 5.3, leading to inaccurate decoupling, as shown in Figure 5.11. The upper part of the figure shows the d component of the distorted signal on the fundamental reference frame and the sum of all the decoupling terms corresponding to the harmonics. It can be observed in the figure that these two waveforms do not cancel exactly. The lower part of the figure shows the d component of the distorted signal after the decoupling: the inaccurate decoupling results in an oscillating d component rather than a constant one.
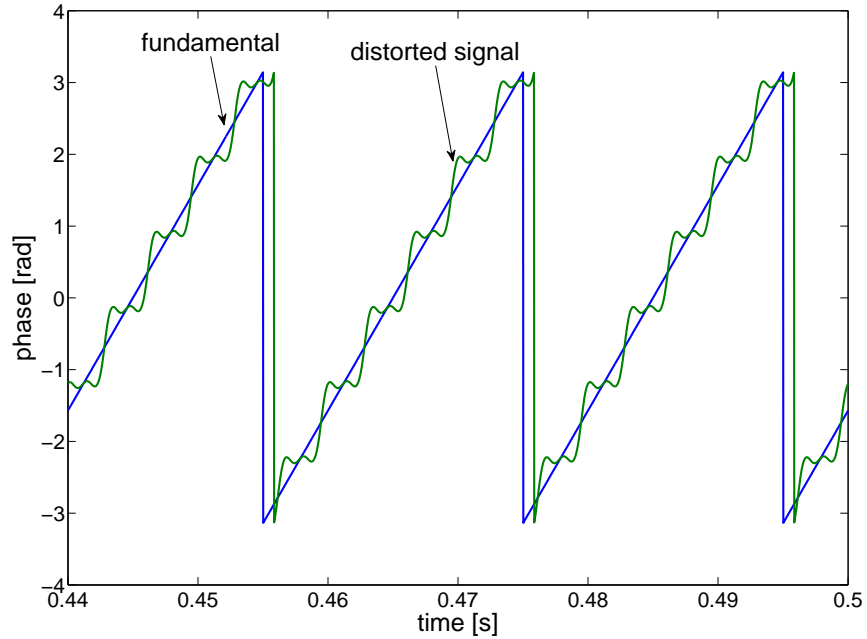
Figure 5.9: Phase angles calculated using inverse tangent

This example shows how important it is to estimate the fundamental phase angle correctly, in order to obtain an accurate decoupling. In the control technique proposed in this work, the fundamental phase angle has been estimated by means
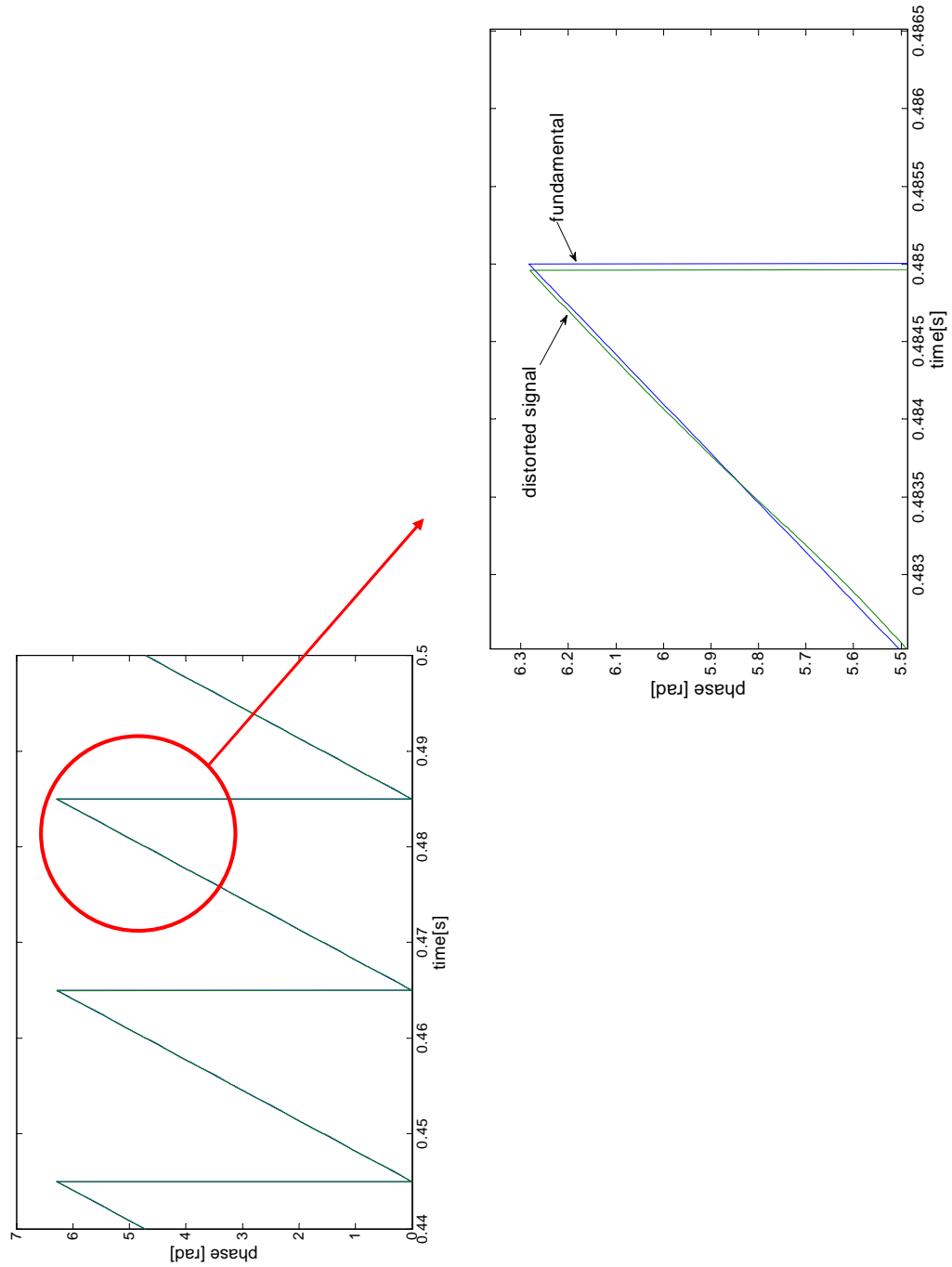
Figure 5.10: Phase angles calculated using the PLL
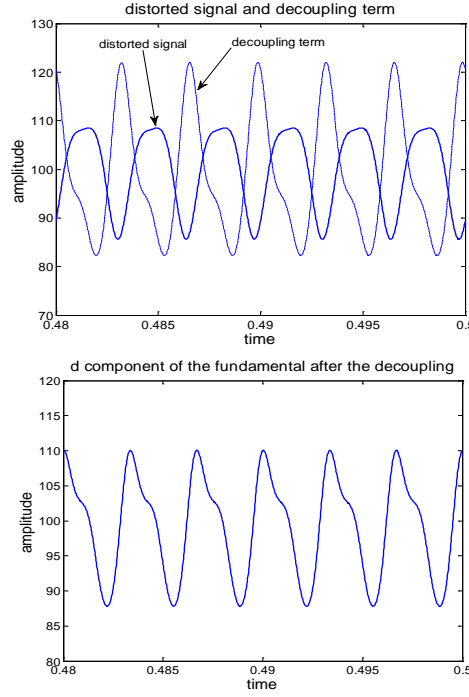
Figure 5.11: Inaccurate decoupling due to inaccurate phase angle estimation

of the DFT detection algorithm described in Chapter 3. This method proved to be highly accurate and showed low sensitivity to distortion and noise, hence it represents an effective means for the decoupling between the harmonic reference frames.

5.5 Control of a shunt active filter

The shunt active filter is a power electronic device designed to compensate the harmonics generated by one or more distorting loads. Connected in parallel with the power supply and the loads, the shunt active filter injects a harmonic current in order to cancel the one absorbed by the distorting load, and make the supply current sinusoidal. This concept is explained in figure 5.12. i_F and i_H represent the fundamental and the harmonic part of the current, respectively.

The circuit topology of a three-phase shunt active filter comprises a three-phase voltage source inverter, a DC link capacitor and a three-phase line inductor. The
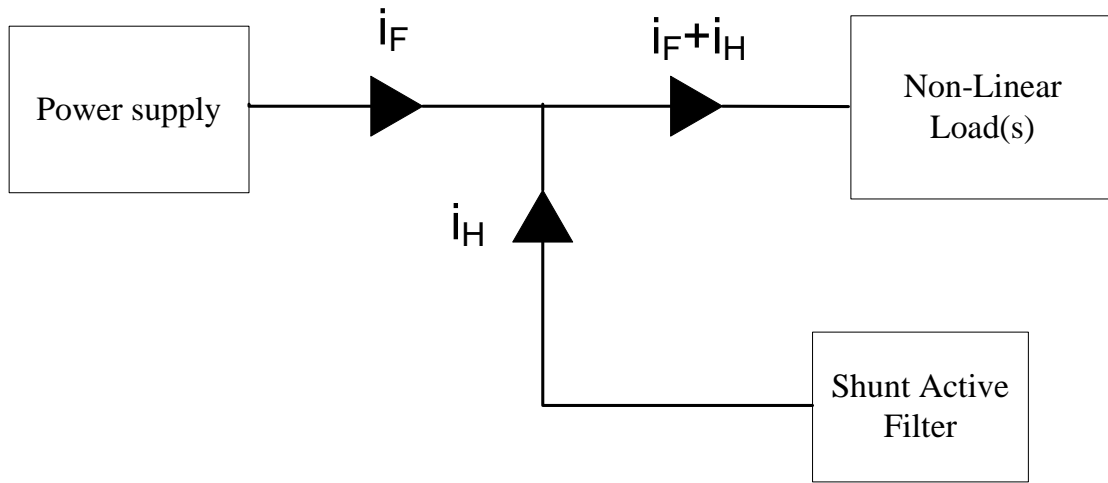
Figure 5.12: Principle of operation of the shunt active filter

switches of the bridge are generally realized with IGBTs and anti-parallel diodes. Figure 5.13 shows the topology. The active filter behaves as a controlled current source by controlling the voltage drop across the line inductor.
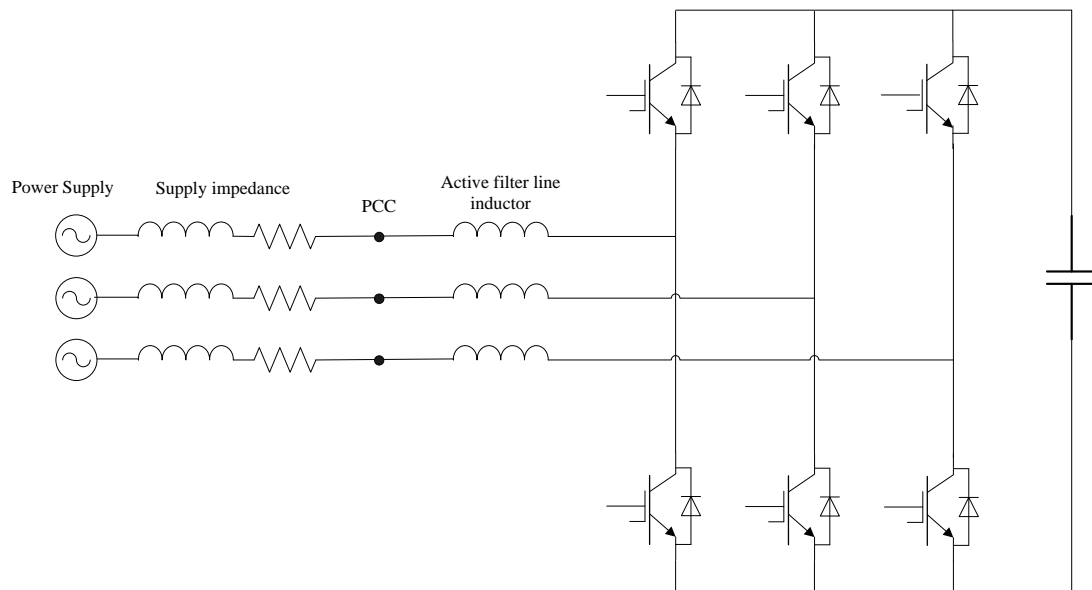
Figure 5.13: Topology of the shunt active filter

The techniques proposed in the scientific literature to generate the compensating current for a shunt active filter can be divided into two main groups: current based (in which the current detected can be either the supply current or the load current) [57–62] and voltage based [63–70].

In the current based methods the reference current can be either calculated on the basis of the supply current or on the basis of the harmonic current drawn by the load. In the former method only the measurement of the PCC voltage and the supply current are needed, but the disadvantage is that the active filter current is not available to the controllers, which can create problems related to overcurrent protection. The latter method, which uses the measurement of the load current, has the advantage that both the load current and the active filter current are available for the controllers, but the measurement of the load current, the active filter current and the PCC voltage are needed.

The voltage detection method has been investigated in the past decade by different authors. In [63] the authors present a control method for a shunt active power filter based on the detection of the voltage at the PCC and the real-time simulation of an LC filter by means of a digital signal processor. The work presented in [65] deals with the control strategy of a shunt active filter, based on voltage detection. Furthermore in this paper the best location of the filter in the power distribution system is selected, in order to obtain the best performance in damping the harmonics generated by resonance between the capacitors and inductors in the network. In [67–69] the authors investigate a control method for voltage feedback, selective harmonic, shunt active filters, analysing the advantages of the technique and the stability issues. In [70] a voltage feedback control technique for shunt active filters is presented, with multiple reference frames.

In the voltage detection methods the reference current is derived from the measurement of the PCC voltage and the active filter current, therefore only these two measurements are needed. Generally also the information about the supply impedance is required, although a rough estimate is sufficient for a robust control (in the method proposed in this work, it has been observed that a mismatch of up to 100% in the supply impedance estimate does not compromise the stability of the control). The advantage of this method is primarily that the active filter can be used for the compensation of both identified loads whose location and characteristics are well known, and unidentified loads. The active filter in this case can be seen as a plug-and-play sensorless system installed directly on the bus bar without requiring any external current transducer to measure the distorting non-linear

load current. In this way a significant reduction of cost and installation disruption is achieved. Furthermore, with this technique, a normal active front-end rectifier already present in the network or ready to be installed can be used also as an active filter simply by modifying the software implementation, without the need for extra transducers. The control technique which has been implemented and analysed for this project is a voltage based one.

5.6   Voltage detection control technique

Consider the system represented in Figure 5.14. It consists of a three-phase power supply which provides sinusoidal, symmetrical voltage V_s, connected in series with a resistive-inductive impedance $R_s - L_s$; a distorting load, represented by a diode bridge rectifier connected to a resistive impedance R_l on its DC side; a three-phase shunt active filter connected in parallel to the supply and the load, at the PCC, through a resistive-inductive impedance $R_f - L_f$. The measurement of the voltage at the PCC V_{pcc}, of the output current of the active filter I_f and of the active filter DC link voltage V_{dc} are processed as inputs of the control, in order to give the voltage demand V_{ref} for the active filter modulation. In the scheme of Figure 5.14 the variables which are measured on the system are represented in red.

The distorting load's non linear nature causes the supply line current to be distorted, because of the harmonics that it absorbs. The shunt active filter functions as a controlled current source which injects harmonic current into the PCC in order to cancel out the harmonics drawn by the distorting load; the current injection is achieved by controlling the voltage drop over the converter output inductance. Because of the harmonic current absorbed by the distorting load, not only is the supply current distorted, but also the PCC voltage, as a consequence of the harmonic voltage drop over the supply impedance. In the current based control methods, the harmonic content to be compensated is derived from the current absorbed by the distorting load; in the voltage based methods, like the one here discussed, the harmonic current is derived from the measurement of V_{pcc}.
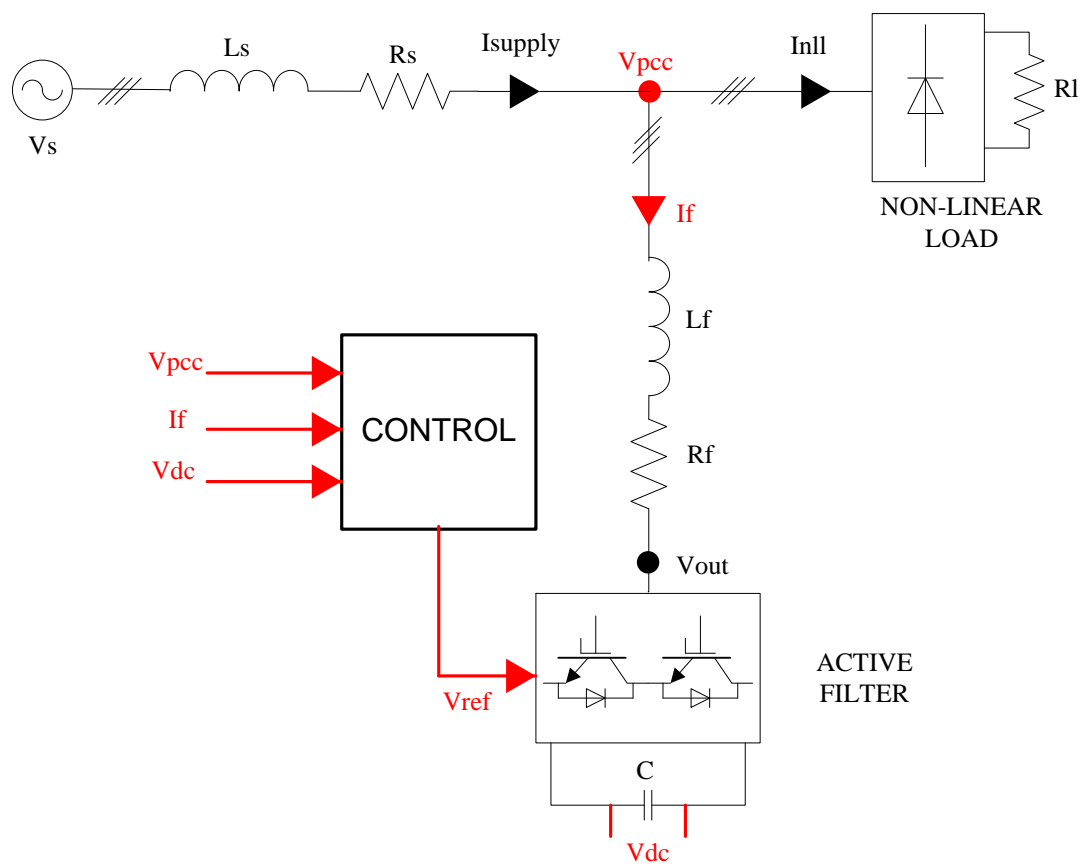
Figure 5.14: Scheme of the system where the active filter is connected

The PCC voltage *abc* components are transformed into *dq* components on different rotating reference frames (as many as the harmonics which need to be compensated, plus the fundamental). The *dq* components on each frame are decoupled from all the other harmonics in order to obtain DC quantities representing the harmonic synchronous with that particular reference frame. The control structure is composed of one control system for the fundamental and one for each harmonic. In the following sections the fundamental and the harmonic control loop structure are described.

5.6.1   The fundamental control loop

The fundamental control system is composed of two sections, one for the *d* axis and the other for the *q* axis. The *d* axis section is represented by two cascaded loops, one for the DC link voltage and one for the *d* component of the fundamental current, while the *q* axis section consists only of the current control loop for the *q* component of the fundamental current. The DC link voltage control keeps the voltage constantly equal to a reference value $Vdcref$ and regulates the exchange of active power between the active filter and the supply. Under ideal conditions, with no losses in the system, the active filter does not exchange active power with the supply and the DC link voltage is kept constant without any control action. In the real system a voltage controller is necessary to achieve that. The output of the voltage loop represents the current reference on the d axis, $id1ref$. The current control on the *q* axis regulates the exchange of reactive power between the active filter and the supply. In the case examined for this work the fundamental current reference on the *q* axis, $iq1ref$, is set to zero as the active filter is utilized only for harmonic compensation and not for reactive power regulation. The two current controllers, one on each axis, process the error between the *dq* components of the measured output current and their references, $id1ref$ and $iq1ref$ and generate a voltage demand in order to ideally reduce the error to zero. The DC link voltage control has been designed with much a lower bandwidth than the current control, so that the two dynamics can be considered independent one from the other, as it is explained in the following section. Figure 5.15 shows a schematic of the whole

fundamental control loop. The cascaded voltage and current loops on the d axis and the q axis current control can be noticed. The PCC voltage abc components $Vpcc_a$, $Vpcc_b$, $Vpcc_c$, the output current abc components I_a, I_b, I_c and the DC link voltage Vdc are represented in red as they are the variables obtained by measurements taken on the system. The PCC voltage is processed in order to estimate the fundamental phase angle ϑ_{fund} , which is utilized for the abc-dq and dq-abc transformations. The d and q components of the PCC voltage on the frame of reference synchronous with the fundamental, $vd1$ and $vq1$, are decoupled from all the harmonics, in the blocks named DECOUPLING, to obtain $vf1d$ and $vf1q$. The same process is carried out for the current, its d and q components on the frame of reference synchronous with the fundamental, $id1$ and $iq1$, are decoupled from all the harmonics to obtain $if1d$ and $if1q$, which are subtracted from the current reference values $id1ref$ and $iq1ref$ respectively and give the input errors for the current controllers. The cross-coupling terms $\omega L_f if1q$ and $\omega L_f if1d$ and the feedforward compensation terms $vf1d$ and $vf1q$ are algebraically summed with the outputs of the current controllers, to yield the voltage demand $vd1mod$ and $vq1mod$. These components are transformed into $va1mod$, $vb1mod$, $vc1mod$ which represent the fundamental component of the reference signal for the active filter modulation. Figure 5.16 shows the structure of the decoupling blocks. As an example, the decoupling of the d component of the fundamental voltage is shown in the figure, but all the other decoupling blocks are similar and the decoupling terms are indicated in equations (5.2) to (5.9) and in Appendix B.

5.6.1.1 The fundamental current control loop

Considering the system in Figure 5.14, a simplified scheme of the equivalent circuit of the active filter connected to the PCC can be drawn, as shown in Figure 5.17, where $Vpcc_a$, $Vpcc_b$, $Vpcc_c$ are the PCC abc voltages, $Vout_a$, $Vout_b$, $Vout_c$ are the output active filter abc voltages and I_a, I_b, I_c are the output active filter abc currents. Assuming that the system is symmetrical and balanced, Equation (5.11) can be written.
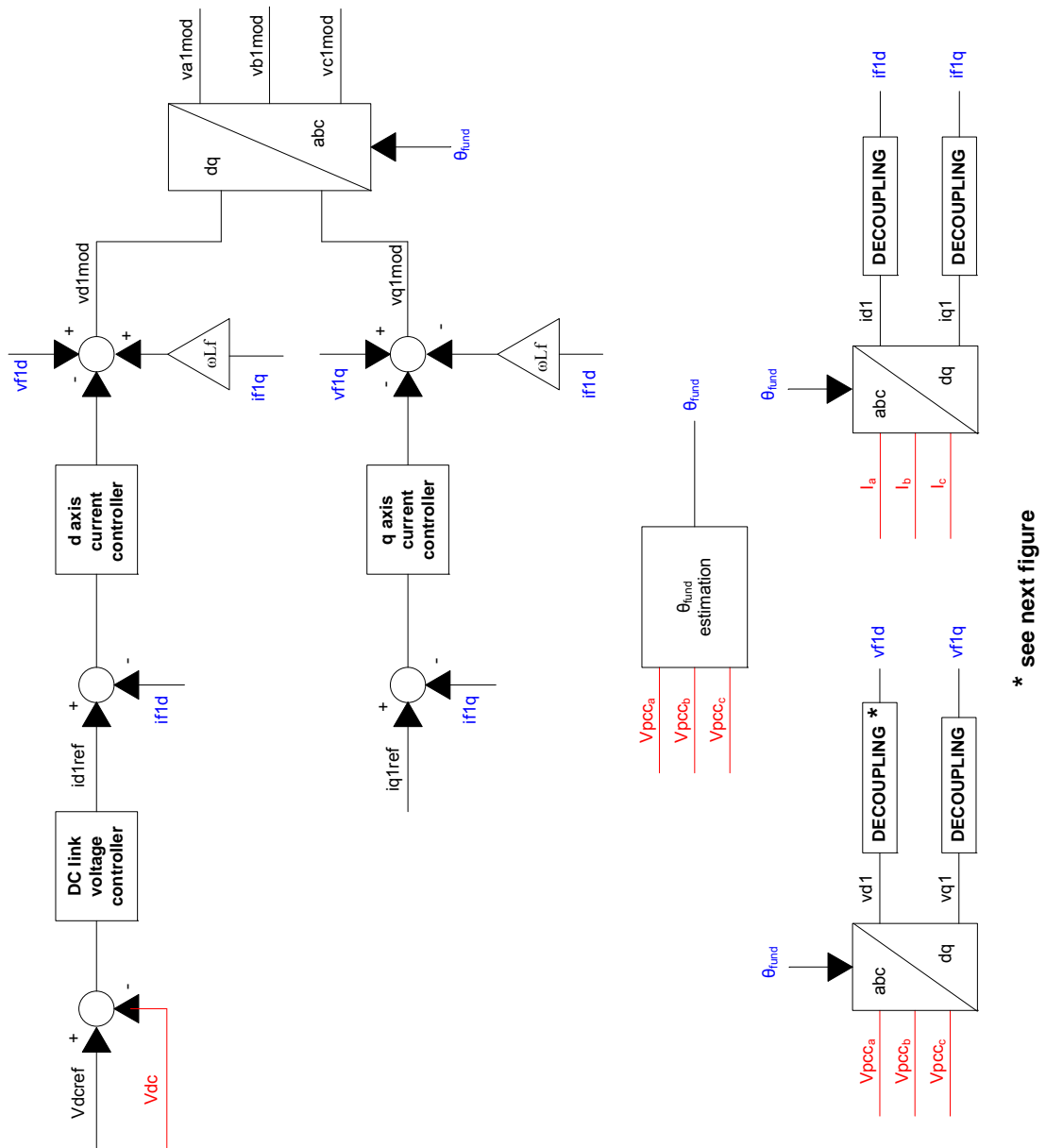
Figure 5.15: Scheme of the overall fundamental control loop
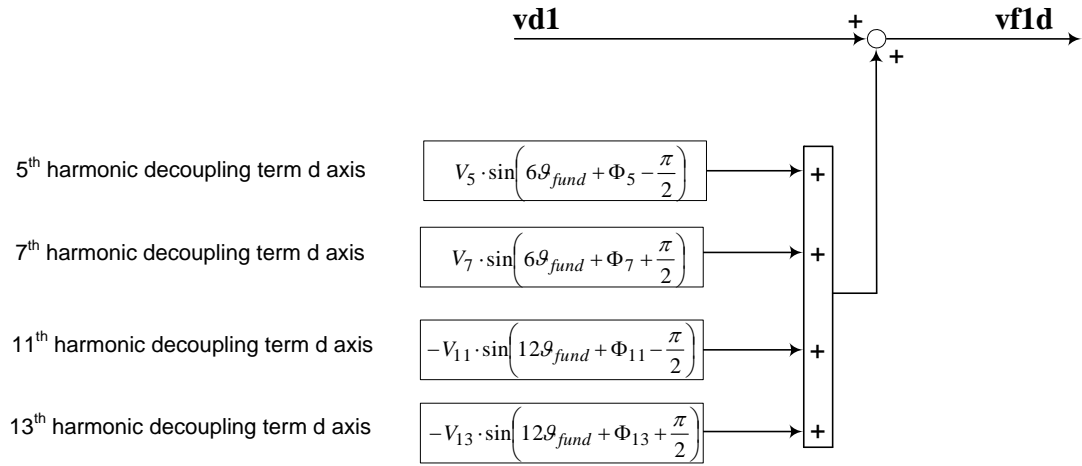
Figure 5.16: Decoupling block
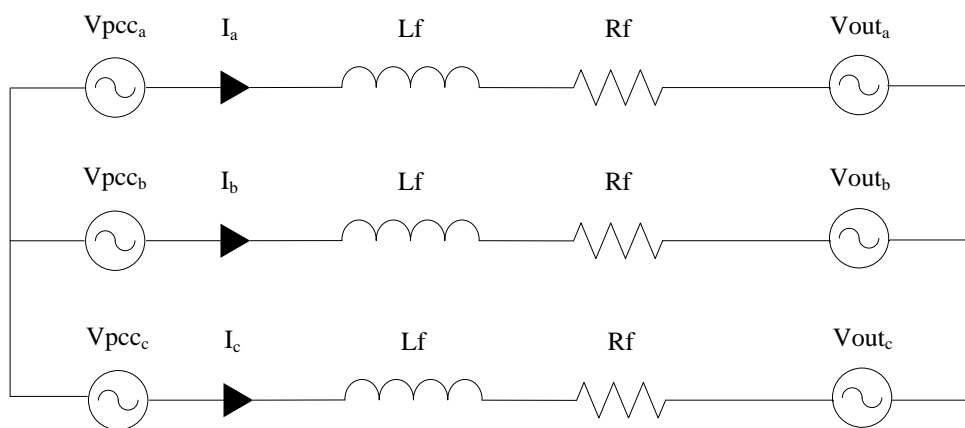
Figure 5.17: Scheme of the circuit for the fundamental current dynamics

$$\begin{bmatrix} Vpcc_a \\ Vpcc_b \\ Vpcc_c \end{bmatrix} = L_f \frac{d}{dt} \begin{bmatrix} I_a \\ I_b \\ I_c \end{bmatrix} + R_f \begin{bmatrix} I_a \\ I_b \\ I_c \end{bmatrix} + \begin{bmatrix} Vout_a \\ Vout_b \\ Vout_c \end{bmatrix} \quad (5.11)$$

Transforming (5.11) into the dq frame of reference synchronous with the fundamental, equations (5.12) and (5.13) can be obtained.

$$Vpcc_d = L_f \frac{dI_d}{dt} + R_f I_d + Vout_d - \omega L_f I_q \quad (5.12)$$

$$Vpcc_q = L_f \frac{dI_q}{dt} + R_f I_q + Vout_q + \omega L_f I_d \quad (5.13)$$

$Vpcc_d$ and $Vpcc_q$ are the d and q components of the PCC voltage on the fundamental rotating frame of reference, $Vout_d$ and $Vout_q$ are the d and q components of the active filter output voltage, I_d and I_q are the d and q components of the active filter output current, and ω is the fundamental angular frequency. From (5.12) and (5.13) it is noted that the d and q equivalent circuits are similar and independent from each other, except for the cross-coupling terms between the axes, $\omega L_f I_q$ and $\omega L_f I_d$. Considering that the fundamental phase angle is estimated by locking onto the fundamental phase angle of the PCC voltage, on the dq rotating frame synchronous with the fundamental, $Vpcc_d$ is maximum and $Vpcc_q$ is zero, hence (5.12) and (5.13) can be re-written as in (5.14) and (5.15).

$$Vpcc_d = L_f \frac{dI_d}{dt} + R_f I_d + Vout_d - \omega L_f I_q \quad (5.14)$$

$$0 = L_f \frac{dI_q}{dt} + R_f I_q + Vout_q + \omega L_f I_d \quad (5.15)$$

From (5.14) and (5.15) equations (5.16) and (5.17) can be derived.

$$Vout_d = -Vd' + (Vpcc_d + \omega L_f I_q) \quad (5.16)$$

$$Vout_q = -Vq' - (\omega L_f I_d) \quad (5.17)$$

where:

$$Vd' = L_f \frac{dI_d}{dt} + R_f I_d \tag{5.18}$$

$$Vq' = L_f \frac{dI_q}{dt} + R_f I_q \tag{5.19}$$

(5.16) and (5.17) show that the current controllers' output demand voltages Vd' and Vq' are summed with the feedforward terms $Vpcc_d$ and $Vpcc_q$ (the latter is equal to zero in this case) and the cross-coupling terms $\omega L_f I_q$ and $\omega L_f I_d$ to yield the reference voltage for the modulation. The output voltage at the AC terminals of the active filter, $Vout_d$ and $Vout_q$, follows this reference. The ratio between the current I_d and I_q and the controllers outputs Vd' and Vq' represent the plant transfer function of the fundamental current control loop, as shown in (5.20), where the relationship in the Laplace transform s domain is represented.

$$G(s) = \frac{I_d(s)}{Vd'(s)} = \frac{I_q(s)}{Vq'(s)} = \frac{1}{L_f s + R_f} \tag{5.20}$$

It is important to note that in the particular case presented in this work all the d and q components of the voltage and the current are the ones obtained after the decoupling between the rotating frame synchronous with the fundamental and the other harmonic components. Therefore:

$$Vpcc_d = vf1d \tag{5.21}$$

$$Vpcc_q = vf1q \tag{5.22}$$

$$I_d = if1d \tag{5.23}$$

$$I_q = if1q \tag{5.24}$$

This can be also seen in Figure 5.15.

The fundamental current control loop, which is the same for both the d and the q axis, is represented in Figure 5.18, where the processing and sampling delays are due to the digital implementation of the control.
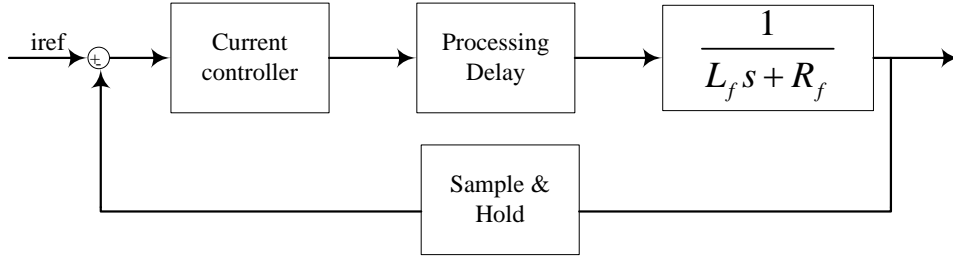
Figure 5.18: Fundamental current control loop

The fundamental current controller has been designed in the form of a Proportional Integral (PI) regulator. Considering that the reference current to be tracked is a slowly variable quantity (on the d axis) or a constant value (on the q axis), and the feedback current presents only very small oscillations due to the small error in the decoupling, the closed loop bandwidth required is not very high. The plant transfer function parameters are based on the active filter inductor used for the simulation and experimental validation:

$$L_f = 3mH; R_f = 0.1\Omega \tag{5.25}$$

The controller has been designed using the MatLab SISOTOOL toolbox. Its transfer function in the s domain is:

$$\frac{4.5s + 2115}{s} \tag{5.26}$$

The closed loop poles coordinates in the s plane are -577+j441, the natural frequency is 116 Hz, the damping factor is 0.794, the closed loop bandwidth is 243 Hz.

5.6.1.2   The DC link voltage control loop

The DC link voltage control aims at regulating the exchange of active power between the active filter and the power supply. Under ideal conditions and with no load connected to the DC side of the converter, there are no losses in the

DC link and in the converter switches, therefore the DC link voltage is kept at a constant value without utilizing a regulation. However in practice there are losses in the DC capacitor, in the switching devices and in the resistive component of the active filter line inductor, therefore it is necessary to regulate the DC link voltage, keeping it constant by absorbing a limited amount of active power from the power network in order to match the losses. The equations that describe the DC link voltage control and from which it is possible to derive the plant transfer function will be now presented [71]. Let the current flowing in the DC link be indicated as Idc and the voltage across the DC link be indicated as Vdc. The power balance between the input and the output can be expressed by the formula (5.27).

$$Idc = 3\frac{I_d Vout_d + I_q Vout_q}{Vdc} \tag{5.27}$$

If the losses in the DC link, in the switches and in the line inductor are neglected:

$$Vout_d = Vpcc_d; Vout_q = Vpcc_q = 0 \tag{5.28}$$

Therefore (5.27) can be written as (5.29); furthermore equations (5.30) and (5.31) can be stated.

$$Idc = 3\frac{I_d Vpcc_d}{Vdc} \tag{5.29}$$

$$m = \frac{2\sqrt{2}Vpcc_d}{Vdc} \tag{5.30}$$

$$C\frac{dVdc}{dt} = Idc \tag{5.31}$$

Where m is the modulation index. (5.29) and (5.30) can be combined to yield equation (5.32):

$$Idc = \frac{3mI_d}{2\sqrt{2}} \tag{5.32}$$

(5.31) and (5.32) can be combined to yield equation (5.33), which represents the s domain transfer function of the DC link voltage control loop plant:

$$\frac{Vdc(s)}{I_d(s)} = \frac{3m}{2\sqrt{2}Cs} \tag{5.33}$$

From (5.12), (5.13) and (5.29) to (5.31) it is possible to draw the active filter fundamental equivalent circuit in the dq reference frame as depicted in Figure 5.19.
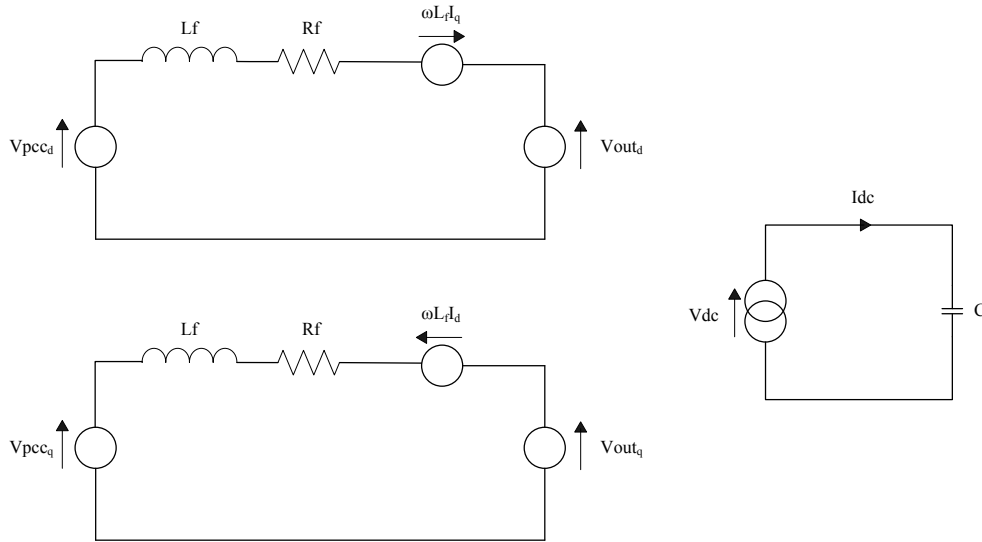
Figure 5.19: dq equivalent circuit of the active filter

The DC link voltage control loop is represented in Figure 5.20, where the processing and sampling delays are due to the digital implementation of the control.

The DC link voltage controller has been designed in the form of a Proportional Integral (PI) regulator, with a much lower bandwidth than the fundamental current control, so that the two control loops can be considered independent one from the other. The plant transfer function parameters are based on the active filter capacitor used for the simulation and experimental validation:
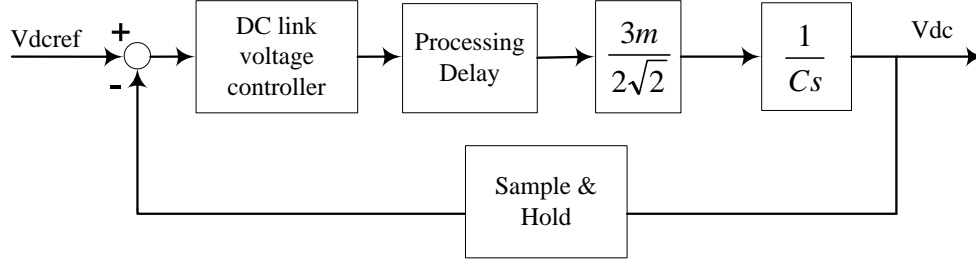
Figure 5.20: DC link voltage control loop

$$C = 2200\mu F \tag{5.34}$$

The controller has been designed using the MatLab SISOTOOL toolbox and its transfer function in the s domain is:

$$\frac{0.03s + 0.33}{s} \tag{5.35}$$

The closed loop poles coordinates in the s plane are -6.82+j10.2, the natural frequency is 1.95 Hz, the damping factor is 0.557, the closed loop bandwidth is 4 Hz.

5.6.2   The harmonics control loops

Each harmonic control system is composed of two sections, one for the d axis and one for the q axis. On each axis the control section is represented by two cascaded loops, one for the PCC voltage and one for the harmonic current. This structure is repeated for each rotating reference frame synchronous with each harmonic. The PCC voltage control regulates the voltage in order to cancel its harmonic content. The output of the voltage control represents the current reference for the current controllers, which yield a voltage demand output to be summed with the fundamental one for the active filter modulation. The current reference resulting from the voltage control represents the harmonic current which the active filter has to inject into the PCC in order to cancel the non-linear load harmonics. The

detection of this current is not carried out by direct measurement of the harmonics absorbed by the non-linear load but from the measurement of the PCC voltage and the analysis of its harmonic content. The voltage harmonics are due to the voltage drop of the current harmonics on the supply impedance, and are generally smaller than the current harmonics, hence good precision in the voltage harmonic analysis is necessary in order for a successful compensation to be achieved.

Figure 5.21 shows a schematic of the 5th harmonic control system, including cascaded voltage and current loop on the d axis and the q axis. The PCC voltage abc components $Vpcc_a$, $Vpcc_b$, $Vpcc_c$ and the output current abc components I_a, I_b, I_c are represented in red as they are the only variables obtained by measurements taken on the system. The d and q components of the PCC voltage on the reference frame synchronous with the 5th harmonic, $vd5$ and $vq5$, are obtained by using the angle $-5\vartheta_{fund}$ and decoupled from the fundamental and all the other harmonics, in the blocks names DECOUPLING, to obtain $vf5d$ and $vf5q$. The same approach is used for the current. Its d and q components on the reference frame synchronous with the 5th harmonic, $id5$ and $iq5$, are decoupled from the fundamental and all the other harmonics to obtain $if5d$ and $if5q$. $vf5d$ and $vf5q$ are subtracted from the voltage reference values $vf5dref$ and $vf5qref$ respectively to give the input error for the voltage controllers. $vf5dref$ and $vf5qref$ are set to zero in order to cancel the voltage 5th harmonic. $if5d$ and $if5q$ are subtracted from the current reference values $if5dref$ and $if5qref$ respectively to give the input error for the current controllers. The output of the current controllers gives the voltage demand for the modulation $vd5mod$ and $vq5mod$. These components are then transformed into $va5mod$, $vb5mod$, $vc5mod$ which represent the 5th harmonic component of the reference signal for the active filter modulation.

The control structure for the other harmonic components is similar to the one just described apart from the decoupling terms, which are calculated as presented in Section 5.3 and Appendix B, and the angle utilized for the dq transformations. This is equal to $\pm h\vartheta_{fund}$, where h is the harmonic order and the sign depends on the harmonic being positive or negative sequence.

Figure 5.22 shows the schematic of the overall control. The fundamental control
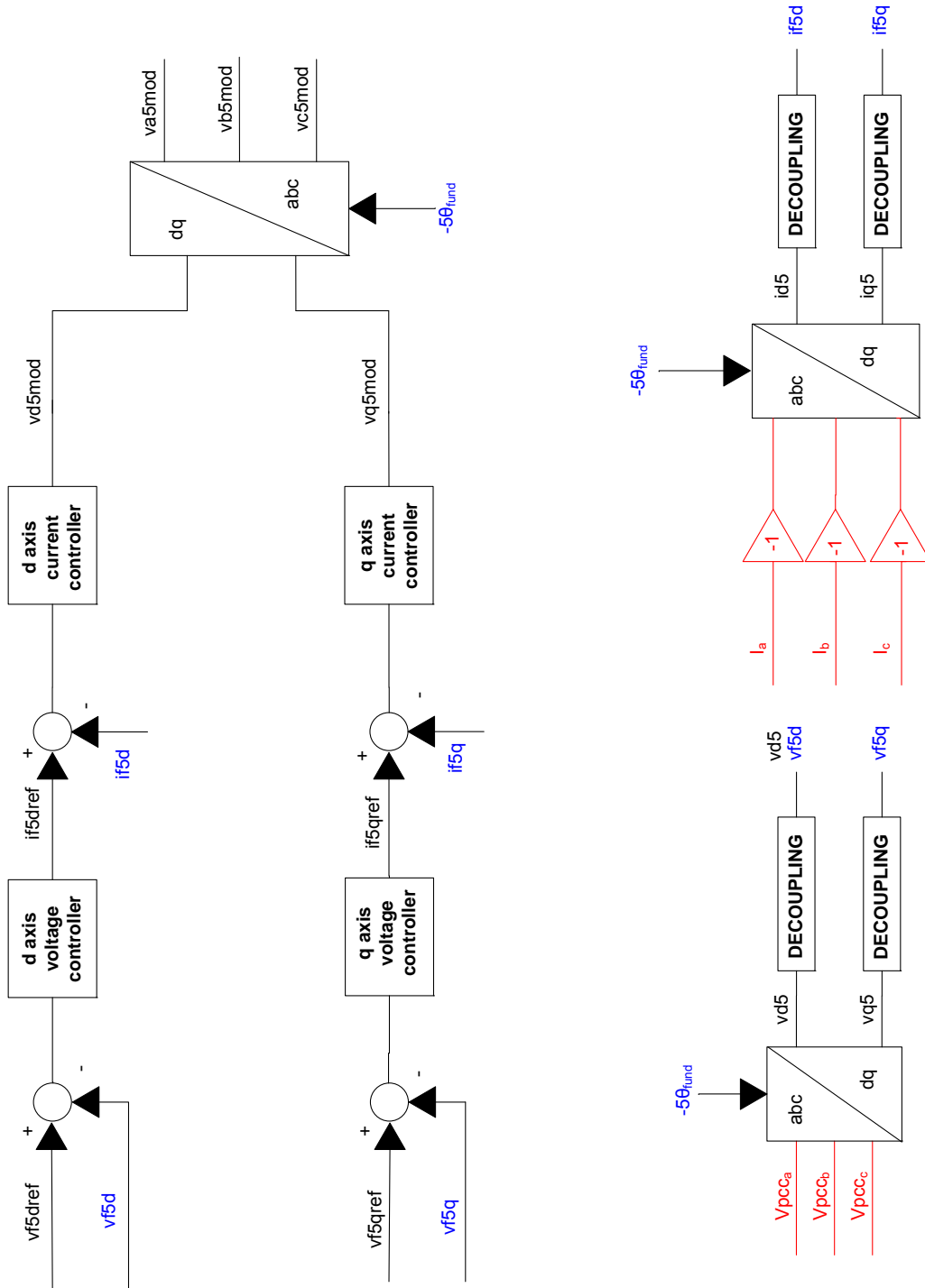
Figure 5.21: Scheme of the 5th harmonic control system

system and the harmonic control systems, from the 5th to the nth harmonic, yield the modulating outputs which, summed together on each phase, represent the reference voltage for the active filter modulation, indicated as $varef$, $vbref$ and $vcref$.

5.6.2.1 The harmonic voltage control loop

This section will show the calculation of the plant transfer function for the harmonic voltage control and the design of the controller. A small signal model of the system is considered for this analysis [72]. Figure 5.23 shows the equivalent circuit for the harmonic frequencies: the power supply is represented as a short circuit in this model as it generates only fundamental voltage. The active filter and the nonlinear load are represented as sources of current at the generic harmonic frequency $\pm h\omega$. They are connected in parallel at the PCC and their generated currents are indicated as I_{asf} and I_{load}. The supply impedance R_s, L_s is also represented in Figure 5.23.

From Figure 5.23 Equation (5.36) can be written.

$$
\begin{bmatrix} 0 - Vpcc_a \\ 0 - Vpcc_b \\ 0 - Vpcc_c \end{bmatrix} = L_s \frac{d}{dt} \begin{bmatrix} I_a \\ I_b \\ I_c \end{bmatrix} + R_s \begin{bmatrix} I_a \\ I_b \\ I_c \end{bmatrix} \tag{5.36}
$$

Transforming (5.36) into the dq frame of reference synchronous with the hth harmonic, equations (5.37) and (5.38) can be obtained.

$$
-Vpcc_d = L_s \frac{dI_d}{dt} + R_s I_d - \omega L_s I_q \tag{5.37}
$$

$$
-Vpcc_q = L_s \frac{dI_q}{dt} + R_s I_q + \omega L_s I_d \tag{5.38}
$$

The current I represents the sum between the active filter current and the nonlinear load current:
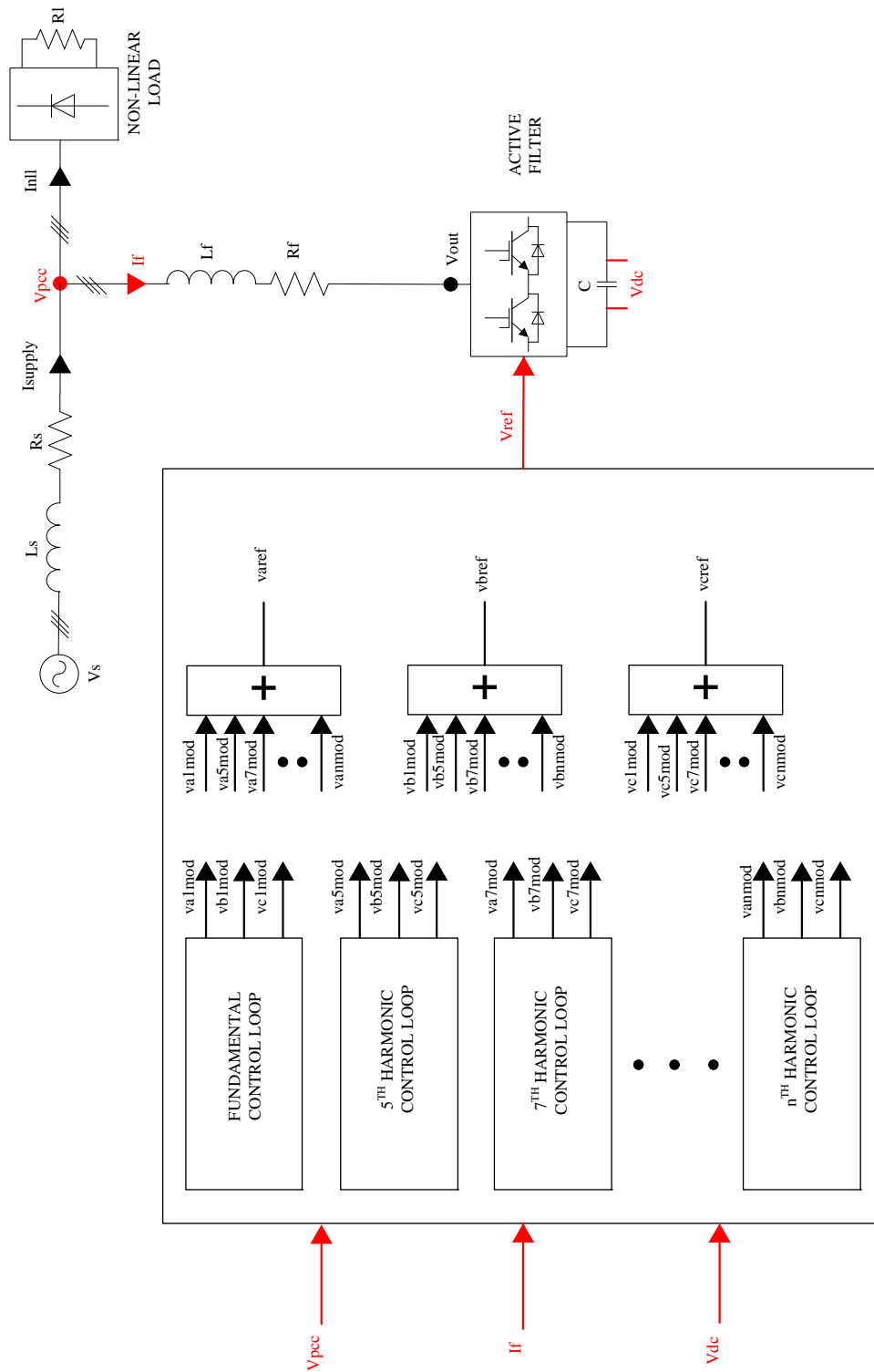
Figure 5.22: Scheme of the overall control system
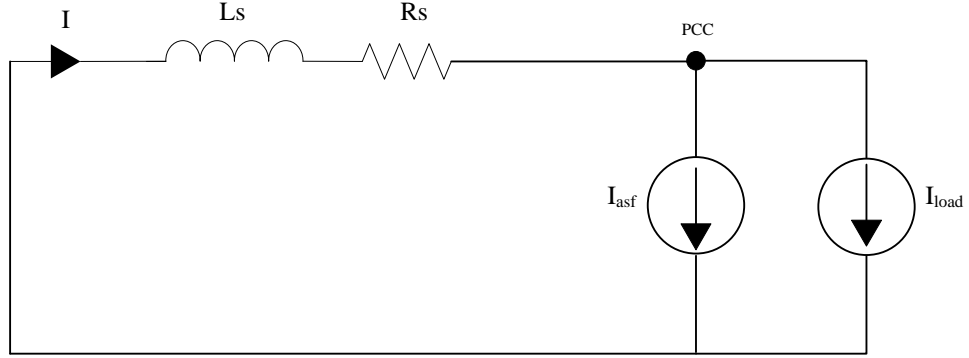
Figure 5.23: Equivalent circuit of the system at the harmonic frequencies

$$I_d = I_{d\_asf} + I_{d\_load} \tag{5.39}$$

$$I_q = I_{q\_asf} + I_{q\_load} \tag{5.40}$$

So equations (5.37) and (5.38) can be written as:

$$-Vpcc_d = L_s \frac{d}{dt}(I_{d\_asf} + I_{d\_load}) + R_s(I_{d\_asf} + I_{d\_load}) - \omega L_s(I_{q\_asf} + I_{q\_load}) \tag{5.41}$$

$$-Vpcc_q = L_s \frac{d}{dt}(I_{q\_asf} + I_{q\_load}) + R_s(I_{q\_asf} + I_{q\_load}) + \omega L_s(I_{d\_asf} + I_{d\_load}) \tag{5.42}$$

Applying a perturbation to each variable and carrying out the Laplace transformation to (5.41) and (5.42):

$$-\Delta Vpcc_d = (L_s s + R_s)(\Delta I_{d\_asf} + \Delta I_{d\_load}) - \omega L_s(\Delta I_{q\_asf} + \Delta I_{q\_load}) \tag{5.43}$$

$$-\Delta Vpcc_q = (L_s s + R_s)(\Delta I_{q\_asf} + \Delta I_{q\_load}) + \omega L_s(\Delta I_{d\_asf} + \Delta I_{d\_load}) \tag{5.44}$$

Assuming that the load current does not change during the short time interval chosen for the small signal analysis, it is possible to write:

$$\Delta I_{d\_load} = 0 \tag{5.45}$$

$$\Delta I_{q\_load} = 0 \tag{5.46}$$

Hence (5.43) and (5.44) can be written as:

$$-\Delta V pcc_d = (L_s s + R_s)(\Delta I_{d\_asf}) - \omega L_s \Delta I_{q\_asf} \tag{5.47}$$

$$-\Delta V pcc_q = (L_s s + R_s)(\Delta I_{q\_asf}) + \omega L_s \Delta I_{d\_asf} \tag{5.48}$$

Equations (5.47) and (5.48) show that the d and q axes present similar dynamics and they are independent one from another, excluding the cross-coupling terms $\omega L_s I_{q_{asf}}$ and $\omega L_s I_{d_{asf}}$. On each axis the ratio between the PCC voltage variation and the variation of the current is given by equation (5.49), which presents the s domain transfer function for the harmonic voltage control :

$$G(s) = \frac{\Delta V pcc_d}{\Delta I_{d\_asf}} = \frac{\Delta V pcc_q}{\Delta I_{q\_asf}} = L_s s + R_s \tag{5.49}$$

It is important to note that in the particular case presented in this work the voltage and current d and q components are the ones obtained after the decoupling between the rotating frame synchronous with the hth harmonic and all the other harmonic components including the fundamental. Therefore:

$$V pcc_d = vfhd \tag{5.50}$$

$$V pcc_q = vfhq \tag{5.51}$$

$$I_{d\_asf} = ifhd \tag{5.52}$$

$$I_{q\_asf} = ifhq \tag{5.53}$$

This can be also seen in Figure 5.21.

The harmonic voltage control loop, which is the same both for the d and the q axis, is represented in Figure 5.24, where the processing and sampling delays are due to the digital implementation of the control.
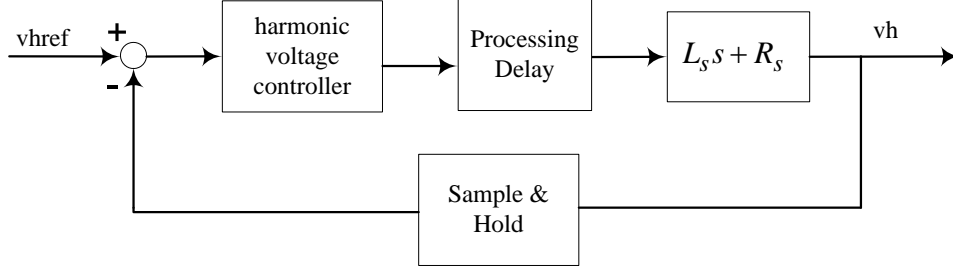
Figure 5.24: Harmonic voltage control loop

The harmonic voltage controller has been designed in the form of a Proportional plus Integral (PI) regulator, with much a lower bandwidth than the one for the harmonic current control, so that the two loops' dynamics can be considered independent from one another. The reference voltage to be tracked is a constant value equal to zero, and the feedback harmonic voltage presents very small oscillations due to the decoupling. The plant transfer function parameters are based on the supply line impedance used for the simulation and experimental validation:

$$L_s = 0.4mH; R_f = 1.5\Omega \tag{5.54}$$

The controller has been designed using the MatLab SISOTOOL toolbox, its transfer function in the s domain is:

$$\frac{0.127s + 5.2}{s} \tag{5.55}$$

The closed loop bandwidth is 1 Hz.

5.7 Summary

This chapter has presented a control technique for active shunt power filters based on the detection of the voltage at the Point of Common Coupling. The extraction of the harmonics is carried out by means of multiple rotating reference frames, decoupled one from each other. The decoupling technique allows accurate identification of the harmonic components to be compensated, without using low-pass or band-pass filters. The decoupling equations, with examples that show accurate decoupling and the possible causes of inaccurate decoupling, have been presented in this chapter. The control structure has also been described, with demonstrations of how the control dynamics are represented mathematically, and description of the controllers design. The description of the control technique shows how it is possible to identify the reference current for the active filter, and to control the current that it injects in the system just by measuring the PCC voltage without the need for extra current sensors on the distorting load. In the next chapter the results obtained in simulation by implementing this technique will be presented and analysed in order to prove the effectiveness of the method.

Chapter 6

Voltage Detection Control Technique: Simulation Results

6.1 Introduction

This chapter presents the results obtained from the simulation of the proposed control technique for active shunt filters described in Chapter 5. The simulation has been carried out using the software Matlab Simulink and the tool package SimPowerSystem. The simulation model of the system has been optimized to make it as close as possible to the real system which has been utilized for the experimental validation (in Chapter 7). Section 6.2 presents a description of the simulation model utilized for the validation, in section 6.3 the simulation results are presented, described and commented.

6.2 Description of the simulation model

The simulation validation of the technique proposed in this thesis has been obtained by modeling the system using the software Matlab Simulink with the toolbox SimPowerSystem [73]. The characteristics of the simulation model have been

POWER SYSTEM PARAMETERS	
Supply voltage V_s	415V AC rms line-line
Supply frequency f	50 Hz
Supply impedance R_s - L_s	$R_s = 1.5 \ \Omega$ $L_s = 0.4$ mH
Active filter line impedance R_f - L_f	$R_f = 0.1\Omega$ $L_f = 3$ mH
Active filter DC link capacitance C	2200 μF
Non-linear load DC resistance R_l	12.5 Ω
CONTROL SYSTEM PARAMETERS	
Sampling frequency f_s	10 kHz
DC link PI controller z domain	$k_p = 0.03$ $k_i = 0.02997$
Fundamental/harmonic current PI controller z domain	$k_p = 4.5$ $k_i = 4.2885$
Harmonic voltage PI controller z domain	$k_p = 0.127$ $k_i = 0.1265$

Table 6.1: Characteristic parameters of the simulation model

chosen to match the real system utilized for the experimental tests. Figure 5.14 and figure 5.22 show the scheme of the power system and of the overall control scheme respectively, the same system is modelled in the simulation. Figure 5.15 and figure 5.21 show the fundamental and harmonic control schemes respectively. In the simulation model the fundamental phase angle estimation and the harmonic identification are carried out by means of the real-time DFT algorithm explained in Chapter 3. The decoupling between the rotating reference frames together with the whole control are implemented in the way described in Chapter 5. Table 6.1 presents the values of the simulation model parameters.

Considering the PI controllers transfer functions in the s domain, reported in Equations (5.26), (5.35), (5.55), these have been transformed into their equivalent z domain transfer functions, by means of the Zero Order Hold discretization command *c2d* (Continuous To Digital) in Matlab, with 10 kHz sampling frequency,

and the gains are indicated in Table 6.1. It is possible to use this method because the ratio between the sampling frequency and the natural frequency of the closed loop system is bigger than 15. The controller is designed in the s domain and its transfer function is discretized directly, with no need to design the controller in the z domain.

$$C(s) = \frac{4.5s + 2115}{s} \qquad \longrightarrow \qquad C(z) = \frac{4.5z - 4.2885}{z - 1} \qquad (6.1)$$

$$C(s) = \frac{0.03s + 0.33}{s} \qquad \longrightarrow \qquad C(z) = \frac{0.03z - 0.02997}{z - 1} \qquad (6.2)$$

$$C(s) = \frac{0.127s + 5.2}{s} \qquad \longrightarrow \qquad C(z) = \frac{0.127z - 0.1265}{z - 1} \qquad (6.3)$$

In the simulation validation, the magnitudes of the PCC voltage harmonics to be compensated are: 11.66V, 6.05V, 4.65V, 3.36V for the 5th, 7th, 11th and 13th respectively. The magnitudes of the current harmonics to be compensated are: 7.18A, 3.50A, 2.27A, 1.50A for the 5th, 7th, 11th and 13th respectively.

6.3   Simulation results

In this section the simulation results are presented and commented. Figures 6.1 to 6.4 show the d and q components of the PCC voltage on the different harmonic rotating reference frames where the compensation of 5th, 7th, 11th and 13th is tested. Particularly the control transient is shown: the control is enabled at 0.5 s. Before the control is enabled, the voltage mean value is different from zero and it depends on the voltage harmonic value. After the control is enabled, the mean value of the voltage settles to zero, which is the reference.

It can be seen that the q component of the voltage on each reference frame is zero not only after the control is enabled but also before that. This is due to the characteristics of the non-linear load included in the simulation model. It consists of an

ideal three-phase diode bridge rectifier and it is simulated by means of the block
"'Universal bridge"' in Simulink SimPowerSystems. When using this block, the
current absorbed by the distorting load is characterized by relative phase between
each harmonic and the fundamental equal to zero. Therefore, when transform-
ing the supply current into each harmonic reference frame, using the fundamental
phase angle multiplied by the harmonic index, the harmonic presents zero q com-
ponent in the rotating frame. Since the supply impedance in the simulation is
mainly resistive (the simulation model represents the system used for the experi-
mental validation, in which a high supply resistance has been used in order to get a
voltage drop high enough to be measured by the voltage transducers), the voltage
harmonics, caused by the voltage drop, are almost in phase with the harmonic
currents, so also the voltage harmonics have zero q component on the different
harmonic reference frames.

Both before and after the control enabling instant, the voltage is decoupled from
all the other harmonics, nevertheless in the figures an oscillation can be noticed.
This is due to the presence of all the other harmonics injected by the non-linear
load, above the 13th, and the harmonics injected by the active filter itself. These
harmonics are not included in the decoupling system, so they are found in the
feedback path of the harmonic voltage control.

Figures 6.5 to 6.8 show the FFT spectrum of the d components of the PCC voltage
on the harmonic rotating reference frames.

From figures 6.5 to 6.8 it can be seen that the 0 Hz component is reduced to nearly
0 V, because of the control action. The components with the highest amplitudes
in the spectrum can be seen at the frequencies: 300 Hz, 600 Hz, 900 Hz, 1200 Hz,
1500 Hz, 1800 Hz, 2100 Hz, 2400 Hz, 2700 Hz. These components correspond to
the harmonics injected by the non-linear load, with an order higher than 13. They
are not compensated by the control system and they are not taken into account
in the decoupling, so they are bound to be observed in the PCC voltage, feedback
of the control. As well as the high order harmonics due to the distorting load,
other harmonics due to the active filter itself can be seen, such as those at 150
Hz and 450 Hz. As explained in Section 5.2, each harmonic is seen on a rotating

Figure 6.1: d and q components of the PCC voltage on the 5th harmonic frame

Figure 6.2: d and q components of the PCC voltage on the 7th harmonic frame

Figure 6.3: d and q components of the PCC voltage on the 11th harmonic frame

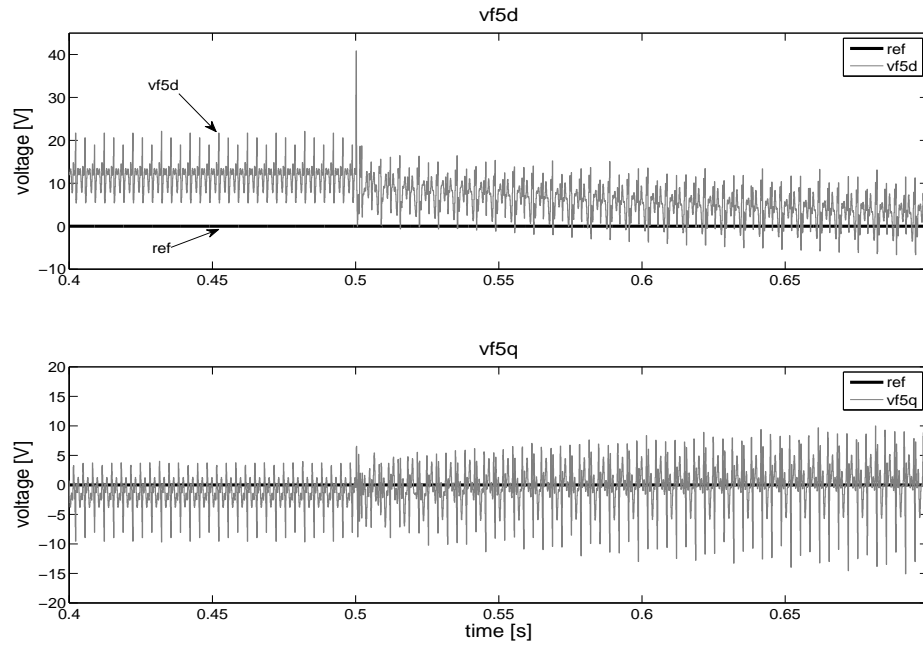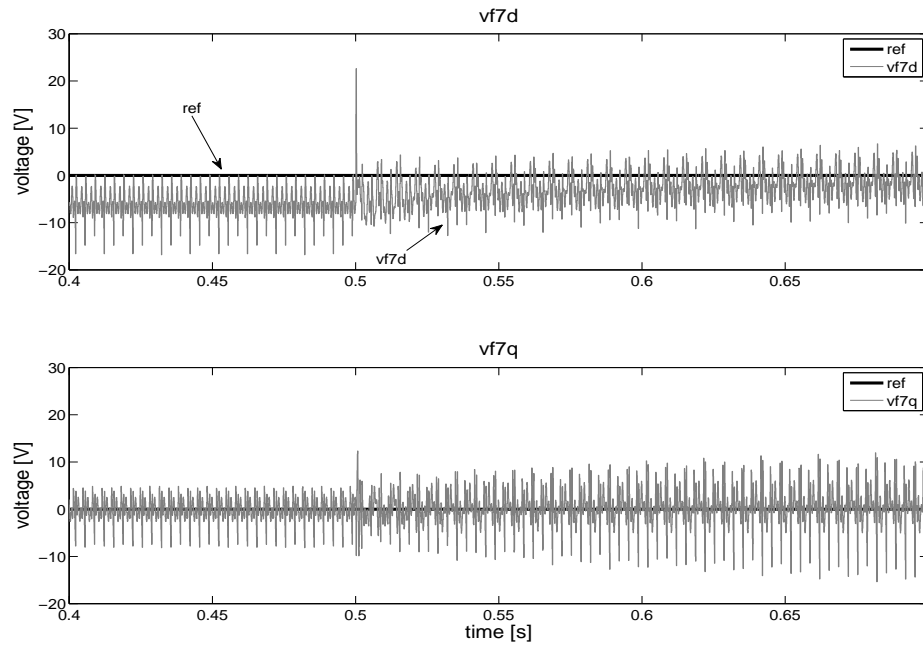Figure 6.4: d and q components of the PCC voltage on the 13th harmonic frame

Figure 6.5: FFT of the d component of the PCC voltage on the 5th harmonic frame

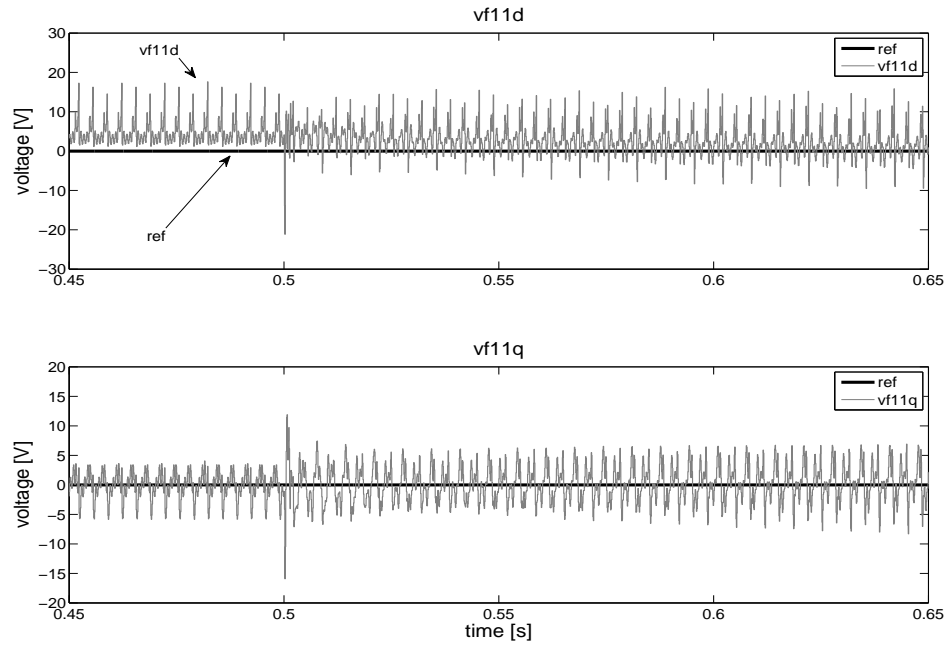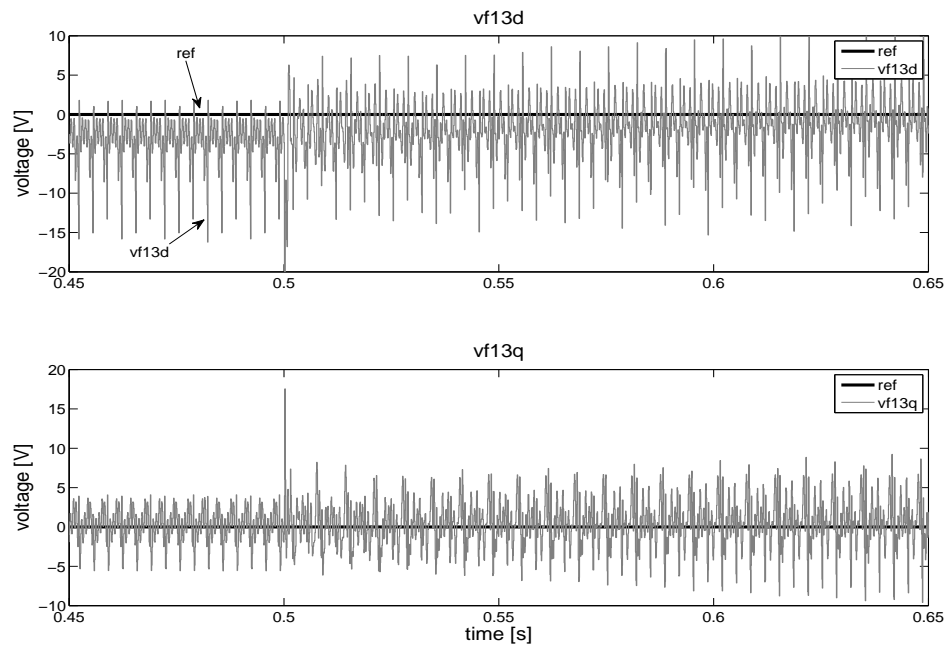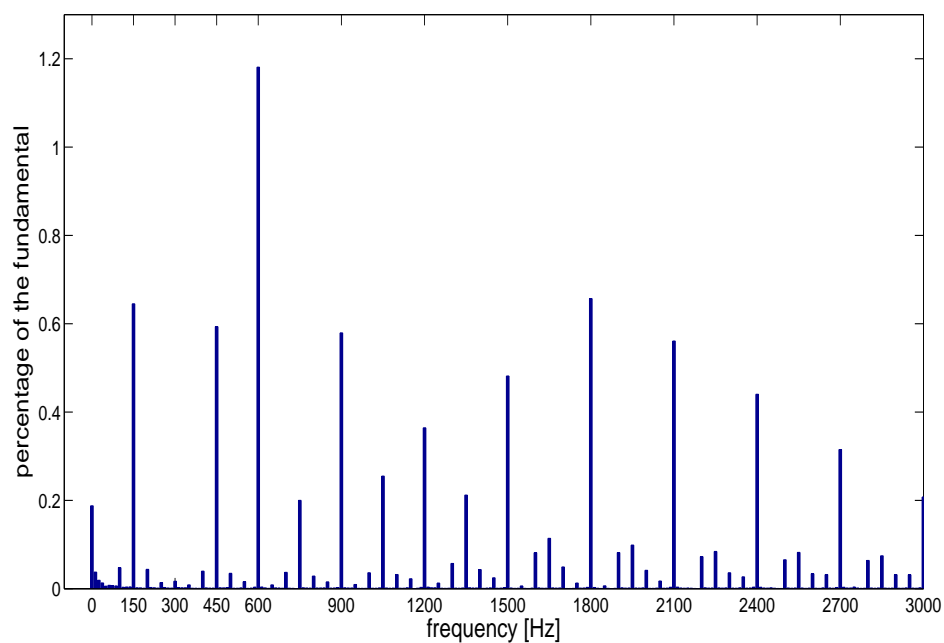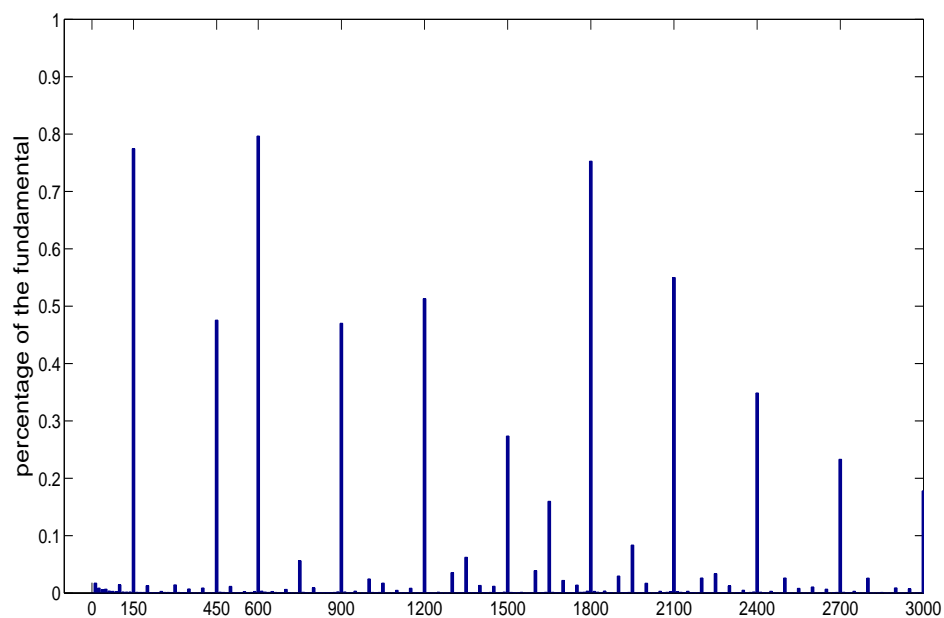

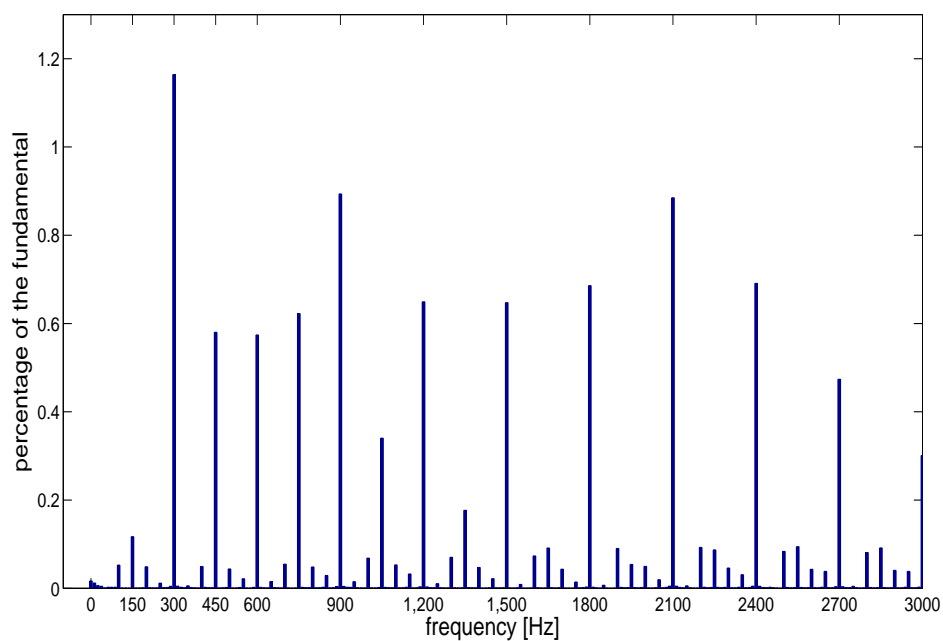Figure 6.6: FFT of the d component of the PCC voltage on the 7th harmonic frame

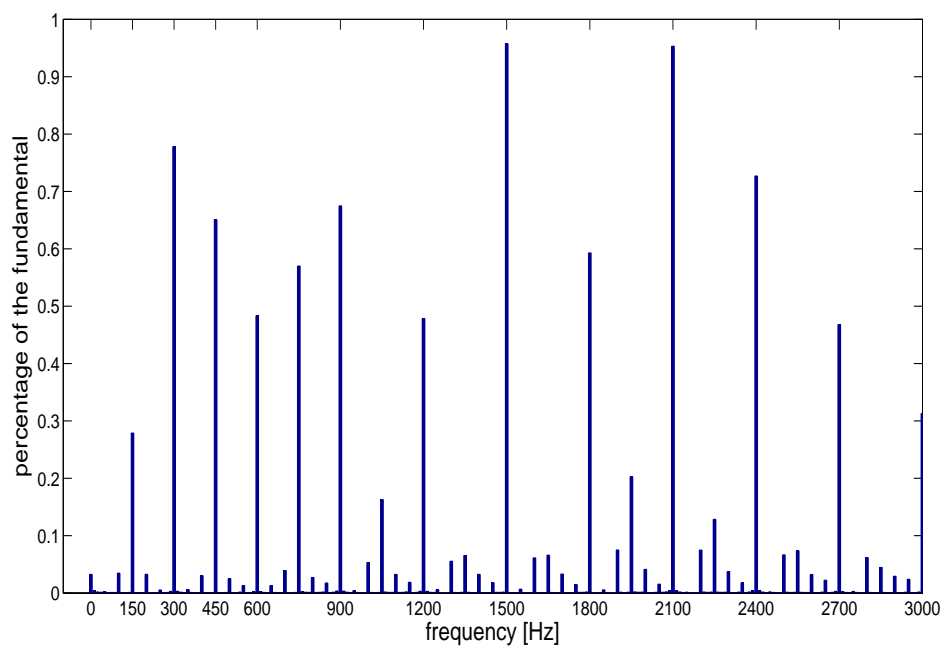Figure 6.7: FFT of the d component of the PCC voltage on the 11th harmonic frame

Figure 6.8: FFT of the d component of the PCC voltage on the 13th harmonic frame

Reference	Harmonics as seen in the spectrum [Hz]										
frame	150	300	450	600	900	1200	1500	1800	2100	2400	2700
5	2;8		4;14	17	23	19;29	25;35	31;41	37;47	43;53	49;59
7	4;10		2;16	19	25	17;31	23;37	29;43	35;49	41;55	47;61
11	8;14	17	2;20	23	29	35	19;41	25;47	31;53	37;59	43;65
13	10;16	19	4;22	25	31	37	17;43	23;49	29;55	35;61	41;67

Table 6.2: Harmonics as seen in the FFT spectrum of the voltage on the different reference frames

reference frame as a sinusoidal component oscillating at its relative angular speed. The relative angular speed is given by (5.1). Table 6.2 specifies the absolute harmonic order corresponding to each harmonic component of the spectrum seen in the rotating reference frames. Only the components with the largest amplitudes have been considered. The cells which have been left blank correspond to the components which have zero amplitude in that particular spectrum: they correspond to harmonics which have been decoupled. The double numbers in some cells correspond to the two harmonics (one positive sequence and one negative sequence) which are seen with the same relative frequency in that reference frame. In some cells only one harmonic order is reported, as the other harmonic seen with the same relative frequency has been decoupled so it does not contribute to the component in the spectrum.

Figures 6.9 to 6.17 show the d and q components of the active filter current on the harmonic rotating reference frames. The same considerations made for the voltage oscillations can be made for the current. Particularly figures 6.11, 6.13, 6.15, 6.17 show an expanded view of the current control steady-state. It can be seen that the reference current and the output current do not match perfectly: the current PI controller has been designed with a low bandwidth, because it does not need to track the high order oscillations of the current, but only the DC component of the reference.

Figures 6.18 and 6.19 show the PCC voltage on the phase A before and after the active filter harmonic compensation.

It is not easy to see the action of the voltage harmonic compensation in the time

Figure 6.9: d and q components of the active filter current on the fundamental frame

Figure 6.10: d and q components of the active filter current on the 5th harmonic frame

Figure 6.11: d and q components of the active filter current on the 5th harmonic frame: expanded view of the steady state
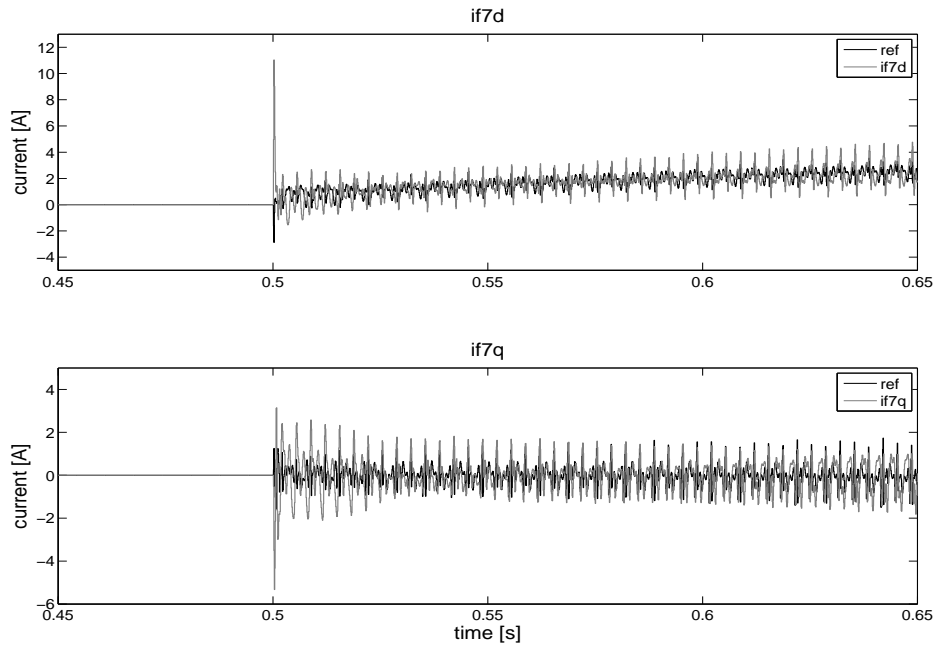
Figure 6.12: d and q components of the active filter current on the 7th harmonic frame
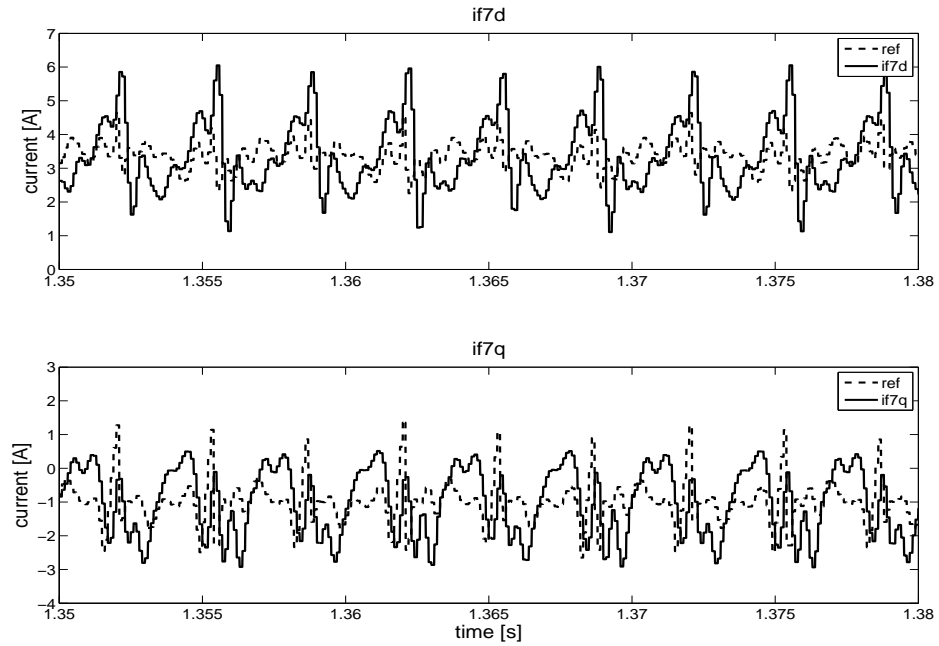
Figure 6.13: d and q components of the active filter current on the 7th harmonic frame: expanded view of the steady state
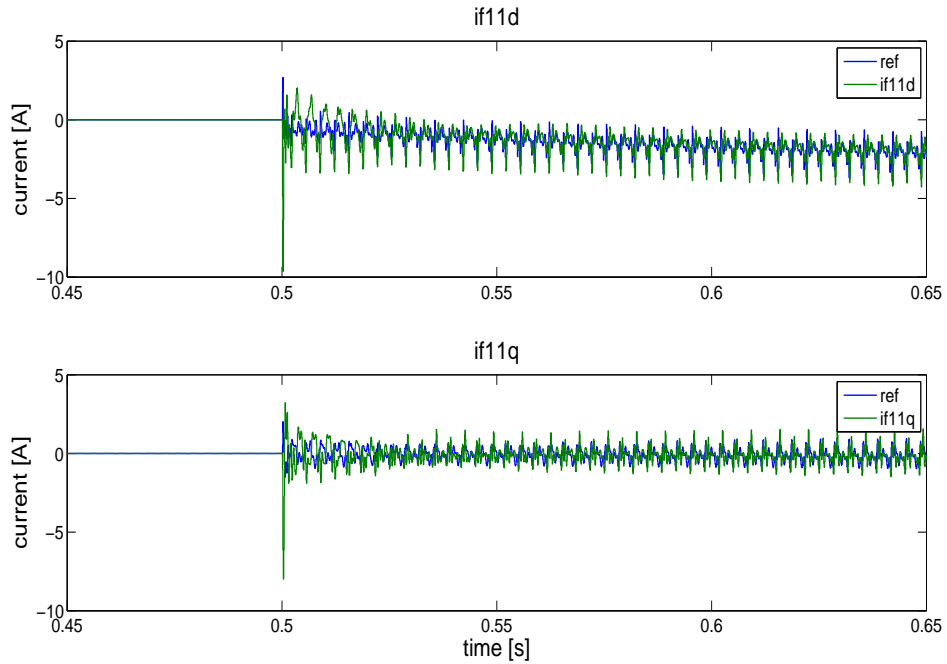
Figure 6.14: d and q components of the active filter current on the 11th harmonic frame
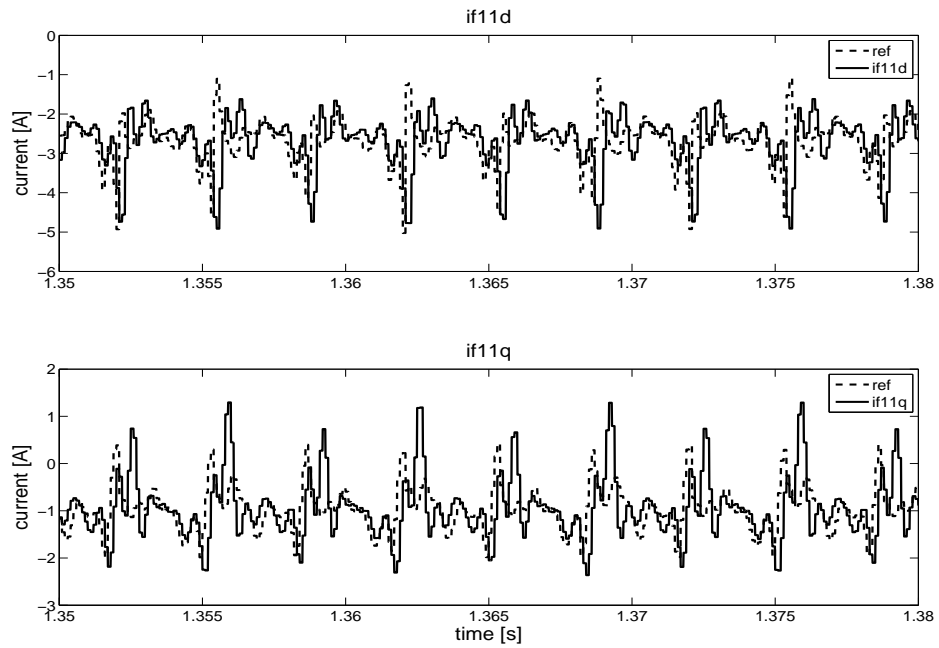
Figure 6.15: d and q components of the active filter current on the 11th harmonic frame: expanded view of the steady state
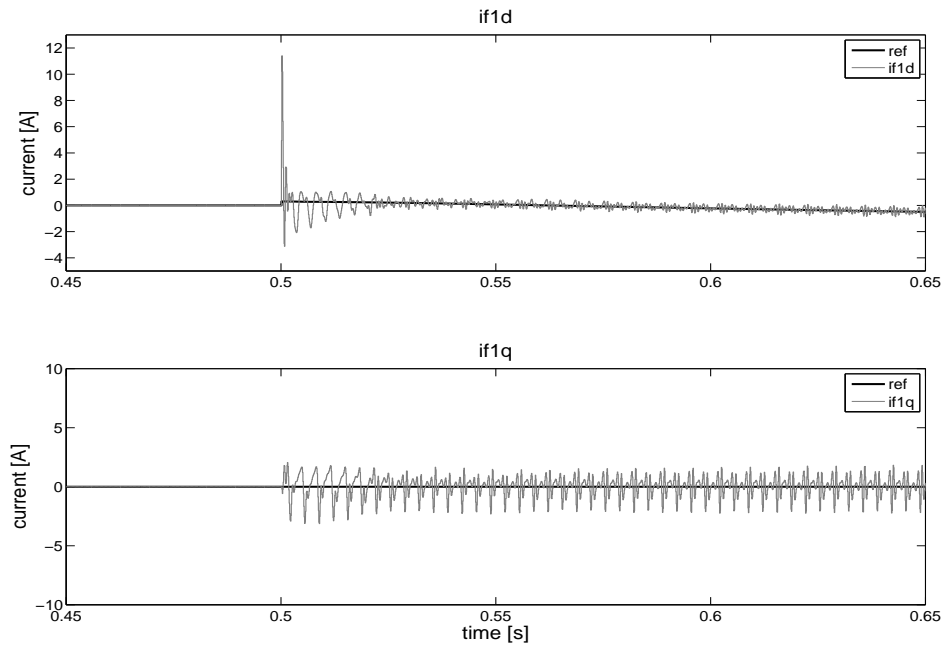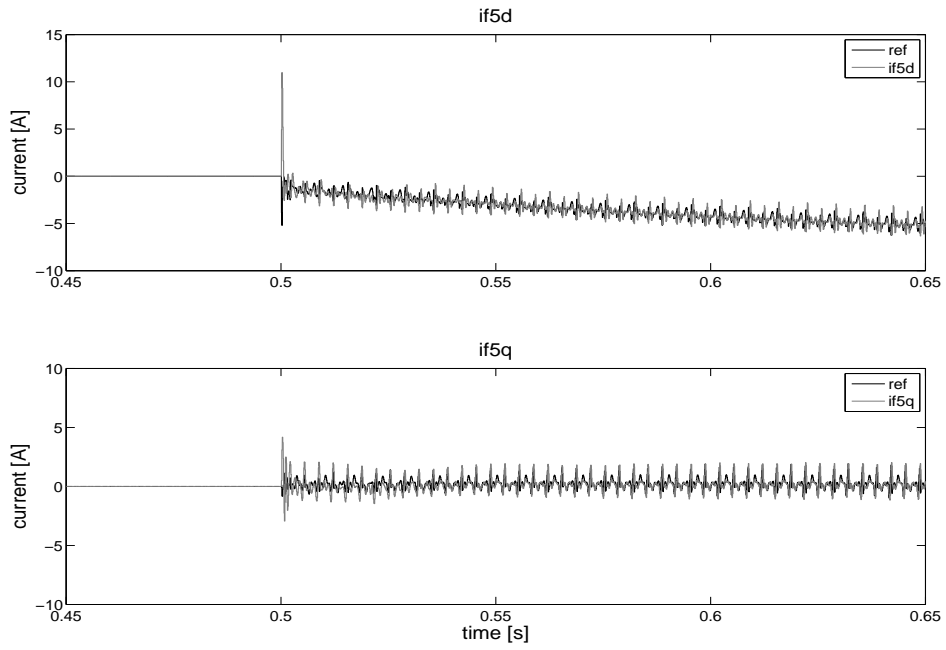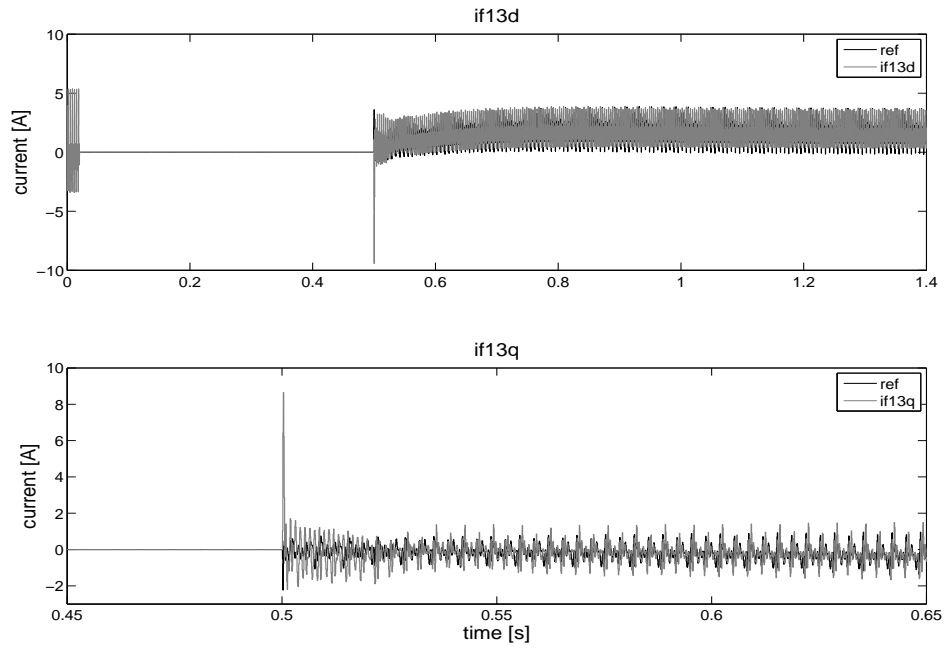

Figure 6.16: d and q components of the active filter current on the 13th harmonic frame
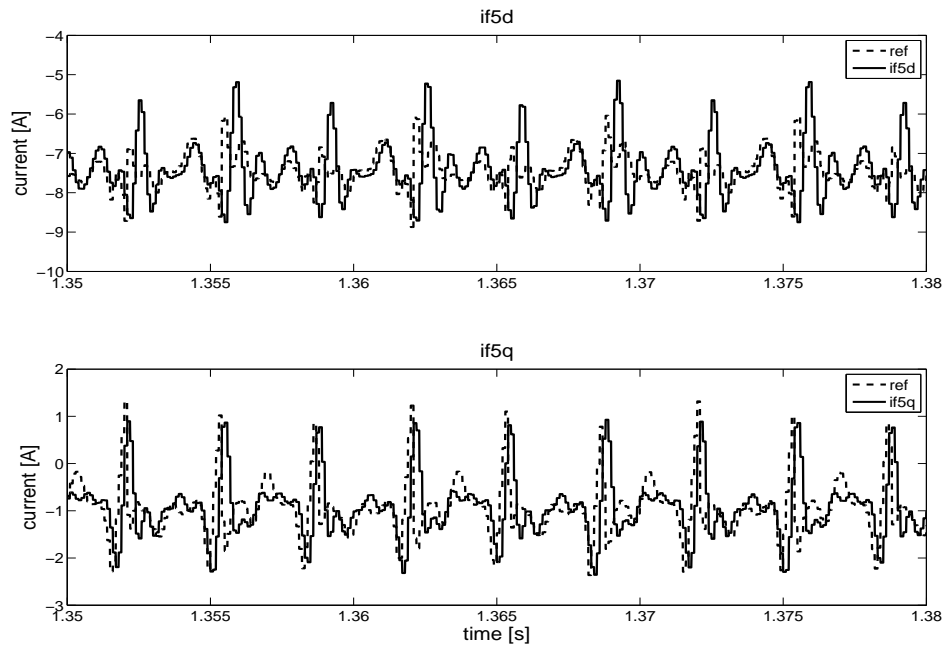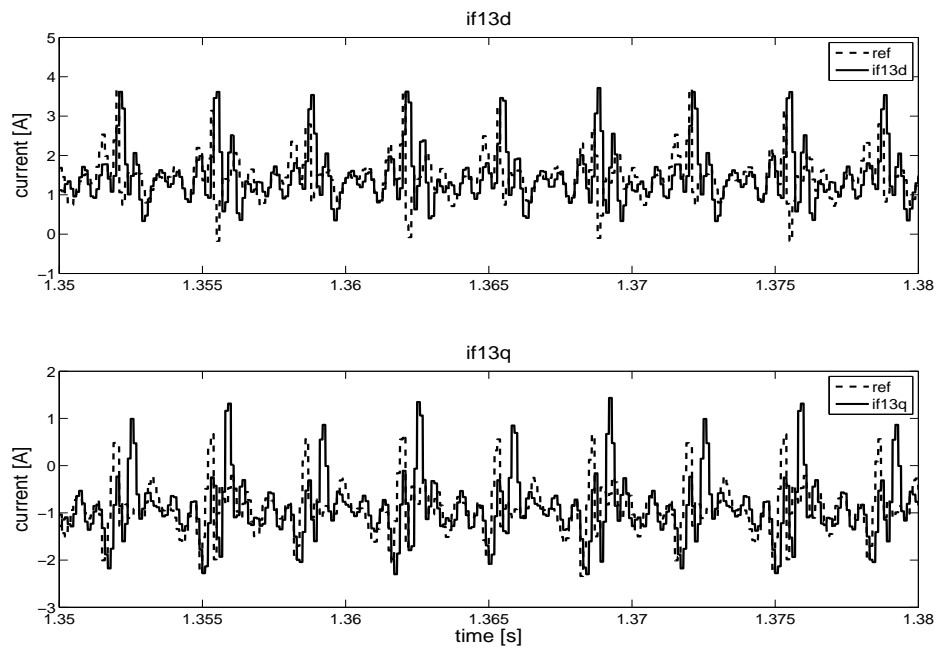
Figure 6.17: d and q components of the active filter current on the 13th harmonic frame: expanded view of the steady state
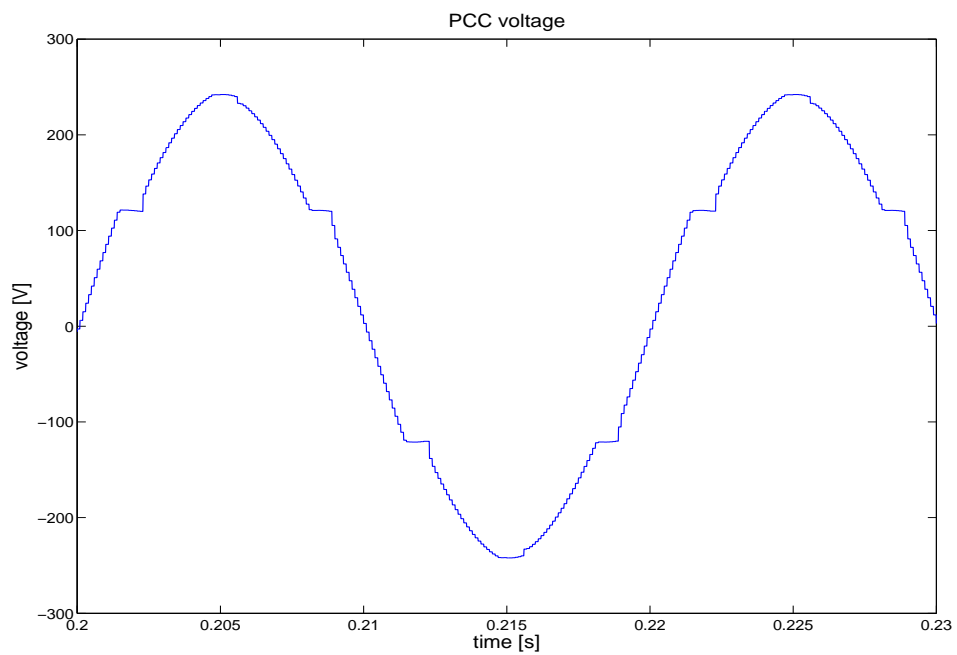
Figure 6.18: PCC three-phase voltage before the active filter compensation
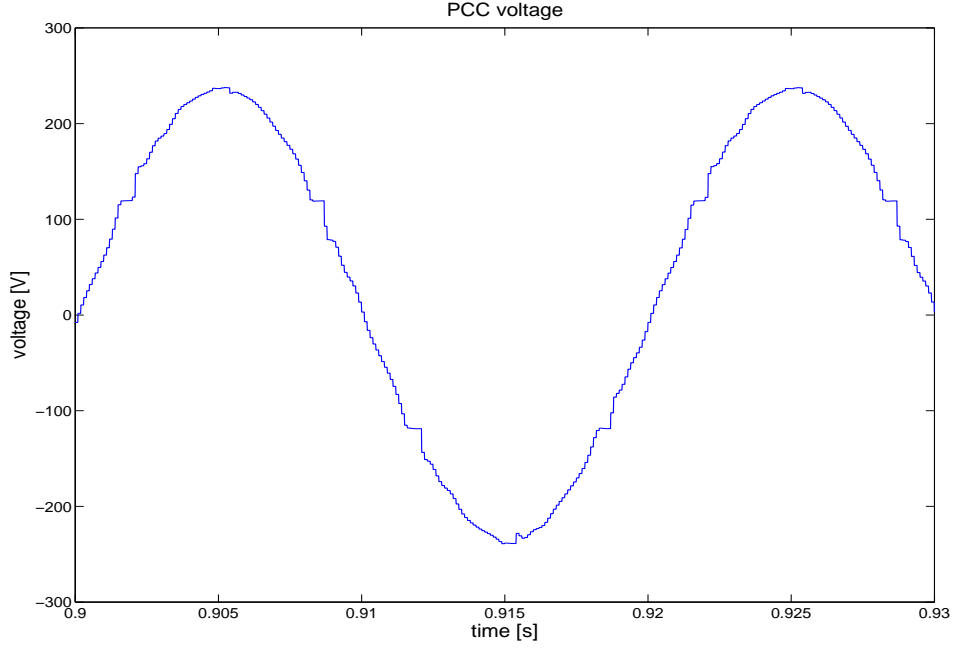
Figure 6.19: PCC three-phase voltage after the active filter compensation

domain: the voltage harmonics are very small compared to the fundamental. In the frequency domain it is possible to evaluate the harmonic reduction obtained with the compensation, as it is shown in figures 6.20 to 6.23. These figures show the FFT spectrum of the PCC voltage before and after the harmonic compensation. Particularly it is useful to compare figure 6.20 with figure 6.21 and figure 6.22 with figure 6.23 for an expanded view of the harmonics.

Table 6.3 reports the amplitude values of the 5th, 7th, 11th and 13th voltage harmonics, comparing them between the case in which the compensation is not active and in which the compensation is active. The voltage THD before the compensation is 6.29 %, while the one achieved after the compensation is 2.31 %. From table 6.3 a remarkable reduction in amplitude can be noticed, for the 5th, 7th, 11th and 13th harmonics. However this does not result in such a high reduction of the voltage THD. This is due to the frequency shift of the harmonic distortion, which is a drawback of this harmonic compensation. The compensation allows a significant reduction of a certain set of harmonics but as a result it increases the amplitude of higher order harmonics. This can be seen by comparing figure 6.22 with figure 6.23: the harmonic amplitudes at frequencies bigger than 1450 Hz
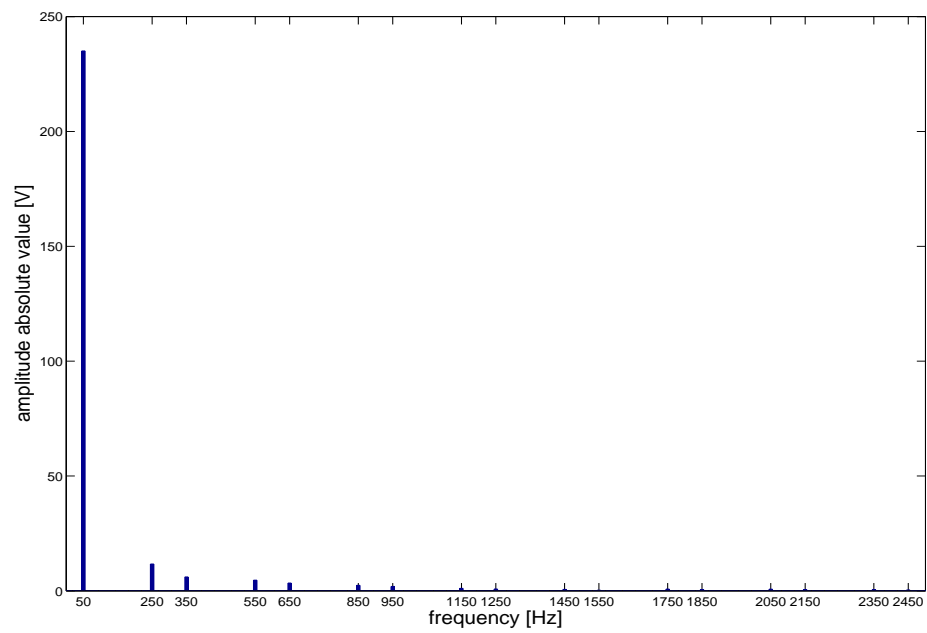
Figure 6.20: FFT spectrum of the PCC voltage before the active filter compensation
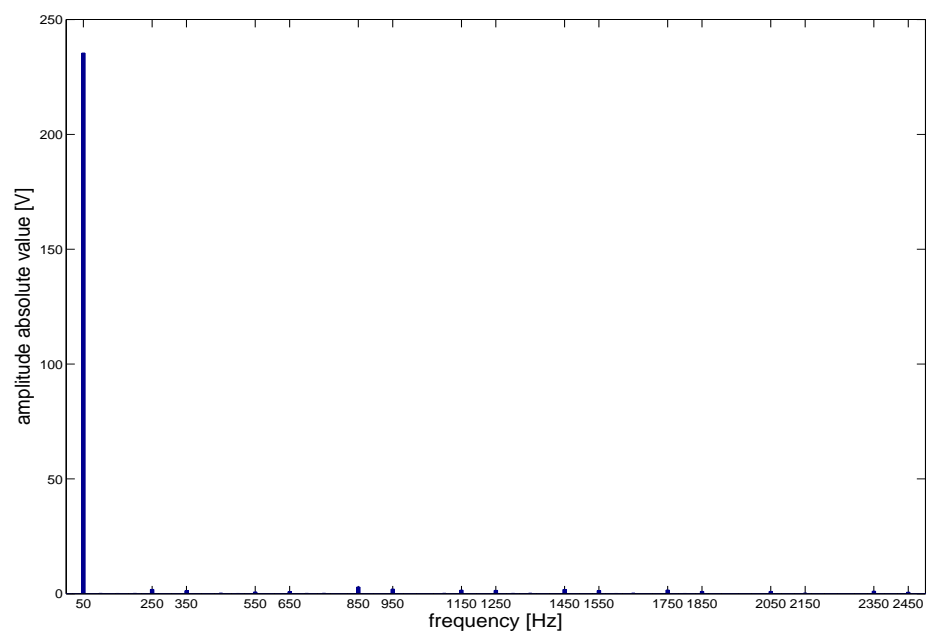
Figure 6.21: FFT spectrum of the PCC voltage after the active filter compensation
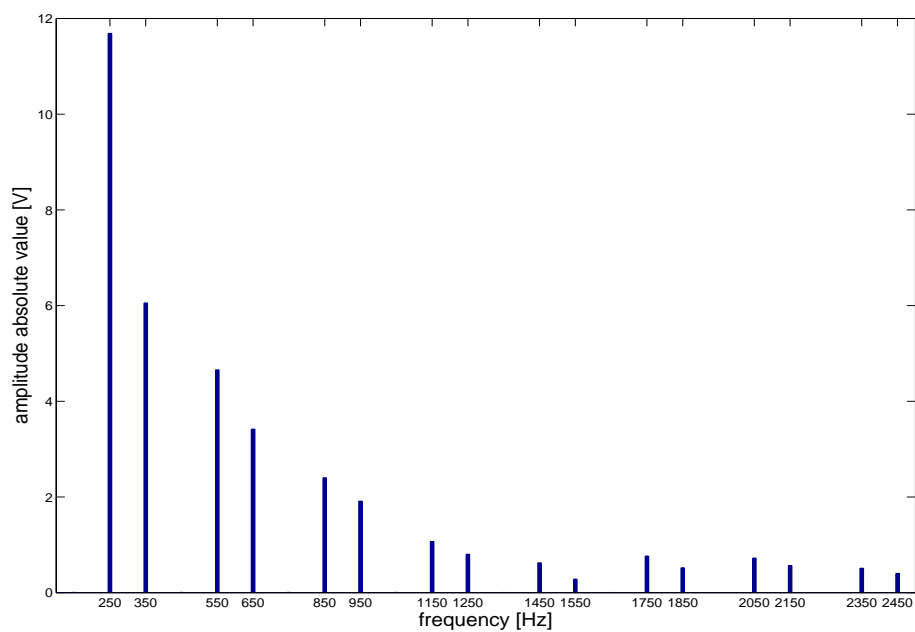
Figure 6.22: FFT spectrum of the PCC voltage before the active filter compensation: expanded view of the harmonics
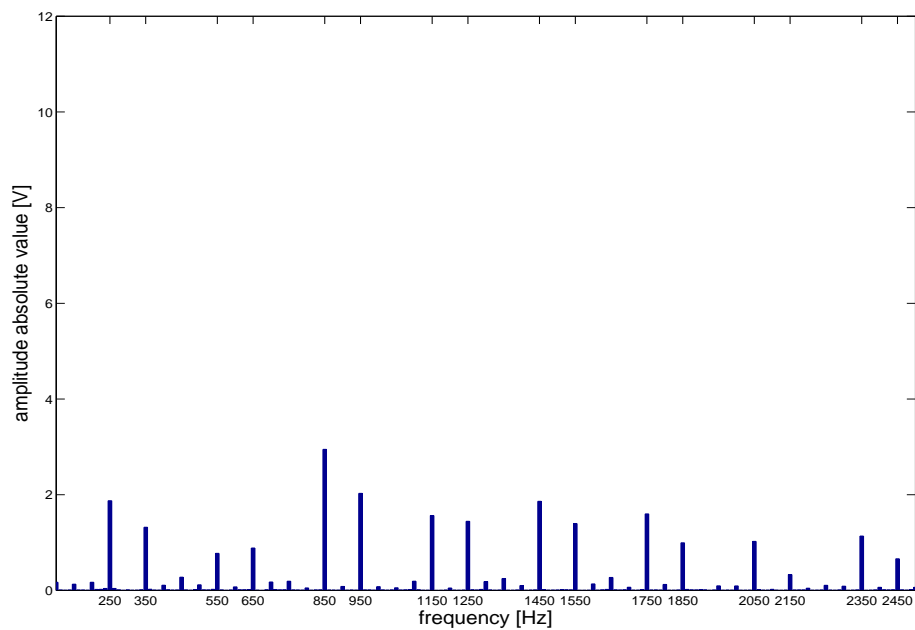
Figure 6.23: FFT spectrum of the PCC voltage after the active filter compensation: expanded view of the harmonics

	Voltage harmonic amplitude				Harmonic
	before compensation		after compensation		reduction
	[V]	[% of fund.]	[V]	[% of fund.]	
5th	11.66	4.97	1.87	0.79	83.96 %
7th	6.05	2.57	1.32	0.56	78.18 %
11th	4.65	1.98	0.77	0.33	83.44 %
13th	3.36	1.43	0.88	0.37	73.81 %

Table 6.3: Voltage harmonic reduction

increase.

Figures 6.24 and 6.25 show the supply current on the phase A before and after the active filter harmonic compensation.

Figures 6.26 to 6.29 show the FFT spectrum of the supply current in both the aforementioned cases. Particularly it is useful to compare figure 6.26 with figure 6.27 and figure 6.28 with figure 6.29 for an expanded view of the harmonics.

Table 6.4 reports the amplitude values of the 5th, 7th, 11th and 13th current harmonics, comparing them between the case in which the compensation is not active and in which the compensation is active. The current THD before the compensation is 25.28 %, while the one achieved after the compensation is 4.64 %.

6.4   Summary

This chapter has presented the simulation results that validate the multiple reference frames voltage detection control technique for shunt active power filters, presented in Chapter 5. The simulations have been carried out using the software Matlab Simulink. The PCC voltage and active filter current, represented on a
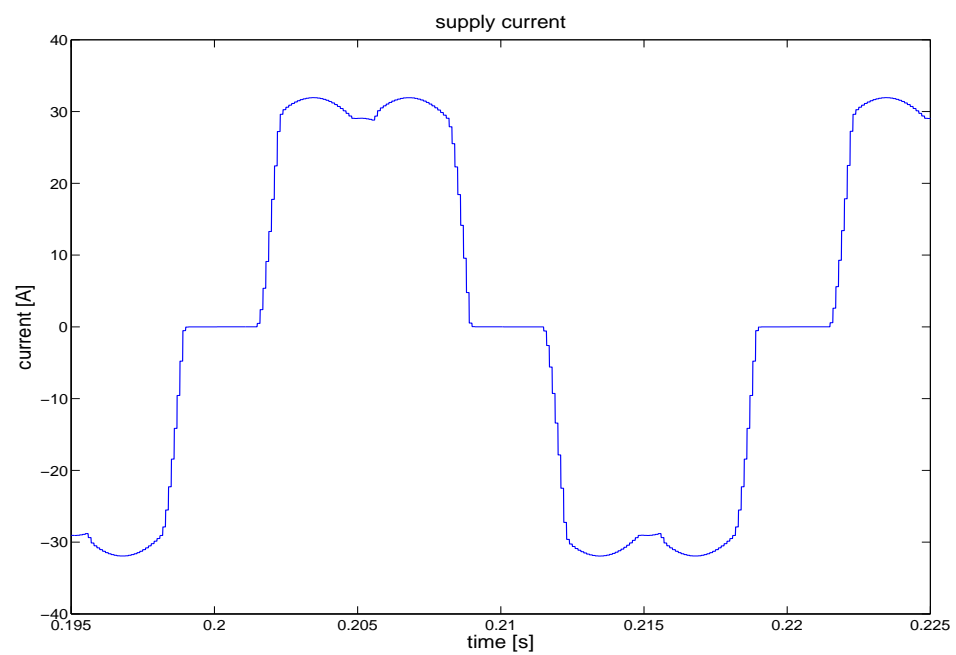
Figure 6.24: Three-phase supply current before the active filter compensation
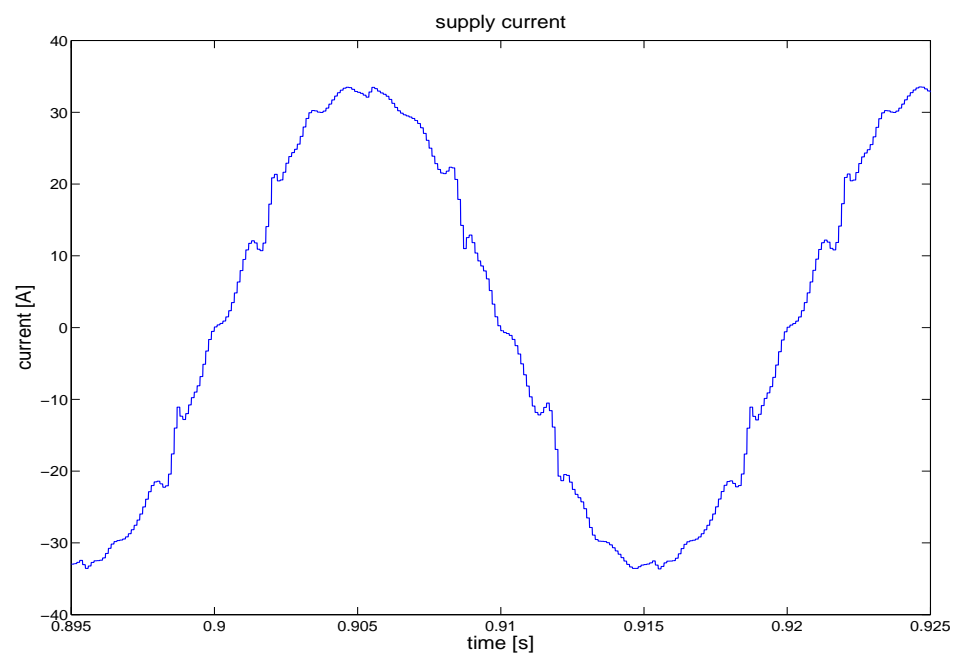
Figure 6.25: Three-phase supply current after the active filter compensation
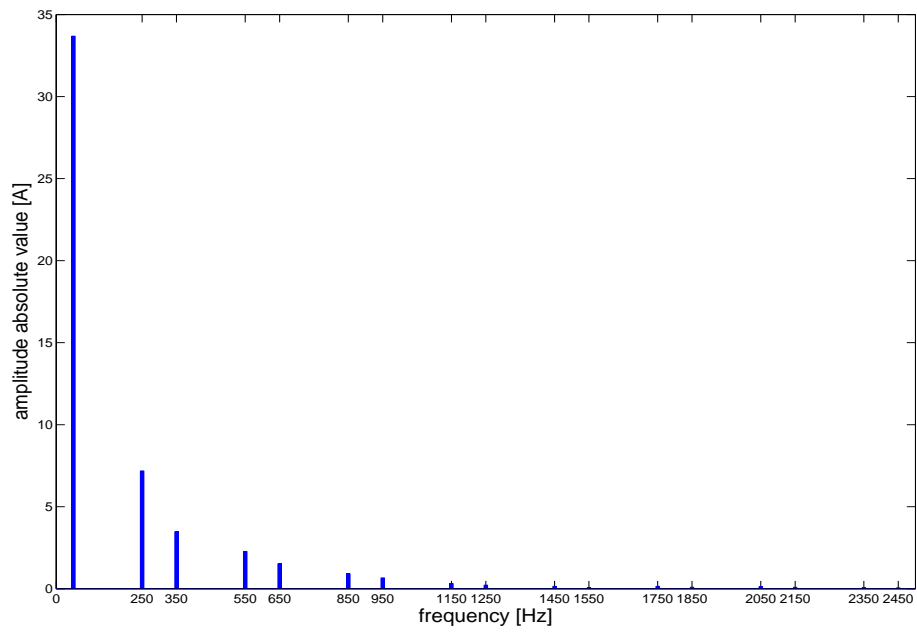
Figure 6.26: FFT spectrum of the supply current before the active filter compensation
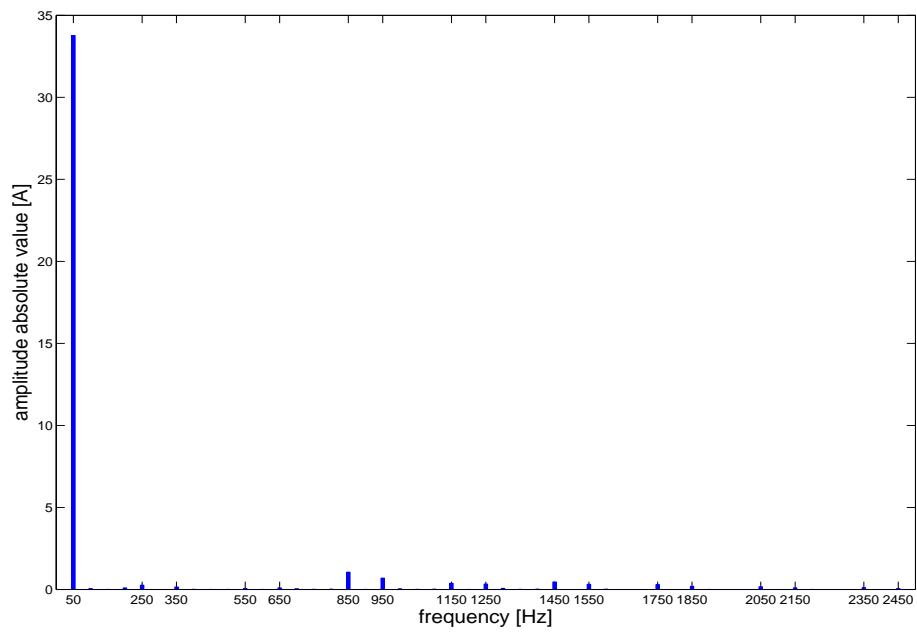
Figure 6.27: FFT spectrum of the supply current after the active filter compensation
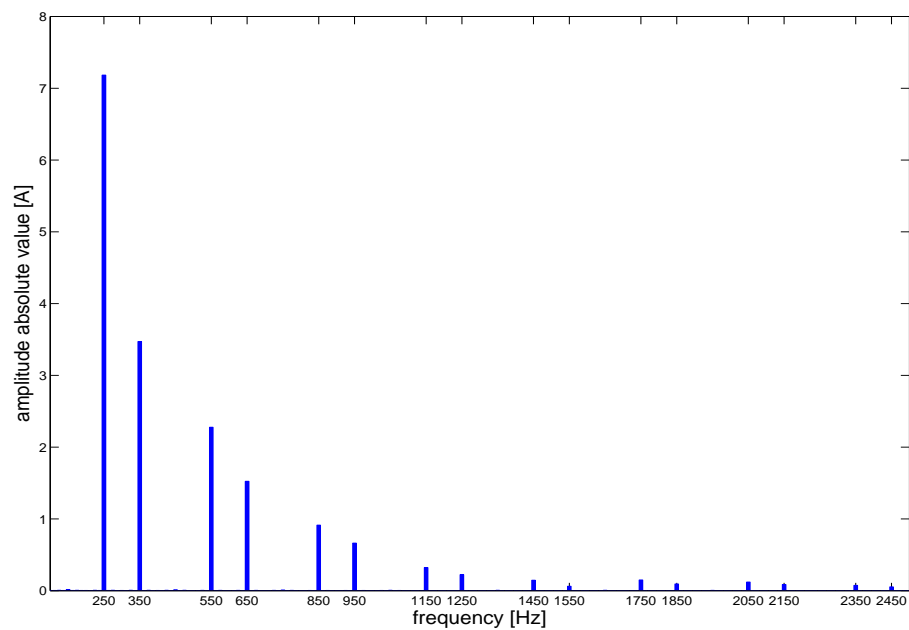
Figure 6.28: FFT spectrum of the supply current before the active filter compensation: expanded view of the harmonics
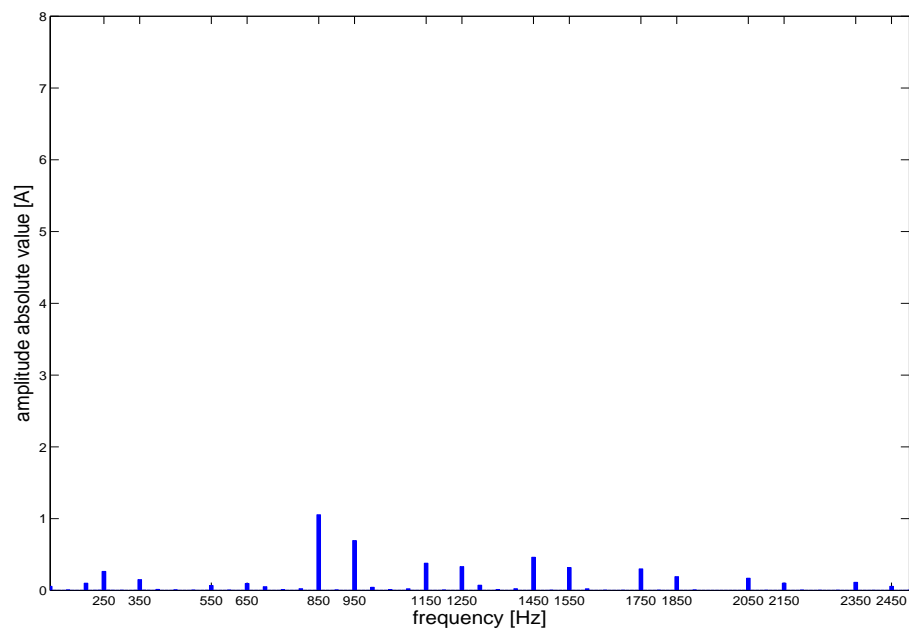
Figure 6.29: FFT spectrum of the supply current after the active filter compensation: expanded view of the harmonics

| | Current harmonic amplitude | | | | Harmonic |
| | before compensation | | after compensation | | reduction |
	[A]	[% of fund.]	[A]	[% of fund.]	
5th	7.18	21.32	0.26	0.77	96.34 %
7th	3.50	10.39	0.15	0.44	95.71 %
11th	2.27	6.74	0.07	0.21	96.92 %
13th	1.50	4.45	0.095	0.28	93.67 %

Table 6.4: Current harmonic reduction

dq reference frame and decoupled from all the other reference frames, follow the reference imposed in the control scheme. Furthermore, FFT analysis has demonstrated that this technique can effectively compensate the harmonics injected by a non-linear load and considerably reduce the THD of both the PCC voltage and the supply current.

Chapter 7

Voltage Detection Control Technique: Experimental Results

7.1 Introduction

This chapter presents the results obtained from the experimental validation of the proposed control technique for active shunt filters described in Chapter 5. The experimental tests have been carried out using a laboratory setup comprising a programmable power supply, a resistive-inductive supply impedance, a three-phase shunt active power filter, a three-phase distorting load. Section 7.2 presents a description of the laboratory experimental setup utilized for the validation, in section 7.3 the experimental results are presented, described and commented.

7.2 Description of the experimental setup

The experimental validation of the multiple reference frames voltage detection control technique for shunt active power filters has been carried out using a laboratory equipment setup. The setup represents a small scale version of a real power network where a shunt active power filter is applied.

The control technique can be utilized both for a normal 50Hz grid and for aircraft power systems, where the fundamental frequency varies in the range 360 to 900 Hz. However, for the work presented in this project, this technique has not been tested at values of frequency typical of an aircraft system, because of the limitations on the computational capability of the digital signal processor utilized for the validation. The whole implementation has been carried out at fundamental frequency equal to 50Hz, as shown in Chapter 6, but the results obtained can be extended to the variable frequency range of the aircraft power networks.

Figure 7.1 shows a scheme of the experimental setup utilized for the laboratory testing. The circuit represented in this figure is similar to the one represented in figure 5.14.
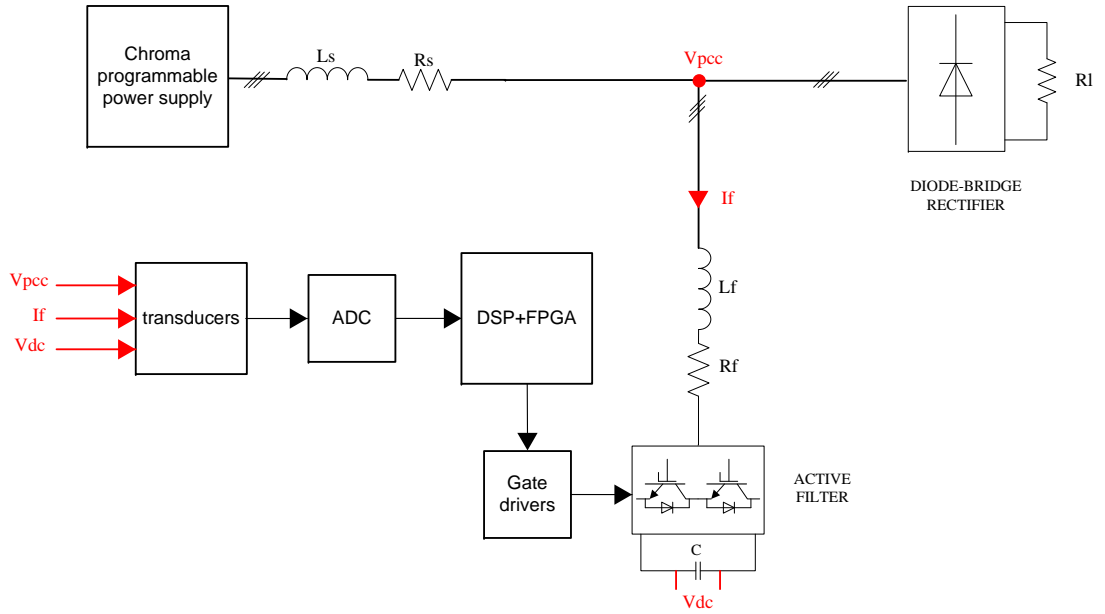
Figure 7.1: Scheme of the laboratory experimental setup

The experimental setup comprises a three-phase programmable power supply connected in series with a resistive-inductive impedance, representing the supply impedance, a laboratory-built three-phase shunt active power filter prototype, a three-phase diode bridge rectifier representing the distorting load that the active filter compensates for. The control algorithm is implemented on a 32 bit floating point Digital Signal Processor (DSP). The data acquisition is carried out by means of a Field Programmable Gate Array (FPGA) board. The variables measured by means of the voltage and current transducers are converted from analog to digital

signals by means of Analog to Digital Converters (ADC) connected to the FPGA.

A detailed description of the devices and components is given here. It can be seen that the supply resistance is 1.5 Ω. This high value has been chosen in order to increase the voltage drop of the harmonic current, as the voltage transducers utilized here present low accuracy for values of voltage smaller than 5V.

POWER SUPPLY

Chroma Programmable AC Source 61705 [47]

SUPPLY IMPEDANCE

Resistors:

resistance = 1.5 Ω
rated current = 11.8A
power rating = 751W

Inductors:

inductance = 0.4mH
rated current = 16A

SHUNT ACTIVE POWER FILTER

IGBT modules: DYNEX DIM200WHS12-A000 [74]

DC link capacitance = 2200 μF

Line inductor:

inductance = 3mH
rated voltage = 750V
rated current = 16A rms

NON-LINEAR LOAD

three IRKD101-14 diode modules [75]

load resistance = 12.5 Ω

MEASUREMENT

Voltage transducers: LEM LV 25-P [51]
Current transducers: LEM LA 55-P [76]

CONTROL

DSP: Texas Instruments TMS320C6713B 32 bit floating point [48]

FPGA: Actel ProAsic A500K050 Package PQ208 [49]

Analog to Digital Converters: 12 bit LTC 1400 [50]

Figures 7.2 to 7.4 show the pictures of the laboratory bench utilized for the experimental tests.

7.3 Experimental results

For the experimental validation, the supply voltage has been set to 120V rms line-line. The DC link voltage during the active filter operation was 200V. The voltage level at which the experimental tests have been carried out is lower than the full voltage of the mains because of the limitations in the rated current of the passive components utilized in the experimental setup. Because of the computational limitations of the DSP, the sampling frequency, equal to the switching frequency, has been set to 4 kHz, and only the 5th and 7th are compensated by the active filter in the tests presented here.

Figures 7.5 to 7.8 show the d and q components of the PCC voltage on the 5th
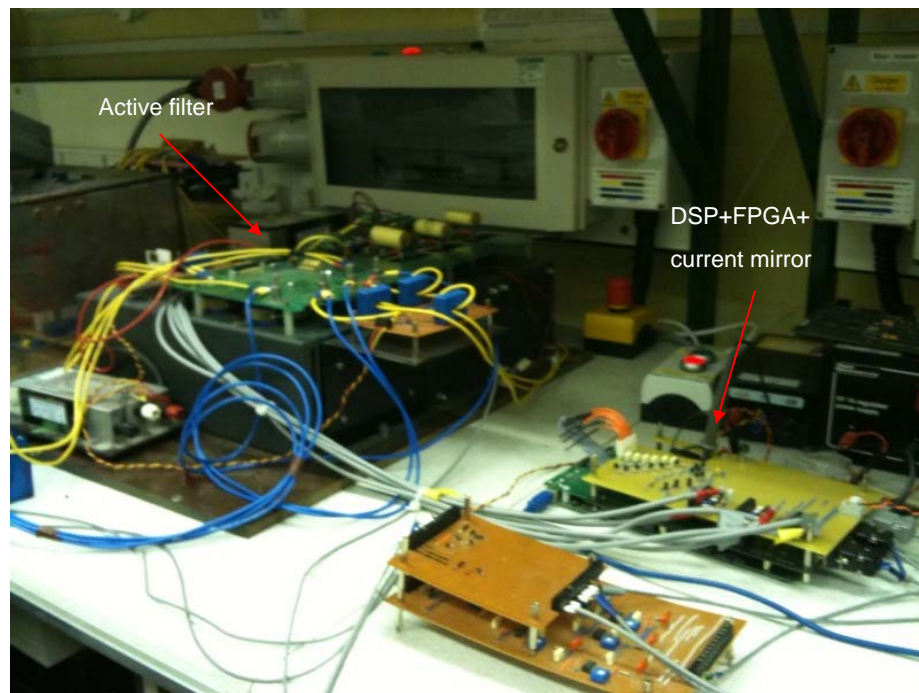
Figure 7.2: Picture of the active filter and the control boards
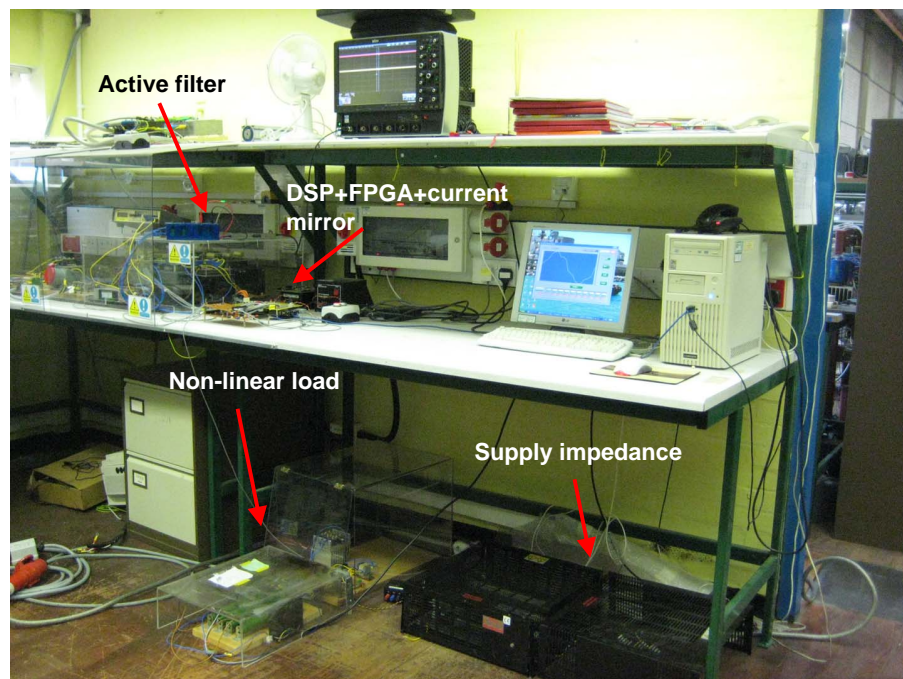
Figure 7.3: Picture of the whole laboratory bench

Figure 7.4: Picture of the programmable power supply

and 7th harmonic rotating reference frames where the compensation of 5th and 7th is tested. Particularly the control transient is shown: the control is enabled at 1.3s. Before the control is enabled, the voltage mean value is different from zero and it depends on the voltage harmonic value. This distortion is caused by the interaction of the harmonic currents drawn by the non-linear load with the supply impedance represented in this rig. After the control is enabled, the mean value of the voltage settles to zero, which is the reference. Both before and after the control enabling instant, the voltage is decoupled from all the other harmonics, nevertheless in the figures an oscillation can be seen. This is due to measurement noise and all the other harmonics injected by the non-linear load, above the 7th, and the harmonics injected by the active filter itself. All these harmonics are not included in the decoupling system, so they are found in the feedback path of the harmonic voltage control.

In order to observe the adherence between the simulation and experimental results, figures 7.5 and 7.6 can be compared to figure 6.1, in Chapter 6. Figures 7.7 and 7.8 can be compared to figure 6.2.
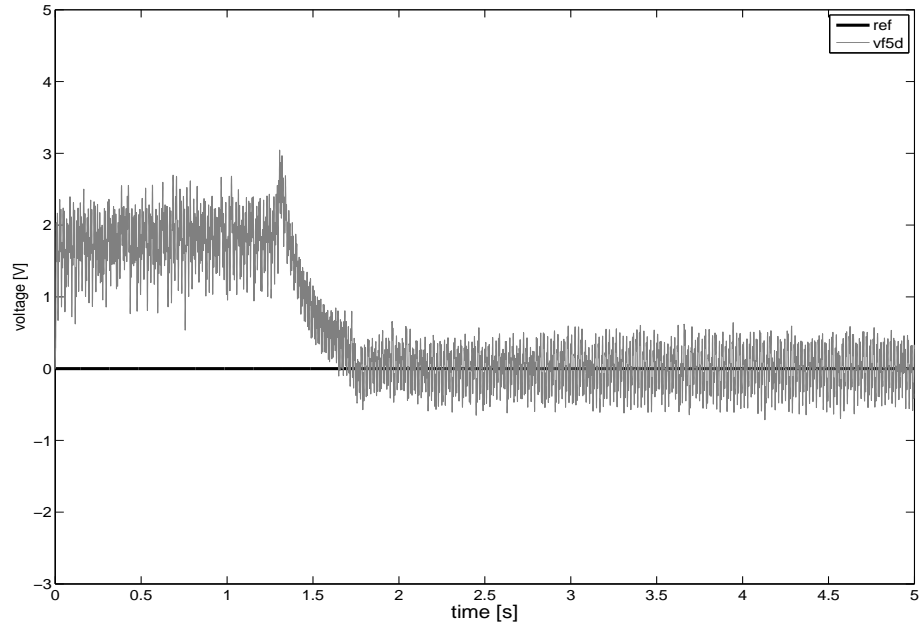
Figure 7.5: d component of the PCC voltage on the 5th harmonic frame
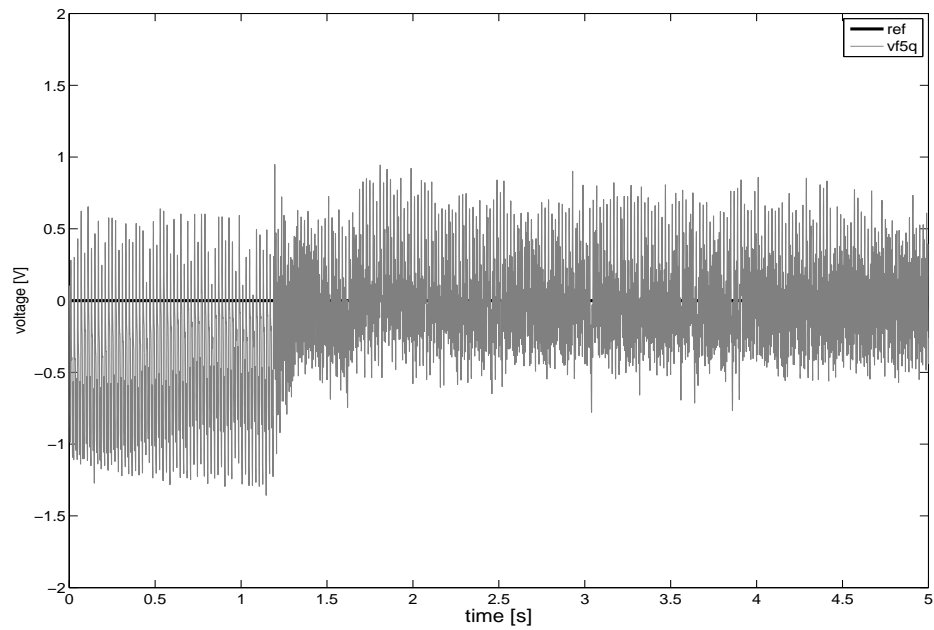
Figure 7.6: q component of the PCC voltage on the 5th harmonic frame
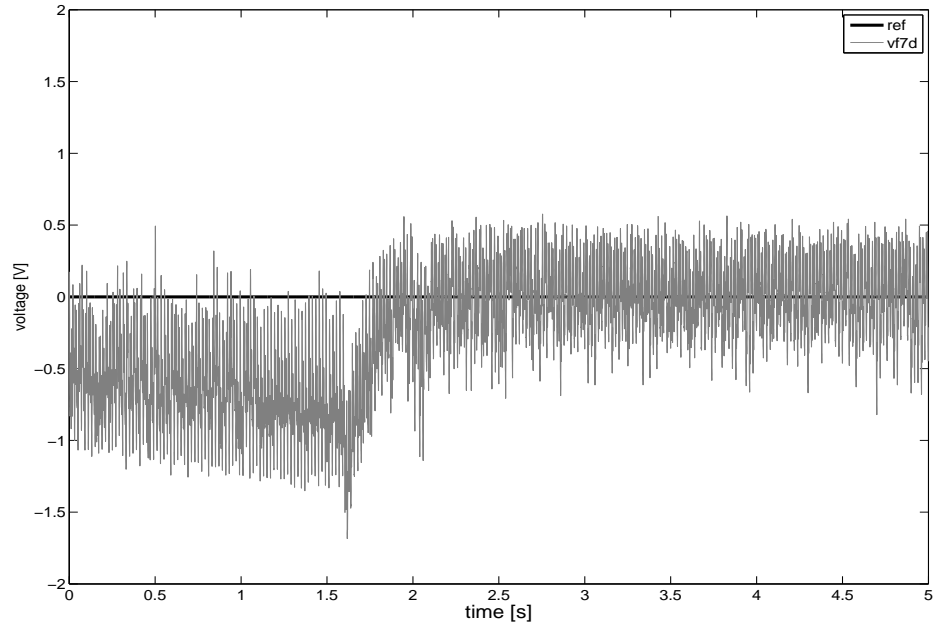
Figure 7.7: d component of the PCC voltage on the 7th harmonic frame
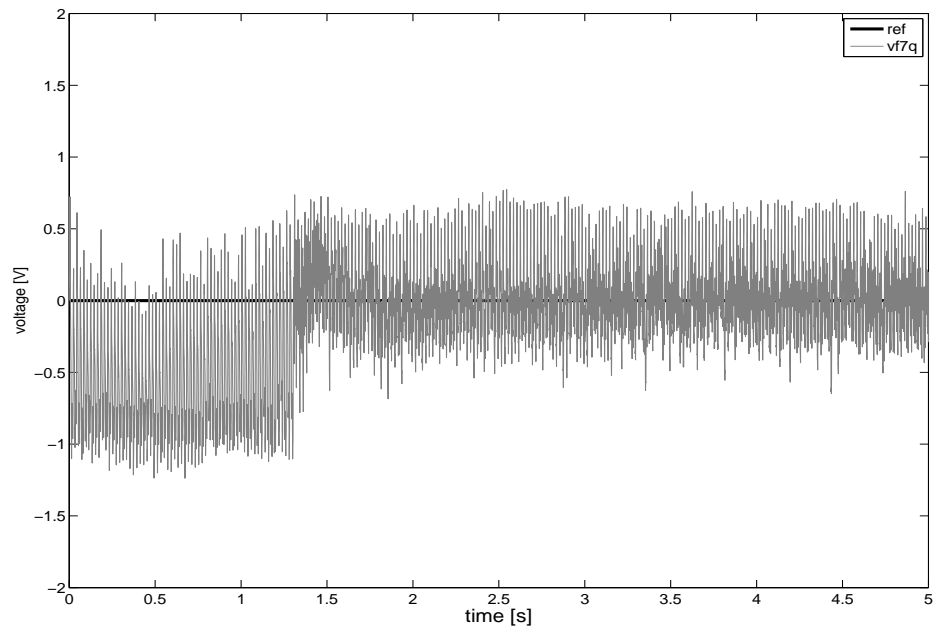
Figure 7.8: q component of the PCC voltage on the 7th harmonic frame

Figures 7.9 and 7.10 show the FFT spectrum of the d components of the PCC voltage on the 5th and 7th harmonic rotating reference frames.
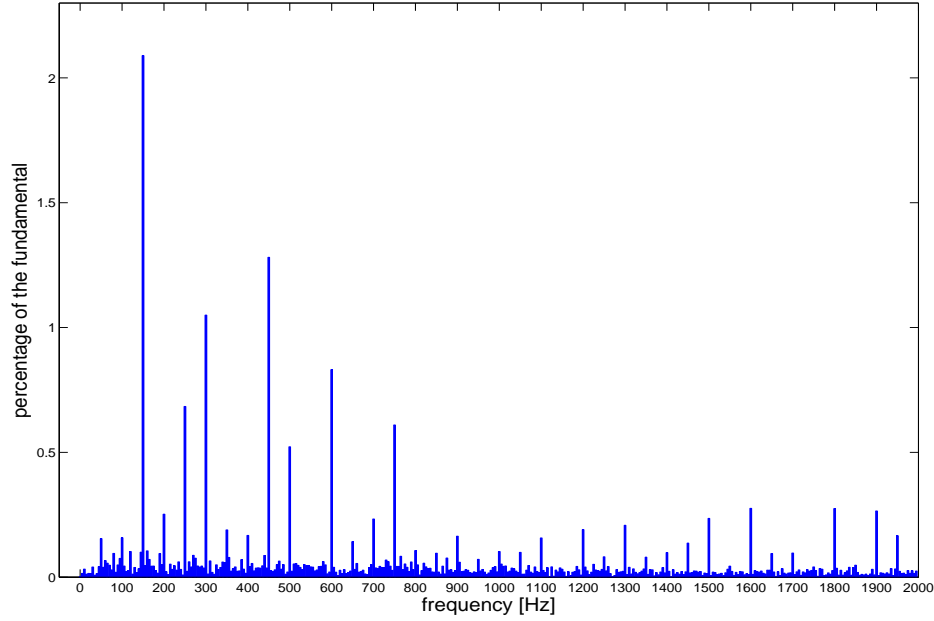
Figure 7.9: FFT of the d component of the PCC voltage on the 5th harmonic frame

From figures 7.9 and 7.10 it can be seen that the 0 Hz component is reduced to nearly 0 V, because of the control action. The components with the highest amplitudes in the spectrum can be seen at the frequencies: 150Hz, 250Hz, 300Hz, 350Hz, 450Hz, 500Hz, 600 Hz, 750Hz, 900 Hz. Some of these components correspond to the harmonics injected by the non-linear load, with an order higher than 7. They are not compensated by the control system and they are not taken into account in the decoupling, so they are bound to be observed in the voltage feedback of the control. Other than the high order harmonics due to the distorting load, also other harmonics can be seen, such as those at 150 Hz and 450 Hz. These components correspond to even harmonics in the stationary reference frame. They are due to the operation of the active filter and its interaction with the system. Particularly, their presence can be explained with unbalances in the experimental system and inaccuracies in the FFT calculation, due to measurement noise. As explained in Section 5.2, each harmonic is seen on a rotating reference frame as a sinusoidal component oscillating at its relative angular speed. The relative angular speed is
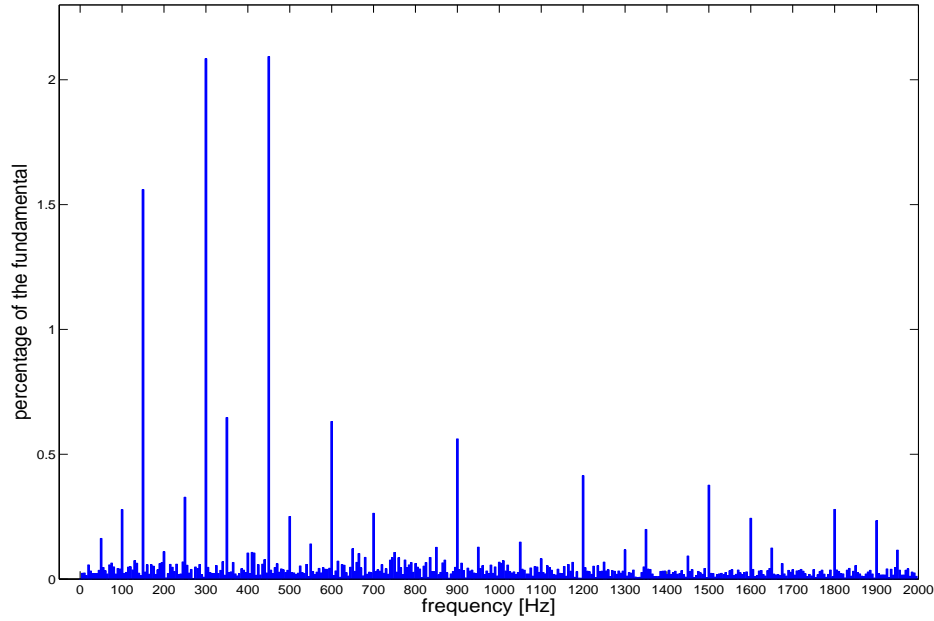
Figure 7.10: FFT of the d component of the PCC voltage on the 7th harmonic frame

given by (5.1). Table 7.1 specifies the absolute harmonic order corresponding to each harmonic component of the spectrum seen in the rotating reference frames. The double numbers in some cells correspond to the two harmonics (one positive sequence and one negative sequence) which are seen with the same relative frequency in that reference frame. In some cells only one harmonic order is reported, as the other harmonic seen with the same relative frequency has been decoupled so it does not contribute to the component in the spectrum. This table is similar to table 6.2, but in this case the compensation of the 11th and 13th harmonic are not carried out, so these two components are not decoupled and are observed on the 5th and 7th harmonic reference frames at the frequencies 300Hz and 900Hz.

Figures 7.11 to 7.16 show the d and q components of the active filter current on the fundamental and harmonic rotating reference frames, during the control steady state. The same considerations made for the voltage oscillations can be made for the current. It can be seen that the reference current and the output current do not match perfectly: the current PI controller has been designed with a low bandwidth, because the aim of the control in this case is not to track the

Reference frame	Harmonics as seen in the spectrum [Hz]										
	150	300	450	600	900	1200	1500	1800	2100	2400	2700
5	2;8	11	4;14	17	13;23	19;29	25;35	31;41	37;47	43;53	49;59
7	4;10	13	2;16	19	11;25	17;31	23;37	29;43	35;49	41;55	47;61
11	8;14	17	2;20	23	29	35	19;41	25;47	31;53	37;59	43;65
13	10;16	19	4;22	25	31	37	17;43	23;49	29;55	35;61	41;67

Table 7.1: Harmonics as seen in the FFT spectrum of the voltage on the different reference frames

high order oscillations of the current, but only the DC component of the reference.

Figures 7.13 and 7.14 can be compared with the corresponding simulation result shown in figure 6.11. In the same way, figures 7.15 and 7.16 can be compared with the result shown in figure 6.13.
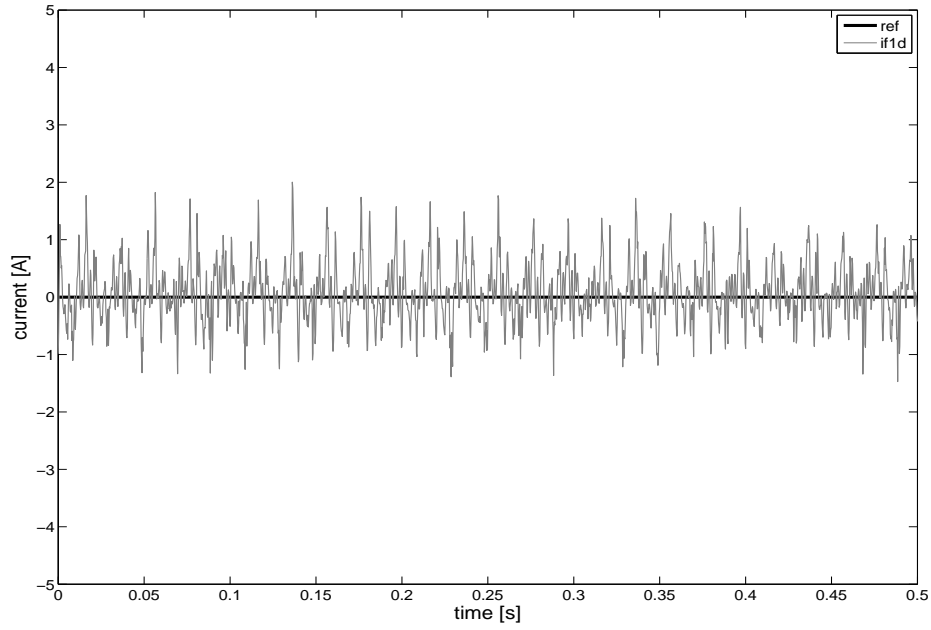
Figure 7.11: d component of the active filter current on the fundamental frame

Figures 7.17 and 7.18 show the PCC line voltage (between phases A and B) before and after the active filter harmonic compensation. These results can be compared to their corresponding ones obtained from the simulation validation, shown in figures 6.18 and 6.19. Comparing figures 6.19 and 7.18 it can be seen that the switching ripple is visible only in the experimental result: this is due to the fact that no anti-aliasing filter has been utilized in the experimental tests, whereas it has been included in the simulation model.

It is not easy to see the action of the voltage harmonic compensation in the time domain: the voltage harmonics are very small compared to the fundamental. In the frequency domain it is possible to evaluate the harmonic reduction obtained with the compensation, as it is shown in figures 7.19 to 7.22. These figures show the FFT spectrum of the PCC line voltage before and after the harmonic compensation.
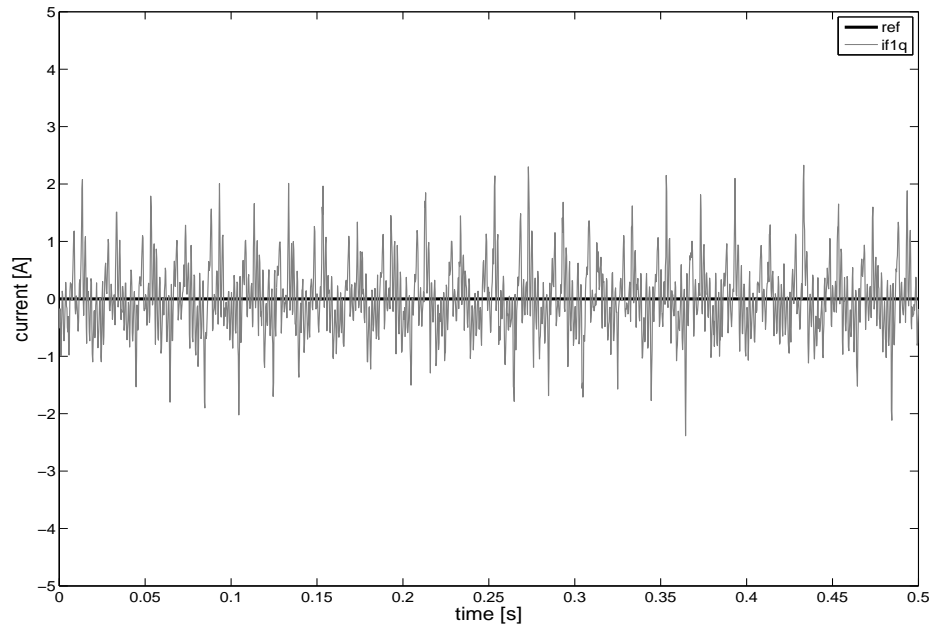
Figure 7.12: q component of the active filter current on the fundamental frame
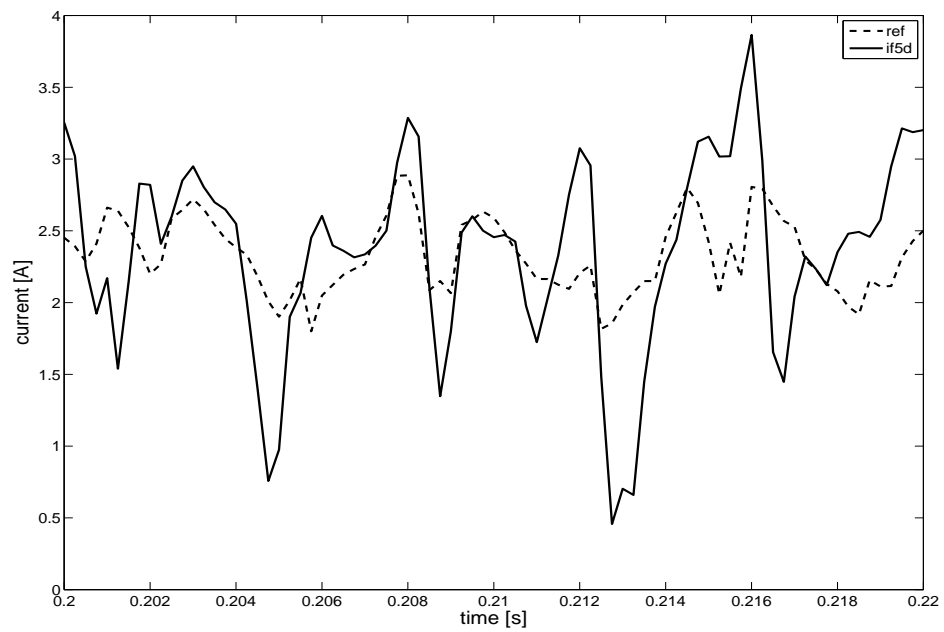
Figure 7.13: d component of the active filter current on the 5th harmonic frame
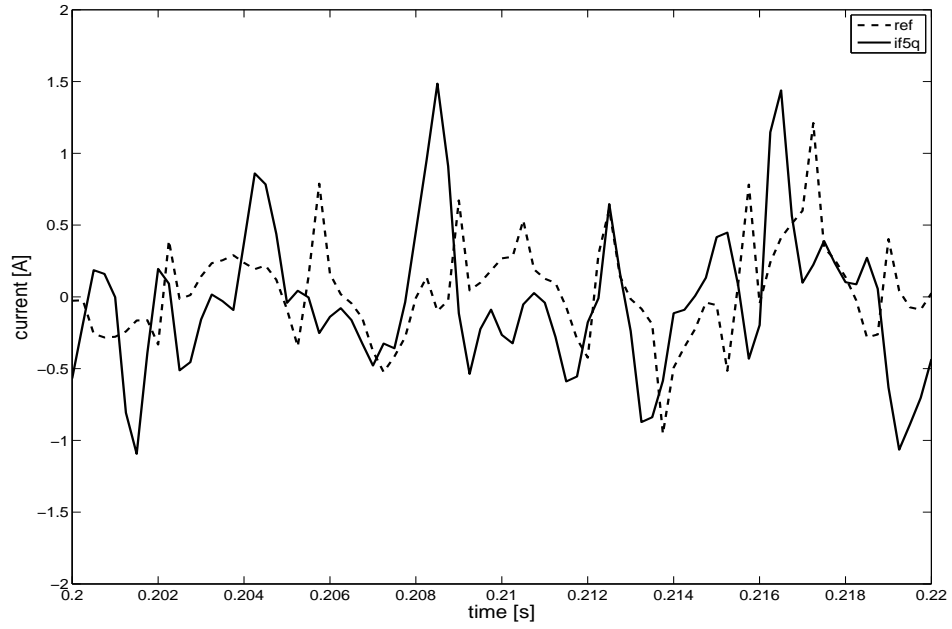
Figure 7.14: q component of the active filter current on the 5th harmonic frame
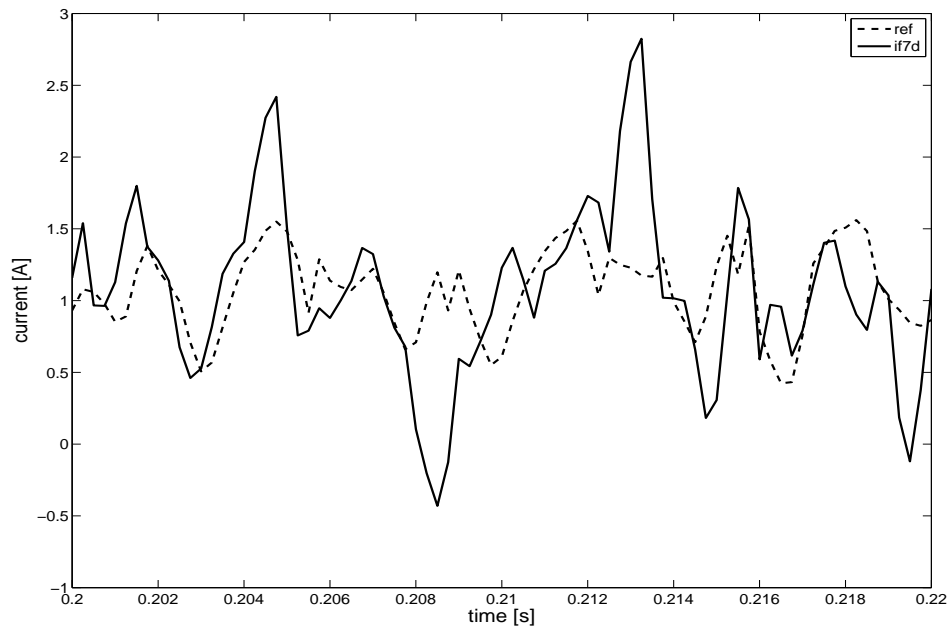
Figure 7.15: d component of the active filter current on the 7th harmonic frame
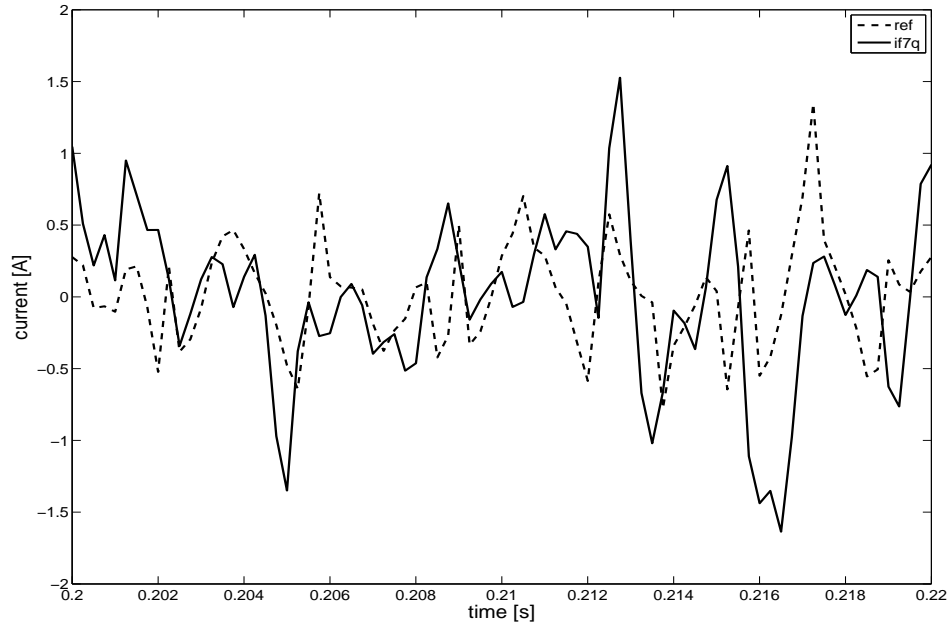
Figure 7.16: q component of the active filter current on the 7th harmonic frame
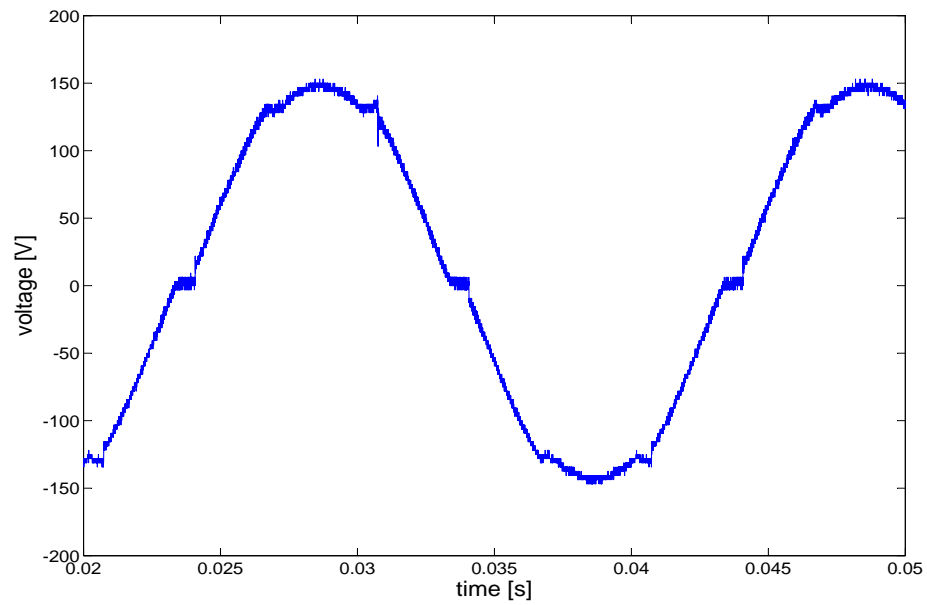
Figure 7.17: PCC three-phase voltage before the active filter compensation
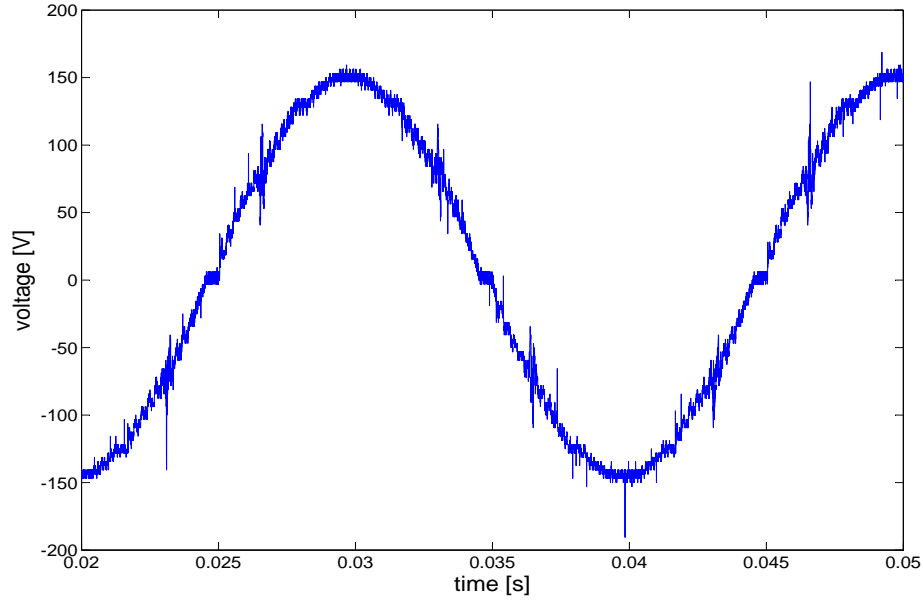
Figure 7.18: PCC three-phase voltage after the active filter compensation

Particularly it is useful to compare figure 7.19 with figure 7.20 and figure 7.21 with figure 7.22 for an expanded view of the harmonics.

In order to compare these experimental results with their corresponding ones obtained in simulation, figures 7.19 and 7.20 can be compared with figures 6.20 and 6.21 respectively. Figures 7.21 and 7.22 can be compared with figures 6.22 and 6.23 respectively. In the comparison, it should be taken into account that in the experimental validation only the 5th and 7th harmonic are compensated, while in the simulation validation also the 11th and 13th harmonic are compensated.

Table 7.2 reports the amplitude values of the 5th and 7th harmonic, comparing them between the case in which the compensation is not active and in which the compensation is active. This table can be compared with table 6.3, which shows the corresponding simulation result. The voltage THD before the compensation is 5.1819 %, while the one achieved after the compensation is 2.5481 %. From table 7.2 a remarkable reduction in amplitude can be noticed, for the 5th and 7th harmonic. However this does not result in such a high reduction of the voltage THD. This is due to the frequency shift of the harmonic distorsion, which is a
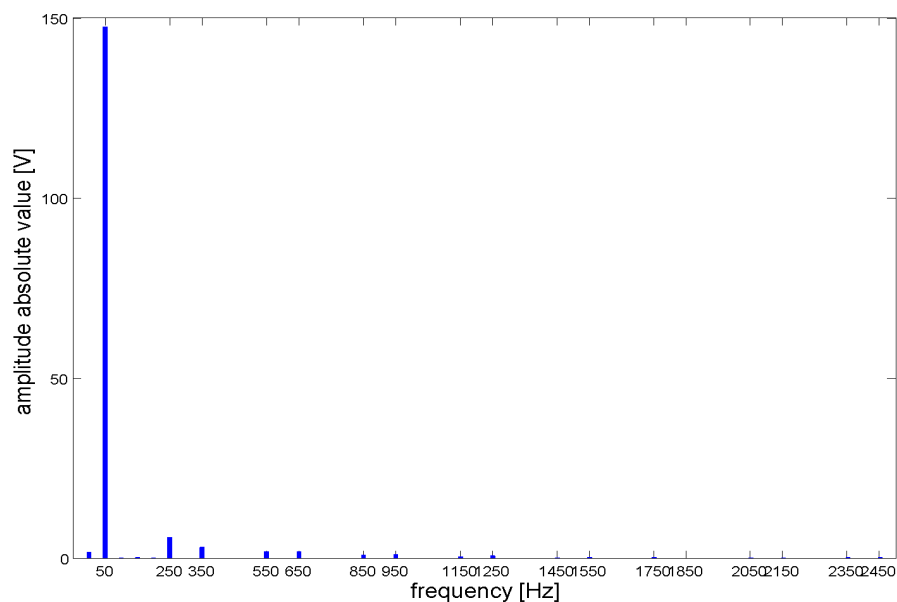
Figure 7.19: FFT spectrum of the PCC voltage before the active filter compensation
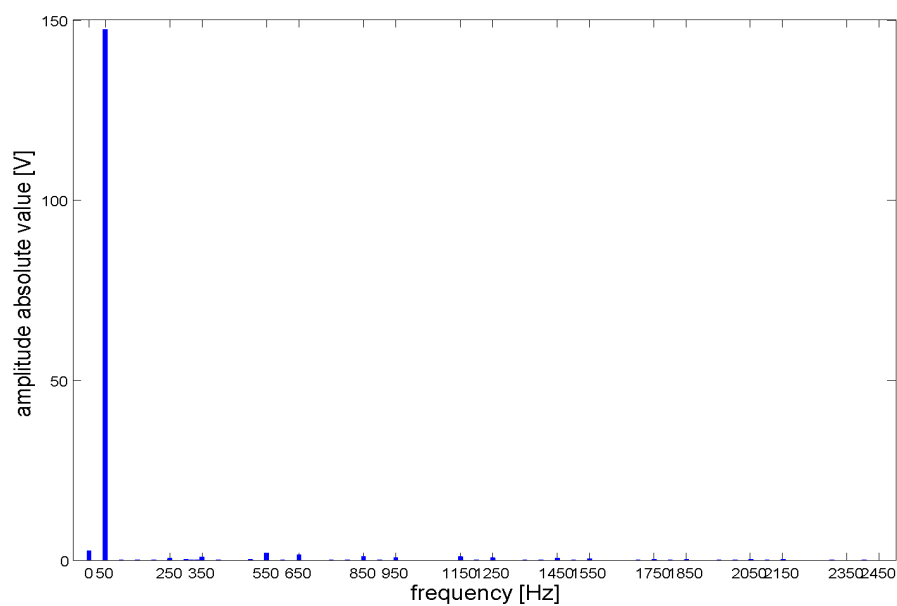
Figure 7.20: FFT spectrum of the PCC voltage after the active filter compensation

Figure 7.21: FFT spectrum of the PCC voltage before the active filter compensation: expanded view of the harmonics

Figure 7.22: FFT spectrum of the PCC voltage after the active filter compensation: expanded view of the harmonics

	Voltage harmonic amplitude				Harmonic
	before compensation		after compensation		reduction
	[V]	[% of fund.]	[V]	[% of fund.]	
5th	5.95	4.03	0.66	0.45	88.90 %
7th	3.18	2.16	1.08	0.73	66.04 %

Table 7.2: Voltage harmonic reduction

drawback of this harmonic compensation. The compensation allows a significant reduction of a certain set of harmonics but as a result it increases the amplitude of higher order harmonics. This can be seen by comparing figure 7.21 with figure 7.22: the harmonic amplitudes at frequencies bigger than 1150Hz increase.

Figures 7.23 and 7.24 show the supply current on the phase A before and after the active filter harmonic compensation. These results can be compared to their corresponding ones obtained from the simulation validation, shown in figures 6.24 and 6.25. The same consideration about the switching ripple, made for the voltage, can be also made for the current.

Figures 7.25 to 7.28 show the FFT spectrum of the supply current in both the aforementioned cases. Particularly it is useful to compare figure 7.25 with figure 7.26 and figure 7.27 with figure 7.28 for an expanded view of the harmonics.

In order to compare these experimental results with their corresponding ones obtained in simulation, figures 7.25 and 7.26 can be compared with figures 6.26 and 6.27 respectively. Figures 7.27 and 7.28 can be compared with figures 6.28 and 6.29 respectively. In the comparison, it should be taken into account that in the experimental validation only the 5th and 7th harmonic are compensated, while in the simulation validation also the 11th and 13th harmonic are compensated.

Table 7.3 reports the amplitude values of the 5th and 7th current harmonic, comparing them between the case in which the compensation is not active and in which the compensation is active. This table can be compared with table 6.4, which
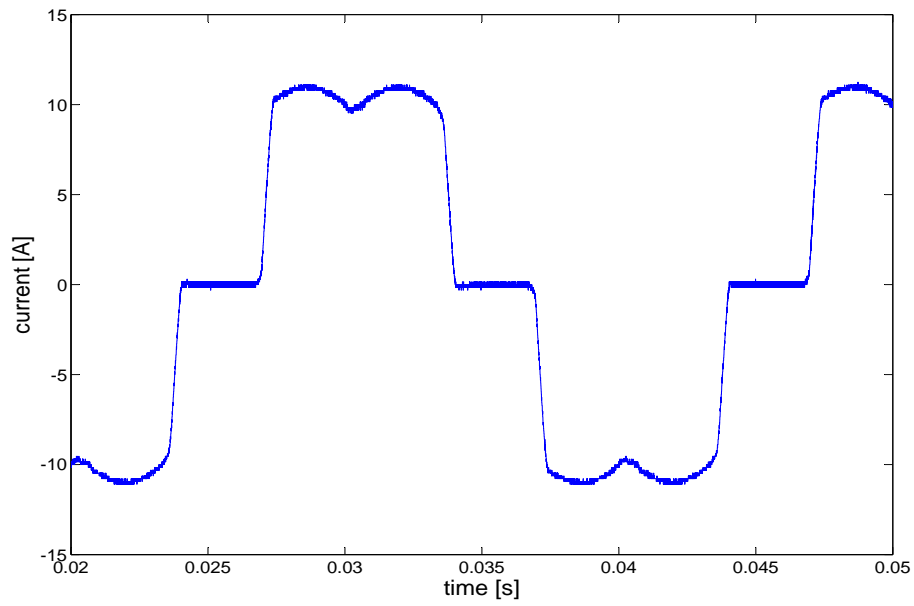
Figure 7.23: Three-phase supply current before the active filter compensation
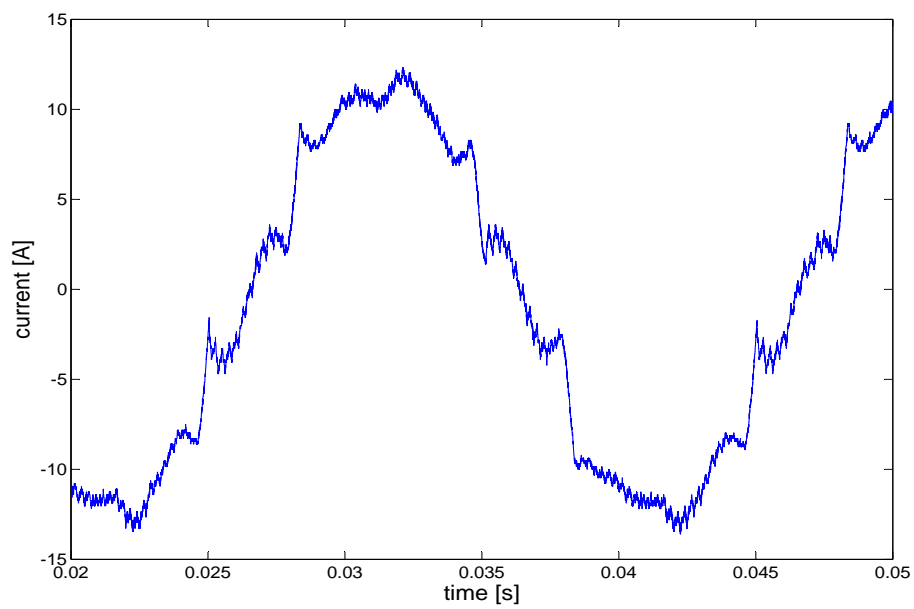
Figure 7.24: Three-phase supply current after the active filter compensation
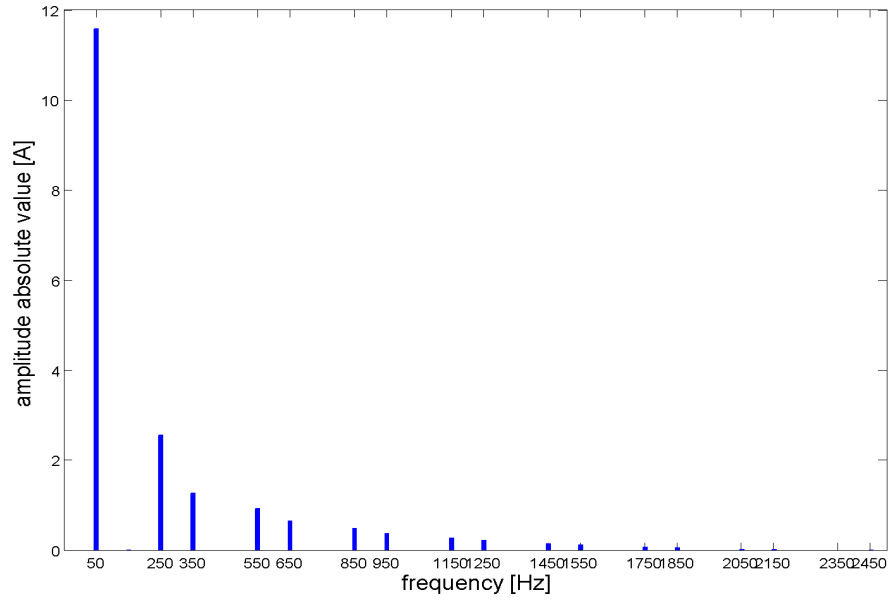
Figure 7.25: FFT spectrum of the supply current before the active filter compensation
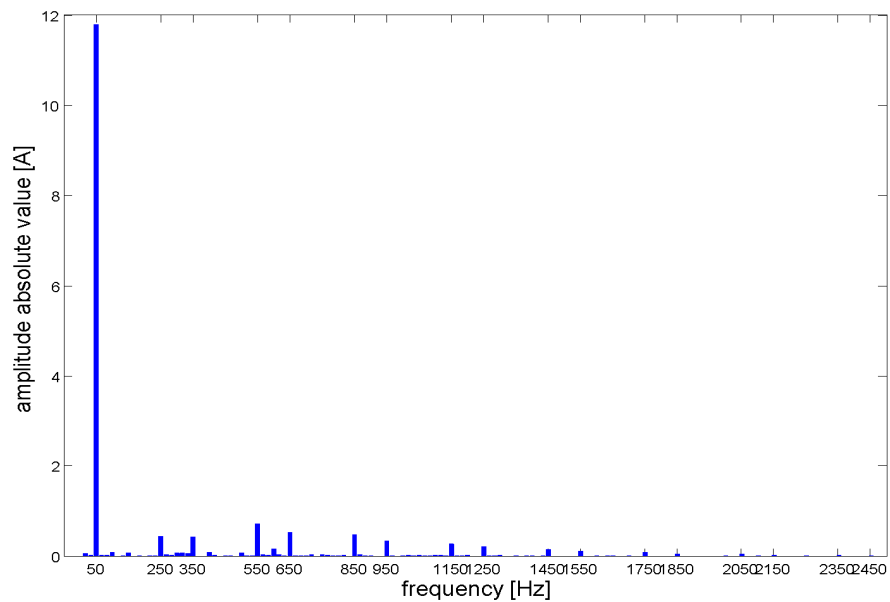
Figure 7.26: FFT spectrum of the supply current after the active filter compensation
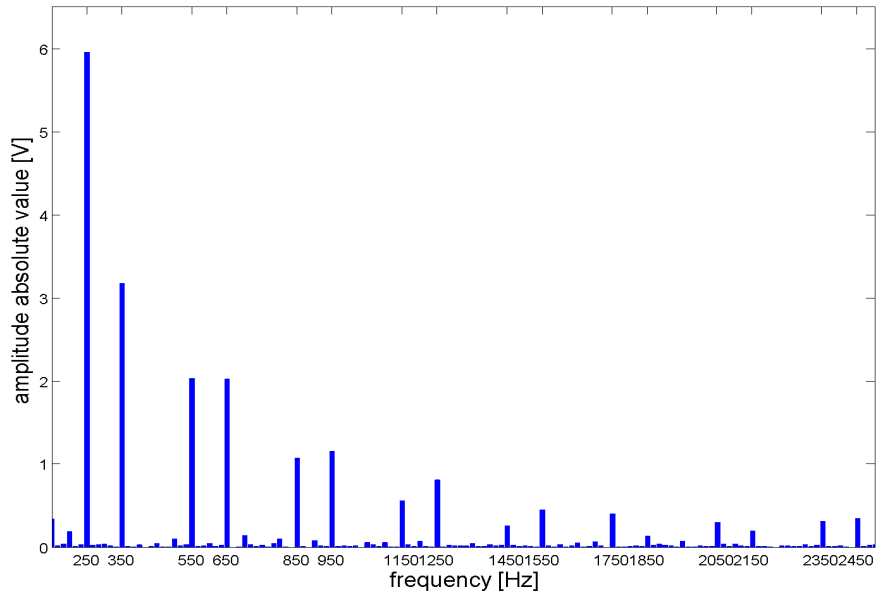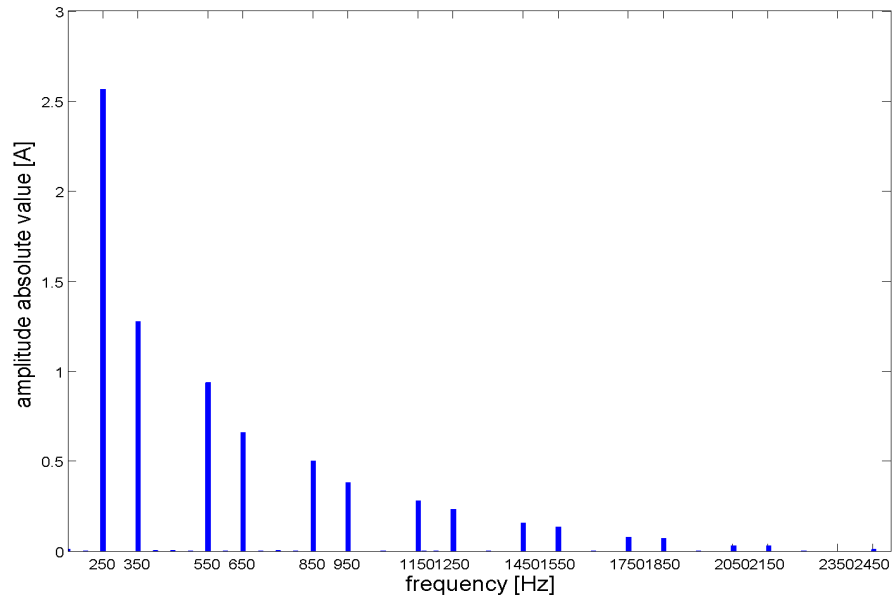
Figure 7.27: FFT spectrum of the supply current before the active filter compensation: expanded view of the harmonics
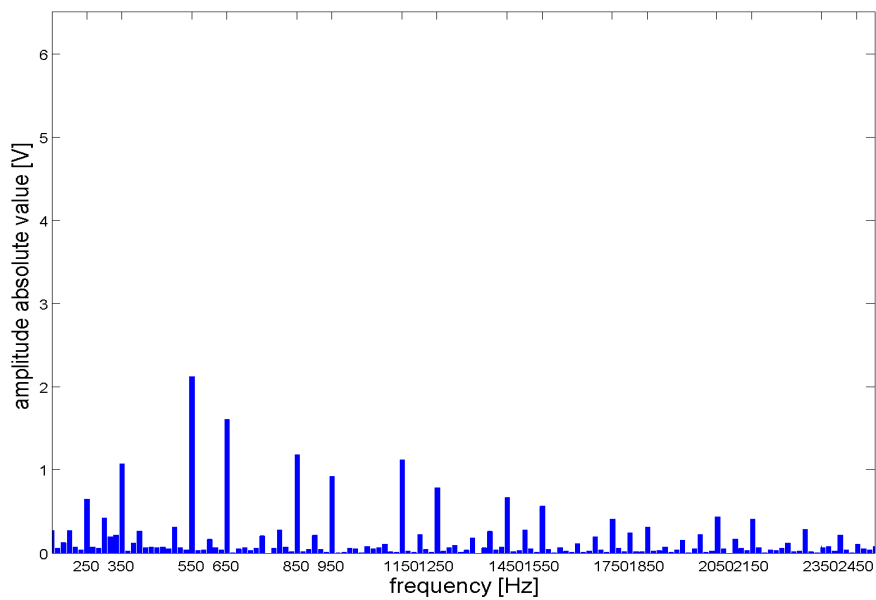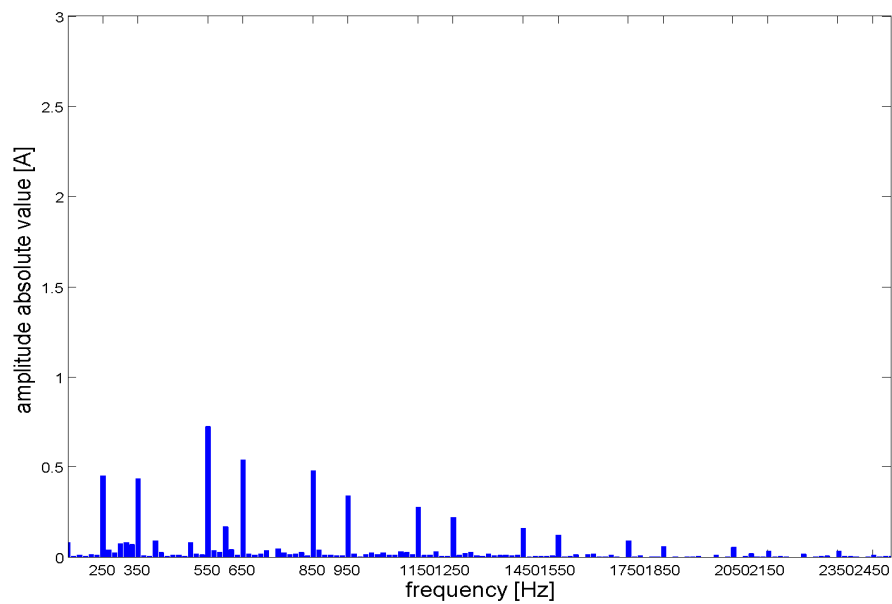

Figure 7.28: FFT spectrum of the supply current after the active filter compensation: expanded view of the harmonics

	Current harmonic amplitude				Harmonic
	before compensation		after compensation		reduction
	[A]	[% of fund.]	[A]	[% of fund.]	
5th	2.56	22.16	0.45	3.90	82.42 %
7th	1.28	11.08	0.45	3.90	64.84 %

Table 7.3: Current harmonic reduction

shows the corresponding simulation result. The current THD before the compensation is 27.4179 %, while the one achieved after the compensation is 11.3931 %.

Figures 7.29 and 7.30 show the oscilloscope screen capture during the experimental tests, before and after enabling the active filter harmonic compensation respectively. In these figures, the supply current, the PCC voltage and the active filter output voltage are represented and indicated. The effectiveness of the harmonic compensation can be seen comparing the supply current and the PCC voltage in the two figures.

7.4 Summary

This chapter has presented the experimental results that validate the multiple reference frames voltage detection control technique for shunt active power filters, presented in Chapter 5. The experimental tests have been carried out using a laboratory built prototype of an active filter, connected in parallel to a three-phase power supply and a distorting load. The experimental results show that the active filter, operating using the proposed control technique, effectively compensates for the 5th and 7th harmonic injected by the non-linear load. Furthermore the experimental results show good adherence with the simulation results presented in Chapter 6.
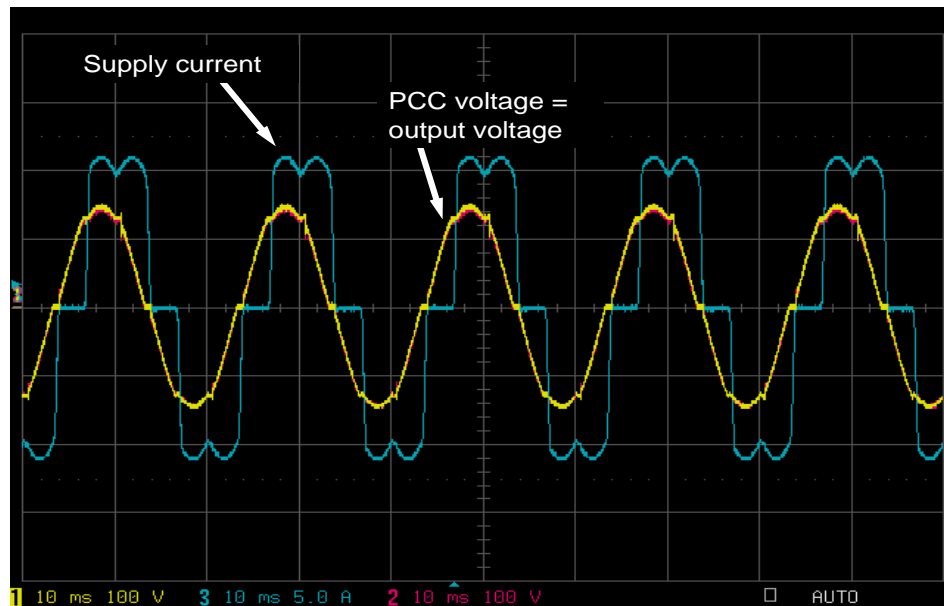
Figure 7.29: Oscilloscope capture before the harmonic compensation
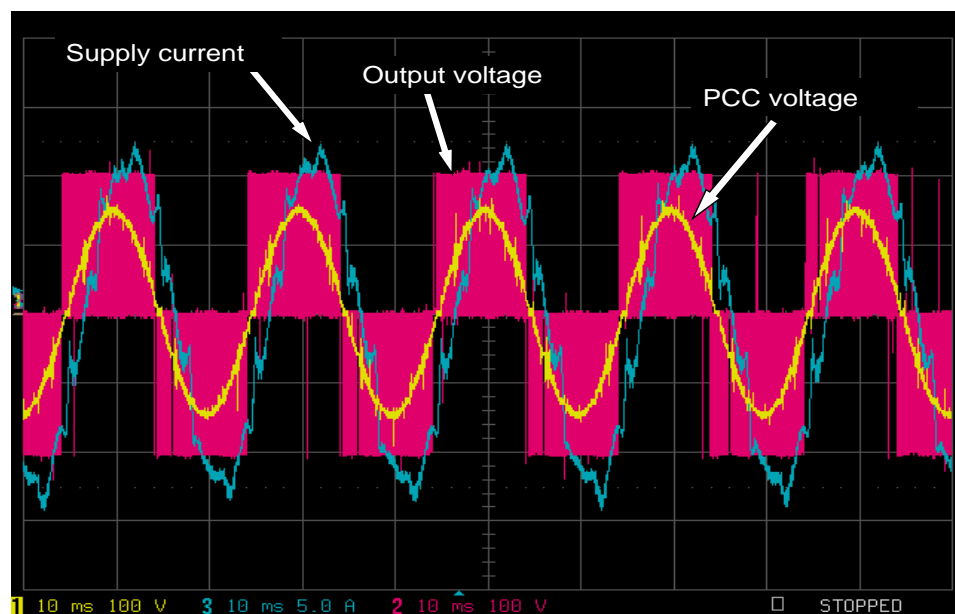
Figure 7.30: Oscilloscope capture after the harmonic compensation

Chapter 8

Conclusions

In the work presented in this thesis, a novel algorithm for the detection of the fundamental frequency and harmonic components of a distorted signal and a novel control technique for shunt active power filters have been proposed. The application for which this work has been developed is the More Electric Aircraft.

In the future civil aircraft systems, the increasing use of electric power in place of conventional sources of power, like mechanical, hydraulic and pneumatic, will bring major changes to the aircraft power system. A more complex topology of the network, a bigger amount of generated and demanded power and an increasing use of power electronic devices on board can give rise to significant stability and power quality problems.

The shunt active power filter is an effective solution for the harmonic elimination and the power quality enhancement in the electrical system. This allows the system to operate within the limits recommended by the aircraft regulations.

The biggest challenge encountered when designing and controlling an active filter in the More Electric Aircraft power system is related to the high values of fundamental frequency, variable between 360 and 900Hz. An accurate algorithm for the real-time estimation of the reference signal and a high bandwidth control system are needed in order for the active filer to inject the right amount of har-

monic current into the Point of Common Coupling. At these values of frequency, the harmonic components occur at high frequencies compared to the conventional 50/60Hz terrestrial systems.

As explained in the Introduction of this thesis, the main goals of the work were: to implement an accurate real-time estimation technique for the generation of the reference signal for the active filter control and to implement an effective control technique, suitable for this kind of application.

The first goal has been achieved by means of a real-time Discrete Fourier Transform based algorithm which estimates the fundamental frequency and phase angle and the harmonic components of a distorted time-varying signal. The second goal has been achieved by implementing a multiple reference frame voltage detection control technique.

The DFT-based detection technique proved effective both in simulation and experimentally for the real-time estimation of the fundamental and harmonic components of a distorted signal. This technique detects the fundamental frequency using a closed loop system, where the estimation error is minimized by a Proportional Integral controller. The fundamental and harmonic components are identified by means of real-time implementation of the Discrete Fourier Transform, where the observation window of the signal is updated at each step. From the validation of the method, a good accordance between the simulation and experimental results has been demonstrated. The results showed that the proposed technique is effective for the harmonic identification of a distorted signal with variable frequency, hence it is a viable solution for the detection of the reference signal for the control of an active shunt filter in the aircraft power system.

The DFT-based technique has been compared with the standard Phase-Locked Loop (PLL) in order to evaluate its performance. The main advantage of the DFT method lies in the possibility to apply the algorithm to a signal varying in a broad range of frequencies and amplitudes without having to re-tune the parameters. On the other hand, the PLL needs an accurate tuning of the PI controller gains, depending on the characteristics of the signal and the required accuracy and speed

of the estimation response. The DFT method also proved more effective than the PLL in cases where noise and distortion affect the input signal. Furthermore, it showed a better performance in tracking the variable fundamental frequency when it presents a fast variation. The comparison has been carried out both in simulation and experimentally, and a good accordance between the simulation and experimental results has been shown in the thesis.

The multiple reference frame voltage detection technique proposed in this work is based on the implementation of several rotating reference frames, one for each harmonic component to be compensated. The reference frames are decoupled from one another by means of equations which are listed in the thesis. The control technique structure consists of as many control loops as the number of the harmonics to be compensated. Each harmonic appears as a DC quantity in the reference frame it is synchronous with, hence a simple low bandwidth PI control can track the reference with zero steady state error. The reference for the control is derived from the measurement of the voltage at the PCC, which is distorted due to the voltage drop of the load harmonics across the supply impedance. Two control loops, an external one for the voltage and an internal one for the active filter current, are implemented. The reference for the voltage loop is set to zero on each axis of every harmonic reference frame, in order to minimize the harmonic content of the PCC voltage, hence of the supply current. The control technique has been implemented in combination with the DFT real-time detection method mentioned above, as an accurate knowledge of the fundamental and harmonic components of the PCC voltage and the active filter current are needed for the transformation into the multiple reference frames and the decoupling between each of them. Simulation and experimental results have been presented, with good adherence between the two. The control method proved successful for the compensation of the harmonics injected by the distorting load and a significant reduction of the voltage and current THD was achieved.

8.1 Further Work

Future developments of the work presented here concern the improvement of the proposed techniques and the validation in different conditions.

The main limitation of the harmonic detection DFT method regards the computational capability of the digital signal processors utilized for its digital implementation. The computational capability of DSPs is constantly increasing and in the future a more powerful processor will be able to perform the real-time estimation in a shorter time, hence with higher sampling frequency. Therefore, an idea for the future development of this work is to implement it on a faster and more powerful DSP, in order to reduce the computational time and increase the estimation accuracy.

With regard to the voltage detection technique, the same considerations mentioned above can be made. In the work presented in this thesis, the simulation and experimental validation has been shown for a fundamental frequency equal to 50Hz, because the computational limitations of the DSP did not allow to work at a higher sampling frequency. By using a more powerful DSP the control method can be easily implemented at a higher sampling frequency, thus allowing the algorithm to process the high frequency harmonics typical of the aircraft frequency-wild power system.

In simulation, the control method has been validated for the compensation of the 5th, 7th, 11th and 13th harmonic, while only the 5th and 7th harmonic have been compensated in the experimental implementation. With a more powerful DSP the compensation can be extended to a higher number of harmonics, thus improving the THD of the voltage and the current, in order to comply with the power quality standards recommended by the regulations for the More Electric Aircraft power systems.

An interesting aspect that can be investigated in the future concerns the characteristics of the PCC voltage. In the work presented in this thesis it has been assumed that the harmonic content of the PCC voltage is only due to the distort-

ing loads connected in parallel with the active shunt filter. An idea for a future development of the control technique is to test it when the distortion also comes from the power supply and other devices connected to the PCC, provided that the power level of the active filter is high enough to allow for an effective compensation of the harmonic distortion.

The interaction between the active filter and the system it is connected to can also be the subject for future investigation. Particularly, it would be interesting to analyse the harmonic distortion introduced by the active filter and caused by the interaction with the system.

Finally, a coordinated control of several active filters in different points of the distribution bus could be implemented. In this way, the power quality of the network can be significantly enhanced, and coordinated energy storage and high reliability can be provided.

References

[1] Maldonado M A, Shah N M, Cleek K J, and Korba J, "Power Management and Distribution System for a More-Electric Aircraft (MADMEL)," *IEEE AES Systems Magazine*, 1999.

[2] Jones R I, "The More Electric Aircraft: the past and the future?," *Electrical Machines and Systems for the More Electric Aircraft (Ref. No. 1999/180), IEE Colloquium on*, pp. 1/1 – 1/4, 1999.

[3] Quigley R E J, "More Electric Aircraft," *Applied Power Electronics Conference and Exposition, 1993. APEC '93. Conference Proceedings 1993*, pp. 906 – 911, 1993.

[4] Rosero J A, Ortega J A, Aldabas E, and Romeral L, "Moving towards a more electric aircraft," *Aerospace and Electronic Systems Magazine, IEEE*, vol. 22, pp. 3 – 9, Mar 2007.

[5] Wheeler P, "The More Electric Aircraft. Why Aerospace Needs Power Electronics," *Presentation. University of Nottingham.*

[6] Emadi A and Ehsani M, "Aircraft power systems: technology, state of the art and future trends," *Aerospace and Electronic Systems Magazine, IEEE*, vol. 15, pp. 28 – 32, Jan 2000.

[7] Rosswurm M A, "Design considerations of dc-link aircraft generation systems," *Proceedings of Aerospace Congress Expo, Anaheim, CA, 1981*, pp. 1 – 15, 1981.

[8] Yorksie D S and Hyvarinen W E, "The effects of critical design parameters on the selection of a VSCF system," *Proceedings of Aerospace Congress Expo, Anaheim, CA, 1981*, pp. 43 – 50, 1981.

[9] Moir I and Seabridge A, "Aircraft systems: mechanical, electrical and avionics subsystem integration," *London: Professional Engineering*, 2001.

[10] Pallett E H J, "Aircraft electrical systems," *London: Addison Wesley Longman Limited*, 1998.

[11] "Environmental conditions and test procedures for airborne equipment," *DO-160D*.

[12] "Characteristics of aircraft electrical systems," *ISO 1540:2006*, 2006.

[13] Sun J, Chen M, and Karimi K J, "Aircraft Power System Harmonics Involving Single-Phase PFC Converters," *IEEE Transactions on Aerospace and Electronic Systems*, vol. 44, pp. 217 – 226, Jan 2008.

[14] Athalye P, Maksimovic D, and Erickson R, "High-performance Front-End Converter for Avionics Applications," *IEEE Transactions on Aerospace and Electronic Systems*, vol. 39, pp. 462 – 470, Apr 2003.

[15] Eid A, Abdel-Salam M, El-Hishky H, and El-Mohandes T, "Active power filters for harmonic cancellation in conventional and advanced aircraft electric power systems," *Electric power system research, Elsevier*, vol. 79, pp. 81 – 88, 2009.

[16] Eid A, Abdel-Salam M, El-Hishky H, and El-Mohandes T, "On Power Quality of Variable-Speed Constant-Frequency Aircraft Electric Power Systems," *IEEE Transactions on Power Delivery*, vol. 25, pp. 55 – 65, Jan 2010.

[17] Hostetter G H, "Recursive discrete Fourier transformation," *IEEE Transactions on Acoustics, Speech and Signal Processing*, vol. 28, pp. 184 – 190, Apr 1980.

[18] Peceli G, "A common structure for Recursive Discrete Transforms," *IEEE Transactions on Circuits and Systems*, vol. 33, pp. 184 – 190, Oct 1986.

[19] Peceli G, "Resonator-based digital filters," *IEEE Transactions on Circuits and Systems*, vol. 33, pp. 184 – 190, Jan 1989.

[20] Padmanabhan M and Martin K, "Resonator-based filter-banks for frequency-domain applications," *IEEE Transactions on Circuits and Systems*, vol. 38, pp. 1145 – 1159, Oct 1991.

[21] Dolen M and Lorenz R D, "An industrially useful means for decomposition and differentiation of harmonic components of periodic waveforms," *Applied Power Electronics Conference and Exposition, 1993. APEC '93. Conference Proceedings 1993*, pp. 906 – 911, Mar 1993.

[22] Sachdev M S and Giray M M, "A least error squares technique for determining power system frequency," *IEEE Transactions on Power Apparatus and Systems*, vol. PAS-104, pp. 437 – 444, Feb 1985.

[23] Terzija V, Djuric M, and Kovacevic B, "A new self-tuning algorithm for the frequency estimation of distorted signals," *IEEE Transactions on Power Delivery*, vol. 10, pp. 1779 – 1785, Oct 1995.

[24] Simon G, Pintelon R, Sujbert L, and Schoukens J, "An efficient nonlinear least square multisine fitting algorithm," *IEEE Transactions on Instrumentation and Measurements*, vol. 51, pp. 750 – 755, Aug 2002.

[25] Chattopadhyay B, Ivanov C, and Sachdev M S, "A new frequency measurement algorithm in the presence of harmonics using instantaneous phasor quantities," *Canadian Conference on Electrical and Computer Engineering*, vol. 1, pp. 130 – 133, May 1996.

[26] Beides H M and Heydt G T, "Dynamic state estimation of power system harmonics using Kalman filter methodology," *IEEE Transactions on Power Delivery*, vol. 6, pp. 1663 – 1670, Oct 1991.

[27] Dash P K, Pradhan A K, and Panda G, "Frequency estimation of distorted power system signals using extended complex Kalman filter," *IEEE Transactions on Power Delivery*, vol. 14, pp. 761 – 766, Jul 1999.

[28] Barros J and Perez E, "An adaptive method for determining the reference compensating current in single-phase shunt active power filters," *IEEE Transactions on Power Delivery*, vol. 18, pp. 1578 – 1580, Oct 2003.

[29] Cupertino F, Marinelli M, and Salvatore L, "EKF and Wavelet-based algorithms applied to harmonic detection for active shunt filters," *11th International Conference on Harmonics and Quality of Power*.

[30] Macias J A R and Exposito A G, "Self tuning of Kalman filters for harmonic computation," *IEEE Transactions on Power Delivery*, vol. 21, pp. 501 – 503, Jan 2006.

[31] Pigazo A and Moreno V M, "3phi-3w signal model for power system harmonics and unbalance identification using Kalman filtering," *IEEE Transactions on Power Delivery*, vol. 23, pp. 1260 – 1261, Apr 2008.

[32] Rolim L G B, da Costa D R, and Aredes M, "Analysis and software implementation of a robust synchronizing PLL circuit based on the pq theory," *IEEE Transactions on Industrial Electronics*, vol. 53, pp. 1919 – 1926, Dec 2006.

[33] Karimi H, Karimi-Garthemani M, and Iravani M R, "Estimation of frequency and its rate of change for applications in power systems," *IEEE Transactions on Power Delivery*, vol. 19, pp. 472 – 480, Apr 2004.

[34] Comanescu M and Xu L, "An improved flux observer based on PLL frequency estimator for sensorless vector control of induction motors," *IEEE Transactions on Industrial Electronics*, vol. 53, pp. 50 – 56, Feb 2006.

[35] Cataliotti A, Cosentino V, and Nuccio S, "A Phase-Locked Loop for the Synchronization of Power Quality Instruments in the Presence of Stationary and Transient Disturbances," *IEEE Transactions on Instrumentation and Measurement*, vol. 56, pp. 2232 – 2239, Dec 2007.

[36] Rodriguez P, Pou J, Bergas J, Candela J I, Burgos R P, and Boroyevich D, "Decoupled Double Synchronous Reference Frame PLL for Power Converters Control," *IEEE Transactions on Power Electronics*, vol. 22, pp. 584 – 592, Mar 2007.

[37] Santos Filho R M, Seixas P F, Cortizo P C, Torres L A B, and Souza A F, "Comparison of three single-phase PLL algorithms for UPS applications," *IEEE Transactions on Industrial Electronics*, vol. 55, pp. 2923 – 2932, Aug 2008.

[38] Macedo R A, da Silva D, Coury D V, and de Carvalho A C P L F, "A new technique based on genetic algorithms for tracking of power system harmonic," *IEEE Proceedings of the VII Brazilian Symposium on Neural Networks*, pp. 7 – 12.

[39] Bettayeb M and Uvais Q, "A hybrid least squares-GA-based algorithm for harmonic estimation," *IEEE Transactions on Power Delivery*, vol. 18, pp. 377 – 382, Apr 2003.

[40] Bertoluzzo M, Buja G S, Castellan S, and Fiorentin P, "Neural network technique for the joint time-frequency analysis of distorted signal," *IEEE Transactions on Industrial Electronics*, vol. 50, pp. 1109 – 1115, Dec 2003.

[41] Liu Y Z, "A Wavelet based model for on-line tracking of power systems harmonics using Kalman filtering," *IEEE Power Engineering Society Summer Meeting*, vol. 2, pp. 1237 – 1242, Jul 2001.

[42] Ming-Tang Chen and Sakis Metiopoulos A P, "A hybrid digital algorithm for harmonic and flicker measurements," *IEEE Power Engineering Society Winter Meeting*, vol. 2, pp. 1488 – 1493, Aug 2002.

[43] Hyosung Kim, Blaabjerg F, and Bak-Jensen B, "Spectral analysis of instantaneous powers in single-phase and three-phase systems with use of p-q-r theory," *IEEE Transactions on Power Electronics*, vol. 17, pp. 711 – 720, Sep 2002.

[44] Andria G, Dell'Aquila A, and Salvatore L, "Analysis of distorted unbalanced waveforms in inverter drives," *IEEE Transactions on Power Electronics*, vol. 4, pp. 298 – 310, Apr 1989.

[45] Lavopa E, Zanchetta P, Sumner M, and Cupertino F, "Real-Time Estimation of Fundamental Frequency and Harmonics for Active Shunt Power Filters in

Aircraft Electrical Systems," *IEEE Transactions on Industrial Electronics*, vol. 56, pp. 2875 – 2884, Aug 2009.

[46] Olkkonen H, "Computation of running discrete Hartley transform coefficients," *IEEE Transactions on Signal Processing*, vol. 25, pp. 107 – 110, Oct 1991.

[47] Chroma, "Programmable AC Source 61705," *User's Manual*, 2007.

[48] Texas Instruments, "TMS320C6713B Floating-Point Digital Signal Processor," *Datasheet*, 2006.

[49] Actel, "Actel ProAsic A500K050 Package PQ208," *Datasheet*.

[50] Linear Technology, "LTC 1400 Complete SO-8, 12-Bit, 400ksps ADC with Shutdown," *Datasheet*, 2006.

[51] LEM, "Voltage Transducer LV 25-P," *Datasheet*.

[52] D'Antona G and Ferrero A, "Digital Signal Processing for Measurement Systems. Theory and Applications," *Springer*, 2006.

[53] Hsieh G C and Hung J C, "Phase-Locked Loop Techniques. A Survey," *IEEE Transactions on Industrial Electronics*, vol. 43, pp. 609 – 615, Dec 1996.

[54] Egan W F, "Phase-Lock Basics, 2nd edition," *Wiley-IEEE Press*, 2007.

[55] Gardner F, "Phaselock Techniques, 2nd edition," *NY Wiley & Sons*, 1979.

[56] Kaura V and Blasko V, "Operation of a phase locked loop system under distorted utility conditions," *IEEE Transactions on Industry Applications*, vol. 33, pp. 58 – 63, Jan 1997.

[57] Pottker F and Barbi I, "Power Factor Correction of Non-linear Loads Employing a Single Phase Active Power Filter," *Conference Recording of IEEE Power Electronics Specialists Conference*, pp. 107 – 109, 1997.

[58] Bhattacharya S, Frank T M, Divan D M, and Banerjee B, "Active Filter System Implementation," *IEEE Industry Applications Magazine*, vol. 4, pp. 47 – 63, Sep-Oct 1998.

[59] Verdelho P and Marques G D, "An Active Power Filter and Unbalanced Current Compensator," *IEEE Transactions on Industrial Electronics*, vol. 44, pp. 321 – 328, Jun 1997.

[60] Lee S-Y, Chae Y-M, Cho J-S, Choe G-H, Mok H S, and Jang D H, "A New Control Strategy for Instantaneous Voltage Compensator using Three-Phase PWM Inverter," *Conference Recording of IEEE Power Electronics Specialists Conference*, pp. 248 – 254, 1998.

[61] Cheng P T, Bhattacharya S, and Divan D M, "Control of Square-Wave Inverters in High Power Hybrid Active Filter Systems," *IEEE Transactions on Industrial Electronics*, vol. 34, pp. 459 – 472, May-Jun 1998.

[62] Buso S, Malesani L, Mattavelli P, and Veronese R, "Design and Fully Digital Control of Parallel Active Filters for Thyristor Rectifiers to Comply with IEC-1000-3-2 Standards," *IEEE Transactions on Industry Applications*, vol. 34, pp. 508 – 517, May-Jun 1998.

[63] Sato Y, Nagayama S, Chigira H, and Kataoka T, "An Adaptive Control Strategy for Active Power Filters with Voltage Detection," *13th IAS Annual Meeting, Industry Application Conference*, vol. 2, pp. 1356 – 1363, 1998.

[64] Sato Y, Nagayama S, Chigira H, and Kataoka T, "A New Control Method for Active Power Filters with Voltage Detection," *Proceedings of Power Conversion Conference*, vol. 1, pp. 169 – 174, 1997.

[65] Akagi H, "Control Strategy and Site Selection of a Shunt Active Filter for Damping of Harmonic Propagation in Power Distribution Systems," *IEEE Transactions on Power Delivery*, vol. 12, pp. 354 – 362, Jan 1997.

[66] Malesani L, Mattavelli P, and Buso S, "On the Applications of Active Filters to Generic Loads," *Proceedings of 8th International Conference on Harmonics and Quality of Power*, vol. 1, pp. 310 – 319, 1998.

[67] Brogan P and Yacamini R, "An Active Filter Based on Voltage Feedback," *Proceedings of 7th International Conference on Power Electronics and Variable Speed Drives*, pp. 1 – 2, 1998.

[68] Brogan P and Yacamini R, "Stability of an Active Filter Based on Voltage Feedback," *Proceedings of 8th European Conference on Power Electronics Applications*, 1999.

[69] Brogan P and Yacamini R, "Stability of Selective Harmonic Active Filters," *Proceedings of 8th International Conference on Power Electronics and Variable Speed Drives*, pp. 416 – 421, 2000.

[70] Ladisa C, Zanchetta P, and Sumner M, "Improved Voltage Harmonic Control for Shunt Active Power Filters using Multiple Reference Frames," *IEEE International Symposium on Industrial Electronics, ISIE 2007*, pp. 844 – 849, 2007.

[71] D. Butt, *An Investigation of Harmonic Correction Techniques using Active Filtering.* PhD thesis, University of Nottingham, England, 1999.

[72] P. Srithorn, *Control of a Statcom with Supercapacitor Energy Storage.* PhD thesis, University of Nottingham, England, 2009.

[73] MathWorks, "Simulink SimPowerSystems 7.0 R2007b," *User's guide*, 2007.

[74] Dynex, "DIM200WHS12-A000 Half Bridge IGBT Module," *Datasheet*, 2004.

[75] International Rectifier, "IRKD101-14 Center-Tapped Silicon Diode Doubler," *Datasheet*.

[76] LEM, "Current Transducer LA 55-P," *Datasheet*.

Appendix A

Papers Published

Cupertino F, Lavopa E, Zanchetta P, Sumner M, Salvatore L, "Running DFT-based PLL Algorithm for Frequency, Phase and Amplitude Tracking in Aircraft Electrical Systems",*IEEE Transactions on Industrial Electronics, Apr. 2010, Digital Object Identifier : 10.1109/TIE.2010.2048293.*

Lavopa E, Zanchetta P, Sumner M, Bolognesi P, "Improved voltage harmonic control for sensorless shunt active power filters",*International Symposium on Power Electronics Electrical Drives Automation and Motion (SPEEDAM), 2010, Pisa*, June 2010.

Cupertino F, Salvatore L, Lavopa E, Sumner M, Zanchetta P, "A DFT-based phase locked loop for phase and amplitude tracking in aircraft electrical systems",*Electric Machines and Drives Conference 2009. IEMDC 2009, IEEE International. Miami, FL*, May 2009.

Lavopa E, Zanchetta P, Sumner M, Cupertino F, "Real-Time Estimation of Fundamental Frequency and Harmonics for Active Shunt Power Filters in Aircraft Electrical Systems",*IEEE Transactions on Industrial Electronics, vol. 56, pp. 2875-2884, Aug. 2009.*

Lavopa E, Sumner M, Zanchetta P, Ladisa C, Cupertino F, "Real-time estimation of fundamental frequency and harmonics for active power filters applications in

aircraft electrical systems",*European Conference on Power Electronics and Applications, EPE 2007, Aalborg*, September 2007.

Appendix B

Decoupling

In Section 5.3 the decoupling terms for the 5th, 7th, 11th and 13th harmonic on the fundamental reference frame are listed.

In this appendix, all the decoupling terms for the fundamental, the 5th, 7th, 11th and 13th harmonic are listed, for each harmonic reference frame.

Reference frame rotating at the 5th harmonic frequency

fundamental d component:

$$A_1 \cdot \sin\left(6\vartheta_{fund} + \Phi_1 - \frac{\pi}{2}\right) \tag{B.1}$$

fundamental q component:

$$A_1 \cdot \sin\left(6\vartheta_{fund} + \Phi_1 - \pi\right) \tag{B.2}$$

7th harmonic d component:

$$-A_7 \cdot \sin\left(12\vartheta_{fund} + \Phi_7 - \frac{\pi}{2}\right) \tag{B.3}$$

7th harmonic q component:

$$-A_7 \cdot \sin\left(12\vartheta_{fund} + \Phi_7 - \pi\right) \tag{B.4}$$

11th harmonic d component:

$$A_{11} \cdot \sin\left(6\vartheta_{fund} + \Phi_{11} + \frac{\pi}{2}\right) \tag{B.5}$$

11th harmonic q component:

$$A_{11} \cdot \sin\left(6\vartheta_{fund} + \Phi_{11} - \pi\right) \tag{B.6}$$

13th harmonic d component:

$$A_{13} \cdot \sin\left(18\vartheta_{fund} + \Phi_{13} - \frac{\pi}{2}\right) \tag{B.7}$$

13th harmonic q component:

$$A_{13} \cdot \sin\left(18\vartheta_{fund} + \Phi_{13} - \pi\right) \tag{B.8}$$

Reference frame rotating at the 7th harmonic frequency

fundamental d component:

$$A_1 \cdot \sin\left(6\vartheta_{fund} - \Phi_1 - \frac{\pi}{2}\right) \tag{B.9}$$

fundamental q component:

$$A_1 \cdot \sin\left(6\vartheta_{fund} - \Phi_1\right) \tag{B.10}$$

5th harmonic d component:

$$-A_5 \cdot \sin\left(12\vartheta_{fund} + \Phi_5 + \frac{\pi}{2}\right) \tag{B.11}$$

5th harmonic q component:

$$-A_5 \cdot \sin\left(12\vartheta_{fund} + \Phi_5 + \pi\right) \tag{B.12}$$

11th harmonic d component:

$$A_{11} \cdot \sin\left(18\vartheta_{fund} + \Phi_{11} + \frac{\pi}{2}\right) \tag{B.13}$$

11th harmonic q component:

$$A_{11} \cdot \sin\left(18\vartheta_{fund} + \Phi_{11} - \pi\right) \tag{B.14}$$

13th harmonic d component:

$$A_{13} \cdot \sin\left(6\vartheta_{fund} + \Phi_{13} - \frac{\pi}{2}\right) \tag{B.15}$$

13th harmonic q component:

$$A_{13} \cdot \sin\left(6\vartheta_{fund} + \Phi_{13} - \pi\right) \tag{B.16}$$

Reference frame rotating at the 11th harmonic frequency

fundamental d component:

$$-A_1 \cdot \sin\left(12\vartheta_{fund} + \Phi_1 + \frac{\pi}{2}\right) \tag{B.17}$$

fundamental q component:

$$-A_1 \cdot \sin\left(12\vartheta_{fund} + \Phi_1\right) \tag{B.18}$$

5th harmonic d component:

$$A_5 \cdot \sin\left(6\vartheta_{fund} - \Phi_5 - \frac{\pi}{2}\right) \tag{B.19}$$

5th harmonic q component:

$$A_5 \cdot \sin\left(6\vartheta_{fund} - \Phi_5 - \pi\right) \tag{B.20}$$

7th harmonic d component:

$$A_7 \cdot \sin\left(18\vartheta_{fund} + \Phi_7 + \frac{\pi}{2}\right) \tag{B.21}$$

7th harmonic q component:

$$A_7 \cdot \sin\left(18\vartheta_{fund} + \Phi_7\right) \tag{B.22}$$

13th harmonic d component:

$$-A_{13} \cdot \sin\left(24\vartheta_{fund} + \Phi_{13} + \frac{\pi}{2}\right) \tag{B.23}$$

13th harmonic q component:

$$-A_{13} \cdot \sin\left(24\vartheta_{fund} + \Phi_{13}\right) \tag{B.24}$$

Reference frame rotating at the 13th harmonic frequency

fundamental d component:

$$-A_1 \cdot \sin\left(12\vartheta_{fund} - \Phi_1 + \frac{\pi}{2}\right) \tag{B.25}$$

fundamental q component:

$$-A_1 \cdot \sin\left(12\vartheta_{fund} - \Phi_1 - \pi\right) \tag{B.26}$$

5th harmonic d component:

$$A_5 \cdot \sin\left(18\vartheta_{fund} + \Phi_5 - \frac{\pi}{2}\right) \tag{B.27}$$

5th harmonic q component:

$$A_5 \cdot \sin\left(18\vartheta_{fund} + \Phi_5\right) \tag{B.28}$$

7th harmonic d component:

$$A_7 \cdot \sin \left(6\vartheta_{fund} - \Phi_7 + \frac{\pi}{2} \right) \tag{B.29}$$

7th harmonic q component:

$$A_7 \cdot \sin \left(6\vartheta_{fund} - \Phi_7 - \pi \right) \tag{B.30}$$

11th harmonic d component:

$$-A_{11} \cdot \sin \left(24\vartheta_{fund} + \Phi_{11} - \frac{\pi}{2} \right) \tag{B.31}$$

11th harmonic q component:

$$-A_{11} \cdot \sin \left(24\vartheta_{fund} + \Phi_{11} \right) \tag{B.32}$$